# APPLIED COMPUTATIONAL ELECTROMAGNETICS SOCIETY JOURNAL

## Special Issue on Finite Difference Methodologies for Microwave, Optical and Photonics, and Superconducting Device Design

### Guest Editors:

Yasushi Kanai, Niigata Institute of Technology, Japan
James B. Cole, Northrop-Grumman, Inc, USA
Saswatee Banerjee, Facebook Research Lab, Cork, Ireland

March 2024
Vol. 39 No. 3
ISSN 1054-4887

**The ACES Journal is abstracted in INSPEC, in Engineering Index, DTIC, Science Citation Index Expanded, the Research Alert, and to Current Contents/Engineering, Computing & Technology.**

The illustrations on the front cover have been obtained from the ARC research group at the Department of Electrical Engineering, Colorado School of Mines

Published, sold and distributed by: River Publishers, Alsbjergvej 10, 9260 Gistrup, Denmark

# MARCH 2024 REVIEWERS

**Mariem Abdi**
**Max J. Ammann**
**Tohid Aribi**
**Saswatee Banerejee**
**Bhattacharya**
**Mahendran C.**
**James B. Cole**
**Thippesha D.**
**Ravi Kumar Goyal**
**Yasushi Kanai**
**Rafał Lech**
**Lihua Li**
**Nithizethe Mhuadthongon**
**Igor Minin**
**Giacomo Paolini**
**Anna Pietrenko-Dabrowska**
**Natarajamani S.**
**Luca Scorrano**
**Lu Wang**
**Dariusz Wojcik**
**Yanlin Xu**
**Hongzheng Zeng**
**Qiwei Zhan**
**Yonghong Zhou**
**Theodoros Zygiridis**

THE APPLIED COMPUTATIONAL ELECTROMAGNETICS SOCIETY JOURNAL

Vol. 39 No. 3 March 2024

## TABLE OF CONTENTS

# Women's History Month Special Article: Interview with Professor Mahta Moghaddam

**Sima Noghanian**

CommScope Ruckus Networks
Sunnyvale, CA, USA
Sima_noghanian@ieee.org

***Abstract –*** March marks Women's History Month, and March 8th is celebrated as International Women's Day. In this Special Article, Sima Noghanian interviews Mahta Mogaddam, renowned scholar in applied and computational electromagnetics.

***Index Terms –*** women in applied computational electromagnetics, women in STEM.

## I. INTRODUCTION

Professor Mahta Moghaddam (Fig. 1) is a Distinguished Professor of Electrical and Computer Engineering (ECE) at the University of Southern California (USC) Viterbi School of Engineering. She also holds various positions including the Ming Hsieh Chair in ECE, at the University of Southern California, Co-Director of the Center for Sustainability Solution, Vice Dean for Research, Head of Microwave Systems, Sensors, and Imaging Lab (MiXIL), Director of USC Viterbi Center for Arid climate WAter REsearch (AWARE), and co-Chair of the President's Working Group on Sustainability. Professor Moghaddam is a Fellow of IEEE and is the Past President of the IEEE Antennas and Propagation Society. She was the Editor-in-Chief of IEEE Antennas and Propagation Magazine and a Distinguished Lecturer of the IEEE Geoscience and Remote Sensing Society. She is a member of the National Academy of Engineering.

Dr. Moghaddam has been an active researcher in various fields including microwave sensing of the environment, electromagnetics for medicine, and smart energy-efficient sensor webs. She has pioneered inventive methodologies and algorithms to quantitatively interpret multichannel radar imagery, utilizing analytical inverse scattering techniques applied to intricate and stochastic media. Dr. Moghaddam has spearheaded the advancement of novel radar instruments and measurement technologies for subsurface and sub-canopy characterization. Notably, she has served as a Systems Engineer for Cassini Radar and held the position of Science Chair for the JPL Team X (Advanced Mission Studies Team). She has also been a member of various NASA missions and program science teams, including SMAP, CYGNSS, and ABoVE [1].

Fig. 1. Professor Mahta Moghaddam.

## II. QUESTIONS AND ANSWERS (Q & A)

***Q1: Could you share a bit about yourself and what drew you to the field of engineering?***

***A1:*** I grew up in a culture that values education and science and that is where it all started. My parents had a big influence on me to appreciate math, physics, and science and how these disciplines explain how the universe works.

While my initial curiosity in these fields was sparked by parental influence, my interest deepened significantly over time. The educational system in Iran is rigorous, inundating students with vast amounts of information. This posed a challenge in discerning what was truly essential from what was not. However, in retrospect, this experience was immensely beneficial. Being exposed to fundamental concepts at an early age proved invaluable, laying a strong foundation for my subsequent education. This foundational understanding proved crucial as I progressed in my studies, fueling my interest further. I developed a strong passion for physics and mathematics.

*Submitted On: May 6, 2024*
*Accepted On: May 6, 2024*



https://doi.org/10.13052/2024.ACES.J.390301

After graduating from high school in Iran, I arrived in the US and began my undergraduate studies. Initially, I enrolled as a physics major, drawn to its explanatory power in understanding the world. However, I soon switched to electrical engineering, seeing it as closely aligned with physics from a more applied perspective, particularly in the realm of electromagnetics. My interest in electromagnetics was further fueled by the guidance of excellent professors during my undergraduate studies. Engaging in hands-on labs in electromagnetics deepened my appreciation for the subject. And so, my journey towards specializing in electromagnetics began, influenced by both practical considerations and inspirational academic experiences.

I attended the University of Kansas in Lawrence, KS. Thanks to the robust educational foundation in Iran, I completed my undergraduate studies in just 3 1/2 years by taking on a heavy course load. The initial years were straightforward as I had covered much of the material in high school. The later semesters became more challenging but also more intriguing. I managed to graduate early and pursue graduate studies, focusing on electromagnetics.

For my graduate studies, I chose the University of Illinois at Urbana-Champaign, where I had the privilege of being advised by Professor Weng Cho Chew. I applied to several schools and it was not customary to visit the school during the application process. Interestingly, Professor Chew was the only one among my prospective advisors who invited me to visit the campus. Despite a short and disrupted visit due to weather conditions, I was deeply impressed by his genuine care and hospitality. This encounter greatly influenced my decision to join his research group.

Professor Chew, renowned for his expertise in theoretical and computational electromagnetics, was an exacting yet excellent mentor. He was a demanding advisor. Under his guidance, I and my peers were pushed to excel, laying a solid foundation for our future endeavors. The experience, akin to ”drinking from a fire hose,” was immensely rewarding, shaping my academic and professional trajectory.

***Q2: Did your interest in electromagnetics begin during high school, undergraduate studies, or when you started working with Prof Chew?***

***A2:*** I would attribute my foundational understanding of electromagnetics to my high school education, although at that time we didn't explicitly refer to it as electromagnetics; rather, it fell under the umbrella of physics. It was during my undergraduate studies that I encountered electromagnetics courses, which solidified my understanding of the subject and reinforced its connection to physics. Looking back, I'm very happy with my choice to specialize in electromagnetics, although there was a period when I entertained the idea of pursuing photonics or semiconductor technology. However, as I reflect on the importance of waves and fields in modern technology, particularly in wireless sensing and communication systems, I am reaffirmed in my decision to focus on electromagnetics. It remains a pivotal area of study with significant relevance in today's technological landscape.

***Q3: You mentioned your transition from Iran to studying in the United States, experiencing a new culture and environment. Despite these challenges, you succeeded. How do you reflect on this experience? Do you feel it made you stronger, or was it exceptionally difficult? Would it have been easier if you weren't an immigrant? What impact did it have?***

***A3:*** That's a profound question that I've pondered over the years. While I can't definitively say whether it would have been easier had I not been an immigrant, undoubtedly, being born in the US would have presented fewer hurdles. Nevertheless, I never perceived my journey as overwhelmingly difficult. Sure, there were adjustments, such as being away from my parents, but I was fortunate to have my sister here. She helped me adjust and not feel overwhelmed. I was immensely grateful for the opportunity and approached it with a positive mindset, recognizing the privilege I had been given. I understood that many others around the world face far greater challenges. This perspective drove me to seize the opportunity and make the most of it.

***Q4: As a woman in the field of engineering, particularly electromagnetics, you are part of a minority. There are relatively few women in engineering, especially in electrical engineering with a specialization in electromagnetics. Why do you think this is the case? Did you notice this lack of representation when you first entered the field, and what do you think can be done to make it more appealing to women?***

***A4:*** It is indeed a complex issue, and I believe there are several factors at play. Firstly, I am not sure if the scarcity of women in electromagnetics is a phenomenon limited to the US or if it is prevalent worldwide. Unfortunately, I don't have the statistics from other regions to make a comparison. It seems in the US to be a cultural bias against women pursuing engineering, which might discourage girls in high school from considering it as a viable career option. This societal pressure can be a significant deterrent.

Secondly, beyond cultural influences, I believe women may inherently seek professions where they perceive a tangible impact from their work. Historically, electromagnetics might not have been seen as a field with immediate societal impact, unlike medicine,

robotics, or biomedical engineering. However, as technology evolves, the significance of electromagnetics in various applications becomes more apparent. From wireless systems to biomedical systems, many imaging, sensing, and therapeutic systems involve electromagnetic fields. This shift in perception could attract more women to the field.

As we continue to highlight the diverse applications and societal impacts of electromagnetics, I believe more women will be drawn to it. Indeed, we are witnessing positive changes in this regard, with increasing numbers of women pursuing careers in electromagnetics.

***Q5: Your work spans various fields, particularly biomedical and environmental, showcasing significant impact. Could you elaborate on your contributions in these areas from grad school to the present?***

***A5:*** Certainly. During my graduate studies, my research focused on theoretical aspects with practical applications, particularly in subsurface sensing for resource exploration and solving inverse problems with biomedical implications. However, the scope of a PhD is limited, and upon joining JPL (Jet Propulsion Laboratory), which was my first job, I delved into environmental remote sensing. Leveraging my background in inverse problems, I applied quantitative inversion techniques to remote sensing applications. That is how I started applying inverse problems to remote sensing, collaborating with scientists from diverse disciplines like ecology and hydrology. This collaboration was enlightening, as it highlighted how engineering and remote sensing technologies could aid in understanding global climate change and improving predictive models (Fig. 2). That was exciting, motivating, and rewarding.

Fig. 2. Professor Moghaddam [2].

In my group, we have also maintained a focus on medical applications, integrating electromagnetics into microwave imaging systems for thermal therapy support (Figs. 3–5). By applying inverse problems to these systems, we developed near-real-time monitoring of ablation therapies. This involves detecting changes in the dielectric constant, which correlates strongly with temperature variations in human tissue due to its high water content. This interdisciplinary approach has the potential to enable much more effective medical treatments, offering precise and effective monitoring during thermal therapies.

Fig. 3. Professor Moghaddam and her research team [3].

Fig. 4. Professor Moghaddam during a fieldwork trip in the boreal forests in Canada.

***A6: You serve as a role model for younger students and aspiring professionals, inspiring them to pursue similar paths. How do you perceive yourself in this role? Have you encountered students who express admiration and a desire to emulate your achievements?***

***A6:*** Thank you for your kind words. I am truly humbled by the notion of being seen as a role model. It is incredibly heartwarming and serves as validation for the efforts I have put forth thus far. Whenever someone expresses


Fig. 5. Professor Moghaddam with her team on Earth Day.

admiration and mentions being inspired by my journey, it deeply touches me. While I don't consciously perceive myself as a role model, hearing such sentiments is truly gratifying. I suppose it could be attributed to my approach of focusing on solutions rather than dwelling on challenges. Engineers inherently adopt this mindset – when faced with a problem, our instinct is to find a solution.

If my attitude resonates with students and junior colleagues, and if it encourages them to adopt a similar problem-solving approach, then I am more than happy to serve as a conduit for that perspective. It's crucial to recognize both the challenges we can address and those beyond our control. Wasting energy on the latter only detracts from our well-being and productivity. Therefore, emphasizing what we can influence is key. Ultimately, if my experiences can guide others in navigating their own paths with resilience and focus, then I consider that a privilege and a responsibility worth embracing.

***Q7: You mentioned transitioning from JPL to university academic positions. What motivated this change, and how do you perceive the pros and cons of working in academia versus a non-academic setting?***

***A7:*** It is challenging to delineate between the two experiences. My tenure at JPL was immensely fulfilling. Initially, I joined with the intention of gaining insights into the "industry," thinking it would be a brief stint before returning to academia. Two years became 12 years. I found myself captivated by the stimulating environment and the intriguing problems to tackle. Despite this, my desire to contribute to student training and nurture the next generation persisted, drawing me towards academia.

One significant distinction lies in the scope of problems tackled. At JPL, the focus is often on a set of issues aligned with the organization's mission. While very exciting, it is not as diverse a portfolio as that of academia, where a broader spectrum of topics can be explored with access to more diverse funding sources. This breadth of focus in academia appealed to me, allowing for a more expansive impact.

I cherish my time at JPL, while currently enjoying a blend of both worlds. Collaborations and joint projects with former colleagues enable me to maintain ties with JPL while embracing the academic realm.

***Q8: Have you ever been passionate about an idea, applied for funding, and faced rejection? If so, how did you handle it?***

***A8:*** Absolutely, it is a common occurrence. I believe most researchers, including myself, face rejection maybe as often as acceptance. There have been instances where I poured my heart into a proposal, convinced it was groundbreaking, only to receive feedback that tore it apart. Initially, such experiences can be disheartening. However, with time, I've learned to view rejection as a learning opportunity.

Each rejection provides valuable feedback, highlighting both the strengths and weaknesses of the proposal. It is crucial to develop a thick skin and embrace rejection as part of the path toward success. Failure, as counterintuitive as it may seem, is an integral step towards success.

Moreover, I have also learned the importance of providing constructive feedback when reviewing others' works. Understanding the impact of harsh criticism, especially on junior colleagues, has made me more mindful of my feedback. It is essential to offer feedback with kindness and empathy, focusing on constructive criticism rather than discouragement.

***Q9: Can you share a memorable moment from your career, one that stands out either positively or negatively?***

***A9:*** I will share two contrasting moments. Early in my career at JPL, I had what I thought was a groundbreaking idea for an internal funding call. Excitedly, I presented it to my section manager with bright eyes; he looked at it and said: "No, it is never going to work, we will not present it." It was disappointing and left me feeling discouraged. He was right, but he did not take any time to explain to me why it could not work. Despite the initial setback, I persevered, reevaluated my concept, and eventually refined it into a successful proposal. This experience taught me the importance of resilience and not allowing rejection to stifle creativity. I also learned not to reject ideas without clarity, causing discouragement in the young engineers.

On a more positive note, decades later, I was deeply honored to receive the Distinguished Alumni Award from the University of Kansas, my undergraduate alma mater (Fig. 6). The unexpected recognition filled me with joy and gratitude, reminding me of the lasting impact of

my education and the connections forged over the years. I couldn't believe that the university still remembered me after decades!

However, the most rewarding moments in my career are witnessing the success of my students. Whether it is seeing them graduate, publish a paper, or defend their thesis, their achievements bring me immense pride and motivation. While I play a role in their journey, their accomplishments belong to them, serving as a reminder of the importance of mentorship and nurturing the next generation of scholars.

Fig. 6. Professor Moghaddam received the Distinguished Service Alumni Award from the University of Kansas [4].

***Q10: What advice do you have for students and young professionals interested in working in this field?***

***A10:*** My advice encompasses both career and personal aspects. Firstly, if you have a passion or strong interest in the field, persevere and pursue it wholeheartedly. Immerse yourself in the problem you are tackling, knowing that obstacles are inevitable but surmountable.

Equally important, prioritize being a thoughtful, kind, and considerate individual. In the grand scheme of life, your character and how you impact others matter far more than specific professional achievements. When you are 90 or 100 years old, people will remember you for the person you were and the overall positive impact you left on your colleagues, mentees, and the technical field, not the number of papers, patents, and amount of research funding you generated. Whether you are a researcher, a professor, or a manager, your career title won't define your legacy. It is the kindness, helpfulness, and positive impact you leave behind that truly resonate.

***Q11: What inspires you the most?***

***A11:*** For me, it is the human factor, which includes the true societal impact of our technical work. I find immense inspiration in considering the people involved: my partners, collaborators, and the team executing the work (Fig. 7). I am driven by questions about the human outcomes, the training opportunities we can provide, and the collective impact we can make. Year after year, this aspect has only grown in importance to me.

Fig. 7. Professor Moghaddam celebrating with her students and their families on their graduation day.

***Q12: What do you envision for your future? What challenges do you aim to tackle, particularly in the field of computationally applied electromagnetics?***

***A12:*** Over the three decades since earning my Ph.D., there has been a persistent challenge in connecting remote sensing and electromagnetic inverse problems. The sheer size of the remote sensing problem, spanning hundreds of thousands or millions of wavelengths, poses a significant computational challenge. Despite advances in computational electromagnetics, we haven't been able to fully address this issue. My goal is to bridge this gap and find a solution that doesn't compromise the underlying physics of the problem. Currently, we're exploring artificial intelligence and machine learning approaches to complement theoretical electromagnetics. However, I still see this as an unsolved problem that needs attention. We need to find a way to reconcile this mismatch without sacrificing the accuracy and integrity of the physics involved. It's about finding a balance between statistical representations and capturing the intricate details of individual scatterers to truly understand the complexity of remote sensing. Apart from addressing the gap between remote sensing and computational domains, I also believe it's crucial to bridge the gender gap in electromagnetics. There's no fundamental reason why there should be significantly fewer women in this field, and I hope to see more gender parity as we continue to demonstrate the impact of our work. Additionally, attracting more individuals to electromagnetics, regardless of gender, is another important challenge. We need to focus on improving our educational approaches, starting from high school and undergraduate levels. Unfortunately, many academic departments are reducing the

emphasis on electromagnetics education, but we must find ways to address the shortfall. This mission is on us.

## REFERENCES

[1] Wikipedia. *Mahta Moghaddam* [Online]. Available: https://en.wikipedia.org/wiki/Mahta_Moghaddam.

[2] tumblr. *Looking 50 years in the future with NASA earth scientists* [Online]. Available: https://nasa.tumblr.com/post/161601655879856947 2/looking-50-years-in-the-future-with-nasa-earth.

[3] USC University of Southern California. *Microwave Systems, Sensors and Imaging Lab (MiXIL)* [Online]. Available: https://mixil.usc.edu/about.

[4] The University of Kansas. *2023 KU EECS KEDS Award Presented* [Online]. Available: https://eecs.ku.edu/2023-ku-eecs-keds-award-presented.

**Sima Noghanian** is the chair of the ACES Communication and Membership Committee and serves as an Associate Editor of the ACES Journal. She received a B.Sc. degree in electrical engineering from the Sharif University of Technology, Tehran, Iran, and an M.Sc. and Ph.D. degrees, both in electrical engineering, from the University of Manitoba, Winnipeg, Canada. She is currently a Distinguished Hardware Engineer at CommScope Ruckus Networks. Her research interests include MIMO antennas for wireless communications, wearable and implanted antennas, 3D printed antennas, wireless power transfer, microwave imaging, and wireless channel modeling.

# Special Issue Preface

Welcome to the special issue of the Journal of the Applied Computational Electromagnetics Society (ACES). Most of the papers included here are extended versions of ones presented at the ACES-2023 conference (Monterey, California, April 2023).

In recent years ACES has broadened its focus from "traditional" engineering electromagnetics to include optics and photonics, materials science, high performance computing, and lately machine learning and quantum computing. Papers now range from scientific theoretical and mathematical to engineering applications and device design.

The contents of this special issue mirror this trend. New computational methodologies are introduced in

> "A Path Integral Representation Model to Extend the Analytical Capability of the Nonstandard Finite-Difference Time-Domain Method" (ACES-2023, paper 22727);
>
> A Simple, Method of Moments Solution for the Integral Equations for Multiple Dielectric Bodies of Arbitrary Shape in Time Domain (ACES-2023, paper 23087);
>
> "Nonstandard Finite Difference Time Domain Methodology to Simulate Light Propagation in Nonlinear Materials" (ACES-2023, paper 23363).

On the other hand

> Parameter Sensitivity Analysis of 3D-Printed W-Band Reflector Fresnel Lens Antenna Based on Acrylonitrile Butadiene Styrene Plastic (ACES-2023, paper 23497);
>
> Reconfigurable multifunctional transmission metasurface polarizer integrated with PIN diodes working at an identical frequency band (ACES-2023, paper 2831)

use computational methods as a tool to design practical devices. Finally

> Impact Evaluation of an External Point Source to a Generalized Model of the Human Neck (ACES-2023, paper 23499)

develops a model for medical applications.

The diversity of ACES conferences and their inclusiveness foster crosstalk between academic researchers and scientists in corporate and government laboratories, and in the broader engineering community to create an environment that incubates new ideas and collaborations.

We hope that this special issue will encourage you, the reader, to contribute your own results to future ACES conferences or publish them in the ACES journal or special issues such as this.

Prof. Yasushi Kanai, Dr. James B. Cole, and Dr. Saswatee Banerjee, editors.
June 2024

https://doi.org/10.13052/2024.ACES.J.390302

# Nonstandard Finite Difference Time Domain Methodology to Simulate Light Propagation in Nonlinear Materials

**James B. Cole**

University of Tsukuba, Japan
cole@cavelab.cs.tsukuba.ac.jp

***Abstract –*** We extend the nonstandard (NS) finite difference time domain (FDTD) methodology, originally developed to solve Maxwell's equations in linear materials, to nonlinear ones. We validate it by computing harmonics generation in a nonlinear dielectric and comparing with theory. The methodology also applies to the quantum electrodynamics that describes the interaction of charged particles with electromagnetic fields, and also to the Ginzburg-Landau model of superconductivity.

***Index Terms –*** Finite difference time domain (FDTD), nonlinear optics, nonlinear susceptibility, nonstandard FDTD, quantum electrodynamics, superconductivity.

## I. INTRODUCTION

The conventional or standard (S) finite difference time domain (FDTD) methodology [1] is widely used for linear electromagnetic calculations, but its accuracy is low relative to the computational cost. At wavelength $\lambda$ for space-step size $h$, its error scales as $(h/\lambda)^4$ and in three dimensions its computational also cost scales as $(\lambda/h)^4$. We [2] have introduced what is called a nonstandard (NS) FDTD methodology [3] for which the error scales as $(h/\lambda)^8$, but computational cost still scales as $(\lambda/h)^4$.

Nonlinear problems are generally difficult to solve analytically, but numerical methods also often fail to yield good solutions unless the discretization steps are small, and even then numerical instability can arise. A classic example is the logistic equation, the discrete form of which is a well-known example of deterministic chaos. In this paper we extend the NS-FDTD methodology to solve Maxwell's equations for nonlinear materials.

Although not the topic of this paper, the methodology is also useful to solve certain problems in quantum mechanics. For example, the Hamiltonian of a changed particle (of mass $m$,charge $q$) in an electromagnetic field [4] (vector potential $\mathbf{A}$, scalar potential $\varphi$) is nonlinear in the form:

$$H = \frac{1}{2m}\left(-i\hbar\nabla - q\mathbf{A}\right)^2 + q\varphi. \tag{1}$$

## II. NONLINEAR OPTICS

In a nonlinear dielectric the electric displacement is $\mathbf{D} = \varepsilon_0\left(\mathbf{E} + \chi^{(1)}\mathbf{E} + \chi^{(2)}\mathbf{E}^2 + \cdots\right)$, where $\varepsilon_0$ is the vacuum electric permeability, and $\mathbf{E}$ the electric field. We use units in which $\varepsilon_0 = 1$ and the vacuum magnetic permeability is $\mu_0 = 1/c^2$ ($c$ =vacuum velocity of light). Retaining only second order nonlinearity, and defining $\varepsilon = 1 + \chi^{(1)}$, then $\mathbf{D} = \varepsilon\mathbf{E} + \chi^{(2)}\mathbf{E}^2$. Taking the magnetic susceptibility to be $\mu_0$ everywhere, Maxwell's equations become:

$$\begin{aligned} \mu_0\partial_t\mathbf{H} &= -\nabla\times\mathbf{E}, \\ \partial_t\mathbf{D} &= \nabla\times\mathbf{H}, \end{aligned} \tag{2}$$

and the index of refraction is $n = \sqrt{\varepsilon}$. In a linear material $\nabla\bullet\mathbf{D} = 0$ implies $\nabla\bullet\mathbf{E} = 0$, but this is not true in a nonlinear one. If, however, $\chi^{(2)}$ is small, $\nabla\bullet\mathbf{E} = 0$ is a good approximation [5], and Maxwells equations reduce to a nonlinear wave equation of the form:

$$\left(\partial_t^2 - \frac{c^2}{\varepsilon}\nabla^2\right)\mathbf{E}(\boldsymbol{x},t) = -\frac{\chi^{(2)}}{\varepsilon}\partial_t^2\mathbf{E}(\boldsymbol{x},t)^2. \tag{3}$$

For simplicity, we first develop the finite difference model of (3) in one dimension, where it reduces to:

$$\left(\partial_t^2 - \frac{c^2}{n^2}\partial_x^2\right)E(x,t) = -\frac{\chi^{(2)}}{n^2}\partial_t^2E(x,t)^2. \tag{4}$$

Before proceeding further, we first introduce the nonstandard methodology for the linear wave equation.

## III. FINITE DIFFERENCE MODELS FOR THE LINEAR WAVE EQUATION

### A. Notation and definitions

Define the partial difference operator ($d_t$) by $d_t f(x,t) = f(x,t+\Delta t/2) - f(x,t-\Delta t/2)$. Then it is easy to show that $d_t^2 = d_t d_t$ is given by:

$$d_t^2 f(x,t) = f(x,t+\Delta t) + f(x,t-\Delta t) - 2f(x,t). \tag{5}$$

The second derivative is thus approximated by:

$$\Delta t^2\partial_t^2 f(x,t) \cong d_t^2 f(x,t). \tag{6}$$

The operator $d_x^2$ is defined analogously to $d_t^2$ and:

$$\Delta x^2\partial_x^2 f(x,t) \cong d_x^2 f(x,t). \tag{7}$$

We now construct finite difference models of the homogeneous wave equation:

$$\left(\partial_t^2 - v^2\partial_x^2\right)\psi(x,t) = 0. \tag{8}$$

*Submitted On: July 17, 2023*
*Accepted On: April 24, 2024*

https://doi.org/10.13052/2024.ACES.J.390303

### B. Standard finite difference model

Writing $\bar{v} = v\Delta t/\Delta x$, and replacing the derivatives in (8) with the FD expressions (6) and (7), gives the conventional or standard (S) finite difference (FD) model of (8):

$$\left(d_t^2 - \bar{v}^2 d_x^2\right)\psi(x,t) = 0. \tag{9}$$

General solutions of (8) are $f(x \mp vt)$ where $f$ is arbitrary. Substituting $f(x \mp vt)$ into the S-FD model above, we find:

$$\left[d_t^2 - \bar{v}^2 d_x^2\right] f(x \mp vt) = -\left(\frac{1-\bar{v}^4}{12}\right)\Delta x^4 f^{(4)}(x \mp vt) + \cdots. \tag{10}$$

The right side of (10) is the model error. Although it vanishes for $\bar{v} = 1$, across multiple media in which $v$ varies, maintaining $\bar{v} = 1$ by adjusting $\Delta x$ or $\Delta t$ gives rise to large errors on the media boundaries and is thus of limited use in practice.

### C. Nonstandard finite difference model

It is, however, possible to construct an exact FD model with respect to harmonic waves, $\varphi(x,t) = e^{i(kx-\omega t)}$, where $\omega = vk$. Writing $\bar{\omega} = \omega\Delta t$, $\bar{k} = k\Delta x$, and substituting $\varphi$ into (9) gives:

$$\left[d_t^2 - \bar{v}^2 d_x^2\right]\varphi = 4\left[-\sin^2\left(\bar{\omega}/2\right) + \bar{v}^2\sin^2\left(\bar{k}/2\right)\right]\varphi. \tag{11}$$

The right side of (11) can be made to vanish with the substitution $\bar{v} \to \tilde{v}$, where:

$$\tilde{v} = \sin\left(\bar{\omega}/2\right)/\sin\left(\bar{k}/2\right). \tag{12}$$

Thus, an exact model of the wave equation with respect to harmonic waves is:

$$\left(d_t^2 - \tilde{v}^2 d_x^2\right)\psi(x,t) = 0. \tag{13}$$

This FD model is exact because $\varphi$ is a solution of both the wave equation (8) and its model (13). This is an example of what is called an NS model [3]. Expanding $d_t^2\psi(x,t)$ via (5) and solving for $\psi(x,t+\Delta t)$, we obtain an exact NS FDTD algorithm:

$$\psi(x,t+\Delta t) = -\psi(x,t-\Delta t) + \left[2 + \tilde{v}^2 d_x^2\right]\psi(x,t). \tag{14}$$

### D. Numerical stability and accuracy

The numerical stability condition [2, 6] for the S- and NS-FDTD algorithms is:

$$\frac{v\Delta t}{\Delta x} \le 1. \tag{15}$$

In the case $v\Delta t/\Delta x = 1$, the S- and NS-FD models are equivalent and exact with respect to any waveform. However, whatever the value of $0 < v\Delta t/\Delta x \le 1$, for a supposition different frequencies, the shortest period ($T_{\min}$) corresponding to the highest frequency ($\nu_{\max}$) must satisfy the Nyquist sampling criterion [7]:

$$T_{\min}/\Delta t > 2, \tag{16}$$

and the minimum wavelength ($\lambda_{\min}$) must satisfy:

$$\lambda_{\min}/\Delta x > 2. \tag{17}$$

### E. Wave equation with a source

To iterate the FDTD algorithm, two initial fields are needed. They can be generated by turning on sources at time = 0. The wave equation with a source $s(x,t)$ is:

$$\left(\partial_t^2 - v^2\partial_x^2\right)\psi(x,t) = s(x,t). \tag{18}$$

#### *Standard finite difference model*

Substituting FD expressions of the derivatives in (18) the S-FD model is:

$$\left(d_t^2 - \bar{v}^2 d_x^2\right)\psi(x,t) = \Delta t^2 s(x,t). \tag{19}$$

It is interesting to note that while the stability conditions of (15), (16) and (17) still hold, the S-FDTD algorithm for the wave equation with a source is not exact even for $v\Delta t/\Delta x = 1$.

#### *Nonstandard finite difference model*

To derive the NS-FD model, we examine the analytic solution of (18). Imposing the initial conditions that $\psi$ and its first time derivative vanish for $t \le 0$, $\psi(x,t)|_{t\le 0} = \partial_t\psi(x,t)|_{t\le 0} = 0$, the Green's function that solves (18) is:

$$G(x-x',t-t') = \frac{1}{2v}\Theta\left(v[t-t'] - |x-x'|\right), \tag{20}$$

where the step function is defined by $\Theta(t) = 0$ for $t < 0$ and $\Theta(t) = 1$ for $t \ge 0$. Using (20) it can be shown that the harmonic point source:

$$s_0(x,t) = 2v\,\omega\,\delta(x)\,\Theta(t)\cos(\omega t), \tag{21}$$

generates an outgoing unit sine wave:

$$\psi_0(x,t) = \Theta\left(\omega t - k|x|\right)\sin\left(t - |x|/v\right). \tag{22}$$

Modeling $\delta(x)$ as $\delta_{x,0}/\Delta x$, where $\delta_{x,0} = 1$ for $x = 0$ and $\delta_{x,0} = 0$ for $x \ne 0$, and putting $s \to s_0$ in (19), the S-FD model becomes:

$$\left(d_t^2 - \tilde{v}^2 d_x^2\right)\psi(x,t) = 2v\,\omega\frac{\Delta t^2}{\Delta x}\,\delta_{x,0}\,\Theta(t)\cos(\omega t). \tag{23}$$

We now postulate the NS-FD model to be:

$$\left(d_t^2 - \tilde{v}^2\partial_x^2\right)\psi(x,t) = 2v\,\omega\tilde{A}\,\delta_{x,0}\,\Theta(t)\cos(\omega t), \tag{24}$$

where $\Delta t^2/\Delta x \to \tilde{A}$, which is to be determined. Requiring that $\psi_0$ be a solution of both (18), with $s = s_0$, and of (24), we find [3]:

$$\tilde{A} = \frac{2}{\omega\,v}\frac{\sin^2(\bar{\omega}/2)}{\tan(\bar{k}/2)}. \tag{25}$$

When a source is abruptly switched on in FDTD calculations it produces extraneous frequency components which give rise to large errors [3]. This is remedied by replacing the step function with a slow switch-on function. A commonly used one is:

$$\Theta_g(t) = \Theta(t)\left[1 - e^{-\beta^2 t^2}\right]. \tag{26}$$

Taking $1/\beta$ to be several wave periods suffices to suppress the errors. The NS source model which generates $\psi_0$ in a NS-FDTD calculation is thus:

$$\tilde{s}_0(x,t) = 4\frac{\sin^2(\bar{\omega}/2)}{\tan(\bar{k}/2)}\,\delta_{x,0}\,\Theta_g(t)\cos(\omega t). \tag{27}$$

With $\tilde{A}$ given by (25) the NS-FD model (24) is exact. As expected, in the limits $\Delta x \to 0$ and $\Delta t \to 0$, the NS-FD model reduces to the S-FD one.

The NS-FDTD model of the wave equation with a harmonic point source is thus:

$$\begin{aligned}\psi(x,t+\Delta t) \;=\; & -\psi(x,t-\Delta t) \\ & +\left[2+\tilde{v}^2 d_x^2\right]\psi(x,t)+\tilde{s}(x,t).\end{aligned} \tag{28}$$

When $\tilde{s}=\tilde{s}_0$ the iteration of (28) generates the outgoing unit sine wave given by (22), where $k$ and $\omega$ are related by:

$$\sin\left(\omega\Delta t/2\right)=\tilde{v}\sin\left(k\Delta x/2\right). \tag{29}$$

***Initialization and iteration***

The FDTD calculation is initialized by taking

$$\psi(x,-\Delta t)=\psi(x,0)=0, \tag{30}$$

and switching on the source at $t=0$ generates the incident field.

The boundary conditions at material interfaces are determined by the wave equation itself, viz. continuity of both the field and its first partial derivative with respect to position. Since null fields obviously satisfy these conditions, and because FDTD derives directly from the wave equation, the generated fields automatically satisfy the boundary conditions as they impinge upon material interfaces when the algorithm is iterated.

### F. Multi-frequency NS-FDTD

It might seem that NS-FDTD is applicable only to monochromatic waves, but it is also valid for multiple frequencies. For a fixed value of $\tilde{v}$, models (13) and (24) are exact for any angular frequency-wavenumber pair $(\omega_i,k_i)$ related by:

$$\sin\left(\omega_i\Delta t/2\right)=\tilde{v}\sin\left(k_i\Delta t/2\right). \tag{31}$$

Thus, the NS-FD model is exact with respect to a multi-frequency wave of the form:

$$\varphi_\Sigma(x,t)=\sum_i a_i e^{i(k_i x\pm\omega_i t)}, \tag{32}$$

which is produced by multi-frequency source superposition. For example:

$$\tilde{s}_\Sigma(x,t)=4\delta_{x,0}\Theta_g(t)\sum_i\frac{\sin^2(\bar{\omega}_i/2)}{\tan(\bar{k}_i/2)}\cos(\omega_i t) \tag{33}$$

generates a frequency superposition of unit sine waves. Such a superposition is useful for high accuracy computations of reflection or transmission spectra. The maximum frequency is limited by the time step according to the Nyquist sampling criterion given by (16).

### G. Nonstandard model of refractive index

Let $k_0$ be the vacuum wave number and $\omega_0=c\,k_0$ be the angular frequency of a light wave. In a medium of refractive index $n$ the wavenumber is $k=nk_0$. From (12) the algorithmic vacuum velocity of light in the NS-model is:

$$\tilde{c}=\sin\left(\bar{\omega}_0/2\right)/\sin\left(\bar{k}_0/2\right). \tag{34}$$

In a medium of refractive index $n$ the algorithmic velocity of light is:

$$\tilde{v}=\sin\left(\bar{\omega}_0/2\right)/\sin\left(n\bar{k}_0/2\right). \tag{35}$$

Define the nonstandard index of refraction to be $\tilde{n}=\tilde{c}/\tilde{v}$:

$$\tilde{n}=\frac{\sin(n\bar{k}_0/2)}{\sin(\bar{k}_0/2)}. \tag{36}$$

The nonstandard FDTD algorithm (28) is thus:

$$\begin{aligned}\psi(x,t+\Delta t) \;=\; & -\psi(x,t-\Delta t) \\ & +\left[2+\tfrac{\tilde{c}^2}{\tilde{n}^2}d_x^2\right]\psi(x,t)+\tilde{s}(x,t).\end{aligned} \tag{37}$$

Before proceeding to the nonlinear NS-model we introduce a simplified and abbreviated notation. Discretizing space time as $x=\chi\Delta x$, $t=\tau\Delta t$ and defining $\psi(x,t)=\psi_\chi^\tau$,

($\tau$, $\chi$ integers), (37) is compactly rewritten as:

$$\psi_\chi^{\tau+1}=-\psi_\chi^{\tau-1}+\left[2+\frac{\tilde{c}^2}{\tilde{n}^2}d_x^2\right]\psi_\chi^\tau+\tilde{s}_\chi^\tau, \tag{38}$$

with the definitions $d_x^2\psi_\chi^\tau=\psi_{\chi+1}^\tau+\psi_{\chi-1}^\tau-2\psi_\chi^\tau$, $d_t^2\psi_\chi^\tau=\psi_\chi^{\tau+1}+\psi_\chi^{\tau-1}-2\psi_\chi^\tau$ (compare with equation 5).

## IV. FINITE DIFFERENCE MODELS OF THE NONLINEAR WAVE EQUATION

### A. Standard finite difference model

First construct the S-FD model of (4). For notational clarity suppress the spatial dependence and denote time as a subscript, thus $E_\tau=E(x,\tau\Delta t)$. Writing $\bar{c}=c\,\Delta t/\Delta x$, the S-FD model of nonlinear wave equation (4) is:

$$\left(d_t^2-\frac{\bar{c}^2}{n^2}d_x^2\right)E_\tau=-\frac{\chi^{(2)}}{n^2}\left[E_{\tau+1}^2+E_{\tau-1}^2-2E_\tau^2\right]. \tag{39}$$

The intractability of this model is immediately evident. Since (39) is quadratic in $E_{\tau+1}$, there are two solutions and it is unclear *a priori* which one to use.

### B. Nonstandard finite difference model

In nonstandard models a term of power $m$ (a positive integer), such as $E(x,t)^m$ is modeled as [3, 8]:

$$E_\tau^m=E_\tau^m E_{\tau-1}^m\cdots E_{\tau-m+1}^m. \tag{40}$$

The NS-model of $E(x,t)^2$is thus $E_\tau^2=E_\tau E_{\tau-1}$. Modeling $d_t^2E(x,t)^2$ as:

$$d_t^2E_\tau^2=E_{\tau+1}E_\tau+E_{\tau-1}E_{\tau-2}-2E_\tau E_{\tau-1}, \tag{41}$$

postulate the NS-FD model of (4) to be:

$$\begin{aligned}&\left(d_t^2-\frac{\tilde{c}^2}{\tilde{n}^2}d_x^2\right)E_\tau=-\frac{\chi^{(2)}}{\tilde{n}^2} \\ &\qquad\left[E_{\tau+1}E_\tau+E_{\tau-1}E_{\tau-2}-2E_\tau E_{\tau-1}\right]+\tilde{s}_\tau,\end{aligned} \tag{42}$$

where $\tilde{s}_\tau$ is a nonstandard source term that generates the fields. Solving for $E_{\tau+1}$ we find:

$$\begin{aligned}&E_{\tau+1}= \\ &\frac{2E_\tau\left[\tilde{n}^2+\chi^{(2)}E_{\tau-1}\right]-E_{\tau-1}\left[\tilde{n}^2+\chi^{(2)}E_{\tau-2}\right]+\tilde{c}^2d_x^2E_\tau}{\tilde{n}^2+\chi^{(2)}E_\tau}+\tilde{s}_\tau.\end{aligned} \tag{43}$$

Whereas the FDTD algorithms for the linear wave equation require two initial fields, the NS-FDTD for nonlinear wave equation requires three. To iterate (43) Take $E_{-2} = E_{-1} = E_0 = 0$, and switch on the source at $t = 0$.

### C. Computational model

We take the computational domain to be $0 \le x \le N\Delta x$. In Fig. 1 the nonlinear dielectric (magenta) is immersed in vacuum (white) and illuminated by a point harmonic source (**S**) of angular frequency $\omega_0$. **S** is located at $x = p > \Delta x$, away from the computational boundary, thus:

$$\tilde{s}_0(x,t) = 4\frac{\sin^2(\bar{\omega}_0/2)}{\tan(\bar{k}_0/2)}\,\delta_{x,p}\,\Theta_g(t)\cos(\omega_0 t), \qquad (44)$$

where $c = \omega_0/k_0$. We choose $\Delta t$ and $\Delta x$ such that $\bar{c} = c\Delta t/\Delta x = 1$, and thus $\tilde{c} = \bar{c} = 1$. Thus (only) in vacuum, as noted in Section II D, the S-FDTD and NS-FDTD algorithms are equivalent and exact. With the choices above in the vacuum:

$$E_{\tau+1} = -E_{\tau-1} + \left[2 + d_x^2\right] E_\tau + \tilde{s}_\tau, \qquad (45)$$

where $s_\tau = s_0(x,t)$. Because the boundaries of the computational domain are vacuum and $\bar{c} = 1$, the Mur absorbing boundary [9, 10] is exact, and is given by:

$$E(0,t+\Delta t) = E(\Delta x,t), \qquad (46)$$

$$E(N\Delta x,t+\Delta t) = E(N\Delta x-\Delta x,t). \qquad (47)$$

Taking the vacuum wavelength of the incident field be $\lambda_0 = 1200\,\text{nm}$, let $\Delta x = \lambda_0/64 = 18.75\text{nm}$, which implies the wave period $T_0 = \lambda_0/c$. Setting

$$\Delta t = T_0/64 = 6.25\times10^{-17}\,\text{sec} \qquad (48)$$

gives $\bar{c} = \tilde{c} = 1$. For this choice, the source simplifies to:

$$\tilde{s}_0(x,t) = 2\,\sin(\bar{\omega}_0)\,\delta_{x,0}\,\Theta_g(t)\cos(\omega_0 t). \qquad (49)$$

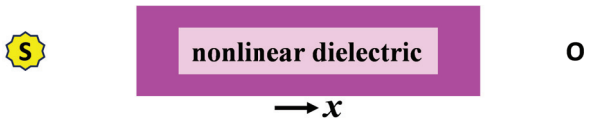


Fig. 1. Computational set-up to simulate propagation and harmonic generation in a non-linear dielectric illuminated by a point harmonic source **S** located in vacuum. The time dependence of the transmitted field is recorded at point **O** outside the dielectric.

## V. RESULTS AND COMPARISON WITH SEMI-ANALYTIC CALCULATION

Take $n$= 1.6, $\chi^{(2)} = 0.05$, the source amplitude to be 1.1, $\omega_0/2\pi = 1/64\Delta t$, and the source rise time $1/\beta = 4T_0$, where $T_0 = 2\pi/\omega_0$.

Figure 2 is a snapshot of the position dependence of $E$. A time series of the electric field amplitude was collected at an observation point outside the dielectric

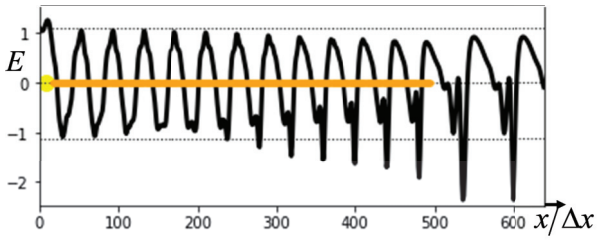


Fig. 2. Light from a source (yellow dot) enters the dielctric material (orange line). As the electric field (black curve) traverses the material, harmonics are generated.

after the source switched on and the field had completely traversed the dielectric. The data were analyzed with a discrete Fourier transform (DFT). The DFT amplitudes of the harmonic frequencies are shown in Fig. 3.

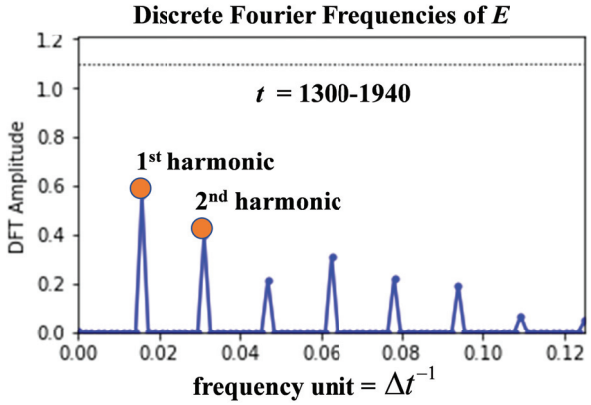


Fig. 3. Harmonics generation in a nonlinear dielectric. Time steps from $1300 \le t/\Delta t \le 1940$ were analyzed. The frequency unit is $\Delta t^{-1} = 16 \bullet 10^{15}$Hz.

In Fig. 4 we compare our simulation with a semi-analytic calculation based on the low depletion approximation [1]. The low depletion model assumes that energy is slowly transferred from the fundamental mode to the higher harmonics. This is the usual case when $\chi^{(2)}$ is small.

## VI. EXTENSION TO TWO AND THREE DIMENSIONS

The linear homogeneous wave equation in three dimensions is:

$$\left(\partial_t^2 - v^2\nabla^2\right)\psi(\boldsymbol{x},t) = 0, \qquad (50)$$

where $\boldsymbol{x} = (x,y,z)$. Defining $d_y^2$ and $d_z^2$ by analogy with $d_x^2$, define the Laplacian difference operator:

$$\mathbf{d}^2 = d_x^2 + d_y^2 + d_z^2. \qquad (51)$$

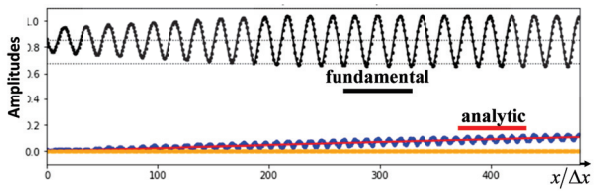


Fig. 4. Amplitudes first harmonic (black) and second harmonic (blue) with position and in the nonlinear material (orange). Comparison with theory (red) in the low depletion approximation.

Taking $\Delta x = \Delta y = \Delta z = h$:

$$\nabla^2 f(x) \cong \frac{\mathbf{d}^2}{h^2} f(x). \tag{52}$$

The S-FD model for the three-dimensional wave equation is thus:

$$\left(d_t^2 - \bar{v}^2 \mathbf{d}^2\right) \psi(x,t) = 0, \tag{53}$$

where $\bar{v} = v\Delta t / h$.

To construct the NS-model, define:

$$\tilde{\mathbf{d}}^2 = \mathbf{d}^2 + \left(\frac{1}{6} + \frac{(k_0 h)^2}{180}\right)\left[d_x^2 d_y^2 + d_x^2 d_z^2 + d_y^2 d_z^2\right] + \frac{1}{30} d_x^2 d_y^2 d_z^2. \tag{54}$$

The motivation and derivation of this definition is found in [3]. The NS-FD model of wave equation (50) becomes

$$\left(d_t^2 - \tilde{v}^2 \tilde{\mathbf{d}}^2\right) \psi(x,t) = 0, \tag{55}$$

where $\tilde{v}$ is given by (12) and $\tilde{k} = kh$. The NS-source model remains the same but with $\Delta x \to h$.

Table 1 lists the stability conditions for the S- and NS- algorithms.

Table 1: Stability conditions for the S- and NS- algorithms

| | Maximum Stable Value Theoretical / Practical | |
|---|---|---|
| | S-FDTD $\bar{v}$ | NS-FDTD $\tilde{v}$ |
| 1-D | 1/1 | 1/1 |
| 2-D | $\frac{\sqrt{2}}{2} \cong 0.70/0.67$ | 0.86/0.80 |
| 3-D | $\frac{\sqrt{3}}{3} \cong 0.57/0.45$ | 0.80/0.70 |

For S-FDTD, the maximum value of $\bar{v}$ is given, while for the NS-FDTD algorithm the maximum value of $\tilde{v}$ is given. The practical stability limits are somewhat lower due to the termination of the computational boundary. Details of the derivation are found in [2]. The greater

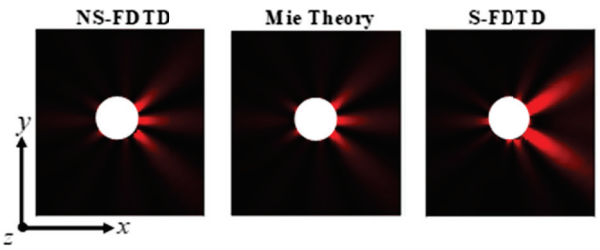


Fig. 5. Mie scattering of an infinite dielectric cylinder (white). Scattered intensity (shades of red) in the exterior was computed using the NS-FDTD and S-FDTD algorithms and compared with Mie theory. Index of refraction = 1.7, vacuum wavelength = 800 nm, cylinder radius = 600 nm, grid spacing = 100 nm.

stability of NS-FDTD allows the solution of problems using fewer time steps. The advantage over S-FDTD is greatest in three dimensions.

The NS-FD model has been validated against analytic solutions of Mie scattering [11, 12], as depicted in Fig. 5. An infinite plane wave (not shown) is incident from the left and the scattered field intensity computed.

In the vacuum (black) the wavelength is $\lambda_0$ =800 nm and in the dielectric (white) it is $\lambda_d = \lambda_0/1.7$, thus in the vacuum $h/\lambda_0 = 1/8 = 0.125$, but in the dielectric $h/\lambda_d = 1.7/8 = 0.2125$, which is just slightly greater that the minimum allowed by the Nyquist criterion for a 2-dimensional (uniform) grid where $h/\lambda$ must satisfy $h/\lambda < 1/(2\sqrt{2}) \cong 0.3536$. Nonetheless the NS-FDTD error remains low. The theoretical error of the NS-FDTD calculation is $\varepsilon_{\mathrm{NS}} \cong (kh)^8 / 438840$, while that of S-FDTD is $\varepsilon_{\mathrm{S}} \cong (kh)^4 / 48$.

The three-dimensional NS-FDTD algorithm for the nonlinear dielectric derives from the one-dimensional form (42) with the substitution $d_x^2 \to \tilde{\mathbf{d}}^2$:

$$\left(d_t^2 - \frac{\tilde{c}^2}{\tilde{n}^2}\tilde{\mathbf{d}}^2\right) E_\tau = -\frac{\chi^{(2)}}{\tilde{n}^2}\left[E_{\tau+1}E_\tau + E_{\tau-1}E_{\tau-2} - 2E_\tau E_{\tau-1}\right] + \tilde{s}_\tau, \tag{56}$$

where $E_\tau$ stands for the $x-$, $y-$, or $z-$component of $\mathbf{E}(\boldsymbol{x}, \tau\Delta t)$.

## VII. SUMMARY AND CONCLUSIONS

We introduced a high precision finite difference time domain algorithm derived from a nonstandard finite difference model to simulate electromagnetic propagation in nonlinear dielectrics. We validated the results of our simulation against an analytic calculation based on the low depletion approximation [5].

This NS-methodology can also be applied to other nonlinear problems, such as quantum electrodynamics in magnetic fields, and to higher order nonlinearities.

We introduced our methodology in one-dimension and extended it to two and three dimensions and have verified its high accuracy and numerical stability [2].

## REFERENCES


[1] K. S. Kunz and R. J. Luebbers, *The Finite Difference Time Domain Method for Electromagnetics*. Boca Raton: CRC Press, 1993.

[2] J. B. Cole and S. Banerjee, *Computing the Flow of Light*, Bellingham: SPIE Press, 2017.

[3] R. Mickens, *Advances in the Applications of Nonstandard Finite Difference Difference Schemes*, Singapore: World Scientific, 2005.

[4] E. Merzbacher, *Quantum Mechanics*, 2nd ed. Hoboken: John Wiley, 1970.

[5] R. W. Boyd, *Nonlinear Optics*, 3$^{rd}$ ed. Cambridge, MA: Academic Press, 2008.

[6] J. Strikwerda, *Finite Difference Schemes and Partial Differential Equations*, 2nd ed. Philadelphia: SIAM, 2004.

[7] J. R. Pierce, *An Introduction to Information Theory: Symbols, Signalsand Noise*, 2nd ed. New York: Dover Publications, 1980.

[8] A. Kiran Güçoğlu, *The Solution of Some Differential Equations by Nonstandard Finite Difference Method*, MS Dissertation, İzmir Institute of Technology, Türkiye, 2005.

[9] B. Engquist and A. Majda, "Absorbing boundary conditions for the numerical simulation of waves," *Mathematics of Computation*, vol. 31, pp. 629–651, 1977.

[10] G. Mur, "Absorbing boundary conditions for the finite- difference approximation of the time domain electromagnetic field equations," *IEEE Transactions on Electromagnetic Compatibility*, vol. 23, pp. 377–382, 1981.

[11] J. A. Stratton, *Electromagnetic Theory*. New York: McGraw-Hill Book Company, 1941.

[12] P. W. Barber and S. C. Hill, *Light Scattering by Particles: Computational Methods*, World Scientific, Singapore, 1990.


**James B. Cole** graduated from the University of Maryland, PhD particle physics. After a post-doctoral fellowship (US National Research Council) at the NASA-Goddard Space Flight Center, he was a research physicist at several US National Laboratories, before joining the faculty of University of Tsukuba (Japan).

After returning to the US, he was a senior research fellow of the National Academy of Sciences, and is now a corporate research physicist. He specializes in mathematical models and high precision algorithm development for applications to computational optics and photonics, quantum mechanics, and machine learning. He is one of the pioneers of the methodology of nonstandard finite differences, and has published numerous papers and a book on the subject.

# A Path Integral Representation Model to Extend the Analytical Capability of the Nonstandard Finite-difference Time-domain Method

**Tadao Ohtani[1], Yasushi Kanai[2], and Nikolaos V. Kantartzis[3]**

[1]Independent Researcher, Asahikawa, 070-0841, Japan
bytcg100@ybb.ne.jp

[2]Department of Engineering, Faculty of Engineering
Niigata Institute of Technology, Kashiwazaki 945-1195, Japan
kanai@iee.niit.ac.jp

[3]Department of Electrical and Computer Engineering
Aristotle University of Thessaloniki, Thessaloniki GR-54124, Greece
kant@ece.auth.gr

***Abstract*** **–** The nonstandard finite-difference time-domain (NS-FDTD) method is a powerful tool for solving Maxwell's equations in their differential form on orthogonal grids. Nonetheless, to precisely treat arbitrarily shaped objects, very fine lattices should be employed, which often lead to unduly computational requirements. Evidently, such an issue hinders the applicability of the technique in realistic problems. For its alleviation, a new path integral (PI) representation model, equivalent to the NS-FDTD concept, is introduced. The proposed model uses a pair of basic and complementary path integrals for the *H*-nodes. To guarantee the same accuracy and stability as the NS-FDTD method, the two path integrals are combined via optimization parameters, derived from the corresponding NS-FDTD formulae. Since in the PI model, *E*-field computations on the complementary path are not necessary, the complexity is greatly reduced. Numerical results from various real-world problems prove that the proposed method improves notably the efficiency of the NS-FDTD scheme, even on coarse orthogonal meshes.

***Index Terms*** **–** Computational electromagnetics, finite-difference time-domain methods, integral equations, radar cross section.

## I. INTRODUCTION

Since its initial advent, the nonstandard finite-difference time-domain (NS-FDTD) method remains a very accurate scheme for electromagnetic field problems [1–15]. Indeed, its accuracy is $10^4$ times higher than that of the FDTD technique [1–4], in the case of coarse grids. Thus, the NS-FDTD method can be suitable for the electromagnetic design and analysis of electrically large structures with various dielectric materials, such as aircraft. Explicitly, the dimensions of a typical aircraft are approximately $500\lambda$-$1800\lambda$, where $\lambda$ is the radar wavelength. Since the wavelength error of the FDTD method, along the axial direction, is $7\lambda$-$25\lambda$ [16–19], it is apparent that such designs are very demanding. On the other hand, the error of the NS-FDTD algorithm is zero [1–4]. Despite this advantage, however, the method is established in differential form and applied to discrete points on orthogonal grids. Thus, its modeling accuracy degrades in the case of real objects with curved surfaces not aligned to the grid axes [16–19].

To overcome these shortcomings, the simplest way is the use of very fine grids, yet at the expense of large overheads. To this aim, a contour-path (CP) model based on the integral form of Maxwell's equations has been presented [16], [17], [20], [21]. As the path integral (PI) scheme, stemming from the Stokes theorem, can handle arbitrary shapes, it can be a potential candidate for such problems, even with coarse lattices. In this context, 2D and 3D PI models have been developed for the NS-FDTD method [22], [23]. Nevertheless, these models are complex for practical applications as they require *E*-node computations for both the complementary and basic paths. Moreover, the numerical stability condition [16], [19] of the prior PI model has not been elaborately derived. The optimization parameters for the PI calculations are approximate values, derived from the numerical dispersion equation. Thus, the efficiency of this PI model could be questionable in some scenarios, e.g., long-term stability and compatibility with the NS-FDTD method in real-world configurations.

In this paper, a new PI form, equivalent to the NS-FDTD formulation in two (2D) and three dimensions (3D), is developed. To achieve a high accuracy with the same isotropy and stability level as the NS-FDTD

*Submitted On: May 18, 2023*
*Accepted On: October 22, 2023*

https://doi.org/10.13052/2024.ACES.J.390304

method, both the basic and complementary path integrals for the $H$-node calculations on square grids are enhanced. Unlike previous PI models [22], [23], the proposed one does not need the $E$-field calculation on the complementary path. The two PIs are combined by new optimization parameters, analytically derived from an equivalency requirement with the NS-FDTD formulae. So, an advanced PI representation model is derived, which can be promptly employed with the NS-FDTD technique. Numerical validations reveal that the featured model drastically extends the applicability of the NS-FDTD algorithm for curved objects on orthogonal grids, attaining high levels of accuracy and convergence.

## II. 2D PATH INTEGRAL FORM

### A. Formulation

Let us consider a PI model on a square lattice that offers the best accuracy for the NS-FDTD method. In the FDTD scheme, a typical propagation error arises along the $0^o$ and $45^o$ directions [16]. For this reason, we adopt two distinct integral paths - the basic and the $45^o$-rotated complementary one - that can mutually cancel their errors, as shown in Fig. 1. For the $H_z$ component, the integral form of Maxwell's equations is given by

$$\begin{aligned}\mu\frac{\partial}{\partial t}\int_S \mathbf{H}\cdot d\mathbf{S} &= -\int_C \mathbf{E}\cdot d\mathbf{l} \Rightarrow \mu\frac{\partial \bar{H}_z(x,y)}{\partial t}\Delta^2 \\ &= -\left[E_y(x+\delta,y) - E_x(x,y+\delta)\right. \\ &\quad \left. -E_y(x-\delta,y) + E_x(x,y-\delta)\right]\Delta,\end{aligned} \tag{1a}$$

for the basic path with $\delta \equiv \Delta/2$, and

$$\begin{aligned}&\mu\frac{\partial \tilde{H}_z(x,y)}{\partial t}2\Delta^2 \\ &= -\left[\tilde{E}_y(x+\delta,y+\delta) - \tilde{E}_x(x-\delta,y+\delta)\right. \\ &\left. -\tilde{E}_y(x-\delta,y-\delta) + \tilde{E}_x(x+\delta,y-\delta)\right]\sqrt{2}\Delta,\end{aligned} \tag{1b}$$

for the complementary path. To guarantee the desired isotropy, the $\partial H_z/\partial t$ terms, obtained from the integral forms of (1a) and (1b), are combined as

$$\frac{\partial H_z(x,y)}{\partial t} = \beta_0^{2D}\frac{\partial \bar{H}_z(x,y)}{\partial t} + (1-\beta_0^{2D})\frac{\partial \tilde{H}_z(x,y)}{\partial t}, \tag{2}$$

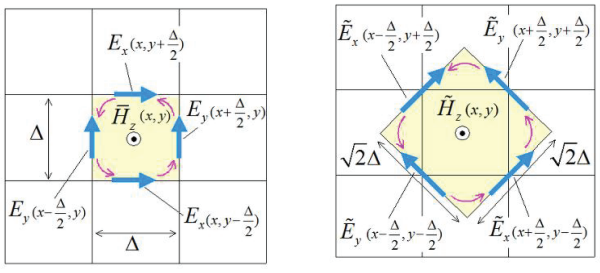


(a) Basic path (b) complementary path

Fig. 1. (a) Basic and (b) complementary (red arrows) integral path on a square grid for the new 2D PI model.

where $\beta_0^{2D}$ is a 2D optimization parameter, to be derived below, that can finely tune the resulting explicit expressions to the same accuracy as those of the NS-FDTD method. Next, the $E_y$ component, on the basic path, in (1a), is calculated as

$$\begin{aligned}&\varepsilon\frac{\partial}{\partial t}\int_S \mathbf{E}\cdot d\mathbf{S} = \int_C \mathbf{H}\cdot d\mathbf{l} \\ &\Rightarrow \varepsilon\frac{\partial E_z(x+\delta,y)}{\partial t} = \frac{H_z(x,y) - H_z(x+\Delta,y)}{\Delta},\end{aligned} \tag{3a}$$

$$\begin{aligned}E_y^{t+\Delta t/2}(x+\delta,y) &= E_y^{t-\Delta t/2}(x+\delta,y) \\ &+ \frac{s_\omega(\Delta t)}{\varepsilon s_k(\Delta)}\left[H_z^t(x,y) - H_z^t(x+\Delta,y)\right].\end{aligned} \tag{3b}$$

Note that in (1)-(3), the cell width $\Delta$ and temporal derivatives $\partial f/\partial t$ are substituted with $s_k(\Delta) = 2\sin(k\Delta/2)/k$ and $\left(f^{t+\Delta t} - f^t\right)/s_\omega(\Delta t)$, respectively, where $k$ is the wave number, $\omega$ the angular frequency, $\Delta t$ the time increment, and $s_\omega(\Delta t) = 2\sin(\omega\Delta t/2)/\omega$ [1–3]. A similar analysis holds for the $E_x$ case, as well. Moreover, the $\tilde{E}_y$ component on the complementary path in (1b), is derived by its existing value on the basic path as

$$\begin{aligned}\tilde{E}_y(x+\delta,y+\delta) &= \left\{\left[E_x(x,y+\delta) + E_x(x+\Delta,y+\delta)\right]\frac{\mathbf{e}_x}{2}\right. \\ &\left. +\left[E_y(x+\delta,y) + E_y(x+\delta,y+\Delta)\right]\frac{\mathbf{e}_y}{2}\right\}\cdot\frac{-\mathbf{e}_x+\mathbf{e}_y}{\sqrt{2}},\end{aligned} \tag{4}$$

while an analogous set for the $E_x$ and $\tilde{E}_x$ components can be equivalently acquired. Also, in (3), $\mathbf{e}_{x,y}$ are the unit vectors on the basic path and $(-\mathbf{e}_x+\mathbf{e}_y)/\sqrt{2}$ the unit vector on the complementary path. Therefore, for the $H_z$ component, in (3), we obtain

$$\begin{aligned}&H_z^{t+\Delta t}(x,y) = H_z^t(x,y) \\ &-\beta_0^{2D}\frac{s_\omega(\Delta t)}{\mu s_k(\Delta)}\left[E_y^{t+\Delta t/2}(x+\delta,y) - E_x^{t+\Delta t/2}(x,y+\delta)\right. \\ &\left. -E_y^{t+\Delta t/2}(x-\delta,y) + E_x^{t+\Delta t/2}(x,y-\delta)\right] \\ &-\left(1-\beta_0^{2D}\right)\frac{s_\omega(\Delta t)}{\mu\sqrt{2}s_k(\Delta)}\left[\tilde{E}_y^{t+\Delta t/2}(x+\delta,y+\delta)\right. \\ &-\tilde{E}_x^{t+\Delta t/2}(x-\delta,y+\delta) - \tilde{E}_y^{t+\Delta t/2}(x-\delta,y-\delta) \\ &\left. +\tilde{E}_x^{t+\Delta t/2}(x+\delta,y-\delta)\right],\end{aligned} \tag{5}$$

which is the formula for the $H_z$ node of our PI model. It is stressed that the use of the interpolated $\tilde{E}_y$ value, from (3), in the PI scheme is different from the 2D PI model of [22], due to the complementary path integral.

### B. Derivation of the $\beta_0^{2D}$ parameter

To obtain the optimal $\beta_0^{2D}$ parameter, we compare the PI form of (3) and the NS-FDTD formula with the operators [1–3]

$$d_x^{(0)} = \alpha_0 d_x^{(1)} + (1-\alpha_0)\,d_x^{(2)}, \tag{6a}$$

$$d_x^{(1)} f(x,y) = f(x+\delta,y) - f(x-\delta,y), \tag{6b}$$

$$d_x^{(2)} f(x,y) = [f(x+\delta,y-\Delta) - f(x-\delta,y-\Delta) + f(x+\delta,y+\Delta) - f(x-\delta,y+\Delta)]/2, \tag{6c}$$

with analogous forms holding for the $d_y^{(*)}$ ones. Note that, herein, we focus on the $\partial_x E_y$ terms to acquire a simple argument. Hence, and after some calculus in (3), one may reach to

$$\begin{aligned} &-\mu \frac{\partial H_z(x,y)}{\partial t}\bigg|_{\partial_x E_y} \\ &= \frac{1+\beta_0^{2D}}{2}[E_y(x+\delta,y) - E_y(x-\delta,y)] \\ &+ \frac{1-\beta_0^{2D}}{4}[E_y(x+\delta,y+\Delta) - E_y(x-\delta,y+\Delta) \\ &\quad + E_y(x+\delta,y+\Delta) - E_y(x-\delta,y+\Delta)]\,|_{\mathrm{PI}} \\ &\equiv \alpha_0 d_x^{(1)} E_y(x,y) + (1-\alpha_0) d_x^{(2)} E_y(x,y)\Big|_{\mathrm{NS-FDTD}}, \end{aligned} \tag{7}$$

Comparing $\beta_0^{2D}$ and $\alpha_0$ from [1–3], we find that

$$\frac{1+\beta_0^{2D}}{2} \equiv \alpha_0 = \frac{1+\gamma_0}{2} \Rightarrow \beta_0^{2D} = \gamma_0 = \frac{2}{3} - \frac{(k\Delta)^2}{90}. \tag{8}$$

Therefore, it is proven that (5) can be equated with the 2D NS-FDTD formula through $\beta_0^{2D}$ given in (8). This implies that the wave propagation characteristics, accuracy, and stability of the new PI model are the same as those of the NS-FDTD method [1–3], [7], [13].

## III. 3D PATH INTEGRAL FORM

### A. Formulation

For the improvement of the 2D PI model, shown in Fig. 1, we must eliminate the propagation error due to angular dependence. To this objective, six square integral paths are devised; i.e., the basic and complementary paths are mutually rotated 45$^o$ (around the $z$-axis) at the $z \pm \Delta$ planes, as in Fig. 2. Using basic and complementary paths in Fig. 2, our PI forms for the $H_z$ component are

$$\begin{aligned} \mu \frac{\partial}{\partial t}\int_S \mathbf{H}\cdot d\mathbf{S} &= -\int_C \mathbf{E}\cdot d\mathbf{l} \Rightarrow \mu \frac{\partial \tilde{H}_z(x,y,z)}{\partial t}\Delta^2 \\ &= -[E_y(x+\delta,y,z) - E_x(x,y+\delta,z) \\ &\quad - E_y(x-\delta,y,z) + E_x(x,y-\delta,z)]\Delta, \end{aligned} \tag{9a}$$

for the basic path, and

$$\begin{aligned} &\mu \frac{\partial \tilde{H}_z(x,y,z)}{\partial t} 2\Delta^2 \\ &= -\left[\tilde{E}_y(x+\delta,y+\delta,z) - \tilde{E}_x(x-\delta,y+\delta,z) \right. \\ &\quad \left. - \tilde{E}_y(x-\delta,y-\delta,z) + \tilde{E}_x(x+\delta,y-\delta,z)\right]\sqrt{2}\Delta, \end{aligned} \tag{9b}$$

for the complementary paths at the $z$ and $z \pm \Delta$ planes. To attain the desired isotropy, we combine the integral forms of (9a) and (9b) as

$$\begin{aligned} \frac{\partial H_z(x,y,z)}{\partial t} &= \beta_1 \left[\beta_0 \frac{\partial \tilde{H}_z(x,y,z)}{\partial t} + (1-\beta_0)\frac{\partial \tilde{H}_z(x,y,z)}{\partial t}\right] \\ &+ \frac{1-\beta_1}{2}\left[\beta_2 \frac{\partial \tilde{H}_z(x,y,z+\Delta)}{\partial t} + (1-\beta_2)\frac{\partial \tilde{H}_z(x,y,z+\Delta)}{\partial t}\right. \\ &\left. + \beta_2 \frac{\partial \tilde{H}_z(x,y,z-\Delta)}{\partial t} + (1-\beta_2)\frac{\partial \tilde{H}_z(x,y,z-\Delta)}{\partial t}\right], \end{aligned} \tag{10}$$

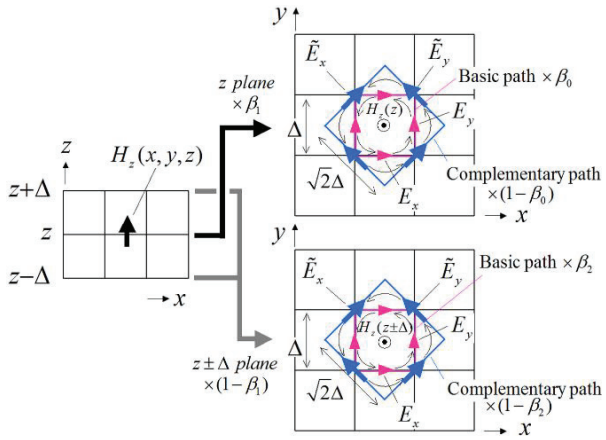


Fig. 2. Basic and complementary integral paths for the calculation of the $H_z$ component on a 3D square grid. Six paths are used at the $z$ and $z \pm \Delta$ planes, while in the two figures on the right, $H_z(z)$ is, actually, $H_z(x, y, z)$ and $H_z(z \pm \Delta)$ is $H_z(x, y, z \pm \Delta)$.

where $\beta_{0,1}$ are the optimization parameters for an isotropic wave propagation. Basically, (9) denotes our 3D PI model. Then, the $E_y$ component in (9a) becomes

$$\begin{aligned} \varepsilon \frac{\partial}{\partial t}\int_S \mathbf{E}\cdot d\mathbf{S} &= \int_C \mathbf{H}\cdot d\mathbf{l} \Rightarrow \varepsilon \frac{\partial E_y(x+\delta,y,z)}{\partial t}\Delta^2 \\ &= [H_z(x,y,z) - H_z(x+\Delta,y,z) \\ &\quad + H_x(x+\delta,y,z+\delta) - H_x(x+\delta,y,z-\delta)]\Delta, \end{aligned} \tag{11a}$$

$$\begin{aligned} E_y^{t+\Delta t/2}(x+\delta,y,z) &= E_y^{t-\Delta t/2}(x+\delta,y,z) \\ &+ \frac{s_\omega(\Delta t)}{\varepsilon s_k(\Delta)}\left[H_z^t(x,y,z) - H_z^t(x+\Delta,y,z)\right. \\ &\left. + H_x^t(x+\delta,y,z+\delta) - H_x^t(x+\delta,y,z-\delta)\right]. \end{aligned} \tag{11b}$$

As with the 2D PI formula, $\Delta$ is replaced with to $s_k(\Delta)$ and $\partial f/\partial t$ with $\left(f^{t+\Delta t} - f^t\right)/s_\omega(\Delta t)$, according to the NS-FDTD concept. A similar procedure can also be performed for the $E_x$ component. In this context, the interpolated $\tilde{E}_{x,y}$ quantities in (9b) are derived from

$$\begin{aligned} &\tilde{E}_x(x-\delta,y+\delta,z) \\ &= \{[E_x(x-\Delta,y+\delta,y,z) + E_x(x,y+\delta,z)]\,\mathbf{e}_x \\ &\quad + [E_y(x-\delta,y,z) + E_y(x-\delta,y+\Delta,z)]\,\mathbf{e}_y\}\cdot\frac{\mathbf{e}_x+\mathbf{e}_y}{2\sqrt{2}}, \end{aligned} \tag{12a}$$

$$\begin{aligned} &\tilde{E}_y(x+\delta,y+\delta,z) \\ &= \{[E_x(x,y+\delta,y,z) + E_x(x+\Delta,y+\delta,z)]\,\mathbf{e}_x \\ &\quad + [E_y(x+\delta,y,z) + E_y(x+\delta,y+\Delta,z)]\,\mathbf{e}_y\}\cdot\frac{-\mathbf{e}_x+\mathbf{e}_y}{2\sqrt{2}}. \end{aligned} \tag{12b}$$

Therefore, the final path integral expression for the $H_z$ component is given by (13) (see top of the next page). Note that the process of (9)-(13) can be analogously applied to the extraction of the $H_{x,y}$ components.

$$
\begin{aligned}
H_z^{t+\Delta t}(x,y,z) &= H_z^{t}(x,y,z) \\
&- \frac{\beta_1 s_\omega(\Delta t)}{\mu s_k(\Delta)} \Big\{ \beta_0 \Big[ E_y^{t+\Delta t/2}(x+\delta,y,z) - E_x^{t+\Delta t/2}(x,y+\delta,z) - E_y^{t+\Delta t/2}(x-\delta,y,z) + E_x^{t+\Delta t/2}(x,y-\delta,z) \Big] \\
&+ \frac{1-\beta_0}{\sqrt{2}} \Big[ \tilde{E}_y^{t+\Delta t/2}(x+\delta,y+\delta,z) - \tilde{E}_x^{t+\Delta t/2}(x-\delta,y+\delta,z) - \tilde{E}_y^{t+\Delta t/2}(x-\delta,y-\delta,z) + \tilde{E}_x^{t+\Delta t/2}(x+\delta,y-\delta,z) \Big] \Big\} \\
&- \frac{(1-\beta_1) s_\omega(\Delta t)}{2\mu s_k(\Delta)} \Big\{ \beta_2 \Big[ E_y^{t+\Delta t/2}(x+\delta,y,z+\Delta) - E_x^{t+\Delta t/2}(x,y+\delta,z+\Delta) - E_y^{t+\Delta t/2}(x-\delta,y,z+\Delta) + E_x^{t+\Delta t/2}(x,y-\delta,z+\Delta) \Big] \\
&+ \frac{1-\beta_2}{\sqrt{2}} \Big[ \tilde{E}_y^{t+\Delta t/2}(x+\delta,y+\delta,z+\Delta) - \tilde{E}_x^{t+\Delta t/2}(x-\delta,y+\delta,z+\Delta) - \tilde{E}_y^{t+\Delta t/2}(x-\delta,y-\delta,z+\Delta) + \tilde{E}_x^{t+\Delta t/2}(x-\delta,y-\delta,z+\Delta) \Big] \Big\} \\
&- \frac{(1-\beta_1) s_\omega(\Delta t)}{2\mu s_k(\Delta)} \Big\{ \beta_2 \Big[ E_y^{t+\Delta t/2}(x+\delta,y,z-\Delta) - E_x^{t+\Delta t/2}(x,y+\delta,z-\Delta) - E_y^{t+\Delta t/2}(x-\delta,y,z-\Delta) + E_x^{t+\Delta t/2}(x,y-\delta,z-\Delta) \Big] \\
&+ \frac{1-\beta_2}{\sqrt{2}} \Big[ \tilde{E}_y^{t+\Delta t/2}(x+\delta,y+\delta,z-\Delta) - \tilde{E}_x^{t+\Delta t/2}(x-\delta,y+\delta,z-\Delta) - \tilde{E}_y^{t+\Delta t/2}(x-\delta,y-\delta,z-\Delta) + \tilde{E}_x^{t+\Delta t/2}(x-\delta,y-\delta,z-\Delta) \Big] \Big\}.
\end{aligned}
\tag{13}
$$

$$
\begin{aligned}
-\mu\Delta \left.\frac{\partial H_z(x,y,z)}{\partial t}\right|_{\partial x} &= \frac{\beta_1(1+\beta_0)}{2}\left[E_y(x+\delta,y,z) - E_y(x-\delta,y,z)\right] \\
&+ \frac{(1-\beta_1)(1-\beta_2)}{8}\left[E_y(x+\delta,y+\Delta,z+\Delta) - E_y(x-\delta,y+\Delta,z+\Delta) + E_y(x+\delta,y-\Delta,z+\Delta) - E_y(x-\delta,y-\Delta,z+\Delta)\right. \\
&\left. + E_y(x+\delta,y+\Delta,z-\Delta) - E_y(x-\delta,y+\Delta,z-\Delta) + E_y(x+\delta,y-\Delta,z-\Delta) - E_y(x-\delta,y-\Delta,z-\Delta)\right] \\
&+ \frac{\beta_1(1-\beta_0)}{4}\left[E_y(x+\delta,y+\Delta,z) - E_y(x-\delta,y+\Delta,z) + E_y(x+\delta,y-\Delta,z) - E_y(x-\delta,y-\Delta,z)\right] \\
&+ \frac{(1-\beta_1)(1+\beta_2)}{4}\left[E_y(x+\delta,y,z+\Delta) - E_y(x-\delta,y,z+\Delta) + E_y(x+\delta,y,z-\Delta) - E_y(x-\delta,y,z-\Delta)\right].
\end{aligned}
\tag{15}
$$

### B. Derivation of the $\beta_0$, $\beta_1$, and $\beta_2$ parameters

Let us decompose the temporal derivative on the left-hand side of (10) into a $\partial x$ and a $\partial y$ term, for a simple argument, in order to derive the $\beta_{0,1,2}$ parameters; i.e.,

$$
\frac{\partial H_z(x,y,z)}{\partial t} = \left.\frac{\partial H_z(x,y,z)}{\partial t}\right|_{\partial x} + \left.\frac{\partial H_z(x,y,z)}{\partial t}\right|_{\partial y}. \tag{14}
$$

Then, the $\partial x$ part of (14) is derived via (15) (see top of this page). Comparing (15) with the 3D NS-FDTD operators

$$
d_x^{(0)} = \alpha_1 d_x^{(1)} + \alpha_2 d_x^{(2)} + \alpha_3 d_x^{(3)}, \tag{16}
$$

and by means of Appendix A and [1–3], [13], we obtain the following coefficient relations

$$
\beta_1(1+\beta_0) = 2\alpha_1, \tag{17a}
$$

$$
(1-\beta_1)(1-\beta_2) = 2\alpha_2, \tag{17b}
$$

$$
\beta_1(1-\beta_0) = (1-\beta_1)(1+\beta_2) = \alpha_3. \tag{17c}
$$

If the system of equations (17a)-(17c) is solved by means of the $\alpha_1 + \alpha_2 + \alpha_3 = 1$ constraint, the new optimization parameters $\beta_{0,1,2}$ can be extracted as

$$
(17a)\ \&\ (17c): \beta_1 = \alpha_1 + 0.5\alpha_3, \tag{18a}
$$

$$
(18a)\ \&\ (17b): \beta_2 = (0.5\alpha_3 - \alpha_2)/(0.5\alpha_3 + \alpha_2), \tag{18b}
$$

$$
(18a)\ \&\ (17c): \beta_0 = (\alpha_1 - 0.5\alpha_3)/(\alpha_1 + 0.5\alpha_3). \tag{18c}
$$

In this manner, the featured PI formula, given in (13), becomes fully equivalent to the corresponding 3D NS-FDTD expression, through the optimization parameters of (18a)-(18c), on cubic grids. Consequently, the wave propagation characteristics along with the numerical accuracy and stability of the developed PI model, in a homogeneous space discretized into cubic cells, are the same as those of the 3D NS-FDTD method.

## IV. NUMERICAL RESULTS

In this section, we modify and extend our PI model to successfully treat curved structures. Then, it is verified whether it can be utilized as the CP technique of the FDTD method. Also, by combining this PI model with the NS-FDTD concept, we prove the superior performance of the former in realistic applications. So it is shown that the novel PI scheme significantly enhances the efficiency of the NS-FDTD algorithm for arbitrary object shapes, without opting for unduly fine lattices.

### A. Analysis of 2D applications

The featured PI scheme is, firstly, applied to the radar cross section (RCS) analysis of a perfect electric conductor (PEC) circular cylinder with a radius of $\lambda/2$. The modification of the PI model near the cylinder is shown in Fig. 3. In particular, the integral area for the computation of the $H_z$ component is enclosed by two paths, i.e., the $S_B$ and the $S_C$, except for the PEC cylinder region. Note that the treatment of the path integrals is based on the typical FDTD principles [16]. So, the PI form for the basic path in Fig. 3 (a) can be written as

$$
\begin{aligned}
\mu\frac{\partial}{\partial t}\int_S \mathbf{H}\cdot d\mathbf{S} = -\int_C \mathbf{E}\cdot d\mathbf{l} &\Rightarrow \mu\frac{\partial \bar{H}_z(x,y)}{\partial t} S'_B \Delta^2 \\
&= E_x(x,y+\delta)\Delta - E_y(x+\delta,y)\Delta \\
&+ E_y(x-\delta,y) l_y \Delta - E_x(x,y-\delta) l_x \Delta,
\end{aligned}
\tag{19}
$$

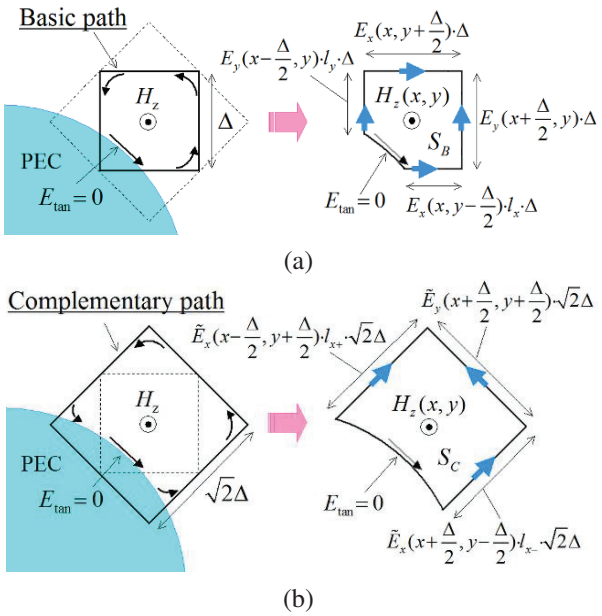


Fig. 3. Modified (a) basic and (b) complementary path for the proposed PI model. Dashed lines indicate the position of the pair paths, and PEC areas are shown in light blue. The integral path and the area for the calculation of the $H_z$ component are shown in the right-hand side figures (except the PEC region).

where $S'_B = S_B/\Delta^2$ and $l_{x,y} = l_{path\ length}/\Delta$. Similarly, we can derive the PI expression for the complementary path by means of $S_C$, as depicted in Fig. 3 (b). It is mentioned that during the evaluation of (19), $\Delta$ must be replaced with $s_k(\Delta) = 2\sin(k\Delta/2)/k$. Furthermore, due to the lack of $H_z$ nodes in the PEC area, there are some $E_{xy}$ and $\tilde{E}_{x,y}$ components that can not be computed via (3b) and (4). In such a case, these quantities are derived through the extrapolation/projection of already calculated $E$-field values on the nearest-neighbor nodes. The remaining $E$- and $H$-field components are acquired in terms of (3)-(5).

Regarding the reference solution of our problem, we examine several FDTD simulations of the PEC cylinder, as illustrated in Fig. 4. Since convergence is attained for $\Delta = \lambda/100$ and $\lambda/120$, we select the $\Delta = \lambda/120$ grid resolution with $\Delta t = T/170$, for $T = 2\pi/\omega$, as our reference. The structure is illuminated by a TE incident plane, with an incidence angle of $\theta^{inc} = 0^o$, and all scattered waves are obtained by the TF/SF formulation [16–18] applied in the NS-FDTD region. Moreover, our domain is discretized into cells of $\Delta = \lambda/10$ ($\lambda = 1$ m) for the basic path and $\Delta = \lambda/7$ for the complementary path, while stability is guaranteed with a $\Delta t = T/15$. The PI area has a size of $14\Delta \times 14\Delta$ (including the cylinder surface) and is surrounded by a $500\Delta \times 500\Delta$ NS-FDTD as well as a $20\Delta$-thick perfectly matched layer (PML) [16–18].

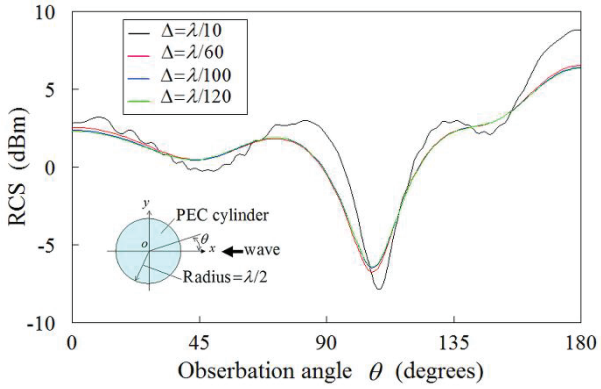


Fig. 4. RCS variation versus the observation angle $\theta$ for diverse grid sizes $\Delta$. The PEC cylinder is modeled via the staircase FDTD method, and $\Delta t = T/15$, $T/85$, $T/145$, $T/170$ are the temporal increments that correspond to $\Delta = \lambda/10$, $\lambda/60$, $\lambda/100$, $\lambda/120$, respectively.

In this context, Fig. 5 compares the RCS of the PEC cylinder computed via the proposed PI model and the NS-FDTD method solely (i.e., without PI treatment). As observed, the proposed technique is in very good agreement with the reference solution, despite the fairly coarse resolution of $\Delta = \lambda/10$ and $\Delta = \lambda/7$ for the basic and complementary paths, respectively. Concerning the small ripple in the PI results, we presume that it is attributed to the $\Delta = \lambda/7$ size of the complementary path cells. Actually, this ripple disappears in the case of a $\Delta = \lambda/12$ mesh resolution, as verified in Figs. 7 and 9 (a) (see below). So, a viable choice for retaining the balance between an acceptable accuracy level and a limited computational burden can be $\Delta \leq \lambda/12$. In addition, Fig. 5 indicates that the NS-FDTD method, without the

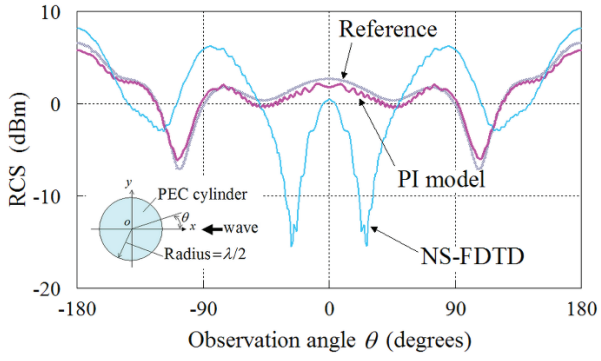


Fig. 5. RCS variation for the 2D PEC cylinder, computed via the proposed PI model and the staircase NS-FDTD method only (without PI treatment). The incidence angle of the TE plane wave is $\theta^{inc} = 0^o$ and $\Delta = \lambda/10$, with $\lambda = 1$ m. The reference solution is obtained in terms of the staircase FDTD technique with $\Delta = \lambda/120$.

PI model, fails to deliver acceptable accuracy. In summary, our PI model achieved a considerable $(120/10)^2 = 144$ times reduction of the memory overhead with regard to the number of cells, and a $(120/10)^2 \times (170/15) = 1632$ times speed improvement, with regard to the number of time steps, compared to those of the reference FDTD ($\Delta = \lambda/120$, $\Delta t = T/170$) solution. Thus, the new PI concept can greatly enhance the efficiency of the NS-FDTD formulation in the case of arbitrarily-curved objects.

Next, we consider the RCS analysis of the PEC wing-like model, described in Fig. 6, whose dimensions are measured in $\Delta$ units, with $\Delta = \lambda/12$ and $\lambda = 1$ m. For its illumination, we use an incident, $H_z^{inc}$, plane wave. Moreover, the space around the structure is modeled via the NS-FDTD method and the modified PI scheme is applied to the cells near the wing-like surface. The RCS variation for different incidence angles, $\theta^{inc}$, is presented in Fig. 7. The simulations are performed through the novel PI model, the staircase NS-FDTD technique only (i.e., without any PI treatment), and the reference FDTD solution with $\Delta = \lambda/96$. From the results, it is deduced that, in all cases, the proposed PI model accomplishes the best accuracy and coincidence with the reference solution, unlike the typical staircase implementations.

The prior 2D applications have also led to some interesting observations. The first one refers to the consistency of the geometrical accuracy of the integral path length with its area, given in Fig. 3. Hence, no discrepancies can arise during the combined basic and complementary path calculations. The second remark is related to the precision in the calculation of the $E$ and $\tilde{E}$ quantities on the modified paths near the surface of the scatterer. Such computations are conducted via an extrapolation/projection process, which uses the inner product of the unit $\mathbf{e}_{x,y}$ vectors with the nearest-neighbor $\mathbf{E}$ field components, as occurs in (12). This procedure is important for our PI evaluations and the geometrical accuracy of the modified PI cells, as well.

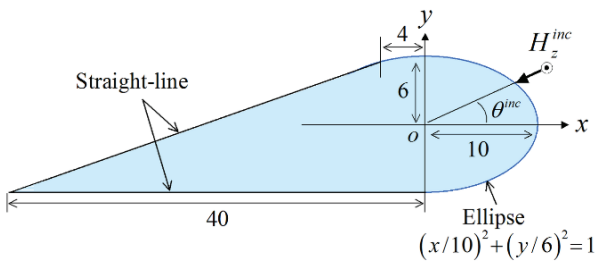


Fig. 6. Cross-section of a PEC wing-like model. All dimensions are in $\Delta$ units, with $\Delta = \lambda/12$ and $\lambda = 1$ m.

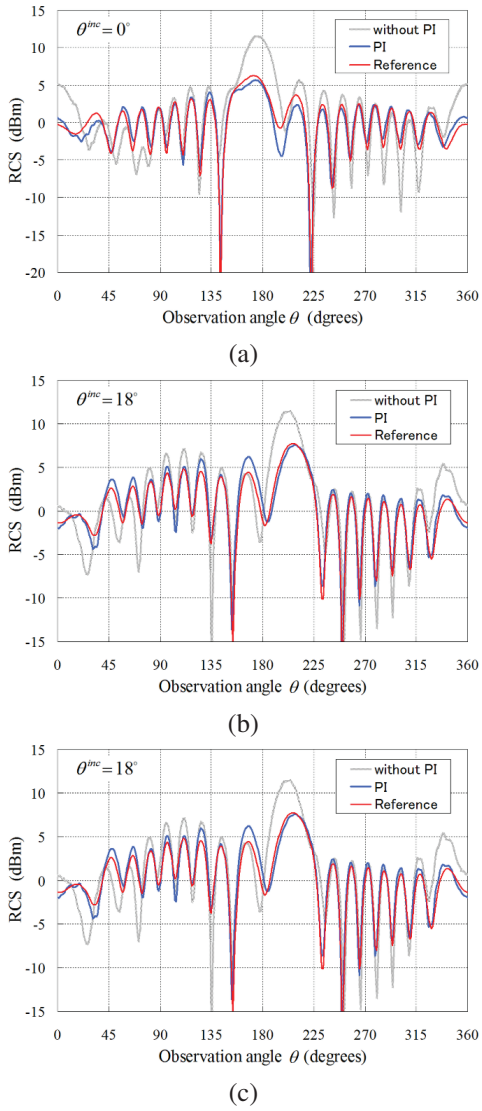


Fig. 7. RCS variation for the 2D wing-like model illuminated by an incident plane wave with (a) $\theta^{inc} = 0^o$, (b) $\theta^{inc} = 18^o$, and (c) $\theta^{inc} = 25^o$, computed through the staircase NS-FDTD method only (without PI treatment, $\Delta = \lambda/12$, $\lambda = 1$ m), the proposed PI model ($\Delta = \lambda/12$), and the reference staircase FDTD solution with $\Delta = \lambda/96$.

### B. Analysis of 3D applications

To prove the efficacy of the developed PI scheme in 3D problems, we focus on the RCS study of a finite-length PEC cylinder and the investigation of a thin-wire antenna impedance using a thin wire model [16], [25], [26]. The radius and the length of the former structure are much larger than $\Delta$, while the latter has a fine form with a curved surface that is smaller than $\Delta$.

*1) RCS study of a finite-length PEC cylinder*

The staircase model (cubic cells with $\Delta = \lambda/12$ and $\lambda = 1$ m) of the $12\lambda$-long PEC cylinder, whose circular

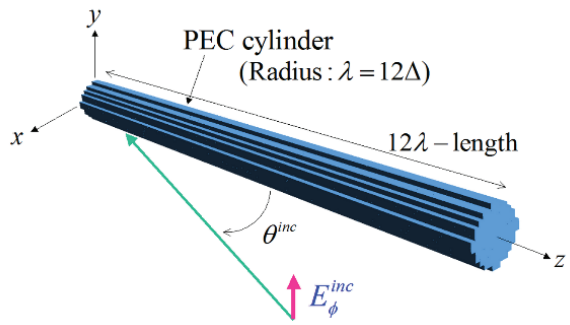


Fig. 8. Staircase model of a 12$\lambda$-long PEC cylinder with a circular cross-section of radius $\lambda$, for $\Delta = \lambda/12$ and $\lambda$ = 1 m. The modified PI cells are applied only to the surface of the structure.

cross-section has a radius of $\lambda$, is illustrated in Fig. 8. The incident plane wave is $E_{\phi}^{inc}$, with its angles ($\theta$, $\phi$) expressed in polar coordinates. In our simulations, the PI scheme of Fig. 3 replaces the staircase approximation only at the smooth surface of the cylinder. Figure 9 gives the RCS results for the $E_{\phi}$ component, evaluated via several techniques. Note that, apart from the schemes already employed in the previous examples, we herein compare our results with the PI formulation of [23], where the interpolated $\tilde{E}$ values are obtained from the PI scheme instead of (12). Again, the outcomes of the novel PI model are pretty close to the reference solution and in satisfactory agreement with the PI model of [23]. The presence of some small discrepancies between the two PI models, at the low RCS levels, is mainly due to the different treatment of the $E$-field components on the modified paths. Indeed, the proposed PI model retrieves the required $\tilde{E}$ terms by means of (12), whereas that of [23] derives them directly from Ampère's law. Nonetheless, another possible reason could be the different handling of those $\tilde{E}$ terms that cannot be promptly computed owing to the presence of the PEC object. In any case, our scheme reduces the overall burden, regarding the number of cells, to $(72/12)^3$ = 216 times, compared to the staircase FDTD method. Hence, the prior facts substantiate the competence of the model to successfully manipulate 3D curved structures.

*2) Study of a thin-wire antenna impedance*

The modified PI model for a thin-wire antenna of length L is elaborately described in Appendix B. The antenna is placed along the $z$-axis at the center of a 10$\Delta$-wide PI region, surrounded by a NS-FDTD area terminated by a 20$\Delta$-thick PML. To calculate the input impedance of the antenna, $Z_{\text{ant}} = R + jX$, we use (B11) and (B12) from Appendix B, while, in our simulations, we consider a normalized wavelength (i.e., $\lambda$ = 1 m);

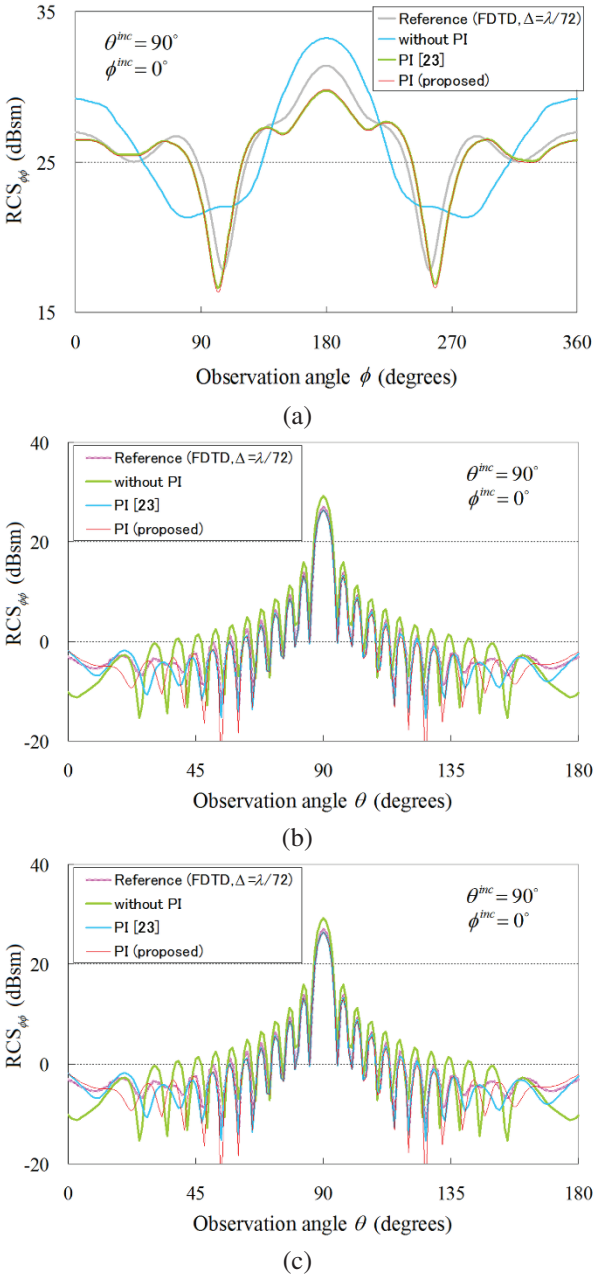


Fig. 9. RCS variation for the 3D finite-length circular PEC cylinder illuminated by an incident plane wave with $\phi^{inc} = 0^o$ and (a) $\theta^{inc} = 90^o$ ($xy$-plane), (b) $\theta^{inc} = 90^o$ ($xz$-plane), and (c) $\theta^{inc} = 75^o$ ($xz$-plane), calculated via the reference staircase FDTD solution with $\Delta = \lambda/72$, the staircase NS-FDTD method only (without PI treatment, $\Delta = \lambda/12$, $\lambda$ = 1 m), the PI scheme ($\Delta = \lambda/12$) of [23], and the proposed PI model ($\Delta = \lambda/12$).

hence, the cell size is set to $\Delta$ = L/21 or L/41. Moreover, for the combined PI and NS-FDTD area, $\Delta t$ is the same as its FDTD counterpart. The antenna is driven by a

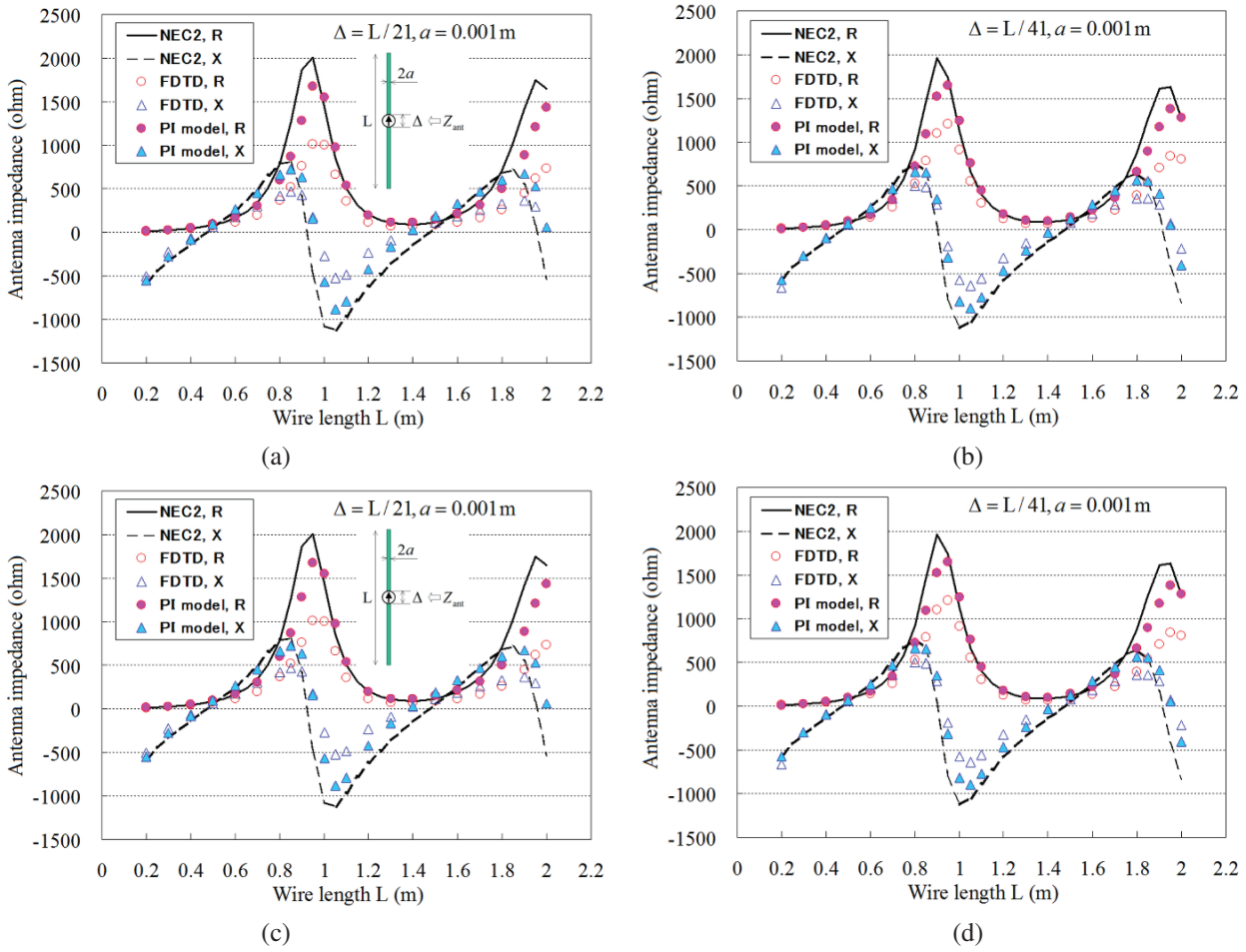


Fig. 10. Antenna impedance, $Z_{ant} = R + jX$, versus the wire length L for (a) $\Delta$ = L/21 and $a$ = 0.001 m, (b) $\Delta$ = L/41 and $a$ = 0.001 m, (c) $\Delta$ = L/21 and $a$ = 0.002 m, and (d) $\Delta$ = L/41 and $a$ = 0.002 m, computed through the proposed PI model and compared to the results from the NEC2 software and the staircase FDTD method.

center feed with a $\Delta$-gap on the $z$-axis and two wire radii are examined, namely $a$ = 0.001 m and 0.002 m. Lastly, our reference solution is obtained via the NEC2 software [27], based on the method of moments (MoM) [28], as well as the staircase FDTD technique [16] with a properly fine lattice. As detected from the antenna impedance results of Fig. 10, the new PI model agrees better with the NEC2 than the FDTD method. This proves that the suggested formulation enables the use of the thin wire model [16], [25], [26] with the NS-FDTD algorithm, a remarkable advantage for the analysis of 3D curved configurations with demanding structural details.

## V. CONCLUSION

The PI model for Maxwell's equations is suitable to treat various arbitrarily-shaped objects when combined with FDTD schemes. To this objective, an efficient PI algorithm, equivalent to the NS-FDTD concept, has been presented in this paper for 2D and 3D problems. To keep this equivalence, the new PI model uses a pair of suitably tailored basic and complementary integral paths. So, its numerical accuracy and stability are the same as those of its NS-FDTD counterparts. Adapting and incorporating the featured PI model in the NS-FDTD analysis of realistic configurations, it has been shown that it offers high precision results for non-orthogonally-shaped structures, even on coarse grids. Thus, its combination with the NS-FDTD method increases the applicability of the latter and leads to notable computational savings.

## APPENDIX A

The 3D NS-FDTD operator $d_x^{(0)}$ is expressed as

$$d_x^{(0)} = \alpha_1 d_x^{(1)} + \alpha_2 d_x^{(2)} + \alpha_3 d_x^{(3)}, \qquad \text{(A1)}$$

with

$$d_x^{(1)} f(x,y,z) = f(x+\Delta/2,y,z) - f(x-\Delta/2,y,z), \quad \text{(A2)}$$

$$
\begin{aligned}
&d_x^{(2)} f(x,y,z) \\
&= \frac{1}{4}[f(x+\Delta/2, y+\Delta, z+\Delta) - f(x-\Delta/2, y+\Delta, z+\Delta) \\
&\quad + f(x+\Delta/2, y+\Delta z-\Delta) - f(x-\Delta/2, y+\Delta z-\Delta) \\
&\quad + f(x+\Delta/2, y-\Delta, z+\Delta) - f(x-\Delta/2, y-\Delta, z+\Delta) \\
&\quad + f(x+\Delta/2, y-\Delta, z-\Delta) - f(x-\Delta/2, y-\Delta, z-\Delta)],
\end{aligned} \tag{A3}
$$

$$
\begin{aligned}
&d_x^{(3)} f(x,y,z) \\
&= \frac{1}{4}[f(x+\Delta/2, y+\Delta, z) - f(x-\Delta/2, y+\Delta, z) \\
&\quad + f(x+\Delta/2, y-\Delta, z) - f(x-\Delta/2, y-\Delta, z) \\
&\quad + f(x+\Delta/2, y, z+\Delta) - f(x-\Delta/2, y, z+\Delta) \\
&\quad + f(x+\Delta/2, y, z-\Delta) - f(x-\Delta/2, y, z-\Delta)],
\end{aligned} \tag{A4}
$$

where $\alpha_1 + \alpha_2 + \alpha_3 = 1$. Note that operators $d_{y,z}^{(0)}$ can also be similarly derived. Parameters $\alpha_{1,2,3}$ are given by

$$
\alpha_1 = \eta_1 + \eta_2/3 + \eta_3/2 \text{ and } \alpha_2 = \eta_2/3, \tag{A5}
$$

for

$$
\eta_1 = 7/15 - 17(k\Delta)^2/864 \text{ and } \eta_2 = \eta_1 - 2\gamma_0 + 1, \tag{A6}
$$

on condition that $\eta_1 + \eta_2 + \eta_3 = 1$. A detailed description for the derivation of operators $d_{x,y,z}^{(0)}$, parameters $\alpha_{1,2,3}$ and coefficient $\gamma_0$ can be found in [1–3].

## APPENDIX B

The modified integral paths for a thin-wire antenna are shown in Fig. B1. Thus, to compute the $\partial_t \int_S \mathbf{H} \cdot \mathrm{d}\mathbf{S}$ quantity, the integral areas are $S = S_B = \Delta^2 - \pi a^2/4$ and $S = S_c = 2\Delta^2 - \pi a^2/2$, as given in Fig. B1 (a). Moreover, after defining unit vector $\mathbf{t}$, we can write

$$
\mathbf{t} = (-\mathbf{e}_x + \mathbf{e}_y)/\sqrt{2}, \tag{B1}
$$

$$
\begin{aligned}
&\tilde{E}_y'(x-\Delta/2, y-\Delta/2) \\
&\quad = [E_x(x, y-\Delta/2)\mathbf{e}_x + E_y(x-\Delta/2, y-\Delta)\mathbf{e}_y] \cdot \mathbf{t},
\end{aligned} \tag{B2}
$$

$$
\begin{aligned}
&\tilde{E}_y''(x-\Delta/2, y-\Delta/2) \\
&\quad = [E_x(x-\Delta, y-\Delta/2)\mathbf{e}_x + E_y(x-\Delta/2, y)\mathbf{e}_y] \cdot \mathbf{t}.
\end{aligned} \tag{B3}
$$

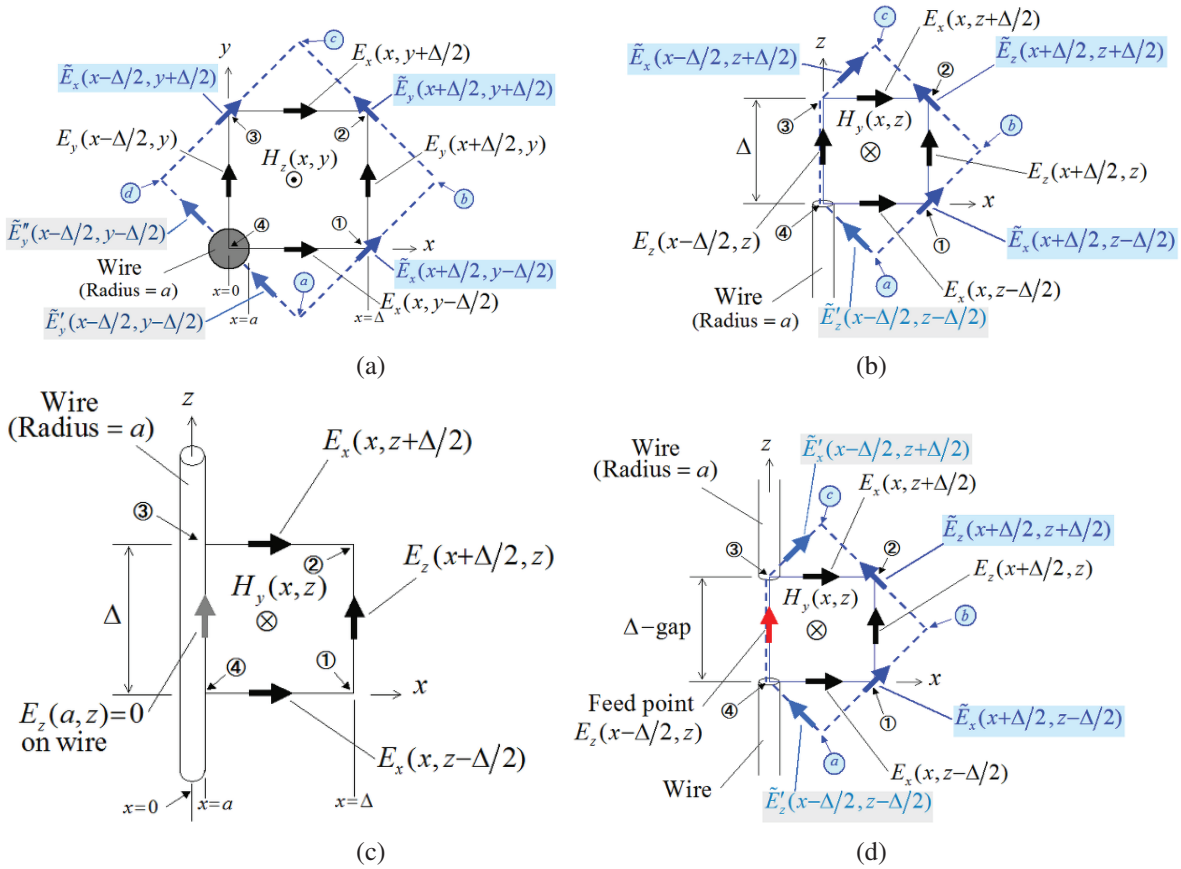


Fig. B1. Modified integral paths for a straight thin wire of radius $a$ [black solid line: basic path; blue dashed line: complementary path]. In particular, integral path (a) near the wire at the $xy$-plane, (b) for a wire end on the $z$-axis, (c) near the wire along the $z$-axis (only the basic path is used), and (d) for a feed point with a Δ-gap on the $z$-axis. For simplicity, coordinate $z$ in (a) and $y$ in (b)-(d) are omitted, while the same procedure can be utilized at the $yz$-plane.

Since, $E_x(x, y-\Delta/2) \propto 1/x$ and $E_y(x-\Delta/2, y) \propto 1/y$,

$$\int_{\textcircled{a}}^{\textcircled{d}} \tilde{\mathbf{E}} \cdot \mathrm{d}\mathbf{l} = \frac{\sqrt{2}\Delta}{2} \int_a^{\sqrt{2}\Delta/2} \tilde{E}'_y(x-\Delta/2, y-\Delta/2) l^{-1}\, \mathrm{d}l + \frac{\sqrt{2}\Delta}{2} \int_a^{\sqrt{2}\Delta/2} \tilde{E}''_y(x-\Delta/2, y-\Delta/2) l^{-1}\, \mathrm{d}l = \frac{\Delta}{\sqrt{2}} \ln\left(\frac{\Delta a}{\sqrt{2}}\right) \left[\tilde{E}'_y(x-\Delta/2, y-\Delta/2) + \tilde{E}''_y(x-\Delta/2, y-\Delta/2)\right]. \tag{B4}$$

For the complementary path of Figs. B1 (b) and (d),

$$\tilde{E}'_z(x-\Delta/2, z-\Delta/2) = -E_x(x, z-\Delta/2)\cos(\pi/4), \tag{B5}$$

$$\tilde{E}'_x(x-\Delta/2, z+\Delta/2) = E_x(x, z+\Delta/2)\cos(\pi/4), \tag{B6}$$

where $E_x(x, y \pm \Delta/2) \propto 1/x$ apart from $E_x(x, y+\Delta/2)$ in Fig. B1 (b). In this manner, one obtains

$$\int_{\textcircled{a}}^{\textcircled{4}} \tilde{\mathbf{E}}' \cdot \mathrm{d}\mathbf{l} = \frac{\sqrt{2}\Delta}{4} \int_{\sqrt{2}a}^{\sqrt{2}\Delta/2} \tilde{E}'_y(x-\Delta/2, y-\Delta/2) l^{-1}\, \mathrm{d}l = \frac{\sqrt{2}\Delta}{4} \ln\left(\frac{\Delta}{2a}\right) \tilde{E}'_y(x-\Delta/2, y-\Delta/2), \tag{B7}$$

$$\int_{\textcircled{3}}^{\textcircled{c}} \tilde{\mathbf{E}}' \cdot \mathrm{d}\mathbf{l} = \frac{\sqrt{2}\Delta}{4} \int_{\sqrt{2}a}^{\sqrt{2}\Delta/2} \tilde{E}'_x(x-\Delta/2, y+\Delta/2) l^{-1}\, \mathrm{d}l = \frac{\sqrt{2}\Delta}{4} \ln\left(\frac{\Delta}{2a}\right) \tilde{E}'_y(x-\Delta/2, y+\Delta/2). \tag{B8}$$

On the other hand, for the basic path in Fig. B1(a),

$$\int_{\textcircled{4}}^{\textcircled{1}} \mathbf{E} \cdot \mathrm{d}\mathbf{l} = \frac{\Delta}{2} \int_a^{\Delta} E_x(x, y-\Delta/2) l^{-1}\, \mathrm{d}l = \frac{\Delta}{2} \ln\left(\frac{\Delta}{a}\right) E_x(x, y-\Delta/2), \tag{B9}$$

which is similar to the ④-③ path in Fig. B1 (a), the ④-① path in Figs. B1 (b)- B1 (d) and the ③-② path in Figs. B1 (c)- B1 (d). So, the surface integral for the $\partial_t \tilde{H}_y$ term in Fig. B1 (c), using the basic path, is

$$\partial_t \int_S \bar{H}_y \, \mathrm{d}S \Rightarrow \partial_t \bar{H}_y(x, z) \frac{\Delta^2}{2} \ln\left(\frac{\Delta}{2a}\right), \tag{B10}$$

assuming that $H_y(x, z) \propto 1/x$. Note that all integral calculations, except for (B1)-(B10), treat field values on the path as a constant. Then, to evaluate the $\partial_t H_{y,z}$ derivatives, we can use (10), after replacing $\Delta$ with $s_k(\Delta)$ through $\mu \partial_t \int_S \mathbf{H} \cdot \mathrm{d}\mathbf{S} = -\int_C \mathbf{E} \cdot \mathrm{d}\mathbf{l}$, while for the $\partial_t \mathbf{E}$ term, the basic path is employed. The feed point with the $\Delta^-$ gap along $E_z(x-\Delta/2, z)$ in Fig. B1 (d), is incorporated as

$$\int_S (\varepsilon \partial_t \mathbf{E} + \sigma \mathbf{E} + \mathbf{j}_{\text{source}}) \cdot \mathrm{d}\mathbf{S} = \int_C \mathbf{H} \cdot \mathrm{d}\mathbf{l}, \tag{B11}$$

where $\sigma$ is the electric conductivity and $\mathbf{j}_{source}$ the driving current. Thus, referring to Fig. B1 (d) [16], [25], [26], the antenna impedance at the feed point is calculated by

$$Z_{\text{ant}} = R + \mathrm{j}X = \frac{-\int_{\textcircled{4}}^{\textcircled{3}} \mathbf{E} \cdot \mathrm{d}\mathbf{l}}{\int_C \mathbf{H} \cdot \mathrm{d}\mathbf{l}}, \tag{B12}$$

with $R$ the resistance and $X$ the reactance.

## REFERENCES


[1] J. B. Cole, "A high accuracy FDTD algorithm to solve microwave propagation and scattering problems on a coarse grid," *IEEE Trans. Microw. Theory Tech.*, vol. 43, no. 9, pp. 2053-2058, 1995.

[2] J. B. Cole, "A high-accuracy realization of the Yee algorithm using non-standard finite differences," *IEEE Trans. Microw. Theory Tech.*, vol. 45, no. 6, pp. 991-996, 1997.

[3] J. B. Cole, "High-accuracy Yee algorithm based on nonstandard finite differences: New developments and verifications," *IEEE Trans. Antennas Propag.*, vol. 50, no. 9, pp. 1185-1191, 2002.

[4] J. B. Cole, "High-accuracy FDTD solution of the absorbing wave equation, and conducting Maxwell's equations based on a nonstandard finite-difference model," *IEEE Trans. Antennas Propag.*, vol. 52, no. 3, pp. 725-729, 2004.

[5] K. Taguchi, T. Ohtani, T. Kashiwa, and Y. Kanai, "Characteristics of evanescent waves in the non-standard FDTD method," *IEEE Trans. Magn.*, vol. 43, no. 4, pp. 1313-1316, 2007.

[6] T. Ohtani, K. Taguchi, T. Kashiwa, Y. Kanai, and J. B. Cole, "Nonstandard FDTD method for wide-band analysis," *IEEE Trans. Antennas Propag.*, vol. 57, no. 8, pp. 2386-2396, 2009.

[7] T. Ohtani and Y. Kanai, "Coefficients of finite difference operator for rectangular cell NS-FDTD method," *IEEE Trans. Antennas Propag.*, vol. 59, no. 1, pp. 206-213, 2011.

[8] N. Okada and J. B. Cole, "Nonstandard finite difference time domain algorithm for Berenger's perfectly matched layer," *Applied Computational Electromagnetics Society (ACES) Journal*, vol. 26, no. 2, pp. 153-159, 2011.

[9] T. Ohtani and Y. Kanai, "Characteristics of boundary model in the 2-D NS-FDTD method," *IEEE Trans. Magn.*, vol. 48, no. 2, pp. 191-194, 2012.

[10] J. B. Cole and N. Okada, "High accuracy models for source terms in the nonstandard FDTD algorithm," in *Proc. Int. Symp. Electromagn. Theory*, art. no. 24PM2C-01, pp. 1098-1100, 2013.

[11] T. Ohtani, Y. Kanai, and N. V. Kantartzis, "A 4-D subgrid scheme for the NS-FDTD technique using the CNS-FDTD algorithm with the Shepard method and a Gaussian smoothing filter," *IEEE Trans. Magn.*, vol. 51, no. 3, art. no. 7201004, 2015.

[12] T. Ohtani and Y. Kanai, "An enhanced Total-field/Scattered-field scheme for the 3-D nonstandard finite-difference time-domain method," *IEEE Trans. Magn.*, vol. 52, no. 3, art. no. 7204705, 2016.

[13] J. B. Cole and S. Banerjee, *Computing the Flow of Light: Nonstandard FDTD Methodologies for Photonics Designs*. Bellingam, WA: SPIE Press, 2017.

[14] J. Jose, S. K. Simon, J. Kizhakooden, J. Andrews, and V. P. Joseph, "Nonstandard FDTD realization of radiation behaviour of epsilon negative metamaterial corner reflector antenna," in *Proc. IEEE 13th Int. Congr. Artif. Mat. Novel Wave Phenom.-Metamat.*, pp. 178-180, Rome, Italy, 2019.

[15] J. B. Cole, R. Katouf, and S. Banerjee, "Nonstandard finite difference time domain methodology for harmonics generation in nonlinear dielectrics," in *Proc. 2021 Int. Appl. Comput. Electromagn. Soc. Symp.*, Online, 2021.

[16] A. Taflove and S. Hagness, *Computational Electrodynamics: The Finite- Difference Time-Domain Method*. 3rd Edition, Chs. 7, 8, 10, and 14. Norwood, MA: Artech House, 2005.

[17] A. Taflove, *Advances in Computational Electrodynamics: The Finite-Difference Time-Domain Method*. Norwood, MA: Artech House, 1998.

[18] D. M. Sullivan, *Electromagnetic Simulation Using the FDTD Method*. New York: IEEE Press, 2000.

[19] K. S. Kunz and R. J. Luebbers, *The Finite Difference Time Domain Method for Electromagnetics.* Ch. 13, New York: CRC Press, 1993.

[20] C. J. Railton, I. J. Craddock, and J. B. Schneider, "The analysis of general two-dimensional PEC structures using a modified CPFDTD algorithm," *IEEE Trans. Microw. Theory Tech.*, vol. 44, no. 10, pp. 1728-1733, 1996.

[21] S. Dey and R. Mittra, "A locally conformal finite-difference time-domain (FDTD) algorithm for modeling three-dimensional perfectly conducting objects," *IEEE Microw. Guided Wave Lett.*, vol. 7, no. 9, pp. 273-275, 1997.

[22] T. Ohtani, Y. Kanai, and N. V. Kantartzis, "A rigorous path integral scheme for the two-dimensional nonstandard finite-difference time-domain method," in *Proc. COMPUMAG 2019*, art. no. PA-M4-9, Paris, France, 2019.

[23] T. Ohtani, Y. Kanai, and N. V. Kantartzis, "A nonstandard path integral model for curved surface analysis," *Energies*, vol. 15, art. no. 4322, 2022.

[24] T. Ohtani, Y. Kanai, and N. V. Kantartzis, "An integral representation model for the nonstandard finite-difference time-domain scheme," in *Proc. COMPUMAG 2021*, art. no. OD1-4, Online, 2022.

[25] S. Watanabe and M. Taki, "An improved FDTD model for the feeding gap of a thin-wire antenna," *IEEE Microwave Guided Wave Lett*, vol. 8, no. 4, pp. 152-154, 1998.

[26] R. M. Makinen, J. S. Juntunen, and M. A. Kivikoski, "An improved thin-wire model for FDTD," *IEEE Trans. Microw. Theory Tech.*, vol. 50, no. 5, pp. 1245-1255, 2002.

[27] *NEC: Numerical Electromagnetics Code*, Available online: https://www.nec2.org/

[28] J. J. H. Wang, *Generalized Moment Methods in Electromagnetics: Formulation and Computer Solution of Integral Equations*. John Wiley & Sons: USA, 1991.

**Tadao Ohtani** received the B.S. and M.S. degrees in electrical and electronic engineering from Toyohashi University of Technology, Japan, in 1983 and 1985, respectively, and received Ph.D. degree in electrical and electronic engineering from Kitami Institute of Technology, Japan, in 2005. From 1985 to 2011, he worked as a researcher at Nagoya Aerospace Systems of Mitsubishi Heavy Industries, Ltd. Currently, he is an independent researcher. His research interests include numerical analysis of the electromagnetic scattering fields for aircraft design via the FDTD and the NS-FDTD method.

**Yasushi Kanai** (Fellow, ACES) received the B.S., M.S. degree in engineering, and Ph.D. degree in information engineering from Niigata University, Japan, in 1982, 1984, and 1989, respectively.

He worked as a research engineer at Alps Electric Co., Ltd., from 1984 to 1992, where he developed magnetic recording heads via numerical methods. In 1992-1995, he was an associate professor at Department of Information Engineering, Niigata University. In 1995, he joined the Engineering Department, Niigata Institute of Technology, Kashiwazaki, Japan, where he is currently a professor. In 2002-2003, he was at Florida International University, Miami, FL, as a visiting scholar. He has authored/co-authored more than 190 peer-reviewed journal papers, more than 270 international conference records, more than 260 national conference records, and several book chapters. He specializes in micromagnetic analysis both in energy-assisted magnetic recording heads and media and in wave propagation via NS-FDTD analysis.

**Nikolaos V. Kantartzis** received the Diploma and Ph.D. degrees in electrical and computer engineering from the Aristotle University of Thessaloniki, Thessaloniki, Greece, in 1994 and 1999, respectively. In 1999, he joined the Department of Electrical and Computer Engineering, Aristotle University of Thessaloniki, where he is currently a professor. He has authored/coauthored 4 books, more than 190 peer-reviewed journal papers, and more than 300 publications in conference proceedings. His main research interests include computational electromagnetics, EMC, metamaterials, graphene, antenna design, and waveguide systems.

# A Simple, Method of Moments Solution for the Integral Equations for Multiple Dielectric Bodies of Arbitrary Shape in Time Domain

**Sadasiva M. Rao**

Naval Research Laboratory
Washington DC 20375, USA.
sadasiva.rao@nrl.navy.mil

***Abstract –*** In this work, we present a straightforward and simple method of moments (MOM) solution procedure, with minimum mathematical manipulations, to solve the coupled integral equations for multiple, homogeneous and inhomogeneous, dielectric bodies of arbitrary shape directly in the time domain. The standard surface and volume integral equation formulations are used for homogeneous and inhomogeneous bodies, respectively. The numerical solution procedure does not involve a time-marching process as is usually adopted for time domain problems and seems to be one of the primary reasons for the late-time instabilities as a result of error accumulation. The present solution method is stable for a very long time as evidenced by several representative numerical examples presented for validation.

***Index Terms –*** dielectric bodies, integral equations, method of moments, time domain.

## I. INTRODUCTION

Many applications developed in recent times, such as short pulse radar and 5G cellular systems, require the calculation of wide-band signature for efficient design and to avoid multi-band interference. The traditional frequency domain techniques for such calculations are expensive and time consuming. As a result, direct time domain techniques received considerable attention to develop user-friendly, general purpose, stable algorithms that can be easily adopted to a wide variety of problems. It may be noted that the goal of the present work is developing an efficient algorithm in time domain to solve a variety of problems and does not target a specific application problem.

The general purpose numerical methods in the time domain can be broadly classified into two categories *viz*. a) Differential Equation (DE) solution techniques and b) Integral Equation (IE) solution techniques. The Finite Difference Time Domain (FDTD) is a popular DE solution method that is applicable to a variety of problems [1–5]. Similarly, Method of Moments (MOM) is the popular IE based solution for solving time domain electromagnetic problems.

In this work, we deal with IE solution methods only. One advantage of the IE method over the DE method is that the solution space is confined to the space occupied by the object. In contrast, for DE based methods the surrounding space also needs to be included in the solution.

Until recently, a time-stepping process based on MOM, popularly known as the Marching-on-in-Time (MOT) method, has been the preferred technique for solving the numerical solution of Time Domain Integral Equation (TDIE) for electromagnetic field problems [6–11]. However, the MOT procedure is prone to late-time instabilities. The primary source of instability seems to be the accumulation of error at each time step eventually resulting into rapidly growing oscillations commonly known as late-time instabilities.

Recently, a new type of algorithm was developed using MOM that did not employ time-stepping procedure and remained stable for a very long time signature [12, 13]. In the present work, we apply this new method to multiple dielectric bodies of arbitrary shape using the surface equivalence principle [14], resulting in a surface integral equation (SIE) formulation or the volume equivalence principle [15] resulting in a volume integral equation (VIE) formulation. We note that SIE formulation is applicable only to homogeneous dielectric bodies whereas VIE formulation is applicable to both homogeneous and inhomogeneous volumes.

This work is organized as follows: In sections II and III we develop the integral equations along with the numerical solution scheme for the VIE and SIE formulations, respectively. In sections IV and V, we present several representative numerical results for validation purposes. Finally, in section VI, we summarize the work and present a few conclusions.

## II. VIE FORMULATION

Although we are developing the solution procedure for multiple dielectric bodies, for the sake of brevity, let us consider only a single inhomogeneous body, illuminated by a Gaussian Plane Wave (GPW). We note that extending the present solution technique to multiple

*Submitted On: June 21, 2023*
*Accepted On: January 20, 2024*

https://doi.org/10.13052/2024.ACES.J.390305

bodies is straightforward and does not require any special treatment.

### A. Integral equation formulation

Let $V$ denote an arbitrarily-shaped, loss-less, inhomogeneous volume, surrounded by a homogeneous material $(\varepsilon_0, \mu_0)$ as shown in Fig. 1. The material parameters inside the volume, $V$, are continuously changing from point to point and denoted by permittivity, $\varepsilon(\mathbf{r})$, and permeability, $\mu(\mathbf{r})$.

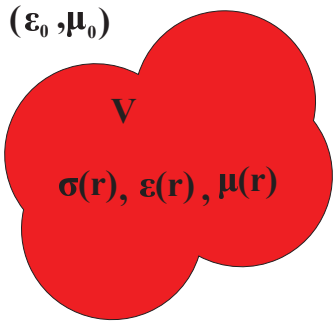


Fig. 1. Inhomogeneous volume surrounded by a homogeneous material (free space).

An electric field, $\mathbf{E}^{inc}(\mathbf{r},t)$, defined in the absence of the scatterer, is incident on and induces polarization volume currents, $\mathbf{J}(\mathbf{r},t)$, in the volume, $V$. These volume currents then generate the scattered field which is a function of space and time. The total electric field is the sum of incident and scattered fields generated by the induced volume currents, and we have the following basic equations:

$$\mathbf{J}(\mathbf{r},t) = \frac{\partial \mathbf{P}(\mathbf{r},t)}{\partial t} = \frac{\partial [\mathbf{D}(\mathbf{r},t) - \varepsilon_0 \mathbf{E}(\mathbf{r},t)]}{\partial t} \quad (1)$$

$$= [\varepsilon_r(\mathbf{r}) - 1]\, \varepsilon_0 \frac{\partial \mathbf{E}(\mathbf{r},t)}{\partial t}, \quad (2)$$

$$\mathbf{E}(\mathbf{r},t) = \mathbf{E}^s(\mathbf{r},t) + \mathbf{E}^{inc}(\mathbf{r},t), \quad (3)$$

$$\mathbf{E}^s(\mathbf{r},t) = -\frac{\partial \mathbf{A}(\mathbf{r},t)}{\partial t} - \nabla \Phi(\mathbf{r},t), \quad (4)$$

where $\mathbf{P}(\mathbf{r},t)$ and $\mathbf{D}(\mathbf{r},t)$ represent the polarization vector and electric flux density vector, respectively. The magnetic vector potential, $\mathbf{A}(\mathbf{r},t)$, and the electric scalar potential, $\Phi(\mathbf{r},t)$, are:

$$\mathbf{A}(\mathbf{r},t) = \mu_0 \int_V \frac{\mathbf{J}(\mathbf{r}', t - \frac{R}{c})}{4\pi R}\, dV', \quad (5)$$

$$\Phi(\mathbf{r},t) = \frac{1}{\varepsilon_0} \int_V \frac{q_v(\mathbf{r}', t - \frac{R}{c})}{4\pi R}\, dV', \quad (6)$$

$$R = |\mathbf{r} - \mathbf{r}'|. \quad (7)$$

In Equations (5) and (6), $\mathbf{r}$ and $\mathbf{r}'$ are the locations of the observation and source points on the scatterer, respectively. The volume charge density, $q_v$, is related to the polarization current, $\mathbf{J}$, by:

$$\frac{\partial q_v}{\partial t} = -\nabla \cdot \mathbf{J} \quad (8)$$

Next, we can re-write Equations (2), using Equations (3) and (4), as:

$$\frac{\mathbf{J}(\mathbf{r},t)}{\varepsilon_r(\mathbf{r}) - 1} = \varepsilon_0 \frac{\partial \mathbf{E}^{inc}(\mathbf{r},t)}{\partial t} - \varepsilon_0 \left[ \frac{\partial^2 \mathbf{A}(\mathbf{r},t)}{\partial t^2} - \nabla \frac{\partial \Phi(\mathbf{r},t)}{\partial t} \right]. \quad (9)$$

Now, we can write the time derivative of the scalar potential, using Equation (8), as:

$$\frac{\partial \Phi(\mathbf{r},t)}{\partial t} = -\frac{1}{\varepsilon_0} \int_V \frac{\nabla \cdot \mathbf{J}(\mathbf{r}', t - \frac{R}{c})}{4\pi R}\, dV'. \quad (10)$$

Next, we define the following relationships:

$$\kappa(\mathbf{r}) = \frac{\varepsilon_r - 1}{\varepsilon_r}, \quad (11)$$

$$\mathbf{D}(\mathbf{r},t) = \varepsilon_r \varepsilon_0 \mathbf{E}(\mathbf{r},t), \quad (12)$$

$$\mathbf{J}(\mathbf{r}) = \kappa(\mathbf{r}) \frac{\partial \mathbf{D}(\mathbf{r},t)}{\partial t}, \quad (13)$$

where $\kappa(\mathbf{r})$ is the contrast ratio.

Note that the normal component of $\mathbf{D}$ is continuous at media interfaces and, hence, provides a convenient way to solve for the unknown quantity, $\mathbf{J}(\mathbf{r},t)$.

Now using Equations (11) - (13), and carrying out a few simple mathematical steps, we can write Equation (1) as:

$$\frac{\mathbf{D}(\mathbf{r},t)}{\varepsilon_r} + \mu_0 \frac{\partial^2}{\partial t^2} \int_V \frac{\kappa(\mathbf{r}')\, \mathbf{D}(\mathbf{r}', t - \frac{R}{c})}{4\pi R}\, dV' - \frac{1}{\varepsilon_0} \nabla \left[ \int_V \frac{\nabla' \cdot \kappa(\mathbf{r}')\, \mathbf{D}(\mathbf{r}', t - \frac{R}{c})}{4\pi R}\, dV' \right] = \mathbf{E}^{inc}(\mathbf{r},t) \quad (14)$$

Equation (14) is the required integro-differential equation that needs to be solved by numerical methods to obtain the unknown quantity, $\mathbf{D}(\mathbf{r},t)$.

### B. MOM solution

As a first step, we define an upper limit on the time variable $t = T$, where $T$ represents the time when the incident pulse becomes negligible. Then, we divide the time axis $0 \to T$ into $N_t$ uniform time intervals given by $\Delta t$ and denote $t_n = n\Delta t$ for $n = 1, 2, ....N_t$. We note that, initially, the MOM scheme is applied to a finite interval $0 \to T$. We also note that extending the time interval to later times is trivial and simply repeats the same steps from $0 \to T$.

Next, we define the triangle functions to approximate the time variable in the interval $0 \to T$ as:

$$g_n(t) \equiv \begin{cases} 1 - \frac{|t - t_n|}{\Delta t} & t \in (t_{n-1}, t_{n+1}) \\ 0 & \text{otherwise.} \end{cases}, \quad (15)$$

for $n = 1, 2, \cdots, N_t$.

Now, we define the Schaubert-Wilton-Glisson (SWG) basis functions to represent the spatial variation of the electric flux density vector $\mathbf{D}$ [18].

Assuming a suitable tetrahedral model for the scattering structure, the basis functions are described as follows:

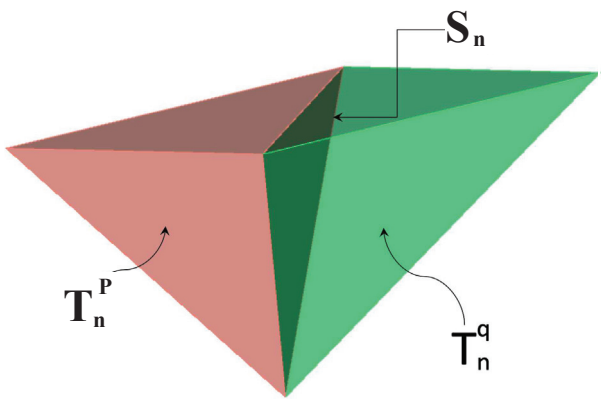


Fig. 2. Description of the basis function.

Figure 2 shows two tetrahedrons $T_n^p$ and $T_n^q$, associated with the $n^{th}$ triangular surface denoted by $S_n$. Points in $T_n^p$ may be designated either by the position vector $\mathbf{r}$, or by $\rho_n^p$ defined with respect to the free vertex of $T_n^p$. Similar remarks apply to the position vector $\mathbf{r}$ in $T_n^q$ except that it is directed toward the free vertex of $T_n^q$. It is assumed that the reference direction for $\mathbf{D}$ associated with the $n^{th}$ triangle is from $T_n^p$ to $T_n^q$.

Referring to Fig. 2, the vector basis functions associated with the $n^{th}$ triangular surface is:

$$\mathbf{f}_n(\mathbf{r}) = \begin{cases} \frac{a_n}{3V_n^p}(\mathbf{r}-\mathbf{r}_n^p) & \mathbf{r}\in T_n^p \\ \frac{a_n}{3V_n^q}(\mathbf{r}-\mathbf{r}_n^q) & \mathbf{r}\in T_n^q \\ 0.0 & \text{otherwise,} \end{cases} \tag{16}$$

where $a_n$ is the area of the triangular surface, $V_n^p$ and $V_n^q$ are the volumes of the $p$ and $q$ tetrahedrons attached to the triangular surface $S_n$, and $\mathbf{r}_n^p$ and $\mathbf{r}_n^q$ represent the position vectors to the free vertex of tetrahedrons $p$ and $q$, respectively.

Now, we approximate the induced electric flux density, $\mathbf{D}(\mathbf{r},t)$, as:

$$\mathbf{D}(\mathbf{r},t) \approx \sum_{m=1}^{N_S}\sum_{n=1}^{N_t} I_{m,n}\,\mathbf{f}_m(\mathbf{r})\,g_n(t), \tag{17}$$

where $N_S$ and $N_t$ represent the number of basis (expansion) functions in space and time, respectively.

The next step in applying the method of moments is to select the testing procedure. As testing functions, we choose the same functions described in [18]. Defining:

$$< \mathbf{f}_m(\mathbf{r})g_n(t), \mathbf{F}(\mathbf{r},t) > = \int_V\int_T \mathbf{f}_m(\mathbf{r})g_n(t)\bullet\mathbf{F}(\mathbf{r},t)\,dV\,dt, \tag{18}$$

we write Equation (14) as:

$$\begin{aligned} &< \mathbf{f}_m(\mathbf{r})g_n(t),\ \tfrac{\mathbf{D}(\mathbf{r},t)}{\varepsilon_r} > \\ &+ < \mathbf{f}_m(\mathbf{r})g_n(t),\ \mu_0\tfrac{\partial^2}{\partial t^2}\int_V \tfrac{\kappa(\mathbf{r}')\,\mathbf{D}(\mathbf{r}',t-\frac{R}{c})}{4\pi R}\,dV' > \\ &- < \mathbf{f}_m(\mathbf{r})g_n(t),\ \tfrac{1}{\varepsilon_0}\nabla\left[\int_V \tfrac{\nabla'\cdot\kappa(\mathbf{r}')\,\mathbf{D}(\mathbf{r}',t-\frac{R}{c})}{4\pi R}\,dV'\right] > \\ &= < \mathbf{f}_m(\mathbf{r})g_n(t), \mathbf{E}^{inc} >, \end{aligned} \tag{19}$$

for $m = 1,2,\cdots N_S$ and $n = 1,2,\cdots N_t$.

The first term, $< \mathbf{f}_m(\mathbf{r})g_n(t),\ \frac{\mathbf{D}(\mathbf{r},t)}{\varepsilon_r} >$, in Equation (19) may be written as:

$$\begin{aligned} &\left\langle \mathbf{f}_m(\mathbf{r})g_n(t),\ \frac{\mathbf{D}(\mathbf{r},t)}{\varepsilon_r}\right\rangle \\ &= \Delta t\left[\frac{a_m}{3V_m^i}\int_{T_m^i}(\mathbf{r}-\mathbf{r}_m^i)\cdot\frac{\mathbf{D}(\mathbf{r},t_n)}{\varepsilon_r}\,dV \right. \\ &\left. + \frac{a_m}{3V_m^j}\int_{T_m^j}(\mathbf{r}-\mathbf{r}_m^j)\cdot\frac{\mathbf{D}(\mathbf{r},t_n)}{\varepsilon_r}\,dV\right], \end{aligned} \tag{20}$$

where $T_m^i$ and $T_m^j$ represent the tetrahedrons attached to the triangular surface, $S_m$. The integrals in Equation (20) may be analytically evaluated after substituting the expansion functions, (17), for $\mathbf{D}(\mathbf{r},t)$.

Next, let us consider the second term in Equation (19):

$$\left\langle \mathbf{f}_m(\mathbf{r})g_n(t),\ \mu_0\frac{\partial^2}{\partial t^2}\int_V\frac{\kappa(\mathbf{r}')\,\mathbf{D}(\mathbf{r}',t-\frac{R}{c})}{4\pi R}\,dV'\right\rangle,$$

which is approximated as:

$$\begin{aligned} &\left[\frac{g(t_n)-2g(t_{n-1})+g(t_{n-2})}{\Delta t}\right] \\ &\times\left[\kappa(\mathbf{r}_m^i)\mathbf{D}(\mathbf{r}_m^{ci},t-\frac{R_m^{ci}}{c})\cdot\int_{T_m^i}\mathbf{f}_m\,dV'\right. \\ &\left. + \kappa(\mathbf{r}_m^j)\mathbf{D}(\mathbf{r}_m^{cj},t-\frac{R_m^{cj}}{c})\cdot\int_{T_m^j}\mathbf{f}_m\,dV'\right]. \end{aligned} \tag{21}$$

Note that in Equation (21), $\mathbf{D}(\mathbf{r},t)$ is evaluated at $\mathbf{r}_m^{ci}$ and $\mathbf{r}_m^{cj}$, which represent the position vectors to centroids of the tetrahedrons $T_m^i$ and $T_m^j$, respectively. The integrals in Equation (21) are trivial and may be carried out analytically.

Using similar mathematical steps, the right hand side of the Equation (19) is written as:

$$\begin{aligned} &\Delta t\left[\mathbf{E}^{inc}(\mathbf{r}_m^{ci},t-\frac{R_m^{ci}}{c})\cdot(\mathbf{r}_m^{ci}-\mathbf{r}_m^i)\right. \\ &\left. + \mathbf{E}^{inc}(\mathbf{r}_m^{cj},t-\frac{R_m^{cj}}{c})\cdot(\mathbf{r}_m^{cj}-\mathbf{r}_m^j)\right] \end{aligned} \tag{22}$$

Lastly, we consider the third term in Equation (19):

$$\left\langle \mathbf{f}_m(\mathbf{r})g_n(t),\ \nabla\left[\frac{1}{\varepsilon_0}\int_V\frac{\nabla'\cdot\kappa(\mathbf{r}')\,\mathbf{D}(\mathbf{r}',t-\frac{R}{c})}{4\pi R}\,dV'\right]\right\rangle. \tag{23}$$

Here, we first perform testing on the time variable and the result is:

$$\Delta t \left\langle \mathbf{f}_m(\mathbf{r}),\ \nabla \left[ \frac{1}{\varepsilon_0} \int_V \frac{\nabla' \cdot \kappa(\mathbf{r}')\, \mathbf{D}(\mathbf{r}', t - \frac{R}{c})}{4\pi R}\, dV' \right] \right\rangle \quad (24)$$

Denoting the term in the square bracket as $\Upsilon$, we can write the previous expression, after using the identity $\nabla \cdot (\mathbf{A}\Upsilon) = \nabla\Upsilon \cdot \mathbf{A} + \Upsilon \nabla \cdot \mathbf{A}$, as:

$$\langle \mathbf{f}_m, \nabla\Upsilon \rangle = \int_V \nabla \cdot (\mathbf{f}_m \Upsilon)\, dV - \int_V \Upsilon \nabla \cdot \mathbf{f}_m\, dV. \quad (25)$$

We note that the first integral in Equation (25) vanishes because of the properties of the basis functions and we are left with the following:

$$-\Delta t \int_V \nabla \cdot \mathbf{f}_m \left[ \int_V \nabla \cdot \kappa(\mathbf{r}') \mathbf{D}(\mathbf{r}')\, G(\mathbf{r}, \mathbf{r}')\, dV' \right] dV. \quad (26)$$

Next, we consider the expansion procedure. Substitution of the expansion function, Equation (17), into Equations (20), (21), and (26) yields a $P \times P$ system of linear equations, where $P = N_S \times N_t$. These equations may be written in a matrix form as:

$$\mathbf{ZI} = \mathbf{V}, \quad (27)$$

where $\mathbf{Z} = [Z_{mn}]$ is an $P \times P$ matrix and $\mathbf{I} = [I_n]$ and $\mathbf{V} = [V_m]$ are column vectors of length, $P$. Obviously, it is possible to obtain the unknown vector $\mathbf{I} = [I_n]$ by inverting the $\mathbf{Z}$-matrix and multiplying by $\mathbf{V}$. However, there is a better and efficient way as described in the following:

Here, we note that the $\mathbf{Z}$-matrix is not a full matrix, unlike in the frequency domain MOM procedure. In fact, it is a lower triangular, block-wise, Toeplitz matrix given by:

$$\mathbf{Z} = \begin{bmatrix} \mathbf{Z}_{1,1} & \emptyset & \cdots & \emptyset \\ \mathbf{Z}_{2,1} & \mathbf{Z}_{2,2} & \cdots & \emptyset \\ \vdots & \vdots & \vdots & \vdots \\ \mathbf{Z}_{N_S,1} & \mathbf{Z}_{N_S,2} & \cdots & \mathbf{Z}_{N_S,N_S} \end{bmatrix}, \quad (28)$$

where each $\mathbf{Z}_{p,q},\ p = 1, 2, \cdots N_S$ and $q = 1, 2, \cdots, N_S$, is a matrix of dimension, $N_S$, representing the mutual interaction between the spatial basis functions for a given pair of testing time function, $g_n$, and source time function, $g_k$. Further, because of the Toeplitz property, we have $\mathbf{Z}_{p,q} = \mathbf{Z}_{|p-q|+1,1}$. Hence, we only need to compute the first column of Equation (28) and distribute the elements accordingly. In other words, we only have to compute the matrix elements for the first source time function and the testing time functions $1, 2, \cdots, N_T$. The solution of such a matrix equation is very efficient, involves inverting only once, a matrix of size $N_S \times N_S$, and solving the matrix equation.

Lastly, the elements of the right hand side of Equation (14) are give by:

$$V_m = \varepsilon_0 \left[ \mathbf{E}^{inc}(\mathbf{r}_m^{ci}, t_k) \cdot (\mathbf{r}_m^{ci} - \mathbf{r}_m^{i}) + \mathbf{E}^{inc}(\mathbf{r}_m^{cj}, t_k) \cdot (\mathbf{r}_m^{cj} - \mathbf{r}_m^{j}) \right]. \quad (29)$$

For a plane wave incidence, we set:

$$\mathbf{E}^{inc}(\mathbf{r}, t) = E_\theta(\mathbf{r}, t - \frac{\mathbf{r} \cdot \hat{k}}{c})\hat{\theta} + E_\phi(\mathbf{r}, t - \frac{\mathbf{r} \cdot \hat{k}}{c})\hat{\phi}, \quad (30)$$

where the propagation vector, $\hat{k}$, is given by:

$$\hat{k} = \sin\theta_0 \cos\phi_0\, \hat{x} + \sin\theta_0 \sin\phi_0\, \hat{y} + \cos\theta_0\, \hat{z}, \quad (31)$$

and $(\theta_0,\ \phi_0)$ defines the angles of arrival of the plane wave in the usual spherical coordinate system.

On the right hand side of the matrix equation, $\mathbf{V}$ is obtained by using Equation (29) and consists of $N_t$ blocks of vectors of dimension $N_S$. At this stage, we note that multiple incident pulses with varying frequency content can be easily accommodated by adding more column blocks to the $\mathbf{V}$-matrix. Also, we note that obtaining currents for $T$ to $2T$ and later instants is similar to solving the equation for 0 to $T$ as presented in [12] and [13].

Lastly, note that the numerical procedure presented so far allows us to obtain the current distribution on the scattering structure as a function of time. Once an accurate current distribution is obtained, it is a simple process to obtain near-fields, far-fields, and any other required parameters. The mathematical details to obtain such parameters are well-known and available in [16] and hence not repeated here.

## III. SIE FORMULATION

Once again, we consider a single, homogeneous dielectric body for developing the integral equations for the sake of brevity.

### A. Integral equation formulation

Let $S_d$ denote the surface of the dielectric body, surrounded by free space and illuminated by an incident plane wave pulse. The regions exterior and interior to the dielectric body, denoted by "e" and "i", are characterized by medium parameters $(\mu_0, \varepsilon_0)$ and $(\mu_d, \varepsilon_d)$, respectively. Using the standard equivalence principle [14], and defining the equivalent currents, $\mathbf{J}_d$ and $M_d$, we derive the following equations:

$$\frac{\partial}{\partial t} \left[ \mathbf{E}_e^s(\mathbf{J}_d) + \mathbf{E}_e^s(\mathbf{M}_d) + \mathbf{E}^{inc} \right]_{tan} = 0, \quad (32)$$

$$\frac{\partial}{\partial t} \left[ \mathbf{E}_i^s(\mathbf{J}_d) + \mathbf{E}_i^s(\mathbf{M}_d) \right]_{tan} = 0. \quad (33)$$

Next, the time derivative of the scattered electric fields radiated by the equivalent electric and magnetic currents are written, in terms of potential functions, as:

$$\frac{\partial}{\partial t} \left[ \mathbf{E}_\nu^s(\mathbf{J}_d, \mathbf{M}_d) \right] = -\frac{\partial^2 \mathbf{A}_\nu}{\partial t^2} - \frac{\partial \nabla \Phi_\nu}{\partial t} - \frac{\partial}{\partial t} \left[ \frac{1}{\varepsilon_\nu} \nabla \times \mathbf{F}_\nu \right], \quad (34)$$

where $\mathbf{A}_\nu$ and $\mathbf{F}_\nu$ are the magnetic and electric vector potentials, respectively, and $\Phi_\nu$ is the electric scalar

potential, given by:

$$\mathbf{A}_\nu(\mathbf{r},t) = \mu_\nu \int_S \frac{\mathbf{J}_d(\mathbf{r}',t-\frac{R}{c_\nu})}{4\pi R}\,ds' , \quad (35)$$

$$\mathbf{F}_\nu(\mathbf{r},t) = \varepsilon_\nu \int_S \frac{\mathbf{M}_d(\mathbf{r}',t-\frac{R}{c_\nu})}{4\pi R}\,ds' , \quad (36)$$

$$\Phi_\nu(\mathbf{r},t) = \frac{1}{\varepsilon_\nu}\int_S \frac{q_e(\mathbf{r}',t-\frac{R}{c_\nu})}{4\pi R}\,ds', \quad (37)$$

for $\nu = e$ or $\nu = i$. In Equations (35) - (37), $R = |\mathbf{r}-\mathbf{r}'|$ is the distance from the field point, $\mathbf{r}$, to the source point, $\mathbf{r}'$. The electric surface charge densities, $q_e$ is related to $\mathbf{J}_d$, by the continuity equation:

$$\nabla\cdot\mathbf{J}_d = -\frac{\partial q_e}{\partial t} \Rightarrow q_e = -\int_{\tau=0}^{t} \nabla\cdot\mathbf{J}_d\,d\tau. \quad (38)$$

Using Equation (38), Equation (37) is re-written as:

$$\Psi_\nu = \frac{\partial\Phi_\nu(\mathbf{r},t)}{\partial t} = -\frac{1}{\varepsilon_\nu}\int_S\int_{\tau=0}^{t}\frac{\nabla\cdot\mathbf{J}_d(\mathbf{r}',\tau-\frac{R}{c_\nu})}{4\pi R}\,ds'\,d\tau. \quad (39)$$

Finally, we have:

$$\left[\frac{\partial^2\mathbf{A}_e}{\partial t^2}+\nabla\Psi_e+\frac{\partial}{\partial t}\left\{\frac{1}{\varepsilon_e}\nabla\times\mathbf{F}_e\right\}\right]_{tan} = \left[\frac{\partial\mathbf{E}^{inc}}{\partial t}\right]_{tan} \quad (40)$$

$$\left[\frac{\partial^2\mathbf{A}_i}{\partial t^2}+\nabla\Psi_i+\frac{\partial}{\partial t}\left\{\frac{1}{\varepsilon_i}\nabla\times\mathbf{F}_i\right\}\right]_{tan} = 0. \quad (41)$$

The integral equations (40) and (41) are solved as described in the next subsection.

### B. MOM solution

Assuming a suitable triangulation for the scattering structure, $\mathbf{J}_d$ and $\mathbf{M}_d$ are approximated as:

$$\mathbf{J}_d(\mathbf{r},t) = \sum_{m=1}^{N_d}\sum_{n=1}^{N_t}\alpha_{m,n}\,\mathbf{f}_m(\mathbf{r})\,g_n(t), \quad (42)$$

$$\mathbf{M}_d(\mathbf{r},t) = \sum_{m=1}^{N_d}\sum_{n=1}^{N_t}\beta_{m,n}\,\mathbf{a}_n\times\mathbf{f}_m(\mathbf{r})\,g_n(t), \quad (43)$$

where $N_d$ and $N_t$ represent the number of basis functions in space and time, respectively, $\mathbf{a}_n$ is the normal vector,

$$g_n(t) \equiv \begin{cases} 1-\frac{|t-t_n|}{\Delta t} & t\in(t_{n-1},t_{n+1}) \\ 0 & \text{otherwise,,} \end{cases} \quad (44)$$

for $n = 1,2,\cdots,N_t$, and, $\mathbf{f}_m(\mathbf{r})$ are the standard Rao-Wilton-Glisson (RWG) functions [17].

Using the symmetric product defined in Equation (18), we can write Equations (40) and (41) as:

$$<\mathbf{f}_m(\mathbf{r})g_n(t),\left[\frac{\partial^2\mathbf{A}_e}{\partial t^2}+\nabla\Psi_e+\frac{\partial}{\partial t}\left\{\frac{1}{\varepsilon_e}\nabla\times\mathbf{F}_e\right\}\right]> = <\mathbf{f}_m(\mathbf{r})g_n(t),\left[\frac{\partial\mathbf{E}^{inc}}{\partial t}\right]>, \quad (45)$$

$$<\mathbf{f}_m(\mathbf{r})g_n(t),\left[\frac{\partial^2\mathbf{A}_i}{\partial t^2}+\nabla\Psi_i+\frac{\partial}{\partial t}\left\{\frac{1}{\varepsilon_i}\nabla\times\mathbf{F}_i\right\}\right]> = 0, \quad (46)$$

for $m = 1,2,\cdots N_d$ and $n = 1,2,\cdots N_t$.

The first term, $<\mathbf{f}_m(\mathbf{r})g_n(t),\ \frac{\partial^2\mathbf{A}_e}{\partial t^2}>$, in Equation (45) may be written as:

$$\left\langle\mathbf{f}_m(\mathbf{r})g_n(t),\ \frac{\partial^2\mathbf{A}_e}{\partial t^2}\right\rangle = \frac{\partial^2}{\partial t^2}\left[\mu\int_S\frac{\mathbf{J}_d(\mathbf{r}',t-\frac{R}{c_e})}{4\pi R}\right] = \mu\left[\frac{\partial^2 g_n}{\partial t^2}\right]\int_S\frac{\mathbf{f}_m(\mathbf{r}',t-\frac{R}{c_e})}{4\pi R}\,ds'. \quad (47)$$

Next, the second term in Equation (45) is written as,

$$\langle\mathbf{f}_m(\mathbf{r})g_n(t),\ \nabla\Psi\rangle = \nabla\left[\int_S\frac{\nabla\cdot\mathbf{f}_m(\mathbf{r}',t-\frac{R}{c_e})}{4\pi R}\right]ds'. \quad (48)$$

The third term in Equation (45) is:

$$\left\langle\mathbf{f}_m(\mathbf{r})g_n(t),\ \frac{\partial}{\partial t}\left\{\frac{1}{\varepsilon_i}\nabla\times\mathbf{F}_i\right\}\right\rangle = \frac{\partial g_n}{\partial t}\int_S\frac{\nabla\times\mathbf{a}_n\times\mathbf{f}_m(\mathbf{r}',t-\frac{R}{c_e})}{4\pi R}\,ds'. \quad (49)$$

It is easy to see that similar expressions are valid for Equation (46) with $c_e$ replaced by $c_i$. The integrals present in Equations (46) - (49) may be carried out analytically using the procedures developed for the triangular domains [17].

Using the standard expansion procedure for MOM problems, it is possible to generate a matrix equation $\mathbf{ZX} = \mathbf{Y}$ of dimension $P = N_t\times 2N_d$. The matrix equation can be efficiently solved using the special procedure developed in [12, 13].

## IV. NUMERICAL RESULTS - VIE FORMULATION

In this section, we present numerical results for several inhomogeneous objects modeled by tetrahedral elements in the TD.

For all the examples presented in this section, and also for the next section, the following statements apply:

1. The object is placed at the center of the right-handed coordinate system, with the origin approximately coinciding with the geometrical center of the object. For all examples, $\theta$ and $\phi$ represent the angles measured with respect to $z$ and $x$ axes, respectively.

2. The incident field is a GPW, given by:

$$\mathbf{E}^{inc}(\mathbf{r}),t = \mathbf{E}_o\frac{4}{T_P\sqrt{\pi}}e^{-\gamma^2}, \quad (50)$$

where:

$$\gamma = \frac{4}{T_P}(ct-ct_o-\mathbf{r}\cdot\hat{k}). \quad (51)$$

In Equations (50) and (51), $\hat{k}$ is the unit vector in the direction of propagation of the incident wave, $T_P$ is the pulse width of the Gaussian impulse, $\mathbf{E}_o\cdot\hat{k} = 0$, $\mathbf{r}$ is a position vector relative to the origin, $c$ is the velocity of propagation in the external medium, and $t_o$ is a time delay which represents the time at which the pulse peaks at the origin. It may be noted that the GPW represents a smoothed impulse and as a result the response obtained may be considered as

the impulse response. It is well-known that once the impulse response is available, the response to any other incident time domain wave form can be obtained by performing straight-forward convolution.

3. The incident plane wave is traveling along the $z$-direction, and the electric field vector is linearly polarized along the $x$-axis.

In the next subsection, we consider only homogeneous dielectric bodies and compare the results with the frequency domain (FD) solution. We note that to generate the TD data, the FD solution must be performed at several frequencies and then take the inverse Fourier transform into the time domain.

### A. Homogeneous dielectric objects

As a first example, consider a dielectric sphere, radius$= 0.1m$, $\varepsilon_r = 3.0$, located with the origin coinciding with the center of the Cartesian coordinate system. The dielectric sphere is illuminated by the GPW described in Equation (50) with $T_p = 4.0$ LM and $t_0 = 6.0$ LM, where the unit "LM" implies Light-Meter (1 LM = $3.333 \times 1.0^{-9}$ s). The sphere is modeled by 119 tetrahedrons resulting in 268 triangle faces implying that we have 268 space basis functions. We modeled the time variable with 36 triangle functions with $\Delta t = 2t_0/36 = 0.33$ LM. We note that the number of triangle functions for time are dictated by the pulse width of GPW and is not very critical. The numerical results are presented in Fig. 3. Here, we compare the RCS obtained as a function of $\theta$ with $\phi = 0$ by the present method with the frequency domain SIE solution at 100 MHz, 200 MHz and 300 MHz. We note that for the sphere problem, it is possible to generate exact solution using Mie series. However, the SIE formulation was well tested for canonical shapes [7] and for the sake of uniformness we compared our results with numerical MOM solution only. We note that both solutions compare very well at the selected frequencies.

Next, we consider a rectangular homogeneous dielectric slab, with dimensions $1.0m \times 1.0m \times 0.2m$ and $\varepsilon_r = 2.0$, located in the Cartesian coordinate system as shown in the Fig. 4. The dielectric slab is illuminated by the GPW described in Equation (50) with $T_p = 8.0$ LM and $t_0 = 12.0$ LM. The slab is modeled by 626 tetrahedrons resulting in 1386 triangles. Thus, we have 1386 basis functions for space, and we modeled the time variable with 36 triangle functions. The numerical results are presented in Fig. 4. Here, we compare the RCS obtained by the present method with the SIE solution at 100 MHz, and 200 MHz. We note that both solutions compare very well for this case also.

Next, we consider a thick dielectric cylinder, with radius and height equal to $0.2m$, and $\varepsilon_r = 3.0$, located

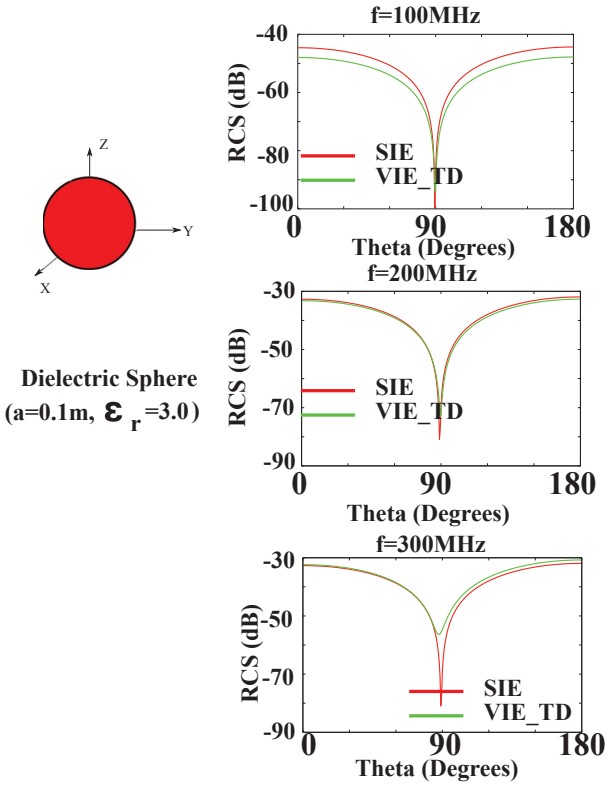


Fig. 3. RCS vs $\theta$ at $\phi = 0$ of a dielectric sphere (radius=0.1m and $\varepsilon_r = 3.0$) illuminated by a GPW.

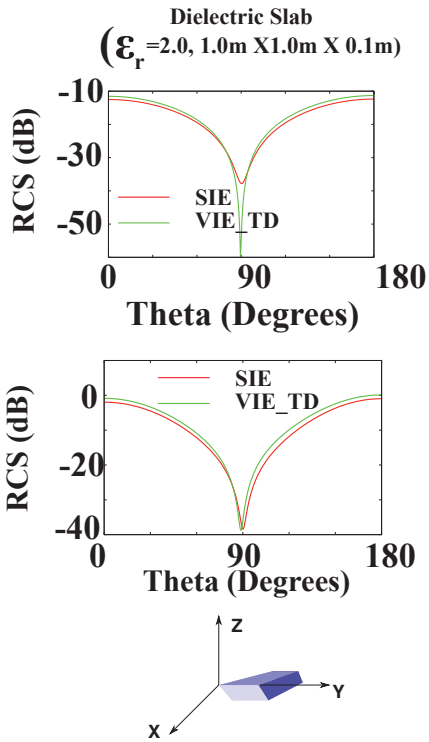


Fig. 4. RCS vs $\theta$ at $\phi = 0$ of a dielectric slab ($1.0m \times 1.0m \times 0.1m$, and $\varepsilon_r = 2.0$) illuminated by a GPW.

with the origin coinciding with the center of the Cartesian coordinate system. The dielectric cylinder is illuminated by the GPW described in Equation (50) with $T_p = 8.0$ LM and $t_0 = 12.0$ LM. The cylinder is modeled by 136 tetrahedrons resulting in 314 basis functions for space. We modeled the time variable with 36 triangle functions. The numerical results are presented in Fig. 5. Here, we plot the normal component of the electric flux density as a function of time and compare that with the solution obtained by the frequency domain MOM solution and Inverse Discrete Fourier Transform (VIE_FD_IDFT) method. The normal component is sampled at the center of the top face. We note that both solutions compare very well and also notice the absence of any late-time instabilities in the direct time domain solution. Although not shown here, the direct time domain solution was obtained up to 300 LM and remained stable.

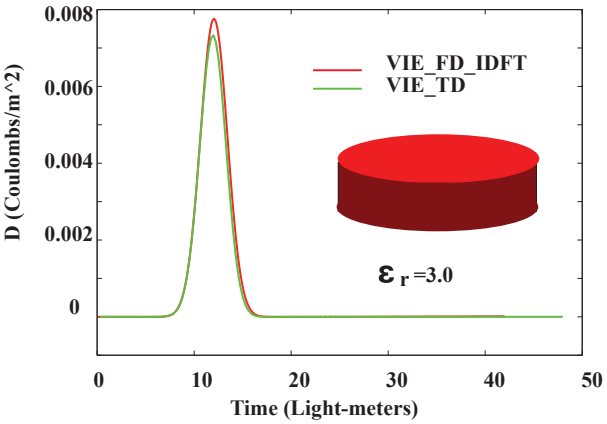


Fig. 5. Dielectric cylinder (radius=0.2$m$, height =0.1$m$, and $\varepsilon_r = 3.0$) illuminated by a GPW.

Next, we consider a few examples of composite bodies where two or more homogeneous bodies are joined to form the inhomogeneous, composite body.

### B. Objects with multiple dielectric materials

As a first example, consider a composite dielectric sphere, formed by combining two homogeneous dielectric hemispheres, each with radius=0.2$m$ and with distinct dielectric materials $\varepsilon_r = 3.0$ and $\varepsilon_r = 5.0$, as shown in the inset of Figs. 6 and 7. The composite dielectric sphere is illuminated by the GPW described in Equation (50) with $T_p = 8.0$ LM and $t_0 = 12.0$ LM. Each hemisphere is modeled by 124 tetrahedrons resulting in 286 triangles. Therefore, the total number of basis functions for this case is 572, and we modeled the time variable with 36 triangle functions. In Fig. 6, we present the normal component of the electric flux density as a function of time. The normal component is sampled at $\theta = 45^0$ and $\phi = 90^0$. The present solution is compared with the solution obtained in the FD, performing the calculations for 128 frequency points between 2- 256 MHz at 2 MHz interval, and performing IDFT. We note a good comparison between the two solutions and the absence of any late-time oscillations. In Fig. 7, we plot the backscattered field ($\theta = 180^0$ and $\phi = 0^0$) as a function of frequency for both solutions. We note that both solutions compare very well for this case in the frequency range set by the pulse-width of the incident field.

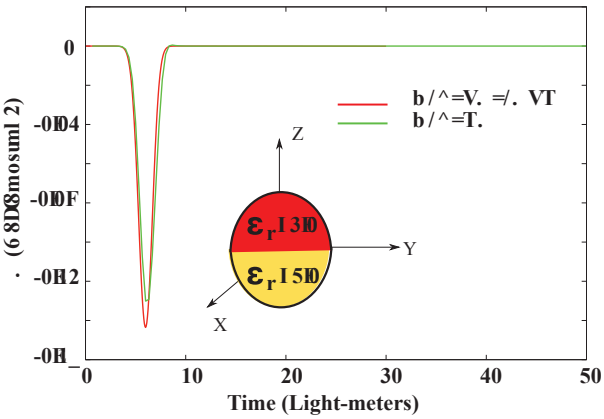


Fig. 6. Composite dielectric sphere illuminated by a GPW.

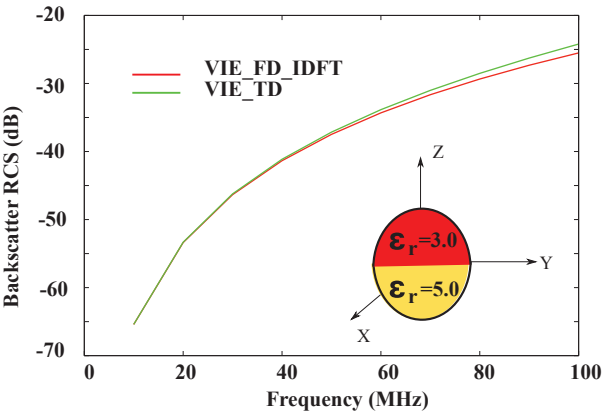


Fig. 7. Backscattering RCS vs Frequency of a composite dielectric sphere illuminated by a GPW.

Next, we consider the case of a composite dielectric slab, formed by placing two slabs, one on top of the other slab, each with a distinct dielectric material as shown in the inset of Fig. 8. The dimensions of each slab are $1.0m \times 1.0m \times 0.2m$ and the dielectric constants are $\varepsilon_r = 2.0$ and $\varepsilon_r = 3.0$, respectively. The dielectric slab is illuminated by the GPW described in Equation (50) with $T_p = 8.0$ LM and $t_0 = 12.0$ LM. Each slab is modeled by 626 tetrahedrons resulting in 1386 triangle faces. Therefore, the total number of basis functions for this problem

is 2772, and we modeled the time variable with 36 triangle functions. The comparison solution is obtained by developing the frequency domain solution using VIE at 128 frequency points and then performing the IDFT to obtain the TD solution. The numerical results are presented in Fig. 8. Here, we plot the electric flux density as a function of time. The normal component is sampled at the center of the top face. We note that both solutions compare reasonably well for this case also, and the direct time domain solution remains stable even at a very late time. The apparent difference in the peak value is due to the small number of frequency samples available for the IDFT solution.

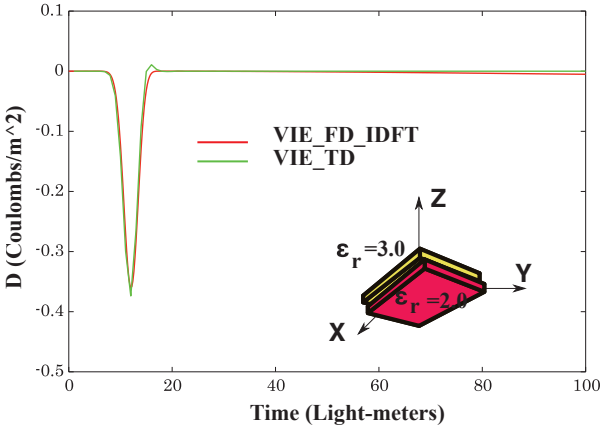


Fig. 8. Composite dielectric slab illuminated by a GPW.

Next, we consider a composite dielectric cylinder, formed by joining two homogeneous cylinders. The height and radius of each cylinder is, $0.5m$ and $0.2m$, respectively. The dielectric constant for each cylinder is $\varepsilon_r = 2.0$ and $\varepsilon_r = 3.0$. The composite cylinder is located with the origin coinciding with the center of the Cartesian coordinate system and the axis coinciding with the $z$-axis. The whole body is illuminated by the GPW described in Equation (50) with $T_p = 8.0$ LM and $t_0 = 12.0$ LM. Each cylinder is modeled by 410 tetrahedrons resulting in 902 triangle faces, and the total number of unknowns for this problem is 1804. We modeled the time variable with 36 triangle functions. The numerical results are presented in Fig. 9. Here, we plot the normal component of the electric flux density as a function of time and compare with the solution obtained using the frequency domain MOM solution and IDFT method. The normal component is sampled at the center of the top face. We note that both solutions compare very well and also notice the absence of any late-time instabilities. We also note that the IDFT solution behaved in a strange fashion (not tending to zero at late time) that can be attributed to a low sampling rate employed in the solution.

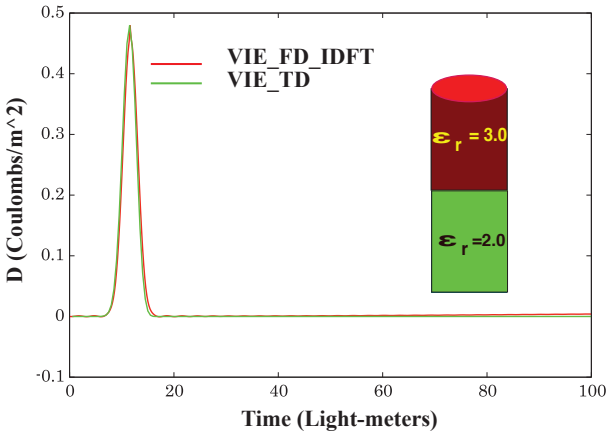


Fig. 9. Composite dielectric cylinder illuminated by a GPW.

As a last example in this subsection, we consider the case of three homogeneous dielectric discs, joined together as shown in the inset of Fig. 10. The radius and thickness of each disk is equal to $0.2m$. The dielectric constants are 3.0, 4.0, and 5.0 as shown in the figure. The whole body is illuminated by the GPW described in Equation (50) with $T_p = 4.0$ LM and $t_0 = 6.0$ LM. Each cylinder is modeled by 136 tetrahedrons resulting in 314 triangle faces. The total number of basis functions for this problem is 942. We modeled the time variable with 24 triangle functions. The numerical results are presented in Fig. 10. Here, we plot the backscattered field as a function of time for both the frequency domain solution and the present algorithm. The back-scattered field data for the present time domain solution is obtained by performing a straightforward Fourier transform. We note that both solutions compare very well for this case in the frequency range set by the pulse-width of the incident field.

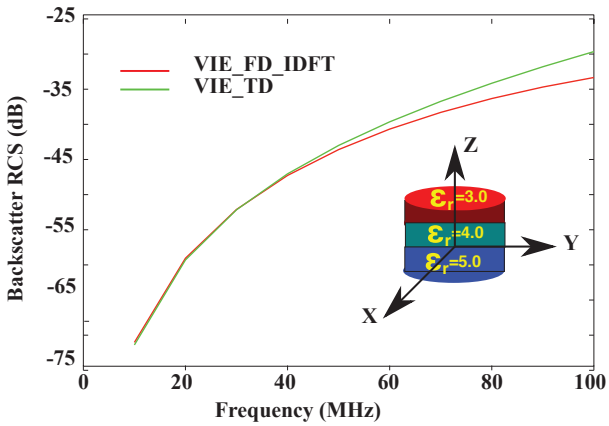


Fig. 10. Composite dielectric disk illuminated by a GPW.

## V. NUMERICAL RESULTS - SIE FORMULATION

In this section, we present numerical results for a few representative single/multiple homogeneous objects using direct time domain SIE formulation. We only consider canonical shapes in this work. For all the examples presented in this section, the incident field is a GPW, given by Equations (50) and (51). We present comparisons for the equivalent electric and magnetic currents, **J** and **M**, respectively, with other methods. Also, note that for all results presented in this section, **M** is normalized with respect to the free space impedance, $\eta$.

### A. Homogeneous dielectric objects

As a first example, consider a dielectric sphere, radius=1.0$m$, $\varepsilon_r = 10.0$, located with the origin coinciding with the center of the Cartesian coordinate system. The dielectric sphere is illuminated by the GPW described in Equation (50) with $T_p = 20.0$ LM and $t_0 = 30.0$ LM. The sphere is modeled by 288 triangles resulting in 432 edges implying that we have 864 unknowns (432 unknowns each for **J** and **M**, respectively) for the solution scheme. We modeled the time variable with 45 triangle functions. The numerical results are presented in Fig. 11. In the figure, we present the induced equivalent current components, $J_x$ and $M_y$, at a selected point, ($\theta = 90^\circ$ and $\phi = 0^\circ$), as a function of time. Note that we are presenting the results only for a single point on the body although the data is available for any point on the sphere. The time domain results are compared with the results obtained by IDFT solution. We further note that the IDFT solution is presented for a relatively shorter duration compared to direct TD solution (120 LM vs 600 LM). It is because the IDFT solution is periodic by nature since the inverse Fourier transform is performed and hence dictated by the frequency interval between two successive samples ($\Delta f$). For a longer time signature, one must sample the frequency scale more closely which dramatically increases the computational time.

Next, we consider a dielectric cube of side length 2.0$m$, and $\varepsilon_r = 10.0$, located with the origin coinciding with the center of the Cartesian coordinate system. The dielectric cube is illuminated by the GPW described in Equation (50) with $T_p = 20.0$ LM and $t_0 = 30.0$ LM. The cube is modeled by 432 triangles resulting in 648 edges implying that we have 1296 unknowns. We modeled the time variable with 45 triangle functions. The numerical results are presented in Fig. 12. In the figure, we present the induced equivalent currents, $J_x$ and $M_y$, at a selected point (at the center of the top face) as a function of time. The comparison between the two results is reasonably well. We note that the currents induced are very weak and the small differences we notice are due to the numerical

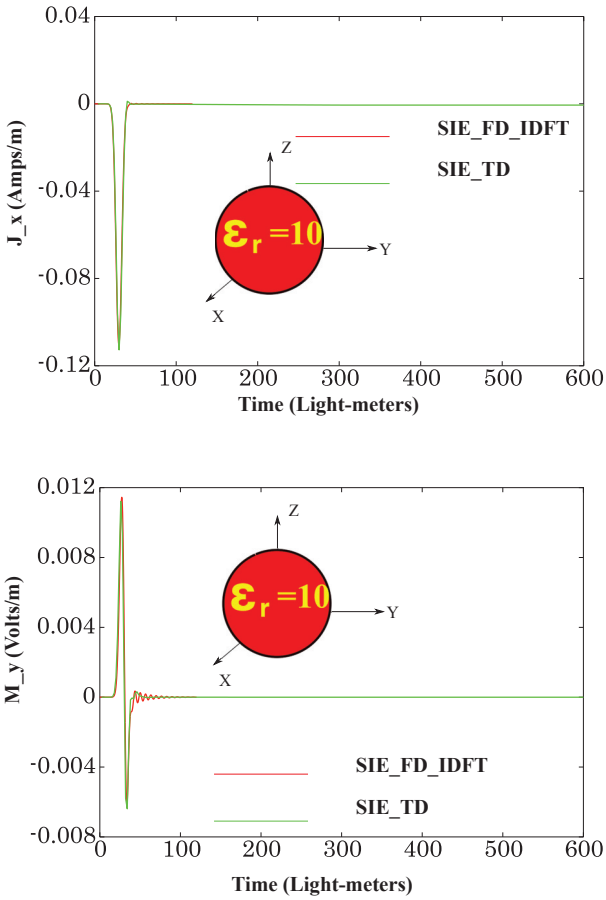


Fig. 11. Dielectric sphere (radius=1.0m and $\varepsilon_r = 10.0$) illuminated by a GPW.

errors. Further, we notice small oscillations for the IDFT scheme and absence of them in the TD scheme. This is due to the large time step in the TD scheme to cover the time scale 0-600 LM.

Next, we consider a circular dielectric disk with 1.0$m$ radius, 0.2$m$ thickness, and $\varepsilon_r = 3.0$, located with the origin coinciding with the center of the Cartesian coordinate system. The disk is illuminated by the GPW described in Equation (50) with $T_p = 20.0$ LM and $t_0 = 30.0$ LM. The body is modeled by 48 triangles resulting in 72 edges implying that we have 144 unknowns. We modeled the time variable with 45 triangle functions. The numerical results are presented in Fig. 13. In the figure, we present the induced equivalent currents, $J_x$ and $M_y$, at a selected point (at $x = 0.0$, $y = 0.5$ on the top face) as a function of time. We note that the results remain stable for a very long time whereas the IDFT solution is terminated much earlier. This is because, to obtain a long time signature using the IDFT solution, the frequency range needs to be densely sampled making the solution very expensive.

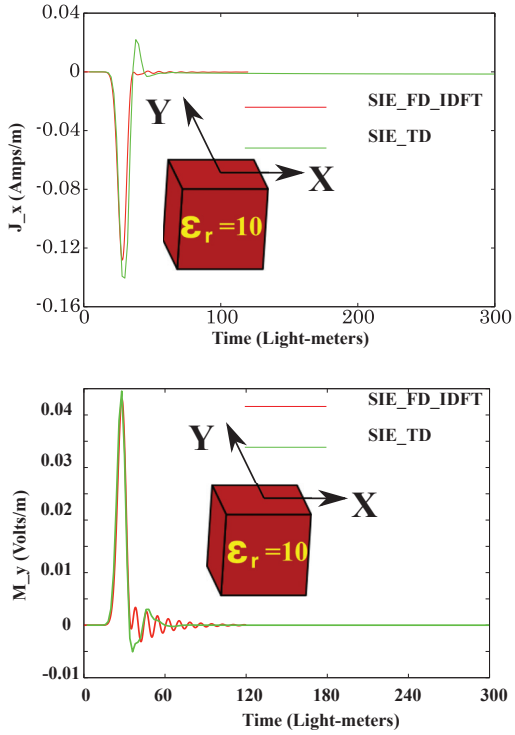


Fig. 12. Dielectric cube (a=2.0m and $\varepsilon_r = 10.0$) illuminated by a GPW.

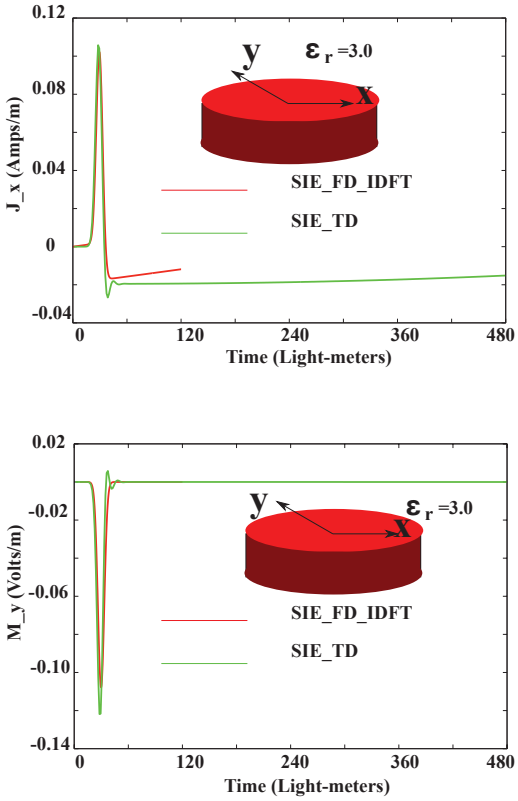


Fig. 13. Dielectric disk (radius 1.0m, thickness 0.2m, and $\varepsilon_r = 3.0$) illuminated by a GPW.

Next, we consider a dielectric cylinder of length $1.0m$, $0.2m$ radius, and $\varepsilon_r = 2.0$, located with the center of the body coinciding with the center of the Cartesian coordinate system. The dielectric cylinder is illuminated by the GPW described in Equation (50) with $T_p = 20.0$ LM and $t_0 = 30.0$ LM. The body is modeled by 176 triangles resulting in 264 edges implying that we have 528 unknowns. We modeled the time variable with 20 triangle functions. The numerical results are presented in Fig. 14. In the figure, we present the induced equivalent currents, $J_x$ and $M_y$, at a selected point (at $x = 0.0$, $y = 0.1$ on the top face) as a function of time. The time domain results are compared with the results obtained by the IDFT solution. Although the results compare well, there is some difference, particularly related to the electric current. We feel that the IDFT solution is showing oscillations because of the loss-less, perfect dielectric material used in the simulation. A small amount of loss would dampen the oscillations but may also contribute to some loss in the peak values.

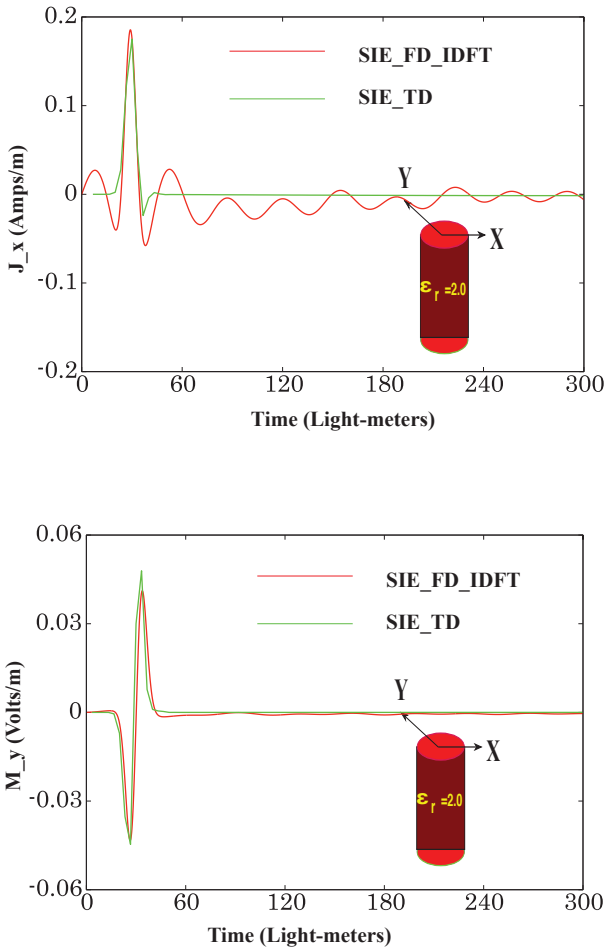


Fig. 14. Dielectric cylinder (radius 0.2m, length 1m, and $\varepsilon_r = 2.0$) illuminated by a GPW.

**B. Objects with multiple dielectric materials**

Now, we consider the case of two dielectric cylinders placed along the $z$-axis and placed one cylinder on the top of the other cylinder as shown in the Figure 15. Each dielectric cylinder is of length $1.0m$ and $1.0m$ radius. The dielectric constant of the top cylinder is $\varepsilon_r = 5.0$, where as the bottom cylinder's dielectric constant is $\varepsilon_r = 1.0$ implying that it is an air-dielectric body. Because of the air-dielectric nature, the result for a single cylinder and the combination of a dielectric cylinder with air-dielectric cylinder should be identical. The dielectric cylinder combination is illuminated by the GPW described in Equation (50) with $T_p = 12.0$ LM and $t_0 = 18.0$ LM. Each body is modeled by 48 triangles resulting in 72 edges implying that we have 288 unknowns for the whole system (144 unknowns per cylinder). We modeled the time variable with 24 triangle functions. The numerical results are presented in Fig. 15. In the figure, we present the induced equivalent currents, $J_x$ and $M_y$, at a selected point (at $x = 0.0$, $y = 0.5$ on the top face of the top cylinder) as a function of time. As expected, the air-dielectric cylinder did not contribute to the scattering phenomenon.

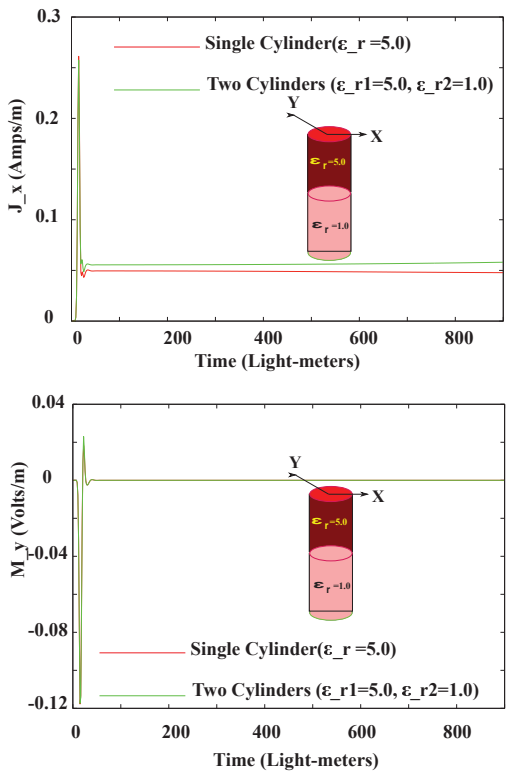


Fig. 15. A system of two dielectric cylinders, radius $1.0m$, length $1.0m$, illuminated by a GPW.

Next, we consider the case of two dielectric cylinders placed along the $z$-axis and touching each other as shown in the Fig. 16. Each dielectric cylinder is of length $1.0m$ and radius $=1.0m$. The dielectric constants of the top and bottom cylinders are $\varepsilon_r = 3.0$, and $\varepsilon_r = 5.0$, respectively. The dielectric cylinders are illuminated by the GPW described in Euation. (50) with $T_p = 12.0$ LM and $t_0 = 18.0$ LM. Each body is modeled by 48 triangles resulting in 72 edges implying that we have 288 unknowns for the whole system (144 unknowns per cylinder). We modeled the time variable with 24 triangle functions. The numerical results are presented in Fig. 16. In the figure, we present the induced equivalent currents, $J_x$ and $M_y$, at a selected point (at $x = 0.0$, $y = 0.5$ on the top face of the top cylinder) as a function of time. The time domain results are compared with the results obtained by the IDFT solution and the comparison is reasonable.

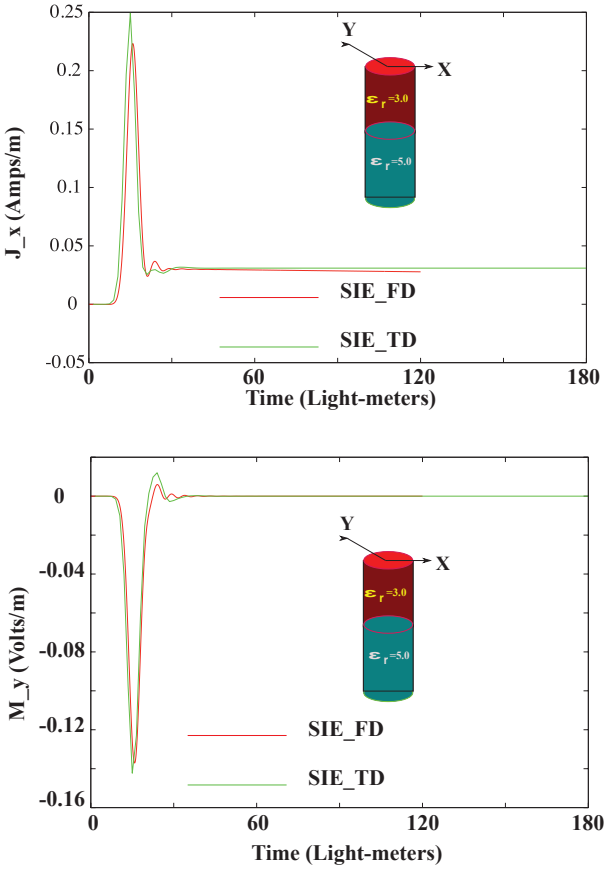


Fig. 16. Dielectric cylinders illuminated by a GPW.

Next, we consider the case of two dielectric cubes touching each other as shown in the Fig. 17. Each dielectric cube is of side length $1.0m$. The dielectric constants of the top and bottom cubes are $\varepsilon_r = 3.0$, and $\varepsilon_r = 5.0$, respectively. The two-body system is illuminated by the GPW described in Equation (50) with $T_p = 12.0$ LM and $t_0 = 18.0$ LM. Each cube is modeled by 108 tri-

angles resulting in 162 edges implying that we have 648 unknowns for the whole system (324 unknowns per cube). We modeled the time variable with 24 triangle functions. The numerical results are presented in Fig. 17. In the figure, we present the induced equivalent currents, $J_x$ and $M_y$, at the center of the top face as a function of time. The time domain results are compared with the results obtained by the IDFT solution and the comparison is reasonable.

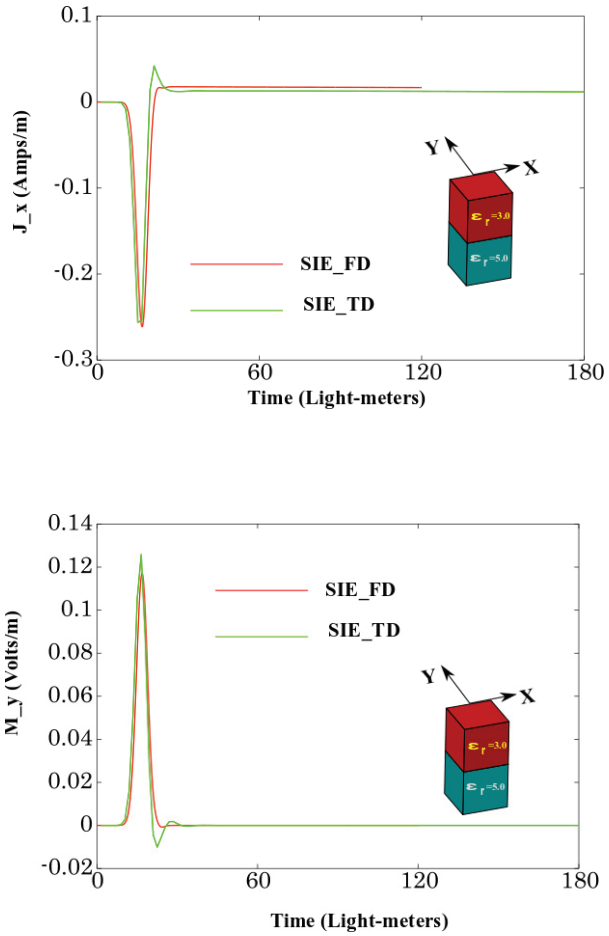


Fig. 17. Dielectric cubes illuminated by a GPW.

As a last example, we consider the case of five dielectric cylinders, each with 0.2 m radius and 10 m length, joined together to form a 50 m long cylinder. The dielectric constant of each cylinder is 16, 14, 12, 8, and 4. The whole structure is placed along the $z$-axis and illuminated by a Gaussian pulse with 20 LM pulse width. The time domain result is transformed into frequency domain and the RCS is compared with the direct frequency domain results at 10, 20 and 25 MHz as shown in the Fig. 18. Each cylinder is modeled by 132 triangles resulting in 198 edges implying that we have 990 unknowns for the whole system. We note that the comparison is excellent for 10 and 20 MHz cases whereas we note a different result for the 25 MHz case. We attribute this difference to the bandwidth of the incident pulse which drops off steeply after 20 MHz. This example also highlights the limitation of the time domain solution. It is often said that one TD simulation is sufficient to obtain the frequency response from DC to daylight via Fourier transform. It is only true if one uses a true impulse for the incident field, which is not possible in our method. Hence, one should note that the frequency response that can be obtained is limited by the bandwidth of the incident pulse.

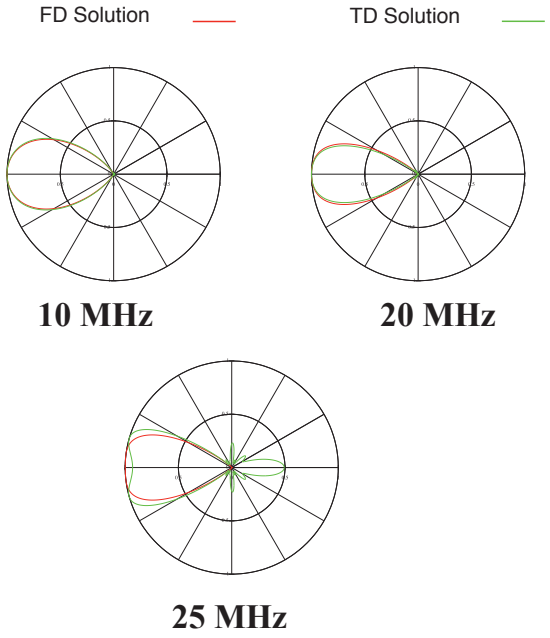


Fig. 18. RCS of a 5-section, 50 m inhomogeneous cylinder.

## VI. CONCLUSIONS

In this work, we presented direct time domain formulations for dielectric bodies of arbitrary shape using surface and volume integral equation formulations. The main objective of this work is to demonstrate that the solution remains stable by eliminating time marching as was done in the previous works. Further, the formulation and the solution methodology is simple, not requiring any complex mathematical manipulations. Lastly, the present method can easily handle multiple right hand sides efficiently as required for monostatic radar cross section (RCS) studies, thus preserving the advantages of MOM solution scheme. Unfortunately, the conventional MOT scheme and all the DE methods including FDTD is not capable of performing this task efficiently and for each right hand side the solution must be started from the beginning.

## ACKNOWLEDGEMENTS

This work is sponsored by the Office of Naval Research via the NRL Base Program.

## REFERENCES

[1] K. S. Yee, "Numerical solution of initial boundary value problems involving Maxwell's equations in isotropic media," *IEEE Transactions on Antennas and Propagation*, vol. 14, pp. 302-307, 1966.

[2] K. S. Yee, J. S. Chen and A. H. Chang, "Conformal finite-difference time domain (FDTD) with overlapping grids," *IEEE Transactions on Antennas and Propagation*, vol. 40, pp. 1068-1075, 1992.

[3] R. Gomez, J. A. Morente and A. Salinas, "Time domain analysis of an array of straight-wire coupled antennas," *IEE Electronic Letters*, vol. 22, pp. 316-318, 1986.

[4] R. Gomez, A. Salinas, A. R. Bretones, J. Fornieles and M. Martin, "Time domain integral equations for EMP analysis," *International Journal of Numerical Modeling*, vol. 4, pp. 153-162, 1991.

[5] R. Gomez, A. Salinas and A. R. Bretones, "Time domain integral equation methods for transient analysis," *IEEE AP-S Magazine*, vol. 34, pp. 15-22, 1992.

[6] S. M. Rao and D. R. Wilton, "Transient scattering by conducting surfaces of arbitrary shape," *IEEE Transactions on Antennas and Propagation*, vol. 39, pp. 56-61, 1991.

[7] D. A. Vechinski, S. M. Rao, and T. K. Sarkar, "Transient scattering from three-dimensional arbitrarily shaped dielectric bodies," *Journal of the Optical Society of America*, vol. 11, pp. 1458-1470, 1994.

[8] G. Manara, A. Monorchio, and R. Reggiannini, "A space-time discretization criterion for a stable time-marching solution of the electric field integral equation," *IEEE Transactions on Antennas and Propagation*, vol. 45, no. 3, pp. 527-533, Mar. 1997.

[9] N. Gres, A. Ergin, E. Michielssen and B. Shanker, "Volume integral equation based electromagnetic scattering from three-dimensional inhomogeneous dielectric objects," *Radio Science*, vol. 36, pp. 379-386, 2001.

[10] B. Shanker, K. Aygun, and E. Michielssen, "Fast analysis of transient scattering from lossy inhomogeneous dielectric bodies,"*Radio Science*, vol. 39, RS2007, doi:10.1029/2003RS002877, 2004.

[11] G. Kobidze, J. Gao, B. Shanker, and E. Michielssen, "A fast time domain integral equation based scheme for analyzing scattering from dispersive objects," *IEEE Transactions on Antennas and Propagation*, vol. 53, pp. 1215-1226, 2005.

[12] S. M. Rao, "A simple and efficient method of moments solution procedure for solving time-domain integral equation - Application to wire-grid model of perfect conducting objects," *IEEE Journal on multiscale and multiphysics computational techniques*, vol. 4, pp. 57-63, Mar. 2019.

[13] S. M. Rao "A straight-forward method of moments procedure to solve the time domain integral equation to PEC bodies via triangular patch modeling," *ACES Journal*, vol. 35, pp. 843-854, Aug. 2020.

[14] R. Harrington, *Time Harmonic Electromagnetic Fields*, New York: IEEE Press, 2001.

[15] R. Harrington, *Field Computation by Moment Methods*, New York: Macmillan, 1968.

[16] S. M. Rao, *Time Domain Electromagnetics*, London: Academic Press, 1999.

[17] S. M. Rao, D. R. Wilton, and A. W. Glisson, "Electromagnetic scattering by surfaces of arbitrary shape," *IEEE Transactions on Antennas and Propagation*, vol. 30, pp. 409-418, 1982.

[18] D. H. Schaubert, D. R. Wilton, and A. W. Glisson, "Tetrahedral modeling method for electromagnetic scattering by arbitrarily shaped inhomogeneous dielectric bodies," *IEEE Transactions on Antennas and Propagation*, vol. 32, pp. 77-85, 1984.

**Sadasiva M. Rao** received the Bachelor's degree in electrical communication engineering from Osmania University in 1974, Master's degree in microwave engineering from Indian Institute of Sciences in 1976, and Ph.D. degree with specialization in electromagnetic theory from University of Mississippi in 1980.

Dr. Rao served as an Assistant Professor in the Department of Electrical Engineering, Rochester Institute of Technology from 1980 to 1985, Senior Scientist at Osmania University from 1985 to 1987, and as a Professor in the Department of Electrical and Computer Engineering, Auburn University, from 1988 to 2009. He also held visiting Professorships at University of Houston (1987-1988), Osmania University, and Indian Institute of Science. Presently, he is with the Radar Division, Naval Research Laboratory, Washington, DC.

Dr. Rao worked extensively in the area of numerical modeling techniques as applied to Electromagnetic/Acoustic Scattering. He and his team at the University of Mississippi, were the original researchers to develop the planar triangular patch model and to solve the problem of EM scattering by arbitrary shaped conducting bodies. For this work, he received the best paper award for the period 1979-1981 from SUMMA

Foundation. He published/presented over 150 papers in international journals/conferences. For his contributions in numerical electromagnetic problems, he was awarded the status of Fellow of IEEE. Further, he was recognized as a Highly Cited Researcher by Thomson ISI in 2001. Dr. Rao's research interests are in the area of numerical methods applied to antennas and scattering.

# Impact Evaluation of an External Point Source to a Generalized Model of the Human Neck

**Anna A. Varvari[1], Dimitrios I. Karatzidis[1], Tadao Ohtani[2], Yasushi Kanai[3], and Nikolaos V. Kantartzis[1]**

[1]Department of Electrical and Computer Engineering
Aristotle University of Thessaloniki, 54124, Greece
{avarvari, karatzidis, kant}@ece.auth.gr

[2]Independent Researcher
Asahikawa, 070-0841, Japan
bytcg100@ybb.ne.jp

[3]Department of Niigata Institute of Technology
Kashiwazaki, 945-1195, Japan
kanai@iee.niit.ac.jp

***Abstract* –** A methodical approach for assessing the effects of an external point source to a non-spherical model of the human neck is presented in this paper. The neck model consists of multilayered spheres to represent the skin, fat, muscle tissues, thyroid, and esophagus. The novel geometry enables the formulation of dyadic Green's functions to accurately calculate the electric fields, considering the suitable surface boundary conditions and the superposition principle. Numerical outcomes for a Hertz dipole (i.e., a wireless network antenna) at the frequency of 2.4 GHz certify the benefits of the technique and elaborately describe the responsiveness of the neck/thyroid to the selected source.

***Index Terms* –** biomedical engineering, computational electromagnetics, Green's function methods, wireless body area networks.

## I. INTRODUCTION

The rapid evolution of healthcare wireless body area networks (WBANs) reflects the escalating need for real-time smart infrastructures to reliably monitor key gauges of the human body [1, 2]. To this aim, an impressive variety of such systems has been developed in terms of specialized antennas [3–5] and advanced biomedical applications [6, 7]. On the other hand, the assessment of electromagnetic radiation effects of several WBANs upon the human body and particularly on the thyroid has lately become a critical problem [8, 9]. Existing studies concerning the radiofrequency spectrum focus mainly on thermal analysis [10, 11]. However, there is an ever-increasing demand for simplified, precise, and economical models of the human neck to further explore the thyroid sensitivity to electromagnetic radiation.

This paper presents a systematic technique for the rigorous calculation of electromagnetic fields involving body area networks near the human neck. The proposed model represents abstractly the neck tissues as spherical layers and structures, permitting the parametric study of the thyroid. Concerning the mathematical formulation and the numerical results, the rapid and accurate derivation of the latter is enabled with the introduction of a new set of dyadic Green's functions (dGfs). In this framework, we define the geometry of the model representing each part of the neck with a spherical body. Then, the electric field is determined using the proposed dGf-based technique. Finally, the results, so derived, are compared and validated through numerical outcomes obtained from a well-known computational package.

## II. GEOMETRY OF THE NECK MODEL

The featured model, presented in Fig. 1, consists of the host sphere that has two spherical layers for the representation of the skin $(S_1)$ and the fat $(S_2)$, while a third cocentric inclusion depicts the muscle tissue $(S_3)$. Also, the non-overlapping spherical eccentric inclusions for the right thyroid lobe $(S_4)$, the left thyroid lobe $(S_5)$, the trachea $(S_6)$, the esophagus $(S_7)$ and the other neck tissues $(S_8)$ render the model non-spherical since the model lacks spherical symmetry. Each inclusion has an outer radius $a_i$ and a thickness $w_i$, for $i = 1, 2, \ldots, 8$, with the cocentric ones centered at origin O and the eccentric ones at $O_j$, defined by vectors $\mathbf{d}_j$, for $j = 4, 5, \ldots, 8$. Note that all parts are occupied by a lossy dielectric medium characterized by a complex relative permittivity

*Submitted On: July 30, 2023*
*Accepted On: November 20, 2023*

https://doi.org/10.13052/2024.ACES.J.390306

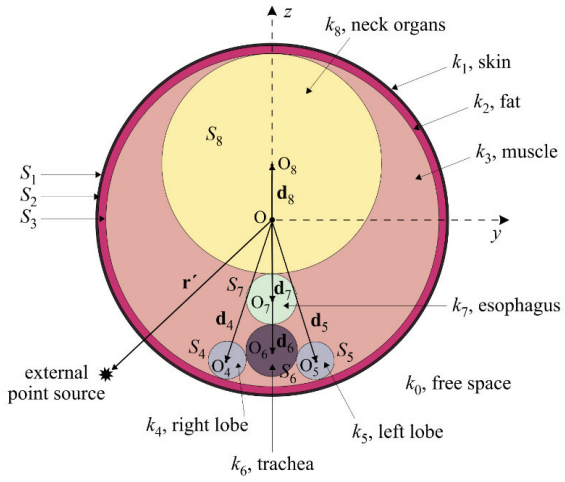


Fig. 1. Cross-section of the generalized neck model.

$\widetilde{\varepsilon}_i$ and a wavenumber $k_i = \omega\sqrt{\mu_0\widetilde{\varepsilon}_i}$, for $i = 1, 2, \ldots, 8$ and $\omega$ the angular frequency. Lastly, in our analysis, the free-space wavenumber is $k_0 = \sqrt{\mu_0\widetilde{\varepsilon}_0}$, regarding a typical $e^{-\mathrm{j}\omega t}$ time dependence and the coordinate system $(\mathrm{O}, r, \theta, \varphi)$ or $(\mathrm{O}_j, r_j, \theta_j, \varphi_j)$, for $j = 4, 5\ldots, 8$, defined at the origin O or $\mathrm{O}_j$, respectively.

## III. MATHEMATICAL FORMULATION

Let us assume that $\overline{\overline{\mathbf{G}}}_{\mathrm{e,s}}^{(0)}$ is the free-space electric-field dGf which provides the electric field of an external point source s. In this case, the free-space electric-field dGf, $\overline{\overline{\mathbf{G}}}_{\mathrm{e,s}}^{(0)}$, manifests as the solution of the dyadic Helmholtz equation $\nabla\times\nabla\times\overline{\overline{\mathbf{G}}}_{\mathrm{e,s}}^{(0)} - k_0^2 = \overline{\overline{\mathbf{I}}}\delta(\mathbf{r}-\mathbf{r}\prime)$, where $\overline{\overline{\mathbf{I}}}$ stands for the unit dyad. By implementing the Ohm-Rayleigh method, discussed in [12], we can derive

$$\overline{\overline{\mathbf{G}}}_{\mathrm{e,s}}^{(0)} = -\frac{1}{k_0^2}\hat{r}\hat{r}'^{\delta}\left(\mathbf{r}-\mathbf{r}'\right) + \mathrm{j}\frac{k_0}{4\pi}\sum_{nm,\alpha} c_{mn}\mathbf{F}_{\alpha,mn}^{(1)}\left(k_0\mathbf{r}\right)\mathbf{F}_{\alpha,mn}^{(3)}\left(k_0\mathbf{r}\prime\right), \quad (1)$$

where $\hat{r}$ and $\hat{r}'$ are the corresponding unit vectors, $m = -n, -n+1, \ldots, n-1, n$ (for $n = 1, 2, \ldots$) and $c_{mn} = (-1)^m(2n+1)/n(n+1) = c_{-mn}$. It is stressed that in (1), according to the theoretical formulation of Green's functions, $\alpha$ indicates the respective vector spherical harmonic $\mathbf{M}$ or $\mathbf{N}$. Therefore, for $\alpha = M, N$, it holds that

$$\mathbf{F}_{M,mn}^{(\iota)}(k\mathbf{r}) = \mathbf{M}_{mn}^{(\iota)}(k\mathbf{r}) = z_n^{(\iota)}(kr)\left(\mathrm{j}m\frac{P_m^n(\cos\theta)}{\sin\theta}\widehat{\theta} - \frac{\mathrm{d}P_m^n(\cos\theta)}{\mathrm{d}\theta}\widehat{\varphi}\right)e^{-\mathrm{j}m\varphi}, \quad (2)$$

$$\mathbf{F}_{N,mn}^{(\iota)}(k\mathbf{r}) = \mathbf{N}_{mn}^{(\iota)}(k\mathbf{r}) = \frac{1}{k}\nabla\times\mathbf{M}_{mn}^{(\iota)}(k\mathbf{r}), \quad (3)$$

with $z_n^{(\iota)}(kr)$ being a spherical Bessel function of the first kind (when $\iota = 1$) or a Hankel function (when $\iota = 3$) and $P_m^n(\cos\theta)$ a Legendre function of the first kind [13, 14]. Observe that (1) holds solely for $r \le r\prime$, otherwise the $\iota = 1, 3$ superscripts of $\mathbf{F}$ must be reversed.

Regarding the proposed neck model, the desired dGf exhibits a bilocal spatial dependence, as the position vector of its various parts and the source are $\mathbf{r}$ and $\mathbf{r}\prime$. Moreover, the latter are likely to not belong to the same coordinate system and/or may not end at the same surface. Consequently, and in terms of [15], we denote as $Q_l$ ($l = 1, 2, \ldots, 8$) the location of the field point of interest, considering that it lies in the region limited by two surfaces, namely $S_{\mathrm{in}}$ and $S_{\mathrm{out}}$. Therefore, the electric dGf at $Q_l$ is acquired through $\overline{\overline{\mathbf{G}}}_{\mathrm{e}}^{(l)}(\mathbf{r},\mathbf{r}\prime) = \overline{\overline{\mathbf{G}}}_{\mathrm{e,in}}^{(l)} + \overline{\overline{\mathbf{G}}}_{\mathrm{e,out}}^{(l)} + \overline{\overline{\mathbf{G}}}_{\mathrm{e,s}}^{(l)}$, with $\overline{\overline{\mathbf{G}}}_{\mathrm{e,in}}^{(l)}$ and $\overline{\overline{\mathbf{G}}}_{\mathrm{e,out}}^{(l)}$ the respective electric dGfs at the $S_{\mathrm{in}}$ and $S_{\mathrm{out}}$ of the region where $Q_l$ is located. As a result, the electric-field intensity at $Q_l$ is derived as

$$\mathbf{E}^{(l)}(\mathbf{r}) = \mathrm{j}\omega\mu_0\iiint_V \overline{\overline{\mathbf{G}}}_{\mathrm{e}}^{(l)}(\mathbf{r},\mathbf{r}\prime)\bullet\mathbf{J}^{(l)}(\mathbf{r}\prime)\mathrm{d}V, \quad (4)$$

for $V$ the volume confined between surfaces $S_{\mathrm{in}}$ and $S_{\mathrm{out}}$ and $\mathbf{J}^{(l)}(\mathbf{r}\prime)$ the electric current density of the external source at $\mathbf{r}\prime$. In this context, the necessary dGfs at every point of interest, confined between surfaces $S_i$ and $S_{i+1}$ (for $i = 1, 2, \ldots, 8$), as well as those in the free space, are

$$\overline{\overline{\mathbf{G}}}_{\mathrm{e}}^{(0)} = \overline{\overline{\mathbf{G}}}_{\mathrm{e,s}}^{(0)} + \overline{\overline{\mathbf{G}}}_{\mathrm{e},1}^{(0)}, \quad (5)$$

$$\overline{\overline{\mathbf{G}}}_{\mathrm{e}}^{(1)} = \overline{\overline{\mathbf{G}}}_{\mathrm{e},1}^{(1)} + \overline{\overline{\mathbf{G}}}_{\mathrm{e},2}^{(1)}, \quad (6)$$

$$\overline{\overline{\mathbf{G}}}_{\mathrm{e}}^{(2)} = \overline{\overline{\mathbf{G}}}_{\mathrm{e},2}^{(2)} + \overline{\overline{\mathbf{G}}}_{e,3}^{(2)}, \quad (7)$$

$$\overline{\overline{\mathbf{G}}}_{\mathrm{e}}^{(3)} = \overline{\overline{\mathbf{G}}}_{\mathrm{e},3}^{(3)} + \overline{\overline{\mathbf{G}}}_{\mathrm{e},4}^{(3)} + \overline{\overline{\mathbf{G}}}_{\mathrm{e},5}^{(3)} + \overline{\overline{\mathbf{G}}}_{\mathrm{e},6}^{(3)} + \overline{\overline{\mathbf{G}}}_{\mathrm{e},7}^{(3)} + \overline{\overline{\mathbf{G}}}_{\mathrm{e},8}^{(3)}, \quad (8)$$

$$\overline{\overline{\mathbf{G}}}_{\mathrm{e}}^{(4)} = \overline{\overline{\mathbf{G}}}_{\mathrm{e},4}^{(4)}, \quad (9)$$

$$\overline{\overline{\mathbf{G}}}_{\mathrm{e}}^{(5)} = \overline{\overline{\mathbf{G}}}_{\mathrm{e},5}^{(5)}, \quad (10)$$

$$\overline{\overline{\mathbf{G}}}_{\mathrm{e}}^{(6)} = \overline{\overline{\mathbf{G}}}_{\mathrm{e},6}^{(6)}, \quad (11)$$

$$\overline{\overline{\mathbf{G}}}_{\mathrm{e}}^{(7)} = \overline{\overline{\mathbf{G}}}_{\mathrm{e},7}^{(7)}, \quad (12)$$

$$\overline{\overline{\mathbf{G}}}_{\mathrm{e}}^{(8)} = \overline{\overline{\mathbf{G}}}_{\mathrm{e},8}^{(8)}. \quad (13)$$

Using the free-space dyad, the above system becomes

$$\overline{\overline{\mathbf{G}}}_{\mathrm{e}}^{(0)} = \overline{\overline{\mathbf{G}}}_{\mathrm{e,s}}^{(0)} + \mathrm{j}\frac{k_0}{4\pi}\sum_{nm,\alpha}\left[\mathbf{F}_{\alpha,mn}^{(3)}(k_0\mathbf{r})\mathbf{A}_{\alpha,mn}^{(0)}(\mathbf{r}\prime)\right], \quad (14)$$

$$\overline{\overline{\mathbf{G}}}_{\mathrm{e}}^{(1)} = \mathrm{j}\frac{k_1}{4\pi}\sum_{nm,\alpha}\left[\mathbf{F}_{\alpha,mn}^{(1)}\left(k_1\mathbf{r}\right)\mathbf{C}_{\alpha,mn}^{(1)}\left(\mathbf{r}'\right) + \mathbf{F}_{\alpha,mn}^{(3)}(k_1\mathbf{r})\mathbf{A}_{\alpha,mn}^{(1)}(\mathbf{r}\prime)\right], \quad (15)$$

$$\overline{\overline{\mathbf{G}}}_{\mathrm{e}}^{(2)} = \mathrm{j}\frac{k_2}{4\pi}\sum_{nm,\alpha}\left[\mathbf{F}_{\alpha,mn}^{(1)}\left(k_2\mathbf{r}\right)\mathbf{C}_{\alpha,mn}^{(2)}\left(\mathbf{r}'\right) + \mathbf{F}_{\alpha,mn}^{(3)}(k_2\mathbf{r})\mathbf{A}_{\alpha,mn}^{(2)}(\mathbf{r}\prime)\right], \quad (16)$$

$$\overline{\overline{\mathbf{G}}}_{\mathrm{e}}^{(3)} = \mathrm{j}\frac{k_3}{4\pi}\sum_{nm,\alpha}\left[\mathbf{F}_{\alpha,mn}^{(1)}\left(k_1\mathbf{r}\right)\mathbf{C}_{\alpha,mn}^{(3)}\left(\mathbf{r}'\right)\right.$$

$$+\mathbf{F}^{(3)}_{\alpha,mn}(k_3\mathbf{r}_4)\,\mathbf{A}^{(34)}_{\alpha,mn}(\mathbf{r}')$$
$$+\mathbf{F}^{(3)}_{\alpha,mn}(k_3\mathbf{r}_5)\,\mathbf{A}^{(35)}_{\alpha,mn}(\mathbf{r}')$$
$$+\mathbf{F}^{(3)}_{\alpha,mn}(k_3\mathbf{r}_6)\,\mathbf{A}^{(36)}_{\alpha,mn}(\mathbf{r}')$$
$$+\mathbf{F}^{(3)}_{\alpha,mn}(k_3\mathbf{r}_7)\,\mathbf{A}^{(37)}_{\alpha,mn}(\mathbf{r}')$$
$$+\mathbf{F}^{(3)}_{\alpha,mn}(k_3\mathbf{r}_8)\,\mathbf{A}^{(38)}_{\alpha,mn}(\mathbf{r}')\Big], \tag{17}$$

$$\overline{\overline{\mathbf{G}}}^{(4)}_{\mathrm{e}} = \mathrm{j}\frac{k_4}{4\pi}\sum_{nm,\alpha}\Big[\mathbf{F}^{(1)}_{\alpha,mn}(k_4\mathbf{r}_4)\,\mathbf{C}^{(4)}_{\alpha,mn}(\mathbf{r}')\Big], \tag{18}$$

$$\overline{\overline{\mathbf{G}}}^{(5)}_{\mathrm{e}} = \mathrm{j}\frac{k_5}{4\pi}\sum_{nm,\alpha}\Big[\mathbf{F}^{(1)}_{\alpha,mn}(k_5\mathbf{r}_5)\,\mathbf{C}^{(5)}_{\alpha,mn}(\mathbf{r}')\Big], \tag{19}$$

$$\overline{\overline{\mathbf{G}}}^{(6)}_{\mathrm{e}} = \mathrm{j}\frac{k_6}{4\pi}\sum_{nm,\alpha}\Big[\mathbf{F}^{(1)}_{\alpha,mn}(k_6\mathbf{r}_6)\,\mathbf{C}^{(6)}_{\alpha,mn}(\mathbf{r}')\Big], \tag{20}$$

$$\overline{\overline{\mathbf{G}}}^{(7)}_{\mathrm{e}} = \mathrm{j}\frac{k_7}{4\pi}\sum_{nm,\alpha}\Big[\mathbf{F}^{(1)}_{\alpha,mn}(k_7\mathbf{r}_7)\,\mathbf{C}^{(7)}_{\alpha,mn}(\mathbf{r}')\Big], \tag{21}$$

$$\overline{\overline{\mathbf{G}}}^{(8)}_{\mathrm{e}} = \mathrm{j}\frac{k_8}{4\pi}\sum_{nm,\alpha}\Big[\mathbf{F}^{(1)}_{\alpha,mn}(k_8\mathbf{r}_8)\,\mathbf{C}^{(8)}_{\alpha,mn}(\mathbf{r}')\Big], \tag{22}$$

where $\mathbf{A}^{(.)}_{\alpha,mn}(\mathbf{r}\prime)$ and $\mathbf{C}^{(.)}_{\alpha,mn}(\boldsymbol{r}')$ are the unknown wave amplitudes. Following the technique described in [13, 16], we then solve the system of (14)-(22) and obtain the required wave amplitudes, which, in turn, allows us to calculate the electric field given by (5).

## IV. NUMERICAL VERIFICATION

The computation of the electric-field intensity (EFI) at the $y$O$z$ (namely, at the neck middle cross-section) plane is deemed an essential step for the validation of the new technique. Thus, for a regular male neck model, as the one in Fig. 1, the average dimensions and the dielectric media properties of its various parts, at the frequency of 2.4 GHz, are given in Table 1. Actually, this structure is fairly challenging owing to the different complex relative permittivities and hence the abruptly varying spherical media interfaces. Also, in (14)-(22), the number of terms, $n$, needed for the convergence of the infinite sums is up to the order of tens, depending on the type of the field. In particular, for the incident field, the value of $n$ can be several times larger ($n$ = 35-40) than the value for the scattered field ($n$ = 10-15), since the former is evaluated near the point source where field fluctuations are more abrupt. The main setup involves a Hertz dipole (in the sense of a wireless network antenna) with a parallel (along the $y$-axis) and a perpendicular (along the $x$-axis) polarization relative to the neck surface. For our comparisons, the exact same model has been numerically simulated by the CST Microwave Studio [17]. This package employs the finite integration technique and the finite-difference time-domain method in a domain discretized into adaptive hexahedral cells.

### A. Electric field calculation

Based on the above aspects, Figs. 2 and 3 illustrate the EFI magnitude at $r \sim 1.5a_1$ ($x$O$y$ plane) for a Hertz dipole (placed on the $x$-axis: $r_0 = 1.5a_1$, $\theta_0 = 90°$, $\varphi_0 = 0°$) at 2.4 GHz, in the absence and presence of the featured neck model, respectively. As promptly detected, the accuracy of our technique is promising, since in both scenarios the retrieved results are certainly in very good agreement with those of the computational package. This deduction is deemed even more important, considering the complicated geometry of the entire neck model, the multitude of materials, and the two different dipole polarizations. In fact, recalling the complex relative permittivities of Table 1, one can comprehend that the generalized dGf-based method is capable of successfully treating strongly dissimilar media (even when rather different $\widetilde{\varepsilon}_i$ imaginary parts are involved). Concerning the consistency of our scheme, the inlet figure of Fig. 3 shows

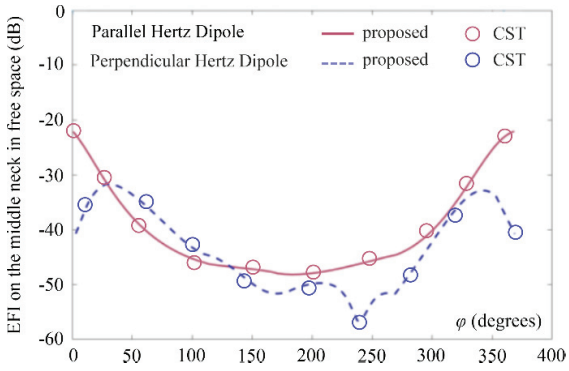


Fig. 2. Magnitude of the electric-field intensity, $|\mathbf{E}_{\mathrm{inc}}|$, at the $x$O$y$ plane without the neck vs angle $\varphi$ at $r \sim 1.5a_1$. The Hertz dipole is placed on the $x$-axis ($r_0 = 1.5a_1$, $\theta_0 = 90°$, and $\varphi_0 = 0°$) and the reference level is set at $r_{\mathrm{ref}} = 1.5a_1$, $\theta_{\mathrm{ref}} = \theta_0$, and $\varphi_{\mathrm{ref}} = \varphi_0$.

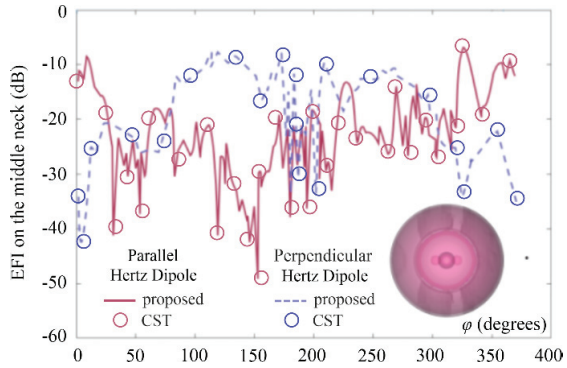


Fig. 3. Magnitude of the electric-field intensity, $|\mathbf{E}^{(0)}(\mathbf{r})|$, at the neck middle cross-section ($x$O$y$) plane vs angle $\varphi$ at $r \sim 1.5a_1$ for the Hertz dipole and the reference level of Fig. 2 [Inlet figure: Electric-field intensity map at the $x$O$_4y$ plane, generated by an $x$-oriented electric Hertz dipole (marked as a dot on the right-hand side), with each shade of grey spanning at a level of 3 dB].

Table 1: Average dimensions and material properties for the different parts of the proposed male neck model

| Neck Model Part | Outer Radius $a_i$ (mm) | Thickness/ Distance $w_i/d_i$ (mm) | Complex rel Permittivity $\widetilde{\varepsilon}_i$ |
|---|---|---|---|
| Skin | 70 | $\boldsymbol{w_1 = 1}$ | $\mathbf{40 + j12.5}$ |
| Fat | 69 | $w_2 = 3$ | $4.8 + j9.5$ |
| Muscle | 66 | – | $60.5 + j22.8$ |
| Right lobe | 7 | $d_4 = 59$ | $56.4 + j15.5$ |
| Left lobe | 7 | $d_5 = 59$ | $56.4 + j15.5$ |
| Trachea | 11 | $d_6 = 44.8$ | $36.3 + j11$ |
| Esophagus | 10 | $d_7 \cong 23.9$ | $68 + j19$ |
| Organs of the neck | 41.8 | $d_8 \cong 28.3$ | $42.4 + j14.1$ |

the EFI map at the $xO_4y$ plane for a $y$-oriented Hertz dipole. Observe the smoothness of the plot along with the absence of any nonphysical numerical artifacts due to scattered waves in the vicinity of the source and at the different media interfaces.

Moreover, Fig. 4 presents the EFI magnitude along the perimeter of the neck middle cross-section at $r \sim 1.5a_1$ ($yOz$ plane), owing to its critical significance at such studies. Note the promising agreement of the results with those of the computational package, despite the demanding configuration of the problem. On the other hand, these outcomes reveal a strong dependence of the EFI magnitude from the polarization of the Hertz dipole. Specifically, the EFI magnitude of the parallel dipole is larger than that of its perpendicular counterpart, for certain values of angle $\theta$. Finally, it should be mentioned that the proposed algorithm is very fast, owing to the straightforward implementation of the dGfs.

### B. Parameterization of the source location

Having validated the accuracy and efficiency of the featured technique, we, now, concentrate on the impact of the Hertz dipole source on the new neck model.

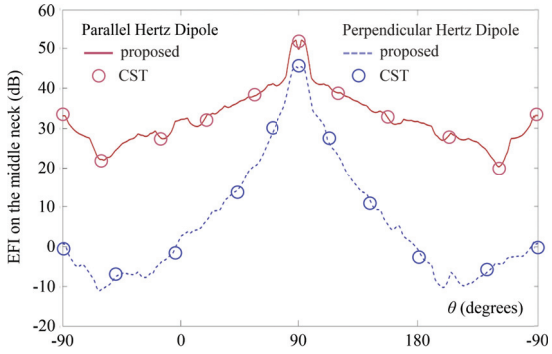


Fig. 4. Magnitude of the electric-field intensity, $\left|\mathbf{E}^{(0)}(\mathbf{r})\right|$, at the neck middle cross-section ($yOz$) plane vs angle $\theta$ at $r \sim 1.05a_1$ for the Hertz dipole and reference level at $r_{\text{ref}} = 1.05a_1$, $\theta_{\text{ref}} = \theta_0$, and $\varphi_{\text{ref}} = \varphi_0$.

To this objective, we compute the electric-field intensity around the neck middle cross-section ($yOz$ plane) for various locations and polarizations of the Hertz dipole.

In this framework, Fig. 5 depicts the EFI magnitude around the neck middle cross-section in the case of a Hertz dipole parallel to $y$-axis and $x$-axis, respectively. The source moves along the $x$-axis; in particular $x \in [0\text{ mm}, 70\text{ mm}]$, with its other coordinates fixed at $z = 0$ and $y = 1.1a_1$. It should be stressed that since in our numerical simulations, the Hertz dipole is not considered as a point source, its coordinates are measured from the edge that it is closest to the neck model. Consequently, the EFI magnitude around the neck middle cross-section increases as the point source approaches the model and decreases when it departs. Moreover, the shape of the curves in Fig. 5 (and magnified regions) is not seriously affected since the dipole moves along the $x$-axis.

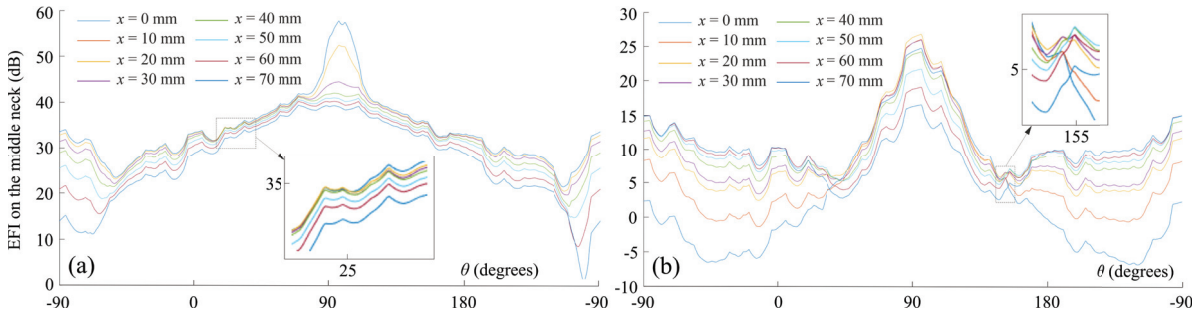


Fig. 5. Magnitude of the electric-field intensity, $\left|\mathbf{E}^{(0)}(\mathbf{r})\right|$, at the neck middle cross-section ($yOz$) plane vs angle $\theta$ for different polarizations of the Hertz dipole, when $z = 0$, $y = 1.1a_1$, and $x \in [0\text{ mm}, 70\text{ mm}]$. (a) Parallel to $y$-axis and (b) parallel to $x$-axis. Angle $\theta$ is measured clockwise from the $z$-axis on the $yOz$ plane, while the inlet figures are magnified plots of the results in the dotted areas.

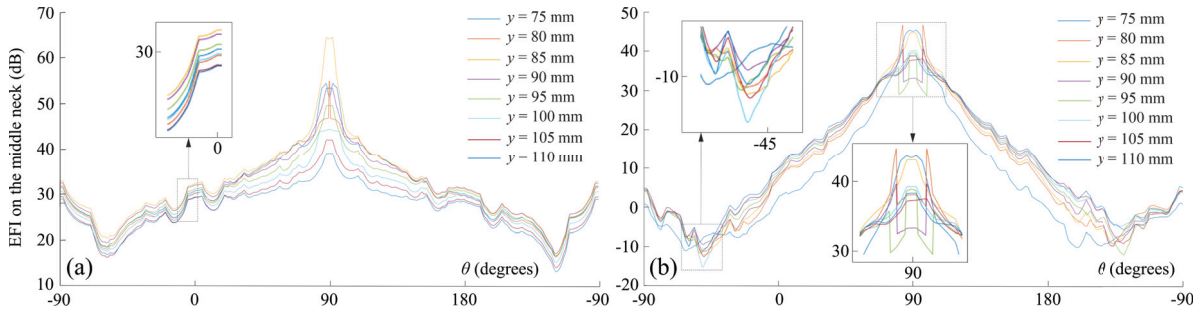


Fig. 6. Magnitude of the electric-field intensity, $\left|\mathbf{E}^{(0)}(\mathbf{r})\right|$, at the neck middle cross-section ($y$O$z$) plane vs angle $\theta$ for different polarizations of the Hertz dipole, when $z = 0$, $x = 0$, and $y \in [75\text{ mm}, 110\text{ mm}]$. (a) Parallel to $y$-axis and (b) parallel to $x$-axis. Angle $\theta$ is measured clockwise from the $z$-axis on the $y$O$z$ plane, while the inlet figures are magnified plots of the results in the dotted areas.

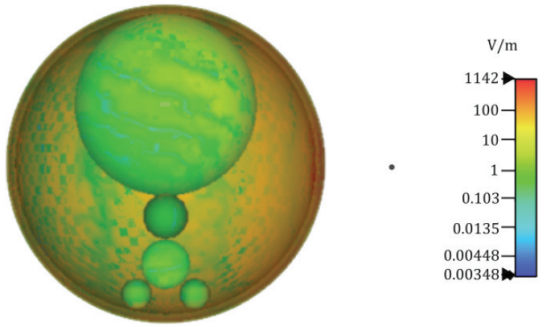


Fig. 7. Electric-field intensity map at a cross-section of the proposed neck model in Fig. 1. The source is represented as a dot on the right-hand side.

Conversely, Fig. 6 examines the scenario of a Hertz dipole (for both polarizations) which moves along the $y$-axis; explicitly $y \in [75\text{ mm}, 110\text{ mm}]$ and $x = z = 0$ for its other coordinates. It is deduced that, now, the EFI magnitude increases and decreases drastically in terms of the distance between the neck model and the dipole. Indeed, the shape of the plots in Fig. 6 is affected, as the dipole moves along the $y$-axis and the vertical distance from the middle neck augments rapidly.

### C. Radiation penetration

The EFI map of Fig. 7 clearly indicates that the majority of the radiation, which penetrates the skin, is absorbed by the multilayered host sphere (i.e., skin, fat, and muscle tissues), leaving a relatively small percentage to penetrate the inner organs. When these organs are surrounded by a very thin (practically negligible) muscle layer, similarly to the thyroid, the radiation absorbed by the tissues increases. So, the maximum limit of the radiation levels on the surface of the thyroid is almost equivalent to the radiation measured at the locations where the thyroid is in contact with the middle neck.

## V. CONCLUSION

A precise, fast, and computationally economical algorithm has been introduced in this paper, for the electromagnetic analysis of a generalized non-spherical human neck model. The latter structure provides a robust representation of the neck tissues as spherical layers and employs a set of properly-formulated dyadic Green's functions with bilocal spatial dependence to compute the desired electric field intensity. Numerical results, concerning the bioelectromagnetic impact evaluation from several wireless network antenna configurations, were in very satisfactory agreement with the reference data obtained from a popular computational package. Lastly, it must be stated that the featured technique can be easily extended at the entire radiofrequency spectrum, taking into account that the electric properties of every tissue can vary with respect to frequency, namely considering the dispersive nature of the involved media.

## REFERENCES

[1] Z. Jiang, W. Liu, R. Ma, S. H. Shirazi, and Y. Xie, "Lightweight healthcare wireless body area network scheme with amplified security," *IEEE Access*, vol. 9, pp. 125739-125752, 2021.

[2] L. Liu, J. Shi, F. Han, X. Tang, and J. Wang, "In-body to on-body channel characterization and modeling based on heterogeneous human models at HBC-UWB band," *IEEE Sensors J.*, vol. 22, no. 20, pp. 19772-19785, 2022.

[3] Y. Liao, M. S. Leeson, and M. D. Higgins, "A communication link based on biological implant wireless body area networks," *Applied Computational Electromagnetics (ACES) Journal*, vol. 31, no. 6, pp. 619-628, 2016.

[4] K. Sun, L. Peng, Q. Li, X. Li, and X. Jiang, "Compact zeroth-order resonance loaded microstrip antenna with enhanced bandwidth for WBAN/brain activity detection," *Applied*

*Computational Electromagnetics (ACES) Journal*, vol. 33, no. 6, pp. 631-640, 2018.

[5] L. Berkelmann, H. Jäschke, L. Mörlein, L. Grundmann, and D. Manteuffel, "Antenna optimization for WBAN based on spherical wave functions deembedding," *IEEE Trans. Antennas Propag.*, vol. 70, no. 11, pp. 11033-11044, 2022.

[6] A. Darvazehban and T. Rezaee, "Ultra-wideband microstrip antenna for body centric communications," *Applied Computational Electromagnetics (ACES) Journal*, vol. 33, no. 3, pp. 355-358, 2018.

[7] A. Moin, A. Thielens, A, Araujo, A. Sangiovanni-Vincentelli, and J. M. Rabaey, "Adaptive body area networks using kinematics and biosignals," *IEEE J. Biomed. Health Informat.*, vol. 25, no. 3, pp. 623-633, 2020.

[8] T. Alkayyali, O. Ochuba, K. Srivastava, J. K. Sandhu, C. Joseph, S. W. Ruo, A. Jain, A. Waqar, and S. Poudel, "An exploration of the effects of radiofrequency radiation emitted by mobile phones and extremely low frequency radiation on thyroid hormones and thyroid gland histopathology," *Cureus*, vol. 13, no. 8, pp. 17329(1-10), 2021.

[9] S. Li, M. Yang, H. Guo, M. Liu, S. Xu, and H. Peng, "Microwave ablation vs traditional thyroidectomy for benign thyroid nodules: A prospective, non-randomized cohort study," *Acad. Radiol.*, vol. 29, no. 6, pp. 801-879, 2022.

[10] J. Rizkalla, W. Tilbury, A. Helmy, V. K. Suryadevara, M. Rizkalla, and M. M. Holdmann, "Computer simulation/practical models for human thyroid thermographic imaging," *J. Biomed. Sci. Eng.*, vol. 8, no. 4, pp. 246-256, 2015.

[11] J. Wang and G. Xiao, "Electromagnetic-thermal analysis of the effect of microwave ablation of thyroid nodules," in *Proc. Photon. & Electromagn. Research Symp. (PIERS)*, pp. 2424-2432, 2021.

[12] G. Gu, J. Shi, J. Zhang, and M. Zhao, "Dyadic Green's function and the application of two-layer model," *Mathematics*, vol. 8, no. 10, pp. 1688(1-20), 2020.

[13] C.-T. Tai, *Dyadic Green Functions in Electromagnetic Theory*, Piscataway, NY: IEEE Press, 1994.

[14] P. De Tillieux and Y. Goussard, "Biomedical magnetic induction tomography: An inhomogeneous Green's function approach," in *Proc. ACES Conf.*, pp. 1-2, 2018.

[15] D. P. Chrissoulidis and J. M. Laheurte, "Radiation from an encapsulated hertz dipole implanted in a human torso model," *IEEE Trans. Antennas Propag.*, vol. 64, no. 12, pp. 4984-4992, 2016.

[16] D. P. Chrissoulidis and J. M. Laheurte, "Dyadic Green's function of a nonspherical model of the human torso," *IEEE Trans. Microw. Theory Tech.*, vol. 62, no. 6, pp. 1265-1274, 2014.

[17] *CST Studio Suite: Electromagnetic Field Simulation Software*, Dassault Systemes, 2021.

**Anna A. Varvari** received the Diploma in electrical and computer engineering from the Aristotle University of Thessaloniki in 2023, where she is pursuing her Ph.D. degree. Her research is on numerical electromagnetics, Green's functions methodologies, wireless body area networks, bioelectromagnetics, and scattering.

**Dimitrios I. Karatzidis** received the Diploma and Ph.D. degrees in electrical & computer engineering from the Aristotle University of Thessaloniki, Thessaloniki, Greece, in 1999 and 2009, respectively. In 2017, he joined the Department of Electrical & Computer Engineering, Aristotle University of Thessaloniki as a member of the Instructional Laboratory Personnel. His research interests include numerical electromagnetics, metamaterials, and antenna/waveguide optimization.

**Tadao Ohtani** received B.S. and M.S. degrees in electrical and electronic engineering from the Toyohashi University of Technology, Japan, in 1983 and 1985, respectively, and the Ph.D. degree in electrical and electronic engineering from Kitami Institute of Technology, Japan, in 2005. From 1985 to 2011, he worked as a researcher at Nagoya Aerospace Systems of Mitsubishi Heavy Industries, Ltd. Currently, he is an independent researcher. His research interests include numerical analysis of electromagnetic fields for aircraft design via the FDTD and the NS-FDTD method.

**Yasushi Kanai** (Fellow, ACES) received Bachelor Degree, Master of Engineering Degree, and Ph.D. in information engineering from Niigata University, Japan, in 1982, 1984, and 1989, respectively.

From 1984 to 1992, he worked as an engineer at Alps Electric Co., Ltd. In 1992-1995, he was an associate professor at Dept. of Information Engineering, Niigata University. In 1995, he joined the Engineering Dept., Niigata Institute of Technology, Kashiwazaki, Japan, where he is a professor. In 2002-2003, he has been at the Florida International University, USA, as a visiting scholar. He has authored/coauthored more than 180 journal papers, more than 260 international conference records, more than 250 national conference records, and several book chapters. He specializes in micromagnetic analysis and in wave propagation via the NS-FDTD analysis.

**Nikolaos V. Kantartzis** received the Diploma and Ph.D. degrees in electrical & computer engineering from the Aristotle University of Thessaloniki, Thessaloniki, Greece, in 1994 and 1999, respectively. In 1999, he joined the Department of Electrical & Computer Engineering, Aristotle University of Thessaloniki, where he is a professor. He has authored/coauthored 4 books, more than 190 peer-reviewed journal papers, and more than 300 publications in conference proceedings. His research interests include computational electromagnetics, EMC, scattering, metamaterials, antennas, and waveguides.

# Reconfigurable Multifunctional Transmission Metasurface Polarizer Integrated with PIN Diodes Operating at Identical Frequencies

**Jianyu Lin, Dongying Li, and Wenxian Yu**

Shanghai Key Laboratory for Intelligent Sensing and Recognition
Shanghai Jiao Tong University, Shanghai, 200240, China
jianyu.l.wl@sjtu.edu.cn, dongying.li@sjtu.edu.cn, wxyu@sjtu.edu.cn

***Abstract* –** Herein, a reconfigurable multifunctional transmission metasurface polarizer, structured with double Jerusalem crosses and integrated with four PIN diodes, is presented. The bottom Jerusalem cross is rotated by 35° with respect to the top cross. Both numerical and experimental observations reveal that a linearly polarized (LP) outgoing wave is transmitted at approximately 4.0 GHz when subjected to a left-handed circularly polarized (LCP) or right-handed circularly polarized (RCP) incident wave. The transmission efficiency reaches -2.5 dB when all elements are in the ON state. Furthermore, active control of switchable PIN diodes operating in various statuses unequivocally demonstrates the ability to convert an incident wave polarized in the *x* or *y* direction to a LCP or RCP wave, respectively, within the identical frequency band, spanning from 3.6 GHz to 4.3 GHz. This conversion is achieved with a transmission coefficient of -3.5 dB or -4.2 dB at the peak frequency. The proposed metasurface polarizer presents a potentially dynamic method for simultaneously manipulating various polarization conversions of electromagnetic (EM) waves within a desired frequency band.

***Index Terms* –** Multifunctional metasurface, polarization conversion, reconfigurable metasurface polarizer.

## I. INTRODUCTION

Polarization, a significant characteristic of electromagnetic (EM) waves, plays a crucial role in polarization imaging, modern communication systems, and radar technology. Conventionally, manipulating the polarization state relies on uniaxial crystals, suffering from their bulky configuration, complex feed systems, and limited polarization states. In recent years, metasurfaces, artificial composites consisting of subwavelength scatterers, have emerged as promising approaches to exhibit strong EM responses, such as zero refractive index [1], asymmetric transmission [2], and perfect absorption [3], offering novel EM characteristics beyond natural materials. Early research focused on passive metasurface polarizers, utilizing gradual geometry changes or layer rotation [4–7]. However, these fixed functions and polarization conversion states do not align with the requirements of contemporary compact communication systems.

By controlling external excitation, a tunable or reconfigurable metasurface equipped with active elements expands the range of possibilities for dynamically manipulating the polarization responses of EM waves [8–10]. For instance, based on the equivalent dipole polarization theory, Kazemi [11] achieved perfect reflection or refraction in a desired direction with orthogonal polarization. In [12], a circular polarization converter demonstrated the production of a circularly polarized (CP) wave with handedness orthogonal to the incident wave. Notably, the PIN diode, known for its compact size and controllable properties in the microwave range, has been shown to integrate into metasurface structures. In [13], a circular polarizer produced an outgoing wave that exhibited circular polarization with orthogonal handedness at dual frequencies. The conversion from linear-to-circular (LTC) polarization was also successfully achieved in reference [14]. However, a limitation in previous studies was the different operating frequencies for LCP or RCP wave, which restricted their practical utility. In [15], an incident wave with *x* polarization direction was transformed into LCP or RCP wave within a frequency range from 9.70 to 9.93 GHz. We propose a LTC polarizer operating within the same frequency band using a double-layer metasurface [16], providing a limited yet practical set of polarization conversion functions at the desired frequency range.

In this paper, a reconfigurable multifunctional transmission metasurface polarizer (MP) depicted in Fig. 1 is proposed, achieving circular-to-linear (CTL) and LTC polarization conversion by controlling the PIN diode states at an identical frequency band, which has not been previously reported. Utilizing the transmission matrix approach, metasurface unit cell comprised two-layered Jerusalem crosses incorporated with four active components of PIN diodes and three-layered feeding network, leading to LTC and CTL polarization conversion. Subse-

*Submitted On: June 1, 2023*
*Accepted On: March 16, 2024*

https://doi.org/10.13052/2024.ACES.J.390307

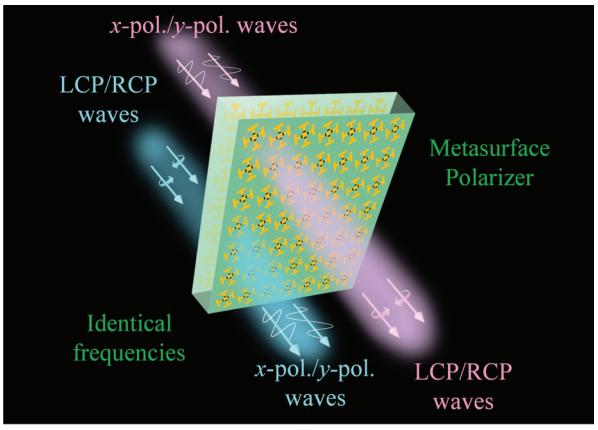


Fig. 1. Schematic of the proposed reconfigurable multifunctional transmission metasurface polarizer.

quently, an 8×8-element reconfigurable multifunctional transmission metasurface polarizer with 256 PIN diodes and 24 inductances was fabricated. The measured performances demonstrate that the emission of an LP wave occurs at approximately 4.0 GHz, with a transmission efficiency of -2.5 dB when all lumped elements are in the ON state, and the structure is illuminated by either a LCP or RCP wave. Furthermore, the ability to convert *x*-polarized and *y*-polarized incident waves to LCP and RCP waves respectively, while maintaining their orthogonal handedness within the desired frequency band of 3.6 GHz to 4.3 GHz, is unambiguously demonstrated with a transmission coefficient of -3.5 dB and -4.2 dB through the active control of the switchable PIN diodes.

## II. RECONFIGURABLE UNIT CELL DESIGN

### A. Unit cell design

Building upon the structural design introduced in our previous study [16], we present an active and reconfigurable multifunctional transmission metasurface polarizer unit cell. By positioning two Jerusalem crosses and feeding network, we facilitate polarization conversion within the resonance frequency band through the distribution of the surface electric field and cross-coupled magnetic field. The layout of our proposed design is patterned on Rogers RO4350B substrates as shown in Fig. 2 (a). The bottom patch exhibits a twist of 35° relative to the top patch, with other geometric dimensions set as follows: $p = 20$ mm, $g = 1$ mm, $f = 6.8$ mm, $h = 6$ mm, $d = 3.66$ mm, and $b = 4.5$ mm. All Jerusalem crosses are constructed using copper sheets. Additionally, we incorporated various metallic biasing lines (0.4 mm) into the substrate, connecting them to the bottom patch through vertical metallic vias, as illustrated in Figs. 2 (d)-(f).

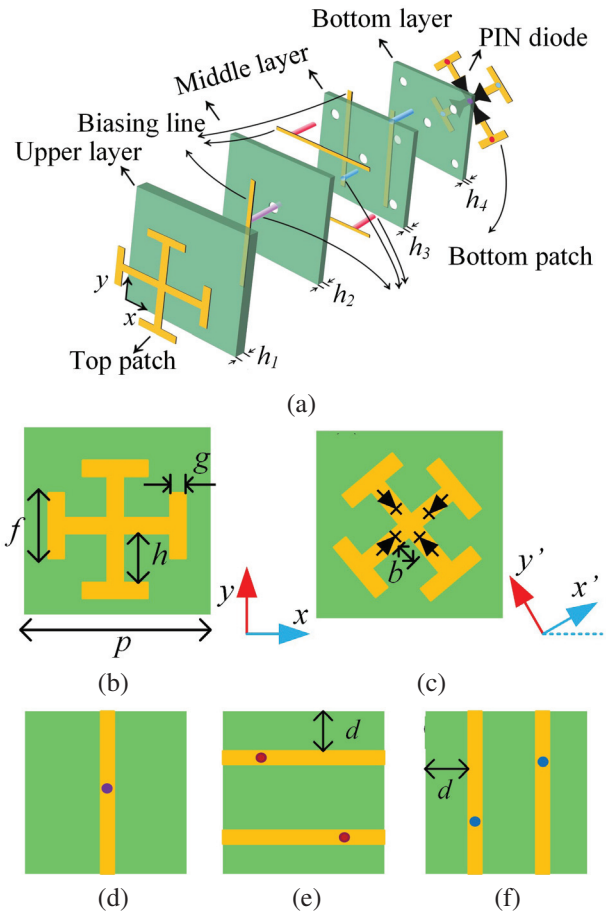


Fig. 2. (a) Layout of the MP unit cell with metallic vias and biasing lines. $h_1 = 0.5$ mm, $h_2 = h_3 = h_4 = 0.3$ mm, (b) top patch on upper layer, (c) bottom patch on bottom layer, and (d)-(f) metallic vias and biasing lines on middle layer.

In our design, the PIN diodes were chosen as MA4AGBLP912 fabricated by MACOM [17] which have ultralow capacitance and series inductance, as well as slight forward resistance and a suitable geometry, thus reducing the mutual coupling and parasitic effect on the structure. The PIN diode can be equivalent to series-parallel RLC circuit with a series inductance of $Ls = 0.5$ nH, reverse resistance of $Rs = 10$ MΩ and a 0.02 pF capacitance in the OFF state. By contrast, a series resistance of $Rs = 4$ Ω is depicted in the equivalent series RL circuit in the ON state. Four lumped elements with equivalent circuit parameters were used to model the PIN diodes by loading them onto a Jerusalem cross over the bottom layer. The four PIN diodes are described as PIN *I*, PIN *II*, PIN *III*, and PIN *IV* arranged counterclockwise. Table 1 shows variable status of those PIN diodes controlled individually.

Table 1: Three status controlled individually

| Status I | All ON |
|---|---|
| Status II | PIN *I* and PIN *III* OFF<br>PIN *II* and PIN *IV* ON |
| Status III | PIN *I* and PIN *III* ON<br>PIN *II* and PIN *IV* OFF |

### B. Design principle

To elucidate the EM characteristics of the designed metasurface unit cell, we consider an incident wave that illuminates the upper layer of the unit cell, as depicted in Fig. 3 (a). The top Jerusalem cross patch can be attributed to $C_{4,z}$ symmetry with respect to the $z$ axis, pertaining to the act of rotating an entity by a constant angular measure of 90° around the $z$ axis during each rotation. This action has the ability to align the entity precisely with itself, leading to its unaltered state. All effects associated with circular dichroism can be observed in such systems, as explained by [18]. Consequently, the Jerusalem cross leads to the dual-frequency transmission of LCP and RCP waves in response to an incident wave with circular polarization. Moreover, we observe a pure linearly polarized (LP) wave at frequency $f_0$ between the dual frequencies, characterized by an ellipticity of zero, demonstrating significant optical activity. As a result, the polarization of $\vec{E}^{t1}$ is linear, not only at the frequency of $f_0$ for circularly polarized incident waves but also within the arbitrary operational frequency range for LP incidences. We define the transmission parameter $T_1$ for the top layer as follows:

$$T_1 = \begin{bmatrix} A_1 & B_1 \\ -B_1 & A_1 \end{bmatrix}. \tag{1}$$

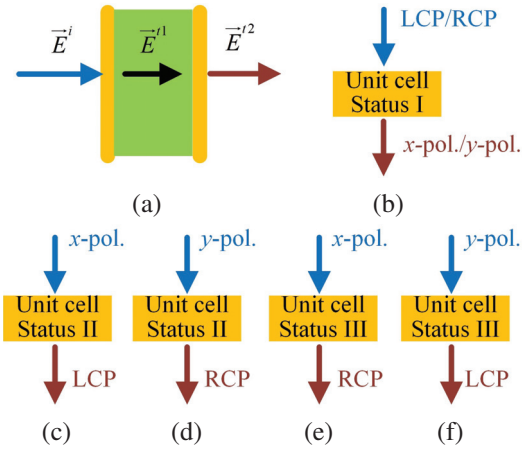


Fig. 3. (a) EM propagation model and (b)-(f) conceptual illustration of incident wave propagation under different status.

In contrast to upper layer, the Jerusalem crosses located on the bottom layer undergoes a counterclockwise rotation about the $z$-axis with a value of $\varphi = 35°$ and is equipped with four PIN diodes. We then introduce a novel set of coordinates $(x', y')$ by rotating the existing $(x, y)$ system by an angle $\varphi$ in $x$Oy plane. The transmission parameter $T_2$ of the bottom layer can be described as follows:

$$\begin{aligned} T_2 &= \begin{bmatrix} t_{x'x'} & t_{x'y'} \\ t_{y'x'} & t_{y'y'} \end{bmatrix} \\ &= \begin{bmatrix} \cos\varphi & -\sin\varphi \\ \sin\varphi & \cos\varphi \end{bmatrix}^{-1} \times T_P \times \begin{bmatrix} \cos\varphi & -\sin\varphi \\ \sin\varphi & \cos\varphi \end{bmatrix}, \end{aligned} \tag{2}$$

where $T_P$ depicts the transmission matrix of identical structure of top layer loaded with four PIN diodes,

$$T_P = \begin{bmatrix} A_P & B_P \\ C_P & D_P \end{bmatrix}, \tag{3}$$

and

$$t_{x'x'} = m^2 A_P + mnB_P + mnC_P + n^2 D_P, \tag{4}$$

$$t_{x'y'} = -mnA_P + m^2 B_P - n^2 C_P + mnD_P, \tag{5}$$

$$t_{y'x'} = -mnA_P - n^2 B_P + m^2 C_P + mnD_P, \tag{6}$$

$$t_{y'y'} = n^2 A_P - mnB_P - mnC_P + m^2 D_P, \tag{7}$$

where $m = cos\varphi$ and $n = sin\varphi$.

Therefore, the total transmission matrix of the proposed unit cell can be described as:

$$T_{total} = T_1 \times T_2 = \begin{bmatrix} A_1 & B_1 \\ -B_1 & A_1 \end{bmatrix} \times \begin{bmatrix} t_{x'x'} & t_{x'y'} \\ t_{y'x'} & t_{y'y'} \end{bmatrix}. \tag{8}$$

When all elements are in the ON state, the structure in second layer also exhibits $C_{4,z}$ symmetry, and $T_P$ and $T_2$ can be expressed as:

$$T_P = \begin{bmatrix} A_P & B_P \\ -B_P & A_P \end{bmatrix}, \tag{9}$$

$$\begin{aligned} T_2 &= \begin{bmatrix} (m^2+n^2)A_P & (m^2+n^2)B_P \\ -(m^2+n^2)B_P & (m^2+n^2)A_P \end{bmatrix} \\ &= \begin{bmatrix} A_P & B_P \\ -B_P & A_P \end{bmatrix}, \end{aligned} \tag{10}$$

suggesting a pure LP wave and giant optical activity at $f_0$ for CP incident wave. Furthermore, under Status II or Status III, the capability to transform linear polarization into circular polarization within a specific frequency range is exhibited in Figs. 3 (c)-(f). The intensity of the transmitted waves can then be associated with the intensity of the incident waves via the transmission matrix $T_{cl}$ [13].

$$T_{cl} = \begin{bmatrix} T_{+x} & T_{+y} \\ T_{-x} & T_{-y} \end{bmatrix} = \frac{1}{\sqrt{2}} \begin{bmatrix} t_{xx} + it_{yx} & t_{xy} + it_{yy} \\ t_{xx} - it_{yx} & t_{xy} - it_{yy} \end{bmatrix}, \tag{11}$$

where the RCP component is indicated by $+$, and the LCP component is denoted by $-$. In addition, the transformation coefficients $T_{+x}$, $T_{-x}$, $T_{+y}$, and $T_{-y}$ represent the conversion abilities of the $x$- and $y$-components of an LP incident wave impinging on a structure. It is imperative to employ polarization azimuth rotation angle denoted by $\theta$, ellipticity represented by $\eta$ and polarization extinction ratio denoted by PER to delineate the salient features of the emitted wave comprehensively. The parameters are defined as follows:

$$\theta = \left[\arg\left(E_{+*}\right) - \arg\left(E_{-*}\right)\right]/2, \tag{12}$$

$$\eta = \arctan\frac{|E_{+*}| - |E_{-*}|}{|E_{+*}| + |E_{-*}|}, \tag{13}$$

$$\text{PER} = 20\log_{10}\left(|T_{+*}|/|T_{-*}|\right), \tag{14}$$

where the symbol $*$ indicates the $x$- or $y$-polarized component. When $\eta = 0$, the emitted wave is considered an LP wave with rotation angle $\theta$. The PER metric quantifies the disparity between the amplitude of the RCP and LCP outgoing waves.

If incident wave is CP, then Transmission Jones matrix $T_{cc}$ can be adopted to better intuitionally exhibit the transformation efficiencies by considering the circular polarization conversion [18]:

$$T_{cc} = \begin{bmatrix} T_{++} & T_{+-} \\ T_{-+} & T_{--} \end{bmatrix}. \tag{15}$$

### C. Simulated results

Based on the previously stated operational principle, a finite element method with frequency-domain solver was utilized in the commercial EM software CST. Figure 4 shows the transmission characteristics of the four lumped elements in the ON state. Under this condition, the overall structure is equivalent to a $C_{4,z}$ asymmetric structure. Therefore, a polarization rotation angle of $\theta = -1.68°$ with $\eta = 0°$ characteristic is presented within the frequency range of 3.0-4.0 GHz, indicating a pure LP emitted wave with a total transmission coefficient of -2.0 dB from a CP incident wave.

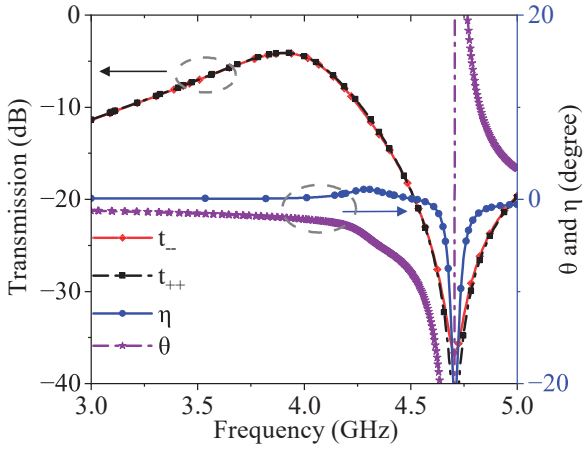


Fig. 4. Transmission coefficients, polarization azimuth rotation angle and ellipticity of MP unit cell for CP incident wave under Status I.

When incidence with $x$ polarization is applied to the structure in Status II, the numerical results illustrated in Fig. 5 (a) indicate that the transmission efficiency of the LCP wave is larger than that of the RCP wave at 3.0-4.5 GHz, whereas the peak intensity of the LCP wave is -2.9 dB at 3.68 GHz, suggesting a prominent LCP emitted wave with $\eta = -5.4°$ and $\theta = -13.4°$. By contrast, the RCP wave is a prominent wave with a transmission efficiency of -3 dB and $\eta = 5.6°, \theta = 12.0°$ at the resonant frequency if the lumped elements are under Status III, as illustrated in Fig. 5 (c). Furthermore, once a $y$-polarized wave occurs and PIN diodes are arranged with Status II, the RCP wave is the prominent outgoing wave at a frequency of 3.0-4.5 GHz (Fig. 5 (b)), and the transmission efficiency reaches a maximum of -4 dB with polarization azimuth rotation angles of ellipticity $\eta = 8.0°$ and $\theta = -16.2°$ at 4.2 GHz, respectively. Similarly, Fig. 5 (d) shows the LCP polarization conversion from $y$ polarization under the opposing states of the PIN diodes. In conclusion, the most intriguing performance of the MP unit cell should be to actively transmit LP emitted waves from the CP incident wave under Status I and also convert LCP or RCP emitted wave from $x$- or $y$-polarized linear wave using switchable PIN diodes under Status II and III.

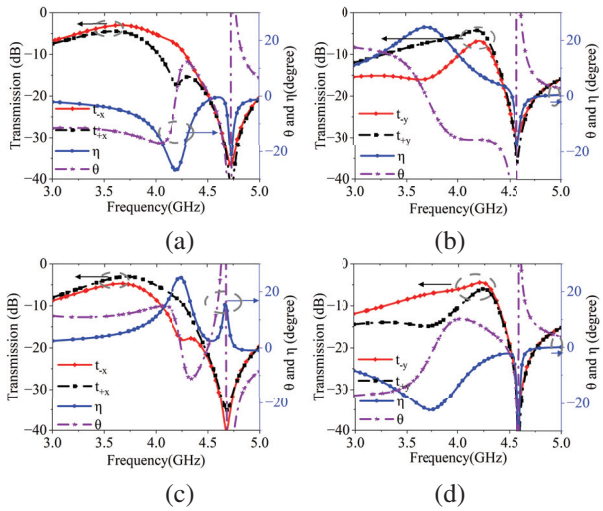


Fig. 5. Simulated switchable properties of MP unit cell. Transmission coefficients, polarization azimuth rotation angle and ellipticity with the PIN diodes under (a) Status II for $x$-polarized wave, (b) Status II for $y$-polarized wave, (c) Status III for $x$-polarized wave, (d) Status III for $y$-polarized wave.

To clearly explain the physical mechanism of MP unit cell, current distributions at an operation frequency 3.68 GHz for $x$ polarization and 4.2 GHz for $y$ polarization with different PIN diodes states were obtained. As shown in Fig. 6 (a), once the PIN diodes are controlled in Status II and $x$-polarized wave is incident, the strong surface current (dashed curve) on bottom patch flows along the metallic arm with the PIN diodes in the ON state while the surface current (solid curve) on top patch is concentrated along $-x$ direction at 3.68 GHz, which can be considered as the primary LCP transmitting wave along propagating direction. Similarly, the LCP wave is a prominent transformed wave at 4.2 GHz if the PIN diodes operate in Status III, and a $y$-polarized wave illuminates the structure in Fig. 6 (e). Moreover, as the current distribution is in the opposite direction in Figs. 6 (c) and (d), the overall result is that the RCP wave is the prominent emitted wave at the operating frequency. Note that the equivalent rotation angles are 125° in Fig. 6 (a) and 145° in Fig. 6 (d), providing different $x$ and $y$ components respectively, and generating different transmittance for the same incident wave with $x$ polarization under Status II and Status III. Obviously, the small difference between $x$- and $y$-polarized incidence arises from the effects generated by the asymmetric feeding network. For example, when the incident wave is $x$-polarized, the surface currents ($\mathbf{J}_2$, $\mathbf{J}_3$, $\mathbf{J}_4$) are mainly located on the biasing lines and can be combined into a black arrow, as shown in Fig. 6 (b). In this case, the synthetic current $\mathbf{J}_0$ can be considered equivalent to an reversed current and counteract the surface currents $\mathbf{J}_4$ flowing along the arm where PIN I and PIN III are OFF. Thus the feeding network has minimal impact on the polarization conversion. For $y$-polarized incidence, the equivalent current ($\mathbf{J}_2$,$\mathbf{J}_3$) in biasing lines flows along $+y$ direction at 4.2 GHz in Fig. 6 (f), which is contrary to the surface current on top patch, leading to a weakness in the transmittance of $y$-polarized incident wave under Status III. The manipulation of incident waves with different polarizations within an identical frequency range was realized by dynamically controlling the states of four PIN diodes, distinguishing the proposed design from other polarizers.

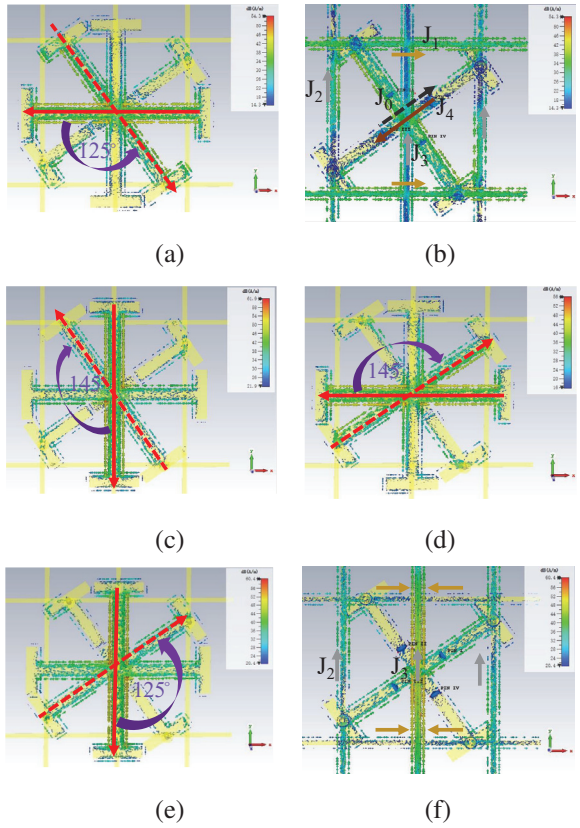


Fig. 6. Surface current distributions of (a) top and bottom patch, (b) and biasing lines, metallic vias under Status II for $x$-polarized wave at 3.68 GHz, (c) top and bottom patch under Status II for $y$-polarized wave at 4.2 GHz, (d) top and bottom patch under Status III for $x$-polarized wave at 3.68 GHz, (e) top and bottom patch, (f) and biasing lines, metallic vias under Status III for $y$-polarized wave at 4.2 GHz.

## III. METASURFACE DESIGN AND PERFORMANCE

In the experiment, the proposed MP prototype comprising 8×8 unit cells was simulated, fabricated, and measured, as shown in Figs. 7 (b) and (c). Simultaneously, 256 PIN diodes connected to a DC bias layer network were demonstrated. Connectivity between the PIN diodes and bias lines was achieved by a large inductance of 16 nH, eliminating RF/DC decoupling and providing the desired isolation in the operation frequency band. The stabilized power supply of Keithley 2231A equipped with three channels in series with 10 Ω resistances provides 1.35 V voltage for each element in the ON state with a forward current of 10 mA. Applying the far-field system, the vector network analyzer of AGILENT N5247A was employed and two identical horn antennas with $x$ and $y$ polarization states were utilized as the transmitter and receiver, as shown in Fig. 7 (a). During measurement, the MP was positioned at the center of the transmitting and receiving antennas with the surrounding microwave absorbing materials to reduce the reflected and diffraction waves. The measurement process comprises distinct components that entail using the same polarization and orthogonal polarization techniques in conjunction with transmitting and receiving antennas operating in three distinct PIN diode statuses, ultimately yielding co-polarized and cross-polarized coefficients. Thereafter, the transmission coefficients of LCP and

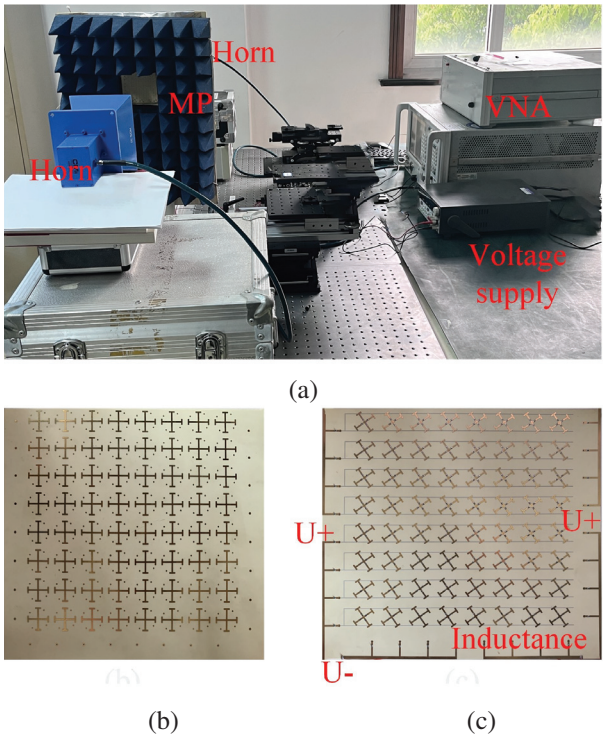


Fig. 7. (a) Measurement system, (b) top view, and (c) and bottom view of the fabricated reconfigurable multifunctional transmission metasurface polarizer.

RCP emitted waves were computed using the transmission matrix.

The measured and simulated scattering parameters of CP incident wave are presented in Fig. 8. By controlling the PIN diodes under Status I, the magnitudes of the LCP and RCP waves are almost identical, demonstrating an LP emitted wave in the vicinity of 4.0 GHz with a total transmission coefficient vale of -2.5 dB and almost zero ellipticity in Fig. 10 (b). Furthermore, the LCP wave is the primary outgoing wave numerically and experimentally within the frequency of 3.6-4.1 GHz for the *x*-polarized incident wave when lumped elements are in Status II. The measured transmission coefficient is above -5 dB within frequency coverage, reaches a maximum of -3.5 dB at 3.74 GHz, and overlaps with the simulated result, as described in Fig. 9 (a). Similarly, the transmittance of RCP wave is observed to be -3.7 dB at 4.0 GHz in Fig. 9 (c) and larger than the LCP wave from 3.6 GHz to 4.1 GHz for *x*-polarized incident wave when PIN diodes are switched to opposite states. For *y*-polarized incidence, the measured transmission coefficients of RCP and LCP components in Status II reach -4.0 dB and -7.0 dB at 4.1 GHz, respectively, as depicted in Fig. 9 (b). Therefore, RCP is the major component within the operational frequency band ranging from 3.95 GHz to 4.3 GHz. Furthermore, the measured transmission coefficient of LCP is -4.2 dB at a peak frequency of 4.0 GHz once the sample is operating in Status III, suggesting that the LCP wave is the outgoing wave. Further, when the frequency increases from 3.86 to 4.24 GHz, the transmission coefficient of the LCP component is above -5 dB, larger than that of the RCP component in Fig. 9 (d). Consequently, the measured results of the fabricated MP operating in various biasing states agreed well with the simulated results. Figure 10 presents the measured ellipticity of the MP. The discrepancy between Status II and Status III for an equivalent normal incidence arises from an incompletely symmetrical structure and feeding network, as well as the loss of PIN diodes. Furthermore, it has been observed that the measured outcome at low frequencies yields unsatisfactory results for both LCP and RCP transmitted waves. This is due to errors resulting from fabrication errors on the surface, as well as a relatively wide beam width in the *y* component at low frequencies generated by horn antennas.

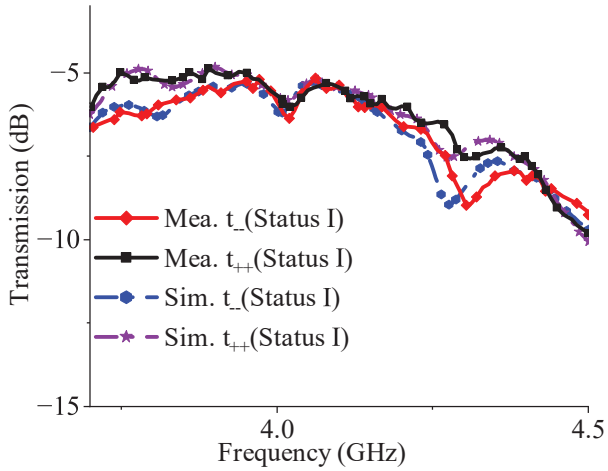


Fig. 8. Measured (solid) and simulated (dashed) properties of the proposed MP under Status I for CP wave.

Table 2 presents a comparison with previously reported CTL and LTC polarization converters. Here, the LTC polarization converters are not reconfigurable and are under *x*- or *y*- polarized incident wave in [19–21]. Both LP and CP waves can be converted into cross-polarization waves; however, they are reflective metasurface polarizers [22]. Most reported metasurface polarizers can only achieve a few types of polarization conversion and operate under dual separate frequency bands. It can be concluded that the proposed design is compact in terms of volume and profile. Meanwhile, the proposed multifunctional transmission metasurface structure can achieve various polarization reconfigurability for both LP and CP incident waves, and it features the identi-

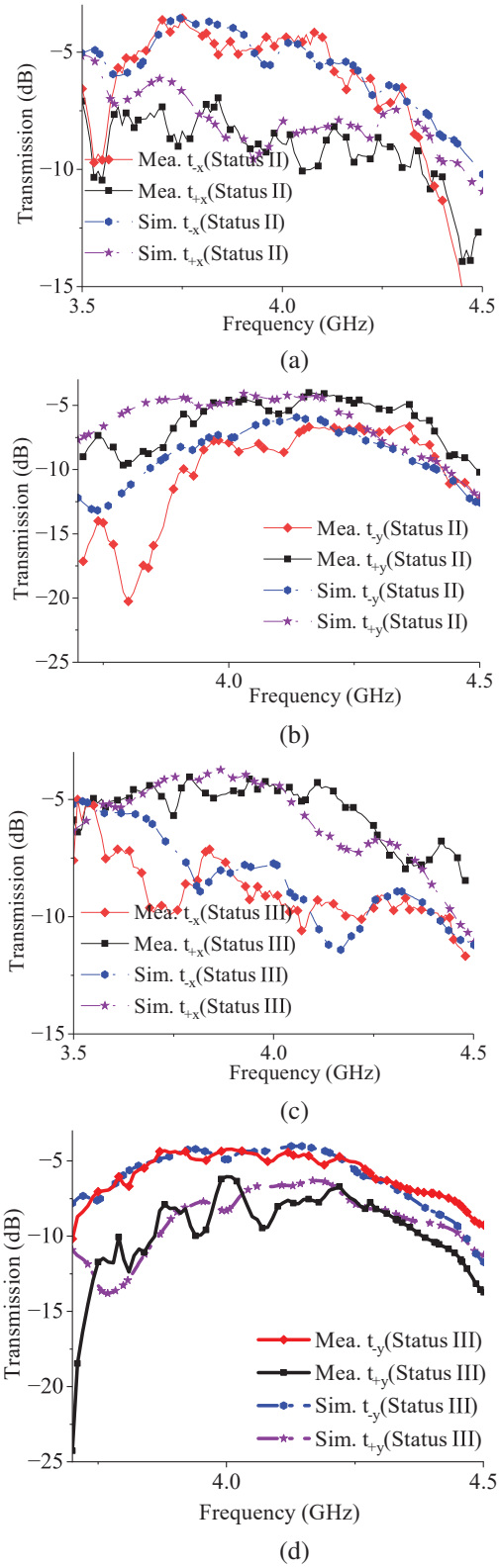


Fig. 9. Measured (solid) and simulated (dashed) properties of the proposed MP under (a) Status II for *x*-polarized wave, (b) Status II for *y*-polarized wave, (c) Status III for *x*-polarized wave and (d) Status III for *y*-polarized wave.

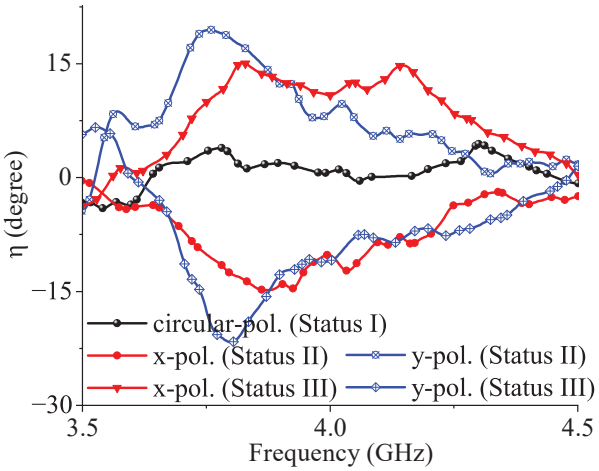


Fig. 10. Measured ellipticity of the MP for circular-, *x*- and *y*- polarized incident wave.

Table 2: Comparisons with previous literatures

| Refs. | Thickness ($\lambda$) | Reconfigurability | Polarization conversion | Frequency (GHz) | Efficiency (dB) |
|---|---|---|---|---|---|
| [19] | 0.07 | No | *y*-pol. to RCP<br>*y*-pol. to LCP | 20<br>30 | -0.1<br>-0.6 |
| [20] | 0.13 | No | *x*-pol. to RCP<br>*x*-pol. to LCP | 20.1-21.7<br>29.4-31.4 | -1.25<br>-1 |
| [21] | 0.53 | No | LP to RCP<br>LP to LCP | 19.7-20.2<br>29.5-30 | -0.61<br>-0.61 |
| [22] | 0.10 | Yes | LP/CP to orthogonal LP /CP | 7.4-12 | -1 |
| [23] | 0.28 | Yes | LP to orthogonal LP | 9.7 | -0.5 |
| This work | 0.02 | Yes | CP to LP<br>*x*-pol. to RCP/ LCP<br>*y*-pol. to RCP/ LCP | 3.6-4.3 | -2.5<br>-3.5<br>-4.2 |

cal operation frequency band. Further investigations are aimed at reducing the loss and improving the transmission efficiency.

## IV. CONCLUSION

Herein, a type of dynamically reconfigurable multifunctional transmission metasurface polarizer that can simultaneously manipulate the polarization conversion of linear or circular incident waves within an identical operation frequency range of 3.6-4.3 GHz with switchable PIN diodes was designed, fabricated, and measured. First, we designed a unit cell and illustrated how the structure interacted with the EM waves in terms of current distributions. Subsequently, we revealed that the LP emitted wave is observed in the vicinity of 4.0 GHz through the MP with a total transmission coefficient of -2.5 dB for CP incidence operating in Status I. Moreover, an incident wave in *x*-polarization or *y*-polarization was

simultaneously transformed into left- and right-handed circular polarization in the case of different PIN diodes states within the desired frequency band of 3.6-4.3 GHz, where transmission coefficients of approximately -3.5 and -4.2 dB, respectively, are achieved at peak frequency. This reconfigurable multifunctional transmission metasurface polarizer operating in an identical resonant frequency band provides an innovative and active approach for EM applications.

## REFERENCES


[1] V. C. Nguyen, L. Chen, and K. Halterman, "Total transmission and total reflection by zero index metamaterials with defects," *Physical Review Letters*, vol. 105, no. 23, p. 233908, 2010.

[2] C. Huang, J. Zhang, Q. Cheng, and T. Cui, "Multiband tunable asymmetric transmission of linearly polarized electromagnetic waves achieved by active chiral metamaterial," in *2019 Photonics & Electromagnetics Research Symposium-Fall (PIERS-Fall)*, pp. 325-331, IEEE, 2019.

[3] Y. Yao, R. Shankar, M. A. Kats, Y. Song, J. Kong, M. Loncar, and F. Capasso, "Electrically tunable metasurface perfect absorbers for ultrathin mid-infrared optical modulators," *Nano Letters*, vol. 14, no. 11, pp. 6526-6532, 2014.

[4] X. Ni, N. K. Emani, A. V. Kildishev, A. Boltasseva, and V. M. Shalaev, "Broadband light bending with plasmonic nanoantennas," *Science*, vol. 335, no. 6067, p. 427, 2012.

[5] X. Ni, A. V. Kildishev, and V. M. Shalaev, "Metasurface holograms for visible light," *Nature Communications*, vol. 4, no. 1, p. 2807, 2013.

[6] N. Yu and F. Capasso, "Flat optics with designer metasurfaces," *Nature Materials*, vol. 13, no. 2, pp. 139-150, 2014.

[7] G. Ding, K. Chen, G. Qian, J. Zhao, T. Jiang, Y. Feng, and Z. Wang, "Independent energy allocation of dual-Helical multi-beams with spin-selective transmissive metasurface," *Advanced Optical Materials*, vol. 8, no. 16, p. 2000342, 2020.

[8] J. Y. Lau and S. V. Hum, "A planar reconfigurable aperture with lens and reflectarray modes of operation," *IEEE Transactions on Microwave Theory and Techniques*, vol. 58, no. 12, pp. 3547-3555, 2010.

[9] S. Liu and T. J. Cui, "Concepts, working principles, and applications of coding and programmable metamaterials," *Advanced Optical Materials*, vol. 5, no. 22, p. 1700624, 2017.

[10] H. Li, F. Costa, Y. Wang, Q. Cao, and A. Monorchio, "A switchable and tunable multifunctional absorber/reflector with polarization-insensitive features," *International Journal of RF and Microwave Computer-Aided Engineering*, vol. 31, no. 4, p. e22573, 2021.

[11] H. Kazemi, M. Albooyeh, and F. Capolino, "Perfect anomalous reflection and refraction accompanied by an ideal polarization conversion: Potential of a chiral metasurface," in *2019 URSI International Symposium on Electromagnetic Theory (EMTS)*, pp. 1-4, IEEE, 2019.

[12] O. Fernández, A. Gomez, J. Basterrechea, and A. Vegas, "Reciprocal circular polarization handedness conversion using chiral metamaterials," *IEEE Antennas and Wireless Propagation Letters*, vol. 16, pp. 2307-2310, 2017.

[13] S. Yan and G. A. Vandenbosch, "Compact circular polarizer based on chiral twisted double split-ring resonator," *Applied Physics Letters*, vol. 102, no. 10, p. 103503, 2013.

[14] H.-X. Xu, G.-M. Wang, M. Q. Qi, T. Cai, and T. J. Cui, "Compact dual-band circular polarizer using twisted Hilbert-shaped chiral metamaterial," *Optics Express*, vol. 21, no. 21, pp. 24912-24921, 2013.

[15] X. Ma, W. Pan, C. Huang, M. Pu, Y. Wang, B. Zhao, J. Cui, C. Wang, and X. Luo, "An active metamaterial for polarization manipulating," *Advanced Optical Materials*, vol. 2, no. 10, pp. 945-949, 2014.

[16] J. Lin, D. Li, L. Lin, W. Yu, and J. Sheng, "Active transmission-type metasurface for linear-to-Circular polarization conversion at a certain frequency band," in *2023 International Applied Computational Electromagnetics Society Symposium (ACES)*, pp. 1-2, IEEE, 2023.

[17] G. I. Kiani, T. S. Bird, and K. L. Ford, "60 GHz ASK modulator using switchable FSS," in *2010 IEEE Antennas and Propagation Society International Symposium*, pp. 1-4, IEEE, 2010.

[18] J. Zhou, J. Dong, B. Wang, T. Koschny, M. Kafesaki, and C. M. Soukoulis, "Negative refractive index due to chirality," *Physical Review B*, vol. 79, no. 12, p. 121104, 2009.

[19] P. Naseri, S. A. Matos, J. R. Costa, C. A. Fernandes, and N. J. Fonseca, "Dual-band dual-linear-to-circular polarization converter in transmission mode application to $K/Ka$-band satellite communications," *IEEE Transactions on Antennas and Propagation*, vol. 66, no. 12, pp. 7128-7137, 2018.

[20] M. A. Sofi, K. Saurav, and S. K. Koul, "Frequency-selective surface-based compact single substrate layer dual-band transmission-type linear-to-circular polarization converter," *IEEE Transactions on Microwave Theory and Techniques*, vol. 68, no. 10, pp. 4138-4149, 2020.

[21] J. Lundgren, O. Zetterstrom, F. Mesa, N. J. Fonseca, and O. Quevedo-Teruel, "Fully metallic dual-band linear-to-circular polarizer for K/K a-band,"

*IEEE Antennas and Wireless Propagation Letters*, vol. 20, no. 11, pp. 2191-2195, 2021.

[22] W. Liu, J. C. Ke, C. Xiao, L. Zhang, Q. Cheng, and T. J. Cui, "Broadband polarization-reconfigurable converter using active metasurfaces," *IEEE Transactions on Antennas and Propagation*, 2023.

[23] Y. Li, Y. Wang, and Q. Cao, "Design of a multifunctional reconfigurable metasurface for polarization and propagation manipulation," *IEEE Access*, vol. 7, pp. 129183-129191, 2019.

**Jianyu Lin** was born in Zhejiang Province, China, in 1993. He received the B.S. degree in electromagnetic field and microwave technology from Xidian University, Xi'an, China, in 2016 and he is currently working toward the Ph.D. degree at Shanghai Jiao Tong University. His research interests include reconfigurable metamaterial and metasurface, electromagnetic wave regulation and high-gain antennas.

**Dongying Li** received the Ph.D. degree in electrical engineering from the University of Toronto, Toronto, ON, Canada. He was a Scientist with the Institute of High Performance Computing, Agency for Science Technology and Research, Singapore, from 2011 to 2014. He joined Shanghai Jiao Tong University, Shanghai, China, in 2014, where he is currently an Associate Professor. His research interests include radar target detection algorithms, artificial microwave materials, and antenna design.

**Wenxian Yu** was born in 1964. He received the Ph.D. degree in communication and electronic system from the National University of Defense Technology (NUDT), Changsha, China, in 1993. From 1996 to 2008, he was a Professor with the College of Electronic Science and Engineering, NUDT. Since 2008, he has been the Executive Dean with the School of Electronic Information and Electrical Engineering, Shanghai Jiao Tong University, Shanghai, China. He is currently the Chief Scientist of information acquisition and processing technology of the National High Technology Research and Development Program of China. His research interests include radar target recognition, remote sensing information processing, and multisensor data fusion.

# Parameter Sensitivity Analysis of 3D-Printed W-Band Reflective Fresnel Lens Antenna based on Acrylonitrile Butadiene Styrene Plastic

**Shunichi Futatsumori**

Surveillance and Communications Department, Electronic Navigation Research Institute
National Institute of Maritime, Port and Aviation Technology, Chofu, Tokyo 182-0012, Japan
futatsumori@mpat.go.jp

***Abstract –*** To improve the design of the 3D-printed W-band reflective Fresnel lens antenna based on acrylonitrile butadiene styrene (ABS) plastic, we have examined the parameter sensitivity related to the dielectric material constant. Although we have developed a high-gain millimeter-wave reflective Fresnel lens antenna, the material constant of the ABS filament used in 3D printing needs further investigation to optimize antenna performance. First, a 150-mm-diameter W-band reflector Fresnel antenna is designed and analyzed using finite-difference time-domain (FDTD) analysis. The analyzed and measured maximum antenna gains are 33.3 and 32.4 dBi, respectively. Subsequent sensitivity analysis focused on the impact of the loss tangent, relative dielectric constant, and folding length of the lens, based on both FDTD analysis and measurements.

***Index Terms –*** 3D printer, acrylonitrile butadiene styrene plastic, finite-difference time-domain method, reflective Fresnel lens antenna, relative dielectric constant.

## I. INTRODUCTION

The fabrication of antennas using 3D printers holds promise for delivering high-performance antennas at reduced costs [1]–[7]. In the context of millimeter-wave radar applications for civilian use, our team has explored radars for uses such as helicopter obstacle detection and airport runway foreign object debris detection system [8]–[12]. For instance, helicopter flight tests are conducted to assess the detection efficacy for high-voltage power lines and their supporting pylons [10]. The radar systems in development utilize a parabolic reflector antenna made of carbon fiber reinforced plastics (CFRP). The CFPR reflector antenna, of size 130 mm height and 130 mm width, has measured antenna gain of 33 dBi gain at 76.5 GHz [13]. By comparing the aperture size and the gain of the proposed 3D printed antenna, they have close characteristics. However, the fabrication cost of the CFPR reflector is much higher than that of a reflector antenna using a 3D printer. The dielectric antennas created with 3D printers, particularly those using acrylonitrile butadiene styrene (ABS) plastic filaments, present certain advantages over the CFRP reflector antenna. Yet, the ABS filaments tend to exhibit pronounced dielectric loss characteristics in the millimeter-wave region. The loss tangent is a parameter that represents the loss of electrical energy in a dielectric material. The dielectric loss is usually caused by the thermal energy generated when an alternating electric field is applied to a dielectric material. When a dielectric material with a high loss tangent is employed as a lens material, the dielectric loss will be large and the maximum gain will be reduced. To address this, a reflective Fresnel lens antenna with an antenna gain exceeding 30 dBi was introduced for millimeter-wave radars [4][5]. Figure 1 illustrates the structure of both the reflector lens and the reflective Fresnel lens antennas.

In this paper, our objective is to refine the design of the 3D-printed reflective Fresnel lens antenna. We conducted a parameter sensitivity analysis concerning the dielectric material constant using the finite-difference time-domain (FDTD) technique. Such an analysis is pivotal for understanding the effects of dielectric material constants and physical dimensions in order to design high-performance lens antennas.

First, we discuss the design and the FDTD analysis results of the W-band reflective Fresnel lens antenna developed up to this point. Subsequently, we compare the analyzed, and fabricated antenna characteristics. We then explore the antenna parameter dependencies on the dielectric loss tangent and relative permittivity of the lens, based on the FDTD analysis. Discussions on the effects stemming from the dielectric loss tangent values are presented. In conclusion, we investigate how maximum gain is influenced by the dielectric constant and the focal length through numerical analysis.

## II. 150 mm-DIAMETER W-BAND REFLECTIVE FRESNEL LENS ANTENNA

For the parameter sensitivity analysis, we utilize the previously designed 150-mm-diameter W-band reflector Fresnel antenna as a typical example [5]. Figure 1 depicts the structures of both the reflector lens antenna and the reflective Fresnel lens antenna. The lens curve for the

*Submitted On: July 30, 2023*
*Accepted On: May 3, 2024*
https://doi.org/10.13052/2024.ACES.J.390308

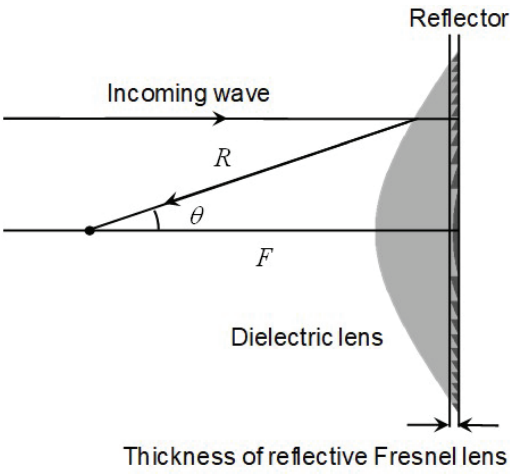


Fig. 1. Structure of the reflector lens antenna and reflective Fresnel lens antenna.

conventional reflector lens antenna is defined by [14]:

$$R = \frac{(n-1)\,2F}{(2n-1)\,cos\theta - 1}, \tag{1}$$

where $n$ and $R$ are the index of refraction and the distance between any point on the lens surface and the focal point, respectively. Furthermore, $\theta$ is the ray angle and $F$ is the focal length. An integral number of wavelengths inside the dielectric lens is then subtracted from the lens curve described in equation (1) to define the Fresnel lens.

Table 1 lists the design and FDTD analysis parameters. The design frequency is 76.5 GHz, which aligns with the central frequency of the low-transmitting power millimeter-wave radar system, while the focal length $F$ is 75 mm. Moreover, the diameter of the reflector lens measures 150 mm. We assumed a relative permittivity of 2.3, based on the fabrication with ABS plastic filament, and $\tan\delta$ is $3\times10^{-2}$. Since the accurate permittivity and permittivity required to design the lens were unknown at the design stage, we used the values of typical ABS resins as a result of a literature review. Therefore, the dielectric constant 2.3 and the dielectric loss tangent $3\times10^{-2}$ are the starting points used for analysis. With the Fresnel structure, the thickness of the reflective Fresnel lens is narrowed down to 4.3 mm, marking a 17.8% reduction from the 24.1 mm seen in conventional lens structures. Figure 2 showcases the analyzed model of the designed reflective Fresnel lens antenna with a diameter of 150 mm. The $zx$-plane in Fig. 2 is defined as the azimuth direction, and the $yz$-plane is defined as the elevation direction. The default value of the folding length is 3.7 mm. The thickness of the lens stands for the sum of the folding length and the basement thickness. The basement thickness is fixed at 0.5 mm throughout the analysis in this paper. A perfect electric conductor is positioned behind the dielectric lens, and the primary source is the

Table 1: Design and FDTD analysis parameters of the reflective Fresnel lens antenna

| | |
|---|---|
| **Frequency (GHz)** | 76.5 |
| **Focal length (mm)** | 75 |
| **Dimensions (diameter in mm)** | 150 |
| **Folding length (mm)** | 3.7 |
| **Thickness (mm)** | 4.3 |
| **Relative permittivity of lens material** | 2.3 |
| **Loss tangent of lens material** | $3\times10^{-2}$ |
| **Cell dimensions** | 518×525×523 |
| **X-axis cell size (mm)** | 0.309 (Min.), 0.465 (Max.) |
| **Y-axis cell size (mm)** | 0.100 (Min.), 0.466 (Max.) |
| **Z-axis cell size (mm)** | 0.165 (Min.), 0.274 (Max.) |
| **Time increment (s)** | $2.7\times10^{-13}$ |
| **Material of bottom of lens** | Perfect electric conductor |
| **Primary source** | WR-10 open-ended waveguide |
| **Specification of computer used for analysis** | CPU: Intel Core i7-9800X<br>Main memory: 128 GB<br>GPU: Nvidia Tesla K40c |
| **Analysis time** | 16 minutes |

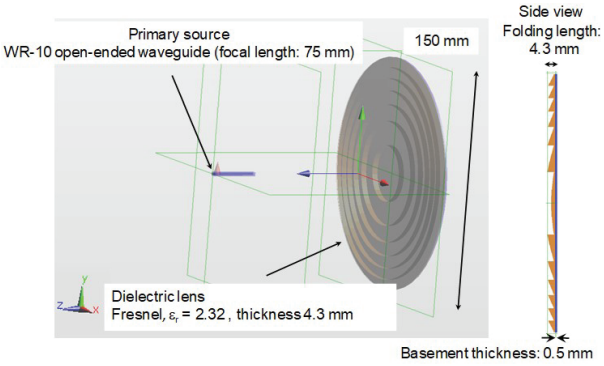


Fig. 2. 150-mm-diameter reflective Fresnel lens antenna analysis model.

WR-10 open-ended waveguide. The antenna's excitation polarization follows a vertical polarization.

The reflective Fresnel lens antenna is analyzed using the commercially available FDTD software SEMCAD X from Schmid & Partner Engineering AG in Zürich, Switzerland [15]. As shown in the Table 1, the cell dimension is 518×525×523. In addition, the nonuniform mesh is applied for the FDTD voxels. The minimum and maximum cell size are shown in Table 1.

The time increment is $2.7\times10^{-13}$ seconds. Based on the nonuniform mesh, the lens surface has a staircase structure in the analysis. The computer with Intel Core

i7-9800X CPU, 128 GB main memory and Nvidia Tesla K40c GPU is used for the analysis. The analysis time is approximately 16 minutes.

Figure 3 presents the analyzed azimuth and elevation radiation patterns at 76.5 GHz. The antenna achieves a maximum gain of 33.3 dBi, with azimuth and elevation half power beamwidth (HPBW) of 1.7 degrees and 1.6 degrees, respectively. Subsequently, the reflective Fresnel lens antenna is manufactured using the Afinia H800 3D Printer from Afinia 3D, Chanhassen, MN. The 3D printer produced laminations in 0.1 mm increments. Figure 4 offers a detailed view of the fabricated reflective Fresnel lens antenna. To serve as a reflective surface, a 0.1 mm thick aluminum tape was affixed to the back of the lens. Moreover, the WR-10 open-ended waveguide is positioned at the focal point, consistent with the FDTD analysis. To enable adjustments to the focal length during measurements, the Fresnel lens is mounted on a stage equipped with a micrometer.

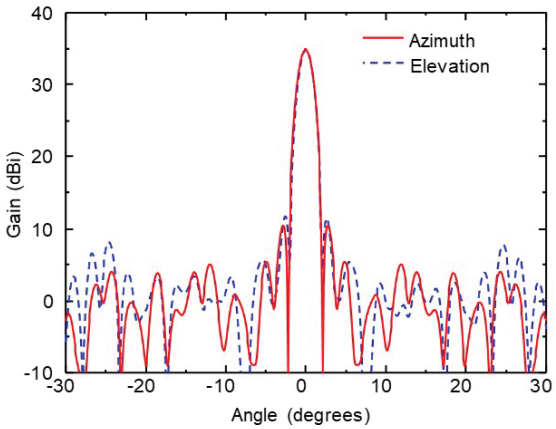


Fig. 3. Analyzed azimuth and elevation radiation patterns at 76.5 GHz.

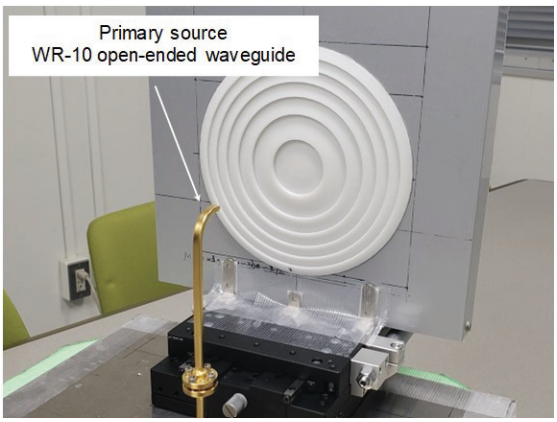


Fig. 4. Overview of the fabricated reflective Fresnel lens antenna using a 3D printer.

Figure 5 compares the analyzed (focal length: 75 mm) and measured (focal length: 79 mm) azimuth radiation patterns at 76.5 GHz. The antenna achieved a maximum gain of 32.4 dBi with a focal length of 79 mm, while its designed focal length is 75 mm. Comparing the analyzed and measured maximum antenna gains reveals a discrepancy of less than 1 dB in gain, but a focal point difference of approximately 5 mm. In contrast, the analyzed, and measured HPBW are 1.1 degrees and 1.0 degrees, respectively. Although the analysis measured results largely align, a parameter sensitivity analysis will be conducted for further refinement.

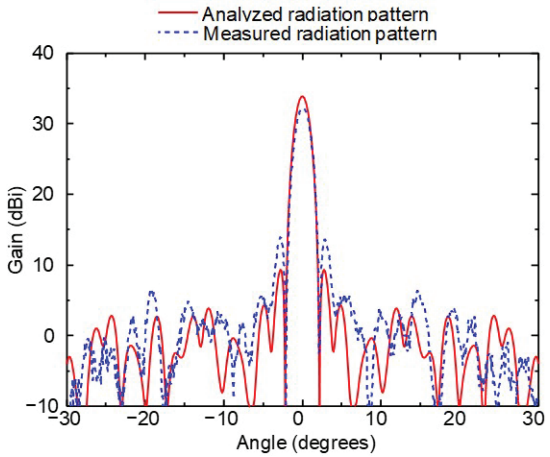


Fig. 5. Analyzed (focal length: 75 mm) and measured (focal length: 79 mm) azimuth radiation patterns at 76.5 GHz.

## III. PARAMETER SENSITIVITY ANALYSIS

The parameter sensitivity of the 3D-printed reflective Fresnel lens antenna has been analyzed using the FDTD method. The relationship between the maximum antenna gains and the loss tangent of the dielectric lens is explored by varying the loss tangent between 0 and 5 $\times 10^{-2}$, while keeping other analysis parameters consistent with those in Table 1. Figure 6 illustrates the maximum antenna gains at 76.5 GHz relative to the loss tangent. An increase in the loss tangent leads to a reduction in antenna gain; for instance, antenna gains of 33.3 dBi and 32.8 dBi are observed for loss tangent values of $3\times10^{-2}$ and $4\times10^{-2}$, respectively. Compared to the measured antenna gain of 32.4 dBi, a loss tangent value of around $4\times10^{-2}$ aligns closely with the measured results.

Subsequently, the maximum antenna gains in relation to the relative permittivity were assessed. Figure 7 displays the analyzed maximum antenna gain at 76.5 GHz for various relative permittivity values, which range between 1.5 and 3. Additionally, the focal lengths considered are 70 mm, 75 mm, and 80 mm. The changes

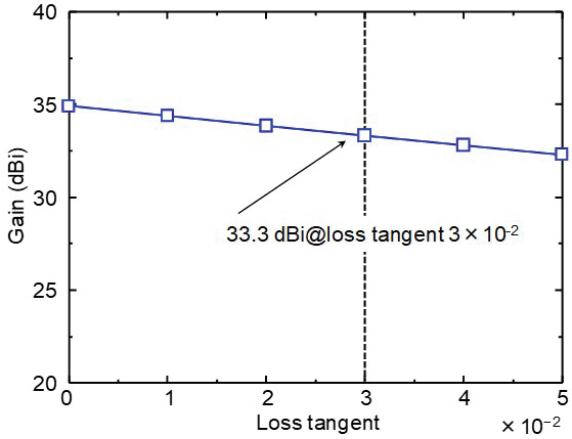


Fig. 6. Analyzed maximum antenna gains for the reflective Fresnel lens antenna at 76.5 GHz, plotted against loss tangent.

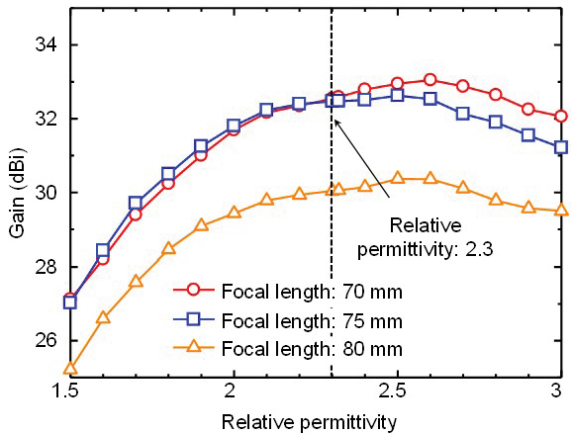


Fig. 7. Analyzed maximum antenna gains of the reflective Fresnel lens antenna at 76.5 GHz, analyzed with respect to relative permittivity.

in maximum gain in response to relative permittivity variations are mild. Specifically, the gain difference when altering the relative permittivity between 2 and 3 registers at approximately 1.4 dB for a focal distance of 75 mm.

Moreover, the effects of varying focal lengths on maximum antenna gains are evaluated. Figure 8 presents the analyzed maximum gains at 76.5 GHz for focal lengths spanning between 60 mm and 85 mm. The relative permittivity values considered are 2.0, 2.3, and 2.6. The graph demonstrates that the variation in gain in response to changes in focal length remains reasonably uniform. When the dielectric constant is 2.3, the maximum gain difference is about 3.5 dB upon shifting the dielectric constant from 65 mm to 80 mm. For dielectric constants 2.0 and 2.6, a rapid maximum gain decrease is

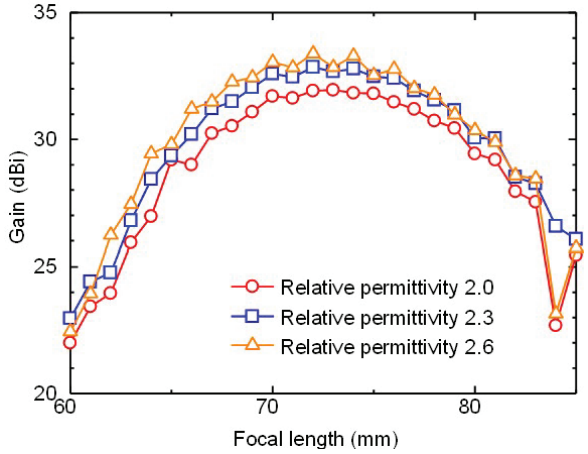


Fig. 8. Analyzed maximum antenna gains for the reflective Fresnel lens antenna at 76.5 GHz, plotted against focal length.

observed at a focal length of 84 mm. This phenomenon occurs due to the drop of the main lobe due to the dielectric lens not being formed due to off-focus region.

Figure 9 compares the maximum gains at 76.5 GHz for focal lengths ranging from 60 mm to 85 mm, with a fixed relative permittivity of 2.3. Analytical results depict a gain exceeding 30 dBi for focal lengths between 66 mm and 80 mm. In contrast, measured data indicates gains surpassing 30 dBi for focal lengths between 75 mm and 85 mm. Figures 9 and 10 shows the maximum gain frequency characteristics and the maximum gain focal length characteristic, respectively. From these results, it is confirmed the focal length between the analysis and the measurement differs by between 5 mm and 10 mm.

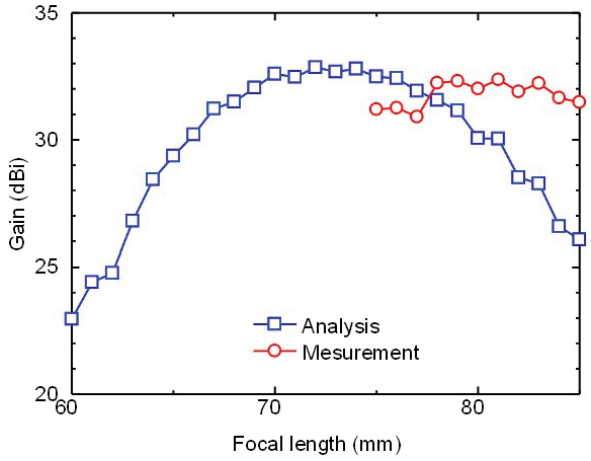


Fig. 9. Analyzed and measured maximum antenna gains for the reflective Fresnel lens antenna at 76.5 GHz, with a fixed focal length of 75 mm.

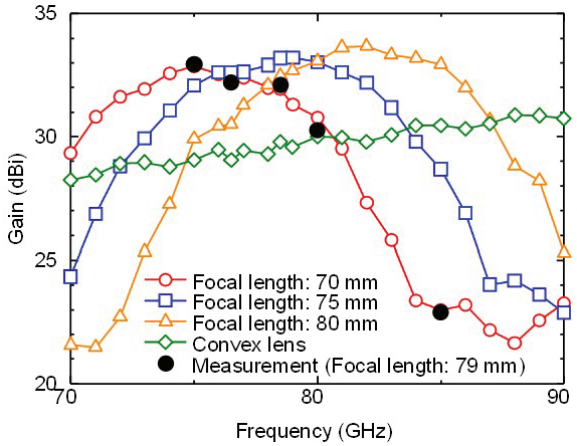


Fig. 10. Analyzed and measured maximum antenna gains of the reflective Fresnel lens antenna across different focal lengths.

Next, the frequency characteristics of the reflective Fresnel lens antenna are probed. Figure 10 shows the analyzed and measured maximum antenna gains against frequency, considering focal lengths of 70 mm, 75 mm, and 80 mm. For reference, the frequency characteristics of a convex lens of the same diameter are included. Unlike the convex lens, which lacks peaks in its frequency band, the reflective Fresnel lens antenna displays a peak frequency contingent on its focal length. The distinct frequency-dependent gain traits are attributed to the Fresnel lens structure. Furthermore, the measured frequency attributes, recorded with a 79 mm focal length, are depicted as black dots. In this scenario, the measured outcomes harmonize well with the analysis for a 70 mm focal length.

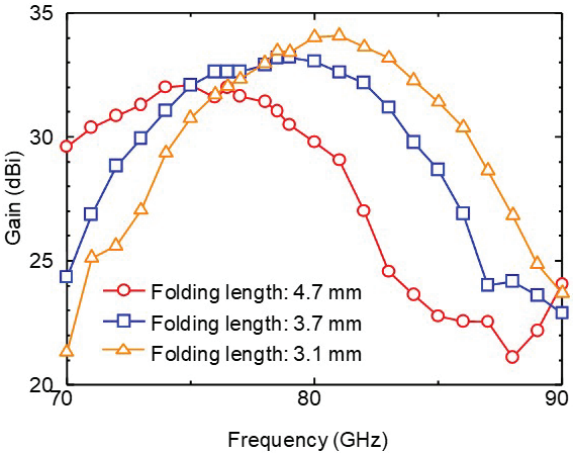


Fig. 11. Analyzed (focal length: 75 mm) antenna gain frequency characteristics of the reflective Fresnel lens antenna with different folding length.

Lastly, we examined how antenna gain characteristics are influenced by the folding length, which represents the thickness of the Fresnel lens. Figure 11 presents the analyzed frequency characteristics of the reflective Fresnel lens antenna for various folding lengths, with the focal length consistently set at 75 mm. The designed and fabricated folding length is 3.7 mm, but for the analysis, this length is also adjusted to 4.7 mm, 3.7 mm, and 3.1 mm. It is important to note that the true thickness of the lens equals the sum of the folding length and the basement thickness. The basement thickness in this design is 0.5 mm. Adjusting the folding length causes the maximum gain frequency to shift, ranging between shifts of 5 GHz/mm and 10 GHz/mm. These results underscore the significant impact that the thickness of the folds, due to the Fresnel structure, has on frequency characteristics. Note that the antenna gain is dropped at 86 GHz and higher frequencies for folding length = 3.1 mm. This is mainly due to the main lobe is not formed by the dielectric lens due to the off-focusing.

## IV. CONCLUSION

The parameter sensitivity of the 3D printed reflective Fresnel lens antenna was scrutinized using the FDTD method. Differences between the analyzed and measured results were explored. Subsequent FDTD analyses were conducted to understand the effects of lens material constants on antenna characteristics. The observed loss tangent value of around $4\times10^{-2}$ aligns closely with measured results. Moreover, the antenna characteristics' dependency on the relative permittivity is relatively moderate. However, the folding length of the reflective Fresnel lens significantly influences frequency characteristics. Insights from these studies will guide future antenna designs aiming for higher gains.

## ACKNOWLEDGMENT

This work was partly supported by JSPS KAKENHI Grant Number 20K04931.

## REFERENCES

[1] P. Nayeri, M. Liang, R. A. Sabory-García, M. Tuo, F. Yang, M. Gehm, H. Xin, and A. Z. Elsherbeni, "3D printed dielectric reflectarrays: Low-cost high-gain antennas at sub-millimeter waves," *IEEE Transactions on Antennas and Propagation*, vol. 62, no. 4, pp. 2000-2008, Apr. 2014.

[2] K. Mazouni, J. Lanteri, N. Yonemoto, J. Y. Dauvignac, C. Pichot, and C. Migliaccio, "78.5GHz Fresnel reflector with circular polarization for collision avoidance radar on rescue helicopters," in *Proceedings of the 3rd European Conference on Antennas and Propagation*, Berlin, pp. 1819-1823, 2009.

[3] S. Futatsumori, A. Kohmura, and N. Yonemoto, "Performance measurement of compact and high-range resolution 76 GHz millimeter-wave radar system for autonomous unmanned helicopters," *IEICE Transactions on Electronics*, vol. E96.C, no. 4, pp. 586-594, Apr. 2013.

[4] S. Futatsumori, K. Morioka, A. Kohmura, N. Sakamoto, T. Soga, and N. Yonemoto, "Feasibility evaluations of three-dimensional-printed high-gain reflectarray antenna for W-Band applications," *IEICE Communications Express*, vol. 7, no. 6, pp. 230-235, 2018.

[5] S. Futatsumori, N. Sakamoto, and T. Soga, "Three-dimensional-printed W-band high-gain reflector Fresnel lens antenna based on acrylonitrile butadiene styrene plastic," *IEICE Communications Express*, vol. 8, no. 7, pp. 275-280, 2019.

[6] S. Futatsumori, "Dielectric material constant sensitivity analysis of 3D-printed W-band reflector Fresnel lens antenna based on acrylonitrile butadiene styrene," *Proceedings of 2023 International Applied Computational Electromagnetics Society*, pp. 1-2, Mar. 2023.

[7] A. Belen and E. Tetik, "Realization of modified elliptical shaped dielectric lens antenna for X band applications with 3D printing technology," *ACES Journal*, vol. 35, no. 8, pp. 916-921, Aug. 2020.

[8] S. Futatsumori, K. Morioka, A. Kohmura, M. Shioji, and N. Yonemoto, "Evaluation of polarization characteristics of power-line RCS at 76 GHz for helicopter obstacle detection," *Electronics Letters*, vol. 51, no. 14, pp. 1110-1111, July 2015.

[9] S. Futatsumori, K. Morioka, A. Kohmura, K. Okada, and N. Yonemoto, "Design and field feasibility evaluation of distributed-type 96 GHz FMCW millimeter-wave radar based on radio-over-fiber and optical frequency multiplier," *Journal of Lightwave Technology*, vol. 34, no. 20, pp. 4835-4843, Oct. 2016.

[10] S. Futatsumori, C. Amielh, N. Miyazaki, K. Kobayashi, and N. Katsura, "Helicopter flight evaluations of high-voltage power lines detection based on 76 GHz circular polarized millimeter-wave radar system," in *Proceedings of the 15th European Radar Conference*, pp. 218-221, 2018.

[11] S. Futatsumori, N. Yonemoto, N. Shibagaki, Y. Sato, and K. Kashima, "Detection probability estimation of 96 GHz millimeter-wave airport foreign object debris detection radar using measured radar cross section characteristics," in *Proceedings of the 15th European Conference on Antenna and Propagation*, pp. 1-4, Mar. 2021.

[12] S. Futatsumori, N. Yonemoto, N. Shibagaki, Y. Sato, and K. Kashima, "Performance evaluations of airport runway foreign object detection system using a 96 GHz millimeter-wave radar system based on international standard," in *Proceedings of the 47th International Conference on Infrared, Millimeter, and Terahertz Waves (IRMMW-THz2022)*, pp. 1-2, 2022.

[13] S. Futatsumori, A. Kohmura, and N. Yonemoto, "Development of compact and high performance 76GHz millimeter-wave radar system for autonomous unmanned helicopters," *Institute of Electronics, Information and Communication Engineers (IEICE) Technical Report*, vol. 110, no. 160, pp. 7-11, July 2010.

[14] J. Kraus, "Some unique reflector-type antennas," *IEEE Antennas and Propagation Society Newsletter*, vol. 24, no. 2, pp. 9-12, Apr. 1982.

[15] SEMDAD X User Manual, Schmid & Partner Engineering AG, Zurich, 2010.

**Shunichi Futatsumori** received the B.E., M.E., and Ph.D. degrees in Electronics and Information Engineering from Hokkaido University, Sapporo, Japan, in 2004, 2006, and 2009, respectively. Between 2008 and 2009, he held the position of Research Fellow with the Japan Society for the Promotion of Science. In 2009, he joined the Electronic Navigation Research Institute (ENRI) in Japan, where his research focused on millimeter-wave radar systems and electromagnetic compatibility issues. He currently serves as a principal researcher at ENRI. In 2009, Dr. Futatsumori was honored with the Young Researcher's Award from IEICE and the APMC prize. He is a member of both IEEE and IEICE.

# An Efficient MLFMA for Accurately Analyzing Electromagnetic Radiation and Coupling Characteristics of Large-scale Antenna Arrays Mounted on Platform

**Lei Yin[1], Ning Ding[1], Peng Hou[1], Zhongchao Lin[1], Xunwang Zhao[1], Shugang Jiang[2], and Yongchang Jiao[1]**

[1]Shaanxi Key Laboratory of Large Scale Electromagnetic Computing
Xidian University, Xi'an, Shaanxi 710071, China
yinlei@stu.xidian.edu.cn, dn95999@163.com, hou_peng@foxmail.com
zclin@xidian.edu.cn, xwzhao@mail.xidian.edu.cn, ychjiao@xidian.edu.cn

[2]Xi'an CETC-Xidian University Collaborative Innovation Institute of Radar Technology Co. Ltd
Xi'an, Shaanxi 710000, China
zaishuiyifang131@126.com

***Abstract*** **–** A multilevel fast multipole algorithm (MLFMA) for analyzing electromagnetic radiation and coupling characteristics of large-scale antenna arrays mounted on the platforms is presented in this paper. Compared with the method of moments (MoM), the MLFMA can be used to calculate larger scale problems with limited resources. First, waveport model of the MLFMA based on the equivalence principle and mode matching theory is established to efficiently and accurately simulate the antenna array. Then, a preconditioning approach for solving the radiation problems with the waveports is designed to improve convergence of the MLFMA. An initial guess construction method is proposed to accelerate the MLFMA computation for the multi-excitation problems, which can reduce the iteration time by at least 50%. Numerical results demonstrate accuracy and efficiency of the proposed method.

***Index Terms*** **–** electromagnetic radiation and coupling, multilevel fast multipole algorithm (MLFMA), multi-excitation problems, preconditioner, waveport.

## I. INTRODUCTION

Electromagnetic (EM) radiation and coupling analysis of large-scale antenna arrays mounted on the platform is an important problem in real-life applications, such as electromagnetic compatibility (EMC) analysis of airborne antennas [1, 2] and optimization of antenna arrays [3, 4]. For the EMC analysis of airborne antennas, the conventional method is to calculate the antenna pattern and S parameters by using the method of moments (MoM) [5], the finite element method (FEM) [6], or the hybrid MoM-physical optics (PO) method [7–9]. In the antenna array optimization problems, the MoM and FEM are used to extract the active element pattern (AEP) for each antenna element [10]. Since the large-scale antenna arrays and platforms lead to a large number of unknowns, the MoM and FEM can hardly be implemented due to the limitation of computational resources, and the hybrid MoM-PO can reduce the consumption of computational resources but cannot satisfy the accuracy requirements for engineering applications. The time-domain EM field calculation methods such as the stabilized DG algorithms are widely used in the simulation of broadband characteristics for ultrawideband (UBW) communication and EMC systems [11–13]. Although these methods can obtain accurate results, they consume huge time resources when calculating electrically large models. Besides, some accurate numerical methods such as the spectral element method (SEM) [14–16] are developed, and SEM is found to be more accurate [17, 18] and could be used for analyzing waveguides and antennas [19, 20]. However, the volume mesh and domain truncation will generate a large number of unknowns, which will lead to excessive consumption of computational resources when calculating the antenna arrays mounted on a large platform. To meet the increasing demands for rapidly designed high-performance antennas and accurate EMC analysis of large-scale arrays, it is imperative to overcome bottlenecks of the existing numerical methods. As a low computational complexity algorithm, the multilevel fast multipole algorithm (MLFMA) can effectively reduce the computation memory and time consumptions [21]. In recent years, thanks to the numerous research works [22–24], capacity and efficiency of the MLFMA have been further significantly improved. However, the

*Submitted On: December 16, 2023*
*Accepted On: April 17, 2024*
https://doi.org/10.13052/2024.ACES.J.390309

MLFMA is still weak for solving radiation and coupling characteristics of antenna arrays due to the bottleneck of related techniques. Most of the research on the MLFMA was focused on analyzing the scattering characteristics of metal or dielectric models, and there are still few researches on solving complex antenna radiation problems by using the MLFMA. Furthermore, although some iterative solvers spend lower computational costs in solving the EM problems, the MLFMA still suffers from convergence problems, and an effective and robust preconditioning method for accurately analyzing complex antenna arrays is urgently needed. Moreover, the iterative solvers are inefficient for solving the multi-excitation problems, which require restarting for each right-hand side (RHS).

In this paper, a preconditioned MLFMA oriented to the radiation and coupling analysis for a large-scale antenna array mounted on the platform is presented. First, waveport model of the MLFMA based on the equivalence principle and mode matching theory is established, which can realize the accurate EM modeling for the antenna excitation source and matching load. In this way, the MLFMA can be used for solving the radiation problems with waveports. Then, a preconditioning approach is designed for the MLFMA to analyze the radiation problems with waveport excitations. Moreover, to improve efficiency of the MLFMA when solving multi-excitation problems, an initial guess construction method by extracting typical characteristic currents is proposed. To demonstrate effectiveness and capability of the proposed method, a slot antenna array with a dielectric radome is analyzed, and the proposed initial guess construction method can reduce the iteration time by at least 50%. Finally, a numerical example of an antenna array consisting of 100 dipole antenna elements mounted on a ship is analyzed, validating that the proposed algorithm can simulate large-scale antenna arrays mounted on the platforms under limited computational resources.

## II. THEORETICAL ANALYSIS

### A. Waveport modeling for MLFMA

To calculate the antenna pattern and S parameters of antenna arrays, the accurate excitation sources model is necessary for the MLFMA. The waveport can be developed to realize the accurate modeling of excitation sources and absorb power of the traveling wave at the matched port. We assume that the semi-infinite waveguides are connected to the original waveguides, and the EM fields propagating to the semi-infinite waveguide will never reflect. In the semi-infinite waveguides, we assumed that the incident wave of a specific mode propagates to the original waveguide, hence the waveports can be used as the excitation sources.

We first establish the integral equations on the boundary surfaces of composite structures, which can be referred to as a multiple region problem. The metal-dielectric models are formulated in terms of the electric field integral equation (EFIE) and the Poggio-Miller-Chang-Harrington-Wu (PMCHW) formulation. As an example, for different regions $i$ and $j$, the electric fields and magnetic fields can be written as:

$$\hat{n}\times(E_{inc}^{(j)}-E_{inc}^{(i)})=\hat{n}\times\{[\eta_i L^{(i)}(J_i)-K^{(i)}(M_i)] - [\eta_j L^{(j)}(J_j)-K^{(j)}(M_j)]\}, \quad (1)$$

$$\hat{n}\times(H_{inc}^{(j)}-H_{inc}^{(i)})=\hat{n}\times\{[K^{(i)}(J_i)+\frac{L^{(i)}(M_i)}{\eta_i}] - [K^{(j)}(J_j)+\frac{L^{(j)}(M_j)}{\eta_j}]\}, \quad (2)$$

where $\hat{n}$ is the unit normal on the boundary surface from region $j$ to region $i$, $\eta_i=\sqrt{\varepsilon_i/\mu_i}$ is the wave impedance of region $i$, and the integral operators $L$ and $K$ are defined as:

$$L(X)=-\int_S(X+\frac{1}{k^2}\nabla\cdot X\nabla)G(r,r')ds', \quad (3)$$

$$K(X)=-\int_S X\times\nabla G(r,r')ds', \quad (4)$$

where $k$ is the wave number, and $G(r,r')$ is the Green function. Equations (1) and (2) are the well-known PMCHW formulation, and Equation (1) can degenerate into the EFIE formulation for modeling metallic waveguides and structures.

Then we formulate the integral equations on the aperture surface $S$ in the original waveguide port. As shown in Fig. 1, the electric field $E^{(p)}$ and magnetic field $H^{(p)}$ satisfy the boundary condition on the surface of $S$ on the origin waveguide side:

$$\hat{n}\times H^{(p)}=J_s, \quad (5)$$

$$\hat{n}\times E^{(p)}=-M_s. \quad (6)$$

Then we formulate the integral equations on the aperture surfaces in the semi-infinite waveguides. Utilizing Schelkunoff's equivalence principle to the semi-infinite waveport region, the currents are related to the tangential fields on outer side of the aperture surface $S$:

$$-\hat{n}\times H^{(port)}=-J_s, \quad (7)$$

$$-\hat{n}\times E^{(port)}=M_s, \quad (8)$$

since the tangential electric currents impressed on a PEC surface, i.e. $J_s$, will not radiate. The total fields in the semi-infinite waveguide region consist of three parts, i.e. the incident fields $E_{inc}$ and $H_{inc}$, the reflected fields produced by the reflection of incident fields, and the fields radiated by $M_s$. Total fields in the semi-infinite

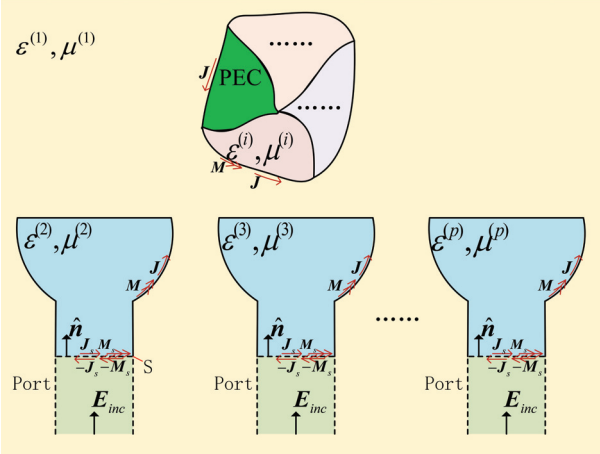


Fig. 1. Composite metallic and dielectric structures with multiport waveguide.

waveguide are expressed as:

$$E^{(port)} = e_j e^{-j\beta_j z} - e_j e^{j\beta_j z} + \sum_{l=1}^{\infty} b_l e_l e^{j\beta_j z}, \quad (9)$$

$$H^{(port)} = \frac{\hat{n}\times e_j}{\eta_j} e^{-j\beta_j z} + \frac{\hat{n}\times e_j}{\eta_j} e^{j\beta_j z} - \sum_{l=1}^{\infty} b_l \frac{\hat{n}\times e_l}{\eta_j} e^{j\beta_j z}, \quad (10)$$

where $z$ is the $z$-direction distance from the aperture surface, $e_j$ is the normalized eigenvector of the waveguide, and $e_l$ is the $l$th excitation mode. The fields on the aperture surface with $z = 0$ can be expressed as:

$$E^{(port)}|_{s^-} = \sum_{l=1}^{\infty} b_l e_l, \quad (11)$$

$$H^{(port)}|_{s^-} = \frac{2\hat{n}\times e_j}{\eta_j} - \sum_{l=1}^{\infty} b_l \frac{\hat{n}\times e_l}{\eta_j}. \quad (12)$$

Based on Equations (11), (12) and the boundary condition on the aperture surface in the waveguide $\hat{n}\times H|_{s^+} = (-\hat{n})\times H|_{s^-} = J_s$, the integral equation on the aperture surface can be written as:

$$-\hat{n}\times J_s - \sum_{l=1}^{\infty} \frac{\hat{n}\times e_l}{\eta_j \int_s (\hat{n}\times e_l)\cdot M_s ds} = \frac{2\hat{n}\times e_j}{\eta_j}. \quad (13)$$

The coupled (1) and (2) equations are applied to the original waveguides and the composite structures, Equation (13) is used to model the waveguide ports. The electromagnetic current distributions can be obtained by solving the integral equations using the MLFMA. The scattering parameters can be derived by using the normalized voltage and current:

$$S_{ij} = \sqrt{\frac{\eta_j}{\eta_i}} \int M \cdot (-\hat{n}\times e_i) ds - \delta(i,j). \quad (14)$$

### B. Preconditioning approach

When solving complex antenna radiation problems in practical engineering, there often are some complex metal-dielectric structures. For the discretization, we utilize the Rao-Wilton-Glisson basis functions [25] to expand the surface currents, the system matrix of metal-dielectric models under the waveport excitation can be written symbolically as:

$$\left[\begin{array}{ccc:c} Z_{JJ}^{NF} & Z_{JD}^{NF} & Z_{JM}^{NF} & Z_{JP} \\ Z_{DJ}^{NF} & Z_{DD}^{NF} & Z_{DM}^{NF} & Z_{DP} \\ Z_{MJ}^{NF} & Z_{MD}^{NF} & Z_{MM}^{NF} & Z_{MP} \\ \hdashline Z_{PJ} & Z_{PD} & Z_{PM} & Z_{PP} \end{array}\right], \quad (15)$$

where the subscript $J$ corresponds to the equivalent electric currents on the metal surfaces, the subscripts $D$ and $M$ correspond to the equivalent electric and magnetic currents on the dielectric surfaces, and the subscript $P$ corresponds to the equivalent magnetic currents on the waveport surfaces. Since the system matrix (15) usually is not well-conditioned, a preconditioning approach is designed to improve convergence of the large-scale antenna array models under the waveport excitations. During implementation of the MLFMA, the matrix is decomposed into two parts, i.e. $Z_{near}$ and $Z_{far}$, and the matrix equation is expressed as:

$$(Z_{near} + Z_{far})\cdot I = V, \quad (16)$$

where $Z_{near}$ is the submatrix corresponding to the interaction between the near-field clusters in the lowest level of the MLFMA octree structure, and $Z_{far}$ is the submatrix corresponding to the interaction among the far-field clusters computed approximately with the matrix-vector-product (MVP). The preconditioning matrix is constructed as:

$$A = \left[\begin{array}{cc} Z_{near} & Z_{12} \\ Z_{21} & Z_{PP} \end{array}\right], \quad (17)$$

where $Z_{12} = [Z_{JP}^T, Z_{DP}^T, Z_{MP}^T]^T$ and $Z_{21} = [Z_{PJ}, Z_{PD}, Z_{PP}]$ are two coupling matrices between the waveguide cavity domain and the waveport domain. We compute the preconditioned residual vector $\tilde{r} = A^{-1} r$ in each iteration, and this is accomplished by solving the equation $A\tilde{r} = r$ by using the direct sparse matrix solver MUMPS [26]. It is important to note that the matrix (17) is fixed and does not change when solving the multi-excitation problems, and factorizations of this matrix are only performed once before the iteration starts. Moreover, this method obtains the full inverse matrix of $A$ instead of its approximate inverse matrix, which leads to a better convergence rate than the commonly used ILU and SAI methods [27].

### C. Initial guess construction method

As a low computational complexity algorithm, the MLFMA can efficiently reduce the consumption of computational resources when analyzing the electrically large EM models. However, when solving the EM radiation problems with multiple excitations, each excitation corresponds to a $V$ vector, and the iterative solver needs

to restart for each excitation. For the iterative solvers, the vector $I$ in Equation (16) refers to the unknown coefficients of system matrix equation, which is commonly equal to zero before the iteration starts. The conventional method is to use the solution of previous excitation as the initial guess for the next excitation. This method is effectively used in the monostatic radar cross section (RCS) calculations but is ineffective for solving the radiation problems.

In this section, we propose an initial guess construction method for the antenna arrays mounted on a platform to improve convergence of the multi-excitation problems. This method is based on the assumption that electric current distribution of the antenna array is similar when different ports are excited separately. Here, two examples are taken to demonstrate this conclusion intuitively. The first example is an antenna array consisting of 5 slot antennas with the rectangular waveport feeding, as shown in Fig. 2. The second example is a $3 \times 4$ dipole antenna array with the coaxial waveport feeding, as depicted in Fig. 4. Both Fig. 3 and Fig. 5 perfectly validate that the electric current distributions have similar characteristics when different ports are excited separately. Based on the above analysis, the initial guess can be constructed by extracting typical characteristic currents from the solution of a given excitation.

For the radiation problems of antenna arrays with $N$ antenna elements mounted on the platform, unknown coefficient vector $I$ of the system matrix equation (16) can be written as:

$$I = [(I^s)^T, (I_k^{sp})^T, (I_k^{wp})^T]^T, k = 1, 2, ..., N, \qquad (18)$$

where $I^s$ denotes unknown coefficient vector of the platform, $I_k^{sp}$ denotes unknown coefficient vector of the k-th antenna waveguide, and $I_k^{wp}$ denotes unknown coefficient vector of the k-th waveport. First, we calculate the solution of one antenna, when that antenna is active and other antennas are passive with an initial value set to zero. To get the most reasonable current distribution possible, usually we first calculate the center element in the array. Then, we extract the typical characteristic currents from the given solution and construct the initial value for the next excitation. The typical characteristic current is

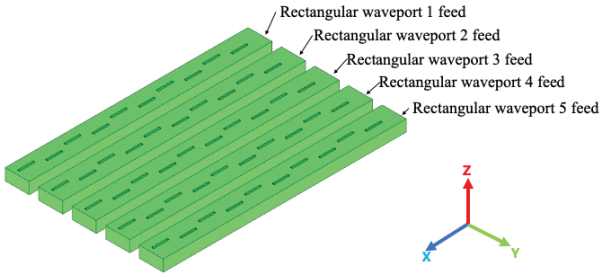


Fig. 2. Slot antenna array simulation model.

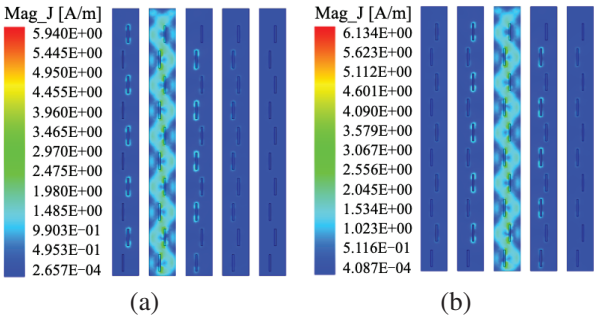


Fig. 3. (a) Electric currents on the surface of slot antenna array with the 2-feed rectangular waveport. (b) Electric currents on the surface of slot antenna array with the 3-feed rectangular waveport.

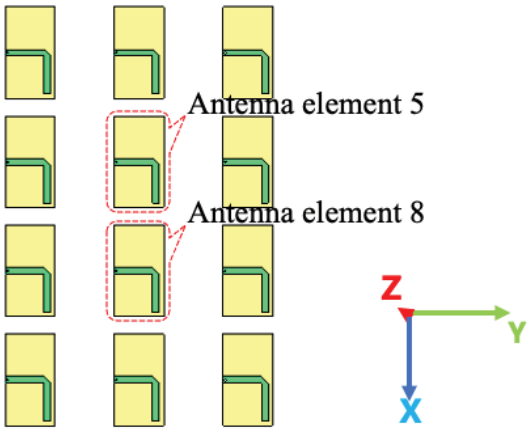


Fig. 4. A $3 \times 4$ dipole antenna array model.

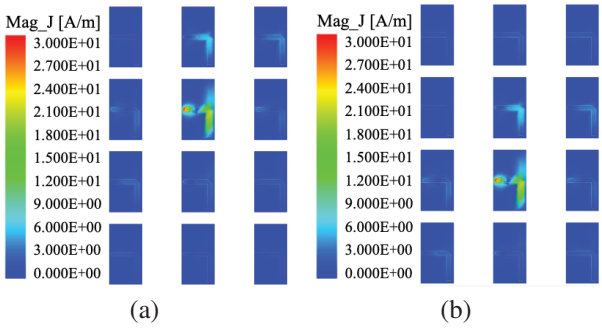


Fig. 5. (a) Electric currents on the surface of dipole antenna array with the 5-feed antenna element. (b) Electric currents on the surface of dipole antenna array with the 8-feed antenna element.

the set of currents of the array center element on the feed port, and the selection criterion can be referred to the S parameter obtained from the first calculation. The typical characteristic current vector $I_{typ}$ extracted from the

solution of the first excitation can be expressed as:

$$I_{typ} = [(I^s)^T, (I_m^{sp})^T, (I_m^{wp})^T]^T, \{m|S_{1,m} > T_s\}, \quad (19)$$

where $T_s$ denotes the threshold for extracting typical characteristic currents, and $T_s$ taken between $-20$ dB and $-30$ dB would be appropriate according to the engineering experience. The initial value for the next excitation can be constructed by using $I_{typ}$ and the antenna element in the relative position. For instance, we first obtain the solution when the 3rd antenna is active and other elements are passive, as shown in Fig. 2, and then extract the typical characteristic currents $I_{typ} = [(I^s)^T, (I_{typ}^{sp})^T, (I_{typ}^{wp})^T]^T$ from the solution. We take $T_s$ to be $-30$ dB in this case, and surface electric currents of the 2nd element, the 3rd element, and the 4th element are chosen to construct $I_{typ}$ according to the S parameters calculated from the first calculation. Hence, the $I_{typ}^{sp}$ and $I_{typ}^{wp}$ can be further expressed as $I_{typ}^{sp} = [0, (I_2^{sp})^T, (I_3^{sp})^T, (I_4^{sp})^T, 0]^T$ and $I_{typ}^{wp} = [0, (I_2^{wp})^T, (I_3^{wp})^T, (I_4^{wp})^T, 0]^T$. We construct the initial value for improving the algorithm convergence when the 2nd element is active, as shown in Fig. 6, by translating $I_{typ}$ according to the antenna element in the relative position, the initial value can be written as $I_{con} = [(I^s)^T, (I_{con}^{sp})^T, (I_{con}^{wp})^T]$, where $I_{con}^{sp} = [(I_2^{sp})^T, (I_3^{sp})^T, (I_4^{sp})^T, 0, 0]^T$ and $I_{con}^{wp} = [(I_2^{wp})^T, (I_3^{wp})^T, (I_4^{wp})^T, 0, 0]^T$. Following this process, we construct a new initial value when the 4th element is active and so on, until we reach the last antenna element.

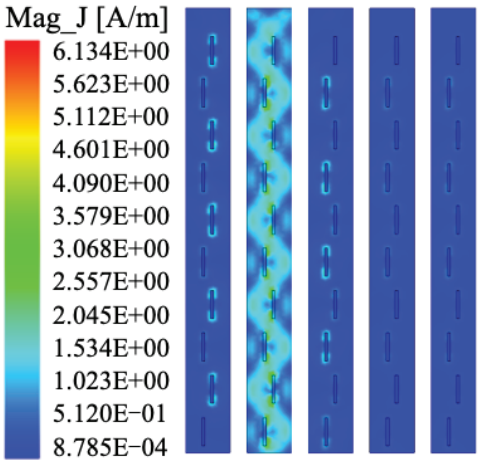


Fig. 6. Initial guess current obtained by reconstructing typical characteristic currents to improve the algorithm convergence when the 2nd antenna element is active.

## III. NUMERICAL EXAMPLES

In this section, two examples are performed on a workstation, with 96 CPU cores (Intel Xeon Gold 6248R CPU @ 3.00 GHz) and 1 TB memory. Mean-square-error (MSE) of the directivity is used to compare the numerical accuracy, which is defined as $(\sum_{n=1}^{N} |x_n - x_n^{ref}|^2)/N$, where $x_n$ denotes the $n$th actual result, and $x_n^{ref}$ denotes the $n$th reference result.

### A. Slot antenna array with dielectric radome

We demonstrate applicability and correctness of the proposed method through the analysis of slot antenna array with the dielectric radome as depicted in Fig. 7. The slot antenna array consists of 5 waveguides shown in Fig. 2. Operating frequency of the antenna is 3 GHz. Figure 8 (a) presents the calculated magnitude of $S_{11}$ parameters for single slot antenna, showing a very good agreement with the commercial software FEKO. The dielectric radome has an inner radius of 540 mm, an outer radius of 600 mm, and a height of 2000 mm. Relative permittivity of the radome material is 1.5 with a loss tangent of 0.001. The number of unknowns is 1 332 741, and the iterative tolerance is set to $1 \times 10^{-3}$. The computing resources with 48 CPU cores are used to perform this simulation, and the proposed method requires 586.44 GB memory and 20542.29 s computing time. Results of this simulation have been compared with the commercial software FEKO. Comparisons of the *xoz*-plane and *yoz*-plane radiation patterns obtained by superimposing magnitude and phase of the feed excitation of each antenna element using the superposition principle at 3 GHz are given in Fig. 9. Taking the FEKO solution as a reference,

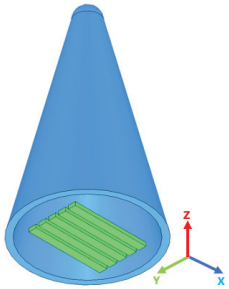


Fig. 7. Simulation model consisting of a waveguide slot antenna array and a dielectric radome.

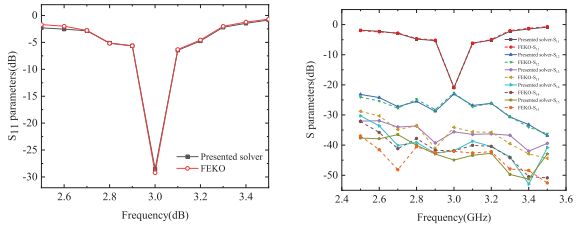


(a) (b)

Fig. 8. (a) Comparison of $S_{11}$ for the single waveguide slot antenna. (b) Comparison of $S$ parameters for the waveguide slot antenna array with dielectric radome.

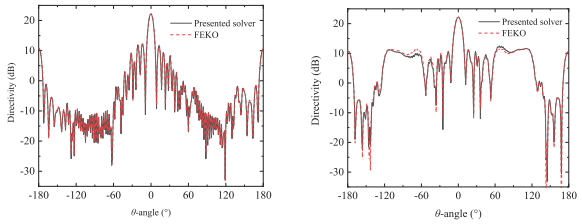


Fig. 9. Radiation patterns of the waveguide slot antenna array with dielectric radome in the (a) *xoz* plane and (b) *yoz* plane.

MSEs of the directivities in the *xoz*-plane and *yoz*-plane patterns are 0.226 and 0.604, respectively, which show good agreements. Figure 8 (b) shows the calculated magnitude of *S* parameters as a function of frequency, and the iteration steps required by different methods at 3 GHz for this example are given in Table 1. We can see that the conventional method is ineffective for solving the radiation problems, and the proposed method can reduce the computing time for the slot antenna array with radome by at least 50%, showing its effectiveness.

Table 1: Comparison of the iteration steps required by different methods at 3 GHz, when different elements are active. Here, * denotes the antenna element chosen in the first calculation

| Active Antenna Element | Initial Value = 0 | Conventional Method | Proposed Method |
|---|---|---|---|
| Antenna 1 | 74 | 74* | 33 |
| Antenna 2 | 76 | 74 | 32 |
| Antenna 3 | 74 | 76 | 74* |
| Antenna 4 | 77 | 76 | 32 |
| Antenna 5 | 73 | 74 | 31 |

### B. Dipole antenna array mounted on a ship

In the second example, an antenna array mounted on a conducting ship model is analyzed. The antenna array consists of $10 \times 10$ dipole antenna elements. This benchmark demonstrates that the proposed method can solve some challenging EM problems as well. The antenna element structure is shown in Fig. 10, and its operating frequency is 3 GHz. Relative permittivity of the dielectric substrate is 4.4 with a loss tangent of 0.02. The conducting ship, as shown in Fig. 11 (a), has a length of 22550 mm, a width of 3024 mm, and a height of 3734 mm. The model is discretized into 3 178 265 unknowns, which require huge hardware resources for

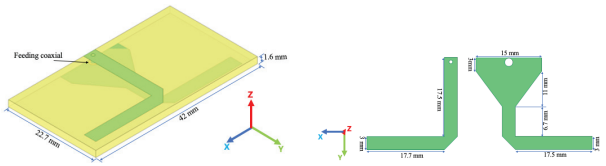


Fig. 10. Simulation model of the dipole antenna element. (a) Structure of the dipole antenna element. (b) Structure of the PEC patch.

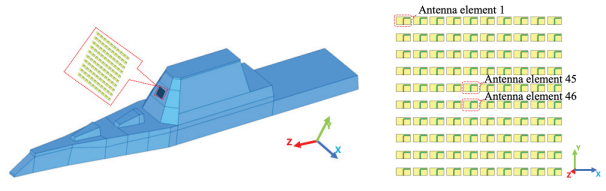


Fig. 11. Simulation model of the antenna array mounted on a conducting ship. (a) Simulation model of the conducting ship. (b) Simulation model of a $10 \times 10$-element antenna array.

the conventional MoM and FEM, and the iterative tolerance is set to $1 \times 10^{-3}$. The computing resources with 48 CPU cores are used to perform this simulation. Table 2 presents the hardware resource consumptions and computation times for the array with different cases where all the elements are fed with equal magnitude and same phase. Here, different cases lead to different number of unknowns. In Case 1, the proposed method requires only 319.8 GB memory and 5124.71 s computing time. Figure 12 shows 3-D radiation pattern of the antenna array at 3 GHz obtained by the proposed method, and Fig. 13 shows the near field distribution on the deck of ship. Figure 14 plots the transmission coefficients $S_{45,45}$, $S_{45,46}$, and $S_{45,1}$ in the frequency range of 2.5 GHz to 3.5 GHz (51 sampling points).

Table 2: Comparison of the hardware resource consumptions and computational times for the antenna array mounted on a conducting ship with different cases

| | Frequency (GHz) | Number of Unknowns | Memory Usage (GB) | Total Time (s) |
|---|---|---|---|---|
| Case 1 | 3 | 3 178 265 | 319.8 | 5124.71 |
| Case 2 | 4 | 5 399 778 | 512.9 | 6899.89 |
| Case 3 | 5 | 8 256 990 | 558.6 | 9884.58 |
| Case 4 | 6 | 11 749 772 | 836.2 | 14180.66 |

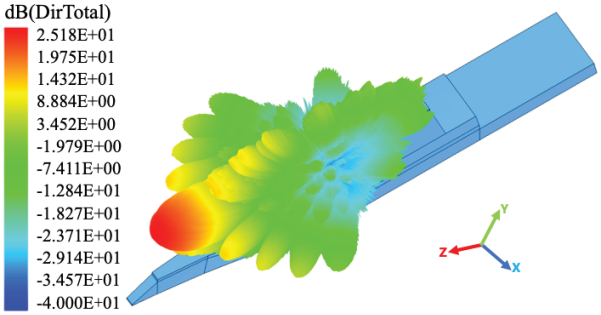


Fig. 12. 3-D radiation pattern of the $10 \times 10$-element dipole antenna array mounted on a ship at 3 GHz.

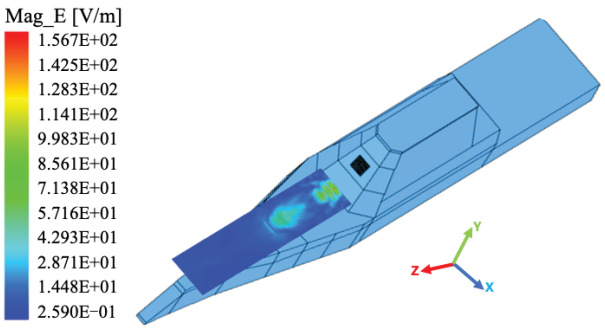


Fig. 13. Near field magnitude distributions on the deck of the ship at 3 GHz.

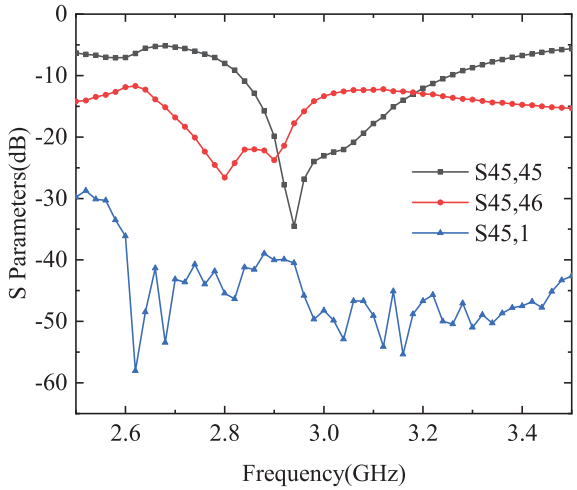


Fig. 14. *S* parameters of the $10 \times 10$-element dipole antenna array mounted on a ship.

## IV. CONCLUSION

In this paper, an efficient preconditioned MLFMA is presented for analyzing radiation and coupling characteristics of large-scale antenna arrays mounted on electrically large platforms. The waveport model is established for the MLFMA, and a preconditioner is designed for the radiation problems with waveports excitations, which improve the efficiency and convergence for analyzing large-scale antenna arrays. In addition, an initial guess construction method is proposed to effectively analyze coupling problems of the antenna arrays with multiple excitations. Numerical results revealed that the presented method can provide accuracy solutions, and reduce the iteration steps by at least 50% for the multi-excitation problems. Simulation of a $10 \times 10$-element antenna array mounted on a conducting ship validates computing power of the method. The proposed method can also be used for calculating the sum and difference beams patterns of antenna arrays with radomes, which also provides an effective method for accurately analyzing radiation and coupling characteristics of the airborne and shipborne antenna arrays.

## ACKNOWLEDGMENT

This work is supported in part by the Key Research and Development Program of Shaanxi under Grant 2022ZDLGY02-02, 2021GXLH-02, and 2023-ZDLGY-09, and in part by the Fundamental Research Funds for the Central Universities under Grant QTZX23018.

## REFERENCES

[1] C. Zhai, X. Zhao, Z. Lin, and Y. Zhang, "Integrated analysis and optimization of the large airborne Radome-Enclosed antenna system," *Applied Computational Electromagnetics Society Journal*, vol. 35, no. 10, pp. 1192-1199, Oct. 2020.

[2] Z. Lin, Y. Chen, X. Zhao, D. Garcia-Donoro, Y. Zhang, and H. Zhang, "Parallel higher-order method of moments with efficient Out-of-GPU memory schemes for solving electromagnetic problems," *Applied Computational Electromagnetics Society Journal*, vol. 32, no. 9, pp. 781-788, 2017.

[3] P. Zhou, Z. Zhang, and M. He, "Radiation pattern recovery of the Impaired-Radome-Enclosed antenna array," *IEEE Antennas and Wireless Propagation Letters*, vol. 19, no. 9, pp. 1639-1643, 2020.

[4] Y. Liu, M. Li, R. L. Haupt, and Y. J. Guo, "Synthesizing shaped power patterns for linear and planar antenna arrays including mutual coupling by refined joint rotation/phase optimization," *IEEE Transactions on Antennas and Propagation*, vol. 68, no. 6, pp. 4648-4657, 2020.

[5] D. S. Jones, "Field computation by moment methods," *Computer Journal*, vol. 1, no. 1, p. 1, 1969.

[6] J. Jin, "The finite element method in electromagnetics," *Journal of the Japan Society of Applied Electromagnetics*, vol. 1, no. 1, pp. 1-876, 1993.

[7] X. C. Wei and E. P. Li, "Wide-band EMC analysis of on-platform antennas using impedance-matrix interpolation with the moment method-physical optics method," *IEEE Transactions on Electromagnetic Compatibility*, vol. 45, no. 3, pp. 552-556, 2003.

[8] W. Zhao, L. Li, and L. Hu, "Efficient Current-Based hybrid analysis of wire antennas mounted on a large realistic aircraft," *IEEE Transactions on Antennas and Propagation*, vol. 58, no. 8, pp. 2666-2672, 2010.

[9] Z. Liu, X. Wang, and C. Wang, "Installed performance modeling of complex antenna array mounted on extremely large-scale platform using fast MoM-PO hybrid framework," *IEEE Transactions on Antennas and Propagation*, vol. 62, no. 7, pp. 3852-3858, 2014.

[10] L. Dai, Y. J. Xie, C. Zhang, and P. Wu, "Fast optimization of array antenna enclosed by asymmetric radome using AEP combined with enhanced HGAPSO," *Progress In Electromagnetics Research M*, vol. 103, no. 1, pp. 161-171, 2021.

[11] Q. Zhan, Y. Fang, M. Zhuang, M. Yuan, and Q. H. Liu, "Stabilized DG-PSTD method with nonconformal meshes for electromagnetic waves," *IEEE Transactions on Antennas and Propagation*, vol. 68, no. 6, pp. 4714-4726, 2020.

[12] Q. Zhan, Y. Wang, Y. Fang, Q. Ren, S. Yang, W. Yin, and Q. H. Liu, "An adaptive High-Order transient algorithm to solve large-scale anisotropic maxwell's equations," *IEEE Transactions on Antennas and Propagation*, vol. 70, no. 3, pp. 2082-2092, 2022.

[13] M. Li, Q. Wu, Z. Lin, Y. Zhang, and X. Zhao, "Novel parallelization of discontinuous galerkin method for transient electromagnetics simulation based on sunway supercomputers," *Applied Computational Electromagnetics Society Journal*, vol. 37, no. 7, pp. 795-804, 2022.

[14] I. Mahariq, I. H. Giden, S. Alboon, W. H. F. Aly, A. Youssef, and H. Kurt, "Investigation and analysis of acoustojets by spectral element method," *Mathematics*, vol. 10, no. 17, 2022.

[15] I. Mahariq and A. Erciyas, "A spectral element method for the solution of magnetostatic fields," *Turkish Journal of Electrical Engineering and Computer Sciences*, vol. 25, pp. 2922-2932, 2017.

[16] I. Mahariq, "On the application of the spectral element method in electromagnetic problems involving domain decomposition," *Turkish Journal of Electrical Engineering and Computer Sciences*, vol. 25, no. 2, pp. 1059-1069, 2017.

[17] I. Mahariq, H. Kurt, and M. Kuzuoğlu, "Questioning degree of accuracy offered by the spectral element method in computational electromagnetics," *Applied Computational Electromagnetics Society Journal*, vol. 30, no. 07, pp. 698-705, 2021.

[18] I. Mahariq, M. Kuzuoğlu, and I. H. Tarman, "On the attenuation of the perfectly matched layer in electromagnetic scattering problems with the spectral element method," *Applied Computational Electromagnetics Society Journal*, vol. 29, no. 09, pp. 701-710, 2021.

[19] I. Mahariq, I. Arpaci, and M. Kuzuoglu, "Analysis of scattering from perfect electric conducting cylinders by spectral element method," in *2015 Computational Electromagnetics International Workshop (CEM)*, pp. 1-2, Izmir, Turkey, 2015.

[20] I. Mahariq, I. Giden, H. Kurt, O. Minin, and I. Minin, "Strong electromagnetic field localization near the surface of hemicylindrical particles," *Optical and Quantum Electronics*, vol. 50, no. 423, pp. 1-8, 2017.

[21] J. Song, C.-C. Lu, and W. C. Chew, "Multilevel fast multipole algorithm for electromagnetic scattering by large complex objects," *IEEE Transactions on Antennas and Propagation*, vol. 45, no. 10, pp. 1488-1493, 1997.

[22] W. He, Z. Yang, X. Huang, W. Wang, M. Yang, and X. Sheng, "Solving electromagnetic scattering problems with tens of billions of unknowns using GPU accelerated massively parallel MLFMA," *IEEE Transactions on Antennas and Propagation*, vol. 70, no. 7, pp. 5672-5682, 2022.

[23] W.-J. He, Z. Yang, X.-W. Huang, W. Wang, M.-L. Yang, and X.-Q. Sheng, "High-Performance evaluation of the interpolations and anterpolations in the GPU-Accelerated massively parallel MLFMA," *IEEE Transactions on Antennas and Propagation*, vol. 71, no. 7, pp. 6231-6236, 2023.

[24] X. Chen, "An MLFMA-Based eigenmode theory for electromagnetic scattering analysis from electrically large and complex conducting objects," *IEEE Transactions on Antennas and Propagation*, vol. 71, no. 5, pp. 4254-4261, 2023.

[25] S. Rao, D. Wilton, and A. Glisson, "Electromagnetic scattering by surfaces of arbitrary shape," *IEEE Transactions on Antennas and Propagation*, vol. 30, no. 3, pp. 409-418, 1982.

[26] "MUMPS," https://mumps-solver.org, 2023.

[27] L. Gürel, T. Malas, and O. Ergül, "Preconditioning iterative MLFMA solutions of integral equations," in *2010 URSI International Symposium on Electromagnetic Theory*, pp. 810-813, 2010.

**Lei Yin** was born in Yinchuan, Ningxia, China, in 1995. He received the B.S. degree in electronic and information engineering from Xidian University, Xi'an, China, in 2017. He is currently pursuing the Ph.D. degree with Xidian University, Xi'an, China. His current research interests include computational electromagnetic, parallel computing, and electromagnetic radiation and coupling.

**Ning Ding** was born in Shanxi, China, in 1995. He received the B.S. degree in electronic and information engineering from Xidian University, Xi'an, China, in 2017. He is currently pursuing the Ph.D. degree with Xidian University, Xi'an, China. His current research interests include computational electromagnetic.

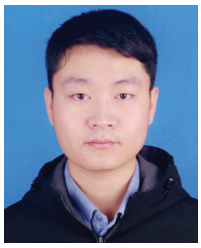

**Peng Hou** was born in Shaanxi, China, in 1995. He received the B.S. degree in electronic and information engineering from Xidian University, Xi'an, China, in 2017, where he is currently pursuing the Ph.D. degree. His current research interests include computational electromagnetic, parallel computing, and electromagnetic scattering.

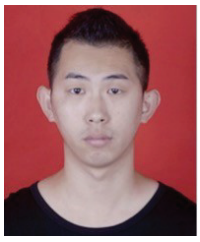

**Zhongchao Lin** was born in Hebei, China, in 1988. He received the B.S. and Ph.D. degrees from Xidian University, Xi'an, China, in 2011 and 2016, respectively. He joined Xidian University, in 2016, as a post doctoral fellow, where he was lately promoted as an associate professor.

His research interests include large-scale computational electromagnetic, scattering, and radiation electromagnetic analysis.

**Xunwang Zhao** was born in Shanxi, China, in 1983. He received the B.S. and Ph.D. degrees from Xidian University, Xi'an, China, in 2004 and 2008, respectively. He joined Xidian University, in 2008, as a faculty member, where he was lately promoted as a full professor. He was a visiting scholar with Syracuse University, Syracuse, NY, USA, from December 2008 to April 2009. As a principal investigator, he works on several projects, including the project of NSFC. His research interests include computational electromagnetic and electromagnetic scattering analysis.

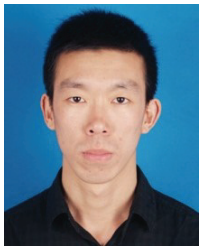

**Shugang Jiang** was born in Hebei, China, in 1985. He received the B.S. and Ph.D. degrees from Xidian University, Xi'an, China, in 2008 and 2016, respectively. He joined Xidian University, in 2019, as an associate researcher. His research interests include transient electromagnetic analysis.

**Yongchang Jiao** was born in Shanxi, China, in 1964. He received the Ph.D. degree in electrical engineering from Xidian University, Xi'an, China, in 1990. Since 1990, he has been with the institute of antennas and EM scattering, Xidian University where he is currently a Professor. From March to June 1996, he was a JSPS visiting priority-area research fellow with the University of Tsukuba, Tsukuba, Japan. From March to September 2002 he was a research fellow with the City University of Hong Kong, Hong Kong. His current research interests include antenna designs, computational electromagnetics, and optimization algorithms.

# Wideband Simultaneous Dual Circularly Polarized Phased Array Subarray with Scalable Characteristics for Satellite Communications

**Yunqi Zhang, Jiateng Chen, Xuping Li, Rui Yang, Qizheng Zhao, Xueyan Song, and Wenjia Zhou**

School of Electronic Engineering
Xi'an University of Posts & Telecommunications, Xi'an 710121, China
zhangyunqi@xupt.edu.cn, chenjiatengxian@163.com, lixuping@163.com, r18329386436@163.com, 201759789@qq.com, xysong6597@126.com, zhouwj1986@163.com

***Abstract –*** This paper proposes a budget-friendly, highly integrated, and low-profile wideband simultaneous dual circularly polarized phased array subarray with scalable characteristics for satellite communications. In order to achieve wideband, the antenna unit is not only fed by double-fed point probe contact, but also by electromagnetic coupling. Moreover, the dual circularly polarized radiation of the antenna unit is realized by a miniaturized 3 dB bridge-type phase-shift network. In addition, the phased array subarray uses metalized vias to reduce inter-element crosstalk, which effectively improves the active voltage standing wave ratio (VSWR) and beam steering characteristics. Also, the subarray has interchangeability and versatility, enabling convenient two-dimensional expansion to form a tile-type phased array antenna. Besides, the phased array subarray can be used to achieve two-dimensional $\pm 40^{\circ}$ beam scanning in both the azimuth and elevation planes. Within $\pm 40^{\circ}$ beam scanning, the active VSWR of the subarray is less than 2.5 in 9.55 - 14.35 GHz (40.17%). At 12.1 GHz, the two-dimensional gain decreases by less than 2.1 dB and 1.95 dB, respectively. The proposed antenna exhibits good performance in terms of matching and beam steering characteristics, which make it suitable for use in future 5G/6G phased array antenna systems.

***Index Terms –*** Modular, phased array, simultaneous dual circular polarization, wideband.

## I. INTRODUCTION

Satellite communication presents a practical approach for worldwide coverage and universal connectivity. The Low-Earth orbit (LEO) satellites, operating in orbits ranging from 200 to 2000 km, necessitate continuous tracking. Thus, phased array technology that is affordable, highly integrated, and low-profile is desperately needed [1–3]. In addition, dual-circularly polarized antenna not only has the advantages of anti-attenuation and anti-multipath interference, but also the aperture efficiency can be improved and the capacity of the communication system can be increased [4–7].

The phased array antenna possesses the characteristics of flexible beam control, fast response speed, and high positioning accuracy [8]. Regrettably, the conventional large-scale phased array is typically built as a whole array, entailing an arduous design process. Also, it has high cost and is not easy to use and maintain. This restricts the comprehensive promotion and large-scale application of phased array technology.

In [9], a dual-circularly polarized antenna is composed of a dual-band monopole antenna and a polarization rotation artificial magnetic conductor (PRAMC). Its application scenarios and implementation forms are novel, yet not wide enough (about 10%). Also, the implementation of dual-circular polarization can also be viably achieved through the employment of PIN diodes, such as [10]. The antenna switches the long axis and short axis of the cross slot by changing the on/off state of the diode. This achieves a switch between left-hand circularly polarized (LHCP) and right-hand circularly polarized (RHCP), with a relative bandwidth of 27.6%. Nevertheless, the regulation of diodes necessitates the integration of supplementary biasing circuits. This not only compounds the intricacy of antenna design but also gives rise to electromagnetic compatibility (EMC) concerns. In addition, an antenna based on a small-size, low-profile, F-shaped waveguide slot circular polarizer is reported in [11]. The height of the circular polarizer is only 1/6 wavelength and the width is about 2/5 wavelength. For all that, the structure of the F-shaped circular polarizer is complex, the processing is difficult, and the relative bandwidth is less than 10%. The metasurface antennas, characterized by their beam-scanning properties and inherent benefits of affordability and ease of conformability, have emerged as a vigorously researched topic in current scientific investigations [12–14]. Also, the metasurface circular polarization patch

*Submitted On: November 10, 2023*
*Accepted On: April 2, 2024*



https://doi.org/10.13052/2024.ACES.J.390310

antenna phased arrays [15] were discussed, though the metasurface antenna requires an independent feed power to excite, and the overall profile size is high.

In this paper, a budget-friendly, highly integrated and low-profile wideband simultaneous dual circularly polarized phased array subarray with scalable characteristics is designed for satellite communication. The proposed antenna profile, characterized by a mere height of 0.15 $\lambda_0$ (free-space wavelength), operates within the Ku-band and is inherently conformal. By using frequency-division-multiple-access (FDMA) technology, LHCP wave and RHCP wave can be radiated simultaneously. The proposed antenna can significantly enhance the aperture efficiency, lower costs, and increase communication system capacity, making it suitable for future satellite communication applications. In addition, based on the modular phased array subarray with dual-circular polarization, the open and scalable design facilitates convenient two-dimensional expansion to form a tile-type phased array antenna.

## II. PHASED ARRAY ANTENNA UNIT ANALYSIS AND DESIGN

The circular microstrip antenna works in the main mode $TM_{01}$, and the theoretical patch radius $R$ of the circular microstrip antenna can be calculated to be 3.91 mm by theoretical empirical formulas (1) and (2). Meanwhile, considering the influence of parasitic patches, the specific size needs to be optimized and adjusted. The configuration of the phased array antenna unit optimized by multiple iterations is depicted in Fig. 1. The optimized process is from prototype 1 of single-stage 3 dB bridge network with single-layer microstrip patch to prototype 2 of multi-stage bridge phase-shifting network with single-layer microstrip patch, and then to the existing prototype 3 of miniaturized bridge phase-shifting network with double-layer microstrip patch.

$$R = \frac{K}{\left[1 + \frac{2h}{\pi\varepsilon_r K}\left\{\ln\left(\frac{\pi K}{2h}\right) + 1.7726\right\}\right]^{1/2}}. \quad (1)$$

$$K = \frac{87.94}{f_r\sqrt{\varepsilon_r}}. \quad (2)$$

$f_r$ is the operating frequency (GHz), $\varepsilon_r$ is the relative dielectric constant, and the unit of $R$ is mm.

As shown in Figs. 1 (a) and (b), the antenna unit consists of five layers (layer 1, layer 2, layer3, phase-shifting network, and layer 4), which are printed on four square dielectric substrates and thickness are $Hsub_1$, $Hsub_2$, $Hsub_3$, $Hsub_4$. The use of thicker dielectric substrates 1 and 2 is effective for bandwidth expansion. Conversely, the selection of thinner dielectric substrates 3 and 4 serves to effectively reduce the width of low-impedance lines, thereby facilitating routing and miniaturization of the phase-shifting network. The substrates are RT/Duroid 5880 ($\varepsilon_r$ = 2.2, tan $\delta$ = 0.0009).

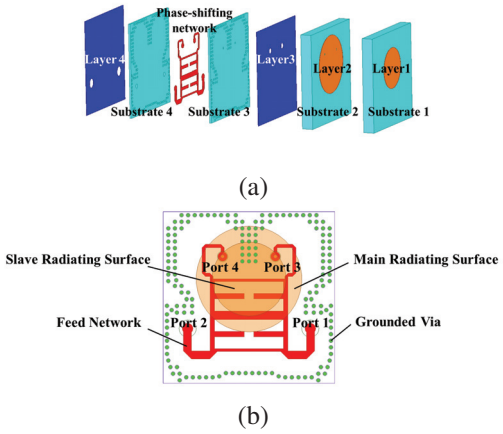


Fig. 1. Geometry of the proposed antenna unit: (a) 3D view and (b) perspective view.

Layers 1 and 2 are circular patches with different radii. As can be observed, layer 1 serves the function of bandwidth broadening and gain enhancement. A wideband 3 dB bridge miniaturized by T-type equivalent method composes the phase-shifting network, which is a stripline structure. The phase-shifting network and layer 2 are connected through a metalized vias. Layers 3 and 4 concurrently fulfill the dual role of serving as reflectors, thereby contributing to the reduction of backlobes in the antenna and simultaneously enhancing the gain of the main lobe.

Theoretically, the amplitude and phase difference required for circular polarization can be provided by the 3 dB bridge network through reasonable design. A phase difference of 90° and -90° exists between port 3 and port 4. When port 1 and port 2 are separately fed with power, the antenna unit correspondingly generates LHCP and RHCP. Ports 1 and 2 are independently connected, with the amplitudes and phases of the excitations generated by the antenna unit being actively controlled by the transmitter and receiver. If a signal with the same frequency as the LHCP port and the RHCP port is excited at the same time, a linear polarization (LP) wave will be synthesized. To achieve simultaneous dual circular polarization, frequency-division-multiple-access (FDMA) technology is employed, allowing signals of different frequencies to be simultaneously excited at both the LHCP port and the RHCP port.

The designed phase-shifting network is capable of stably delivering excitation signals across a wide bandwidth, as depicted in Fig. 2. Figure 2 (a) shows that the simulated -10 dB impedance bandwidth of phase-shifting network ranges from 8.3 to 14.7 GHz (55.7%).

Meanwhile, the insertion loss is less than 3.65 dB, and the difference between them is less than 0.8 dB from 8.8 to 15 GHz (52.1%). Furthermore, it can be seen from Fig. 2 (b) that the phase difference of the phase-shifting network falls within the range of 85.2° to 95.1°.

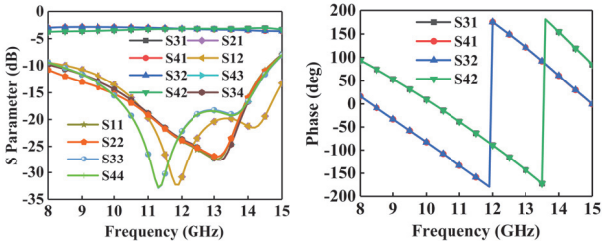


(a) (b)

Fig. 2. Results of phase-shifting network simulation: (a) S parameter and (b) phase.

In Fig. 3 (a), it is observed that the -10 dB impedance bandwidth of the antenna unit covers the range from 8.15 to 14.95 GHz (58.9%), exhibiting preferable matching and isolation characteristics. In addition, the majority frequency band demonstrates stable and high gain with low axial ratio (AR), as shown in Fig. 3 (b). It is noteworthy that the gain and axial ratio curves for LHCP and RHCP demonstrate a commendable level of consistency, an outcome attributed to the inherent high degree of symmetry in the proposed structure.

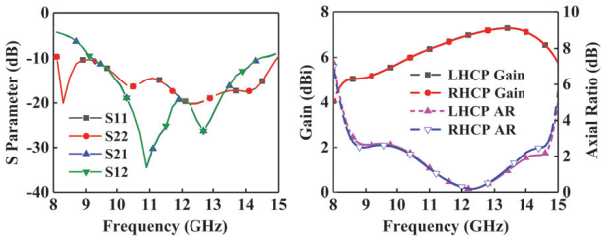


(a) (b)

Fig. 3. Simulation results of the phased array antenna unit: (a) S parameter and (b) gain and axial ratio.

## III. ANALYSIS AND DESIGN OF MODULAR PHASED ARRAY SUBARRAYS

Moreover, a modular phased array subarray is developed by employing the aforementioned wideband dual circularly polarized antenna unit. The adoption of a modular design leads to reduced cable usage, thereby enhancing the reliability and maintainability of product. Upon the occurrence of a fault and subsequent identification of the problematic component, a swift replacement of the modular subarray serves as the remedy to rectify the issue.

The anticipated beam scanning range of the proposed antenna is ± 40°. Nevertheless, the presence of grating lobes not only diminishes antenna gain but also passively contributes to inaccurate assessments in target localization and direction finding. To prevent the emergence of grating lobes, formula (3) can be used to calculate the theoretical maximum inter-element spacing of 14.33 mm [16]. An ideal inter-element spacing would be 13 mm, taking into account different radiative indices like gain and grating lobe, as well as structural factors like feed network wiring.

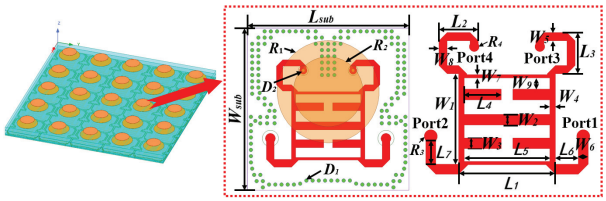


(a) (b)

Fig. 4. Modular phased array subarrays: (a) 3D view and (b) perspective view of the antenna unit and the optimized phase shift network.

Table 1: Optimized design parameters (in millimeters)

| | | | | | |
|---|---|---|---|---|---|
| $W_{sub}$ | 13 | $R_1$ | 4.10 | $L_4$ | 2.25 |
| $W_1$ | 5.47 | $R_2$ | 2.80 | $L_5$ | 5.21 |
| $W_2$ | 0.65 | $R_3$ | 0.4 | $L_6$ | 1.38 |
| $W_3$ | 0.65 | $R_4$ | 0.34 | $L_7$ | 1.44 |
| $W_4$ | 0.35 | $D_1$ | 0.3 | $Hsub_1$ | 1.524 |
| $W_5$ | 0.5 | $D_2$ | 0.25 | $Hsub_2$ | 1.524 |
| $W_6$ | 0.62 | $L_{sub}$ | 13 | $Hsub_3$ | 0.254 |
| $W_7$ | 0.2 | $L_1$ | 5.90 | $Hsub_4$ | 0.254 |
| $W_8$ | 0.5 | $L_2$ | 2.40 | | |
| $W_9$ | 0.78 | $L_3$ | 2.49 | | |

$$d \leq \frac{\lambda}{1+|\sin\theta_s|}. \tag{3}$$

$\lambda$ is the wavelength and $\theta_s$ is the maximum scanning angle of the antenna.

The phased array subarray, as depicted in Fig. 4, is composed of the aforementioned antenna units. The optimized design parameters are shown in Table 1 of the antenna unit. The utilization of scalable concepts enables an easy expansion of the low-profile, wideband, dual-circularly polarized modular subarray into arbitrarily scaled tile-type two-dimensional phased array antennas.

Too small unit spacing will produce serious coupling phenomena. Also, the phase-shifting network with stripline structure is prone to resonance. To mitigate

coupling interference among individual antenna units, a cavity-like structure can be effectively established by strategically positioning metallized ground vias around the phase-shifting network and radiating elements. The active voltage standing wave ratio (VSWR) characteristics of wideband dual-circularly polarized modular phased array subarrays can be effectively improved through this approach. In addition, double-layered metallized ground vias can be strategically placed in certain regions to further reinforce the formation of a cavity-like structure for more effective suppression of coupling interference.

As shown in Fig. 5, it can be discerned that the modular phased array subarray exhibits commendable matching characteristics within a beam scanning range of ±40°. The active VSWR in both the azimuth and elevation planes remains below 2.5 across a frequency range spanning from 9.55 to 14.35 GHz (40.17%). During two-dimensional scanning of the subarray, the gain decrease is observed to be less than 3.25 dB from 9.3 to 14.2 GHz. Among them, at 12.1 GHz, the gain reduction in the azimuth and elevation planes is less than 2.1 dB and 1.95 dB, respectively. From 10 to 14.2 GHz (34.71%), the AR of the two-dimensional scan performed by the subarray stays below 3 dB. The performance of the wideband, dual-circularly polarized modular phased array subarray, as evidenced by the presented data, passively demonstrates its excellence in maintaining consistent and stable radiation of circularly polarized waves.

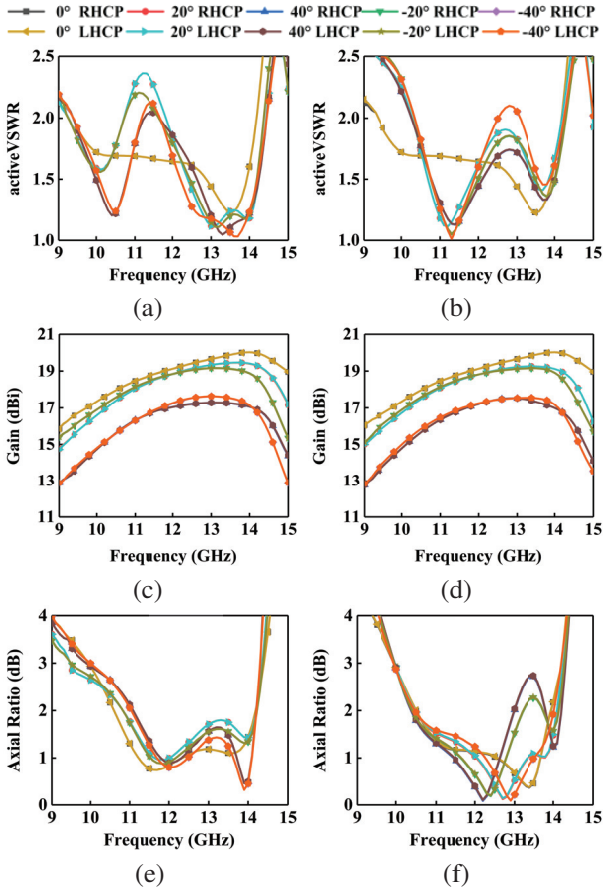


Fig. 5. Simulation results of the modular subarray: (a) Azimuth plane active standing wave, (b) elevation plane active standing wave, (c) azimuth plane gain, (d) elevation plane gain, (e) azimuth plane axial ratio, and (f) elevation plane axial ratio.

## IV. PROCESS AND MEASUREMENT

To validate the effectiveness of the design proposed in this paper, the subarray of the modular phased array antenna was fabricated according to the dimensions provided in the preceding text. This includes 5×5 wideband dual circularly polarized phased array antenna elements. The picture of the processed subarray antenna and its measurement environment is presented in Fig. 6 (a). To verify the performance of the proposed antenna, a transmitter and receiver platform covering the Ku-band in Fig. 6 (b) is used. After determining the target scanning angle $\theta$ of antenna array, the phase difference $\varphi$ is fed between the adjacent antenna units, and the beam of the array antenna can be scanned to the target scanning angle $\theta$. Among them, the phase difference $\varphi$ is calculated by formula (4), and provided by the phase shifter shown in Fig. 6 (b), and $d$ is the antenna element spacing. If the target scanning angle $\theta$ is 30°, the unit spacing $d$ is 13 mm, and the frequency $f$ is 12.1 GHz, the phase difference $\varphi$ can be calculated to be 94.38°. Other cases are similar.

$$\varphi = \frac{2\pi}{\lambda} d \sin\theta. \tag{4}$$

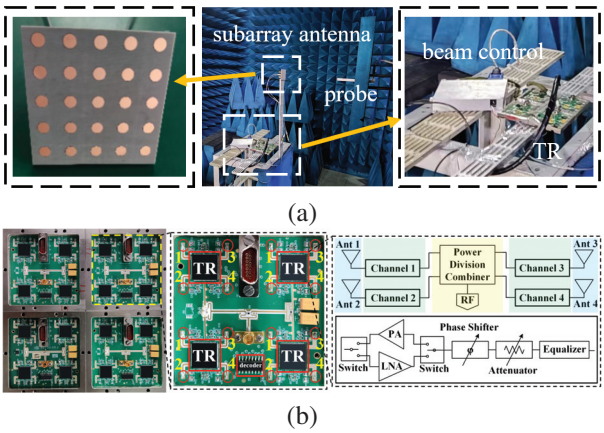


Fig. 6. Process and measure: (a) Processed of subarray antenna and measurement environment and (b) transmitter and receiver.

Table 2: Comparison between reported works and proposed antenna

| Ref. | Type of Unit | Polar | Scanning Angle and Dimension | Size ($\lambda_0{}^3$) | AR Bandwidth (GHz) | Gain (dBic) | Impedance Bandwidth (GHz) | Diode |
|---|---|---|---|---|---|---|---|---|
| [9] | Monopole and PRAMC | Dual circular | 1-D | 0.72×0.72×0.06 | 3.5/5.8 (2%/8.2%) | 6.6/ 7.2 | 3.5/5.8 (11.7%/9.1%) | No |
| [10] | Microstrip antenna | Dual circular | - | 0.4×0.4×0.04 | 2.0-2.7 (29.8%) | 5.95 | 1.97-2.72 (32%) | Yes |
| [11] | Waveguide slot antenna | Single circular | ±60°/1-D | 8×46.08×1.46 | Ka (less than 10%) | 35.9 | Ka (less than 10%) | No |
| [12] | Metasurface antenna | Single circular | ±42°/1-D | 0.53×17.07×0.155 | 24.15-27.5 (13.4%) | 19.3 | 22.5-27.5 (20%) | No |
| [15] | Metasurface antenna | Single circular | ±30°/2-D | 4.08×4.08 | 27.3-31.3 (13.65%) | - | 28-31 (10.177%) | No |
| This work | Stacked microstrip antenna | Dual circular | ±40°/2-D | 15.73×15.73×0.15 | 10-14.2 (34.71%) | 32.77 | 9.55-14.35 (40.17%) | No |

Also, the antenna and the transmitter and receiver are connected by RF cables. Based on this subarray, the results of synthesizing an array composed of 6×6 such subarrays have been derived. Due to the large array size, the method based on the array factor approach was employed to measure the array factor of the center element of the modular phased array subarray for obtaining the scanning characteristics of the phased array beam. The radiation characteristics of a tile-type two-dimensional phased array antenna can be obtained by integrating the directional patterns of each element and gradually adjusting their phases using analysis software.

The measured normalized gain patterns in the azimuth and elevation planes for the central antenna unit are respectively presented in Figs. 7 (a) and (b), using the vector network analyzer Ceyear 3656D and the planar near-field microwave anechoic chamber for measurement. It can be discerned from Fig. 8 that the return loss curves for the LHCP port and the RHCP port exhibit commendable consistency, with a -10 dB return loss bandwidth spanning from 9.5 to 14.3 GHz (40.34 %).

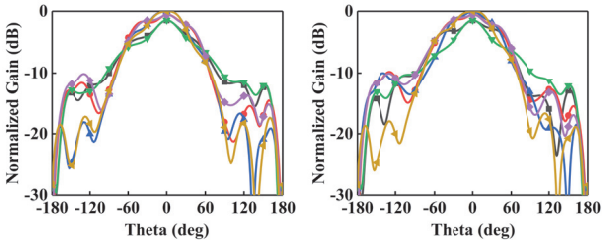


(a) (b)

Fig. 7. (a) Azimuth plane measured unit normalized gain curve and (b) elevation plane measured unit normalized gain curve.

According to the measured radiation parameters of the antenna element in the array, the normalized gain scanning curve of the tiled two-dimensional phased array antenna can be obtained by using the pattern in the array [17], as shown in Figs. 9 and 10.

Furthermore, the gains of the scanning beams across the azimuthal and elevational dimensions are individually presented in Tables 3 and 4, respectively. It can be seen that the antenna exhibits good directionality and

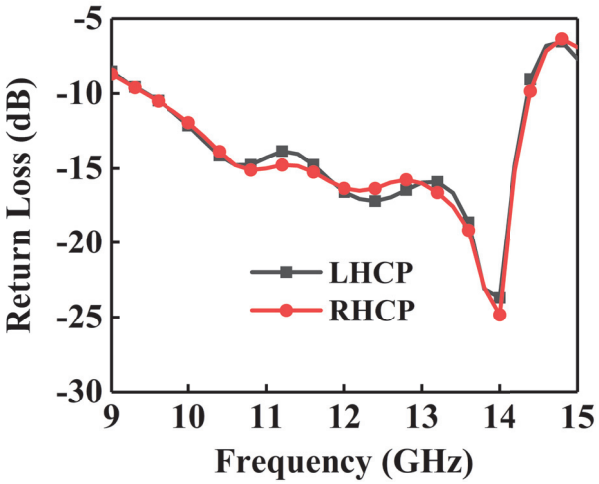


Fig. 8. Return loss of the central element of process of subarray antenna.

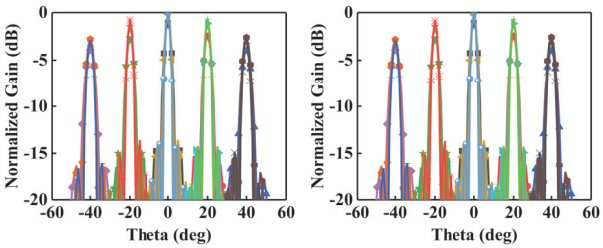


Fig. 9. Normalized gain scanning curves for azimuthal two-dimensional phased array antennas: (a) LHCP and (b) RHCP.

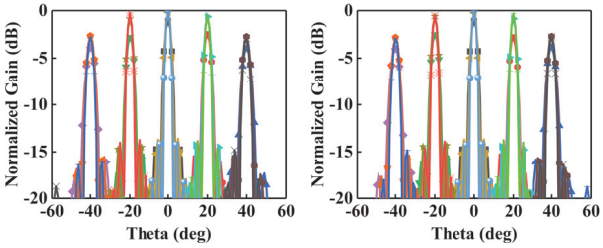


Fig. 10. Normalized gain scanning curves for elevating two-dimensional phased array antennas: (a) LHCP and (b) RHCP.

scanning characteristics, enabling phased scanning in the operational frequency range of $\pm 40^\circ$ in two dimensions.

The detailed performance comparison between the previously developed antenna prototype and the recently reported related works is presented in Table 2. In contrast to the monopole, PRAMC, microstrip and waveguide slot antenna in [9], [10], and [11], our prototype features wideband, simultaneously dual-circularly polarized, and scalable. Besides, compared with the metasurface antennas in [12] and [15], our prototype not only has almost the same or wider scanning range, but also achieves dual circular polarization. Most importantly, the prototype has a wider impedance bandwidth and axial ratio bandwidth,

Table 3: The gain of the scanning beam for azimuthal dimension (dBic)

| S.A.* | Gain for Azimuthal Dimension LHCP/RHCP | | |
|---|---|---|---|
| | 10 GHz | 12.1 GHz | 14.2 GHz |
| -40° | 28.03 / 28.09 | 30.71 / 30.7 | 30.69 / 30.86 |
| -20° | 29.65 / 29.52 | 31.69 / 31.67 | 32.17 / 32.05 |
| 0° | 30.84 / 30.88 | 32.76 / 32.74 | 33.94 / 33.96 |
| 20° | 29.51 / 29.49 | 31.8 / 31.85 | 32.26 / 32.23 |
| 40° | 27.95 / 27.9 | 30.66 / 30.68 | 30.75 / 30.83 |

*: S.A. represents the beam scanning angle.

Table 4: The gain of the scanning beam for elevating dimension (dBic)

| S.A.* | Gain for Elevating Dimension LHCP/RHCP | | |
|---|---|---|---|
| | 10 GHz | 12.1 GHz | 14.2 GHz |
| -40° | 28.04 / 27.93 | 30.82 / 30.87 | 30.78 / 30.84 |
| -20° | 29.52 / 29.46 | 32.06 / 32.13 | 32.35 / 32.2 |
| 0° | 30.85 / 30.89 | 32.77 / 32.73 | 33.93 / 33.91 |
| 20° | 29.43 / 29.47 | 32.29 / 32.18 | 32.22 / 32.09 |
| 40° | 27.94 / 28.02 | 30.91 / 30.86 | 31.01 / 30.96 |

*S.A. represents the beam scanning angle.

and its outstanding wideband performance is achieved in a compact size.

## V. CONCLUSION

In this paper, a wideband simultaneous dual circularly polarized phased array subarray with scalable characteristics is designed for satellite communication. The subarray exhibits inherent advantages such as a wide operational bandwidth, dual-circular polarization capability, low profile, and ease of maintenance. It has interchangeability and versatility, allowing for rapid two-dimensional expansion and assembly into a tile-type phased array. This approach inherently enables the passive reduction of design complexity, enhancement of research and development efficiency, shortening of manufacturing cycles, and minimization of production costs. The wideband dual circularly polarized modular phased array subarray with excellent performance index is designed, simulated, fabricated and measured by using the wideband dual circularly polarized antenna unit. It can achieve two-dimensional $\pm 40^\circ$ phase-scanned scanning within a wide frequency band while radiating LHCP waves and RHCP waves simultaneously. Moreover, it possesses the characteristic of maintainability, such that upon the occurrence of a malfunction, once the fault location is swiftly identified, repair and replacement can promptly ensue. This has positive significance for engineering applications and aligns with the future trends of wideband, arrayed, versatile, and miniaturized phased array technology. It also has important application value in the fields of telemetry, reconnaissance and satellite communication.

## ACKNOWLEDGMENT

This work is supported in part by Key Research and Development Program of Shaanxi (2021GY-049), Xi'an Science and Technology Plan Project (21XJZZ0071), Scientific Research Program Funded by Shaanxi Provincial Education Department (22JC058), Shanxi province science and technology department (2021ZDLGY08-03), and Natural Science Basic Research Program of Shaanxi (2022JQ-699).

## REFERENCES


[1] G. Gültepe, T. Kanar, S. Zihir, and G. M. Rebeiz, "A 1024-element ku-band SATCOM phased-array transmitter with 45-dBW single-polarization EIRP," *IEEE Transactions on Microwave Theory and Techniques,* vol. 69, no.9, pp. 4157-4168, 2021.

[2] S. Rao, M. Tang, and C.-C. Hsu, "Multiple beam antenna technology for satellite communications payloads," *Applied Computational Electromagnetics (ACES) Journal*, vol. 21, no. 3, pp. 353-364, 2022.

[3] C.-N. Chen, Y.-H. Lin, L.-C. Hung, T.-C. Tang, W.-P. Chao, C.-Y. Chen, P.-H. Chuang, G.-Y. Lin, W.-J. Liao, Y.-H. Nien, and W.-C. Huang, "38-GHz phased array transmitter and receiver based on scalable phased array modules with endfire antenna arrays for 5G MMW data links," *IEEE Transactions on Microwave Theory and Techniques,* vol. 69, no. 1, pp. 980-999, 2021.

[4] L.-H. Ye, Y.-J. Li and D.-L. Wu, "Dual-wideband dual-polarized dipole antenna with t-shaped slots and stable radiation pattern," *IEEE Antennas and Wireless Propagation Letters*, vol. 21, no. 3, pp. 610-614, 2022.

[5] Q. Xu, S.-B Liu, Y.-X Wang, L. Song, and H. Cao, "Dual-polarized antenna based on printed dipole and microstrip patch," *Journal of Electronics & Information Technology*, vol. 39, no. 7, pp. 1764-1768, 2017.

[6] M. Kanagasabai, P. Sambandam, M. G. N. Alsath, S. Palaniswamy, A. Ravichandran, and C. Girinathan, "Miniaturized circularly polarized UWB antenna for body centric communication," *IEEE Transactions on Antennas and Propagation*, vol. 70, no. 1, pp. 189-196, 2022.

[7] Q.-C. Ye, J.-L. Li, and Y.-M. Zhang, "A circular polarization-reconfigurable antenna with enhanced axial ratio bandwidth," *IEEE Antennas and Wireless Propagation Letters*, vol. 21, no. 6, pp. 1248-1252, 2022.

[8] J. Zhang and H. Wu, "Simultaneous transmit and receive phased array system architecture and prototype comprehensive verification," *Applied Computational Electromagnetics (ACES) Journal*, vol. 37, no. 12, pp. 1257-1264, 2023.

[9] H.-C. Yang, X.-Y. Liu, Y. Fan, and L.-P. Xiong, "Dual-band textile antenna with dual circular polarizations using polarization rotation AMC for off-body communications," *IEEE Transactions on Antennas and Propagation*, vol. 70, no. 6, pp. 4189-4199, 2022.

[10] M. Li, Z.-H. Zhang, M.-C. Tang, L. Zhu, and N.-W. Liu, "Bandwidth enhancement and size reduction of a low-profile polarization-reconfigurable antenna by utilizing multiple resonances," *IEEE Transactions on Antennas and Propagation*, vol. 70, no. 2, pp. 1517-1522, 2022.

[11] B. Liu, S.-M. Gu, M.-X. Meng, K.-Y. Shi, K.-Q. Ding, L. Xu, Y.-T. Yang, and Y.-L. Chen, "A circularly polarized wide-scan waveguide slot phased array antenna with high efficiency for ka band application," *Journal of Electronics & Information Technology*, vol. 43, no. 6, pp. 1630-1636, 2021.

[12] Y.-S. Zhang, W. Hong, Z.-D. Ding, L. Yang, C. Zhu, and Y. Hu, "Circularly polarized metasurface phased array antenna system with wide axial-ratio beamwidth for LEO mobile satellite communication," *IEEE Transactions on Antennas and Propagation*, vol. 71, no. 6, pp. 4823-4833, 2023.

[13] S. Tiwari, A. K. Singh, A. K. Poddar, U. L. Rohde, and A. Dubey, "Active beamsteerable digital metasurface lens antenna for millimeter-wave applications," *IEEE Antennas and Wireless Propagation Letters ( Early Access )*, 2023.

[14] C. Ni, Z.-K. Yu, L. Zhang, and Z.-X. Zhang, "A wide-band circularly polarized and beam deflection antenna based on two metasurfaces," *IEEE Antennas and Wireless Propagation Letters (Early Access )*, 2023.

[15] Z.-N. Chen, X.-M. Qing, X.-L. Tang, W. Liu, and R.-L. Xu, "Phased array metantennas for satellite communications," *IEEE Communications Magazine*, vol. 60, no. 1, pp. 46-50, 2022.

[16] C. A. Reddy, K. V. Janardhanan, K. K. Mukundan, and K. S. V. Shenoy, "Concept of an interlaced phased array for beam switching," *IEEE Transactions on Antennas and Propagation*, vol. 38, no. 4, pp. 573-575, 1990.

[17] D. M. Pozar, "A relation between the active input impedance and the active element pattern of a phased array," *IEEE Transactions on Antennas and Propagation*, vol. 51, no. 9, pp. 2486-2489, 2003.


**Yunqi Zhang** was born in Bao-Tou, Inner Mongolia, China. He received the master's degree and the Ph.D. degree in micro-electronics from Xidian University in 2012 and 2015, respectively. He is currently working in the Xi'an University of Posts & Telecommunications. His research interests include CP antennas, OAM, omnidirectional antennas, and phase array antennas.

**Jiateng Chen** is with the School of Electronic Engineering, Xi'an University of Posts & Telecommunications, Xi'an 710121, China. His main research interests include phased array antennas and CP antennas.

**Xuping Li** was born in Xi'an, Shanxi, China in 1981. He received the Ph.D. degree in electromagnetic fields and microwave technology from Xidian University, Xi'an, China, in 2015. His research interests are antenna theory and engineering.

**Rui Yang** is with the School of Electronic Engineering, Xi'an University of Posts & Telecommunications, Xi'an 710121, China. Her main research interests are array antennas and vortex electromagnetic waves.

**Qizheng Zhao** is with the School of Electronic Engineering, Xi'an University of Posts & Telecommunications, Xi'an 710121, China. His current research interests are signal processing and CP antennas.

**Xueyan Song** was born in Henan Province, China, 1989. She received the Ph.D. degree from Xidian University in 2018. Her research interests include artificial magnetic conductors, low RCS antennas, low-profile antennas, frequency selective surfaces, and reflector antennas.

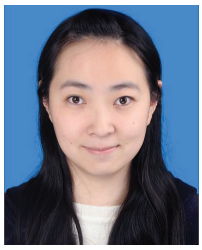

**Wenjia Zhou** was born in Xi'an, Shanxi, China in 1986. She received the Ph.D. degree in control science and engineering from Northwestern Polytechnical University, Xi'an, China, in 2017. Her main research interests are antenna theory and engineering, and microwave signal delay and simulation.

# A Dual Circularly Polarized Ultrawideband Rectenna with High Efficiency for Wireless Energy Harvesting

**Jian Liu and Jun Yi Li**

School of Integrated Circuits
Guangdong University of Technology, Guangzhou, 510006, China
xzliujian@gdut.edu.cn, 18374203633@163.com

***Abstract –*** This paper presents an ultrawideband dual circularly polarized (CP) rectenna for wireless energy harvesting (WEH) applications. It is mainly composed of a dual CP antenna and an ultrawideband rectifier. The receiving antenna is fed by a coplanar waveguide (CPW) and it has two input ports. The proposed ultrawideband rectifier has a two-cascaded voltage doubler configuration. This configuration means the proposed rectifier's input impedance has less sensitivity to frequency variation. Thus, a wide bandwidth can be achieved. For validation, a prototype is designed, fabricated and measured. The measured results show that the axial ratio (AR) bandwidth of the proposed rectenna is from 1.35 to 3.10 GHz (for AR $<$3 dB). In this frequency range, the rectenna's power conversion efficiency (PCE) is higher than 55%. These results indicate that the proposed rectenna is highly efficient and suitable for wideband high-efficiency WEH systems.

***Index Terms –*** Coplanar waveguide (CPW), dual circularly polarized antenna, ultra-wideband rectifier, wireless energy harvesting (WEH).

## I. INTRODUCTION

In recent years, the wireless energy harvesting (WEH) technique has attracted more and more attention as this technology can be employed to extend the battery life of some low-power electronic devices, such as wireless sensor networks (WSN) [1], RFID systems [2], and implantable medical devices [3]. Rectenna is a key component of a WEH system. Its main function is to receive the radio frequency (RF) electromagnetic energy and convert it into direct current (DC) power [4].

One of the most important performance parameters of the rectenna is power conversion efficiency (PCE). In order to improve PCE, various technologies have been investigated [5]-[8]. One approach is to employ multiband or broadband rectenna to increase the received RF power [9]-[12]. The main goal of this approach is to expand the operating bandwidth of the rectenna to cover more communication bands. In [9], a dual-band (2.45 and 5.8 GHz) rectenna was proposed. Its peak PCEs are 63% at 2.45 GHz and 54.8% at 5.8 GHz, respectively. A broadband rectenna (from 1.8 to 2.5 GHz) [10] was presented and its peak PCE is higher than 55% in the range 1.8-2.5 GHz. However, its operating bandwidth is not wide enough for covering most communication systems.

Another approach to enhance rectenna's PCE is to make the rectenna not only work efficiently in a wide bandwidth but also receive arbitrary polarization electromagnetic waves. This is because circular polarization rectenna is capable of receiving more energy from the complex environment with multipath reflection and refraction. Nevertheless, it is challenging to design a wideband rectenna with circularly polarized characteristics. A novel wideband resistance compress-ion network (WRCN) is proposed [11] to improve the impedance matching performance between the rectifier and circularly polarized antenna, enabling the rectenna to attain high PCE over a wide frequency and input power ranges. However, the rectenna has a relatively complicated structure. Moreover, due to the opposite rotation directions of the electric field of LHCP and RHCP, polarization loss occurs when the polarization direction of the receiving antenna (e.g. LHCP) does not match that of the transmitted wave (e.g. RHCP), leading to partial signals being unable to be effectively received. Dual circularly polarized antennas are capable of receiving both LHCP and RHCP signals. In [13], a dual CP rectenna is presented. Its PCE is around 51% within the frequency range of 5.75 and 5.83 GHz when the input power is 0.5 dBm. The inherent challenges in designing a broadband dual CP rectenna are bandwidth expansion and efficiency improvement.

In this paper, we propose an ultrawideband dual circularly polarized rectenna (1.35-3.37 GHz) for ambient wireless energy harvesting systems. The main contribution of this work can be summarized as two aspects. On the one hand, we propose a novel broadband dual circular polarized antenna. It features compact dimension and simple structure. On the other hand, we propose

*Submitted On: January 23, 2024*
*Accepted On: April 26, 2024*



https://doi.org/10.13052/2024.ACES.J.390311

an ultra-wideband rectifier with a compact physical size. Finally, we combine the proposed antenna and rectifier to implement an UWB rectenna with the capability of receiving arbitrary polarized electro-magnetic waves. The receiving antenna is a chamfered square patch with double U-shape branches fed by two orthogonal coplanar waveguide (CPW) ports. These two ports are used for generating simultaneous right-hand CP (RHCP) and left-hand CP (LHCP). The rectifier has a compact size as its input impedance matching network is very simple. Furthermore, the input impedance of the rectifier has less sensitivity to the frequency. This characteristic is beneficial for designing a wideband rectifier. The experimental results have verified the proposed design methodology. Moreover, we provide a design guideline for the proposed ultrawideband rectenna, summarized below.

Step 1: Specification Definition. Define the operational requirements and specifications of the rectenna, including the frequency range, efficiency.

Step 2: Antenna Design. Determine the dimensions and shape of the monopole antenna based on the desired operating frequency and other specifications. Select an appropriate ground plane configuration, substrate and feeding network. Take out the simulation in CST Studio Suite to optimize the physical sizes of the monopole antenna. Then, get the optimized parameters and good performance parameter (such as impedance matching bandwidth, port isolation, and axial ratio).

Step 3: Rectifier Design. Choose appropriate Schottky diodes. Take out the source-pull simulation to determine the optimum load (RL) and input power (Pin). Design a two cascaded voltage doubler topology and wideband impedance matching network. Tuning the parameters of microstrip lines to obtain optimum performance.

Step 4: Measurement. Fabricate the prototype of the rectenna and establish a testing platform to evaluate its performance.

## II. ULTRAWIDEBAND RECTENNA DESIGN

### A. Antenna design and analysis

The proposed dual circular polarized ultra-wideband antenna and its optimized dimensions are shown in Fig. 1. This antenna occupies an area of 60 mm * 60 mm.

Figure 2 illustrates the evolution of antenna design improvement using three prototypes. The corresponding plots for return loss ($S_{11}$), port isolation ($S_{12}$), radiation efficiency and axial ratio (AR) are shown in Fig. 3. The radiator of Ant 1 is a compact chamfered square patch with two orthogonal microstrip feed lines. When port 2 is terminated with a matched load and port 1 is excited, Ant 1-3 exhibit good symmetry and reciprocity properties. When port 2 is excited, similar characteristics can

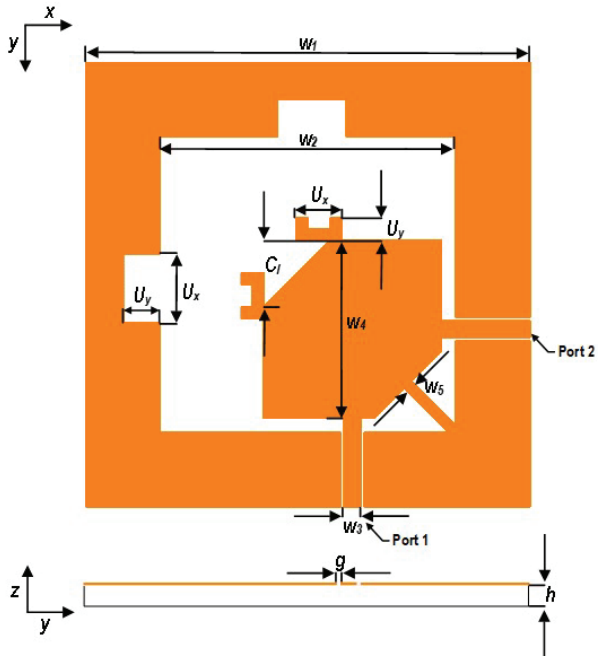


Fig. 1. Dual circular-polarized ultrawideband antenna with optimized dimensions (W1 = 60, W2 = 40, W3 = 2.2, W4 = 26, W5 = 1.3, h = 0.8, g = 0.5, Cl = 8.5, Ux = 9.4, Uy = 5, unit: millimeters).

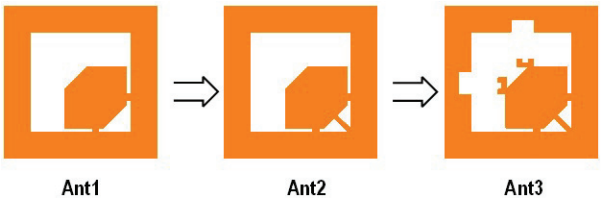


Fig. 2. Evolution of antenna.

be observed. From Figs. 2 and 3 (b) it can be observed that the two ports in Ant 1 are strongly coupled. Thus, we add a microstrip at the diagonal vertex of radiator to decouple the signals. Hence, within its operating frequency, Ant 2 provides 15-dB port isolation. Based on the above analysis, double U-shape branches are added in Ant 3 to modify the direction of electric currents, as shown in Fig. 4. Besides, two rectangular slots on the ground can be used to reduce the coupling between U-shape branches and the ground. The enhancement of AR bandwidth in comparison to that of Ant 2 is evident from Fig. 3 (c). According to Fig. 3 (d), it can be observed that Ant 3 achieves over 90% radiation efficiency within the 1.5-3.5 GHz frequency range. The surface current distributions of Ant 1-3 at 2.5 GHz are presented in Fig. 4. It can be observed that the currents are equal in amplitude and the flow direction is orthogonal at $\omega$t = 0° and $\omega$t

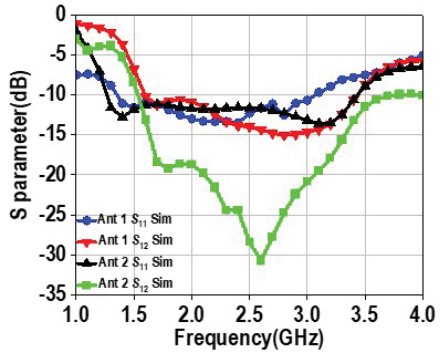


(a)

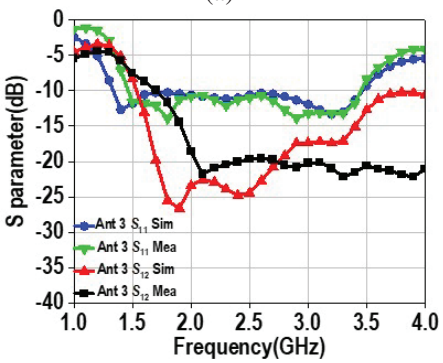


(b)

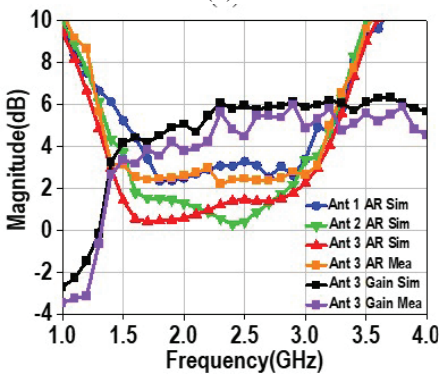


(c)

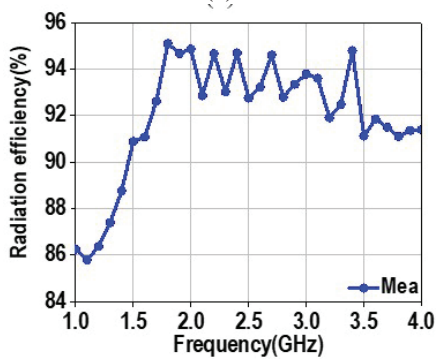


(d)

Fig. 3. Simulated and measured Ant 1-3: (a) return loss and port isolation of Ant 1-Ant 2, (b) return loss and port isolation of Ant 3, (c) gain and AR of Ant 1-Ant 3, and (d) radiation efficiency of Ant 3.

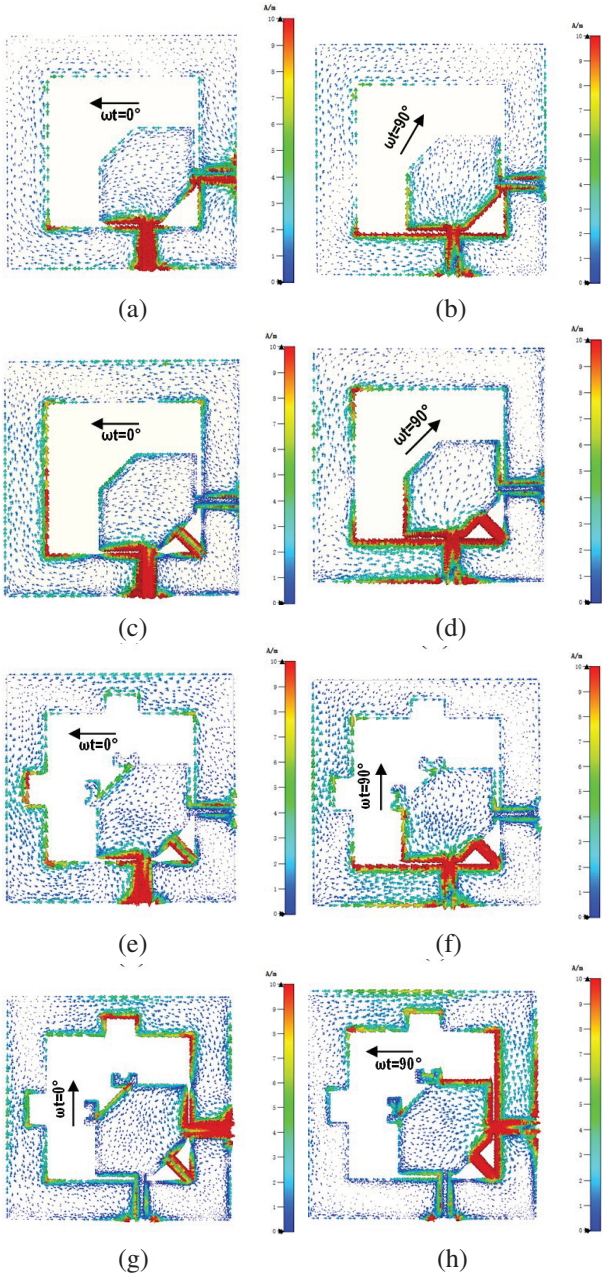


(a) (b) (c) (d) (e) (f) (g) (h)

Fig. 4. The surface current distributions at 2.5 GHz: (a) Ant 1 excitation at port 1, $\omega t = 0°$, (b) Ant 1 excitation at port 1, $\omega t = 90°$, (c) Ant 2 excitation at port 1, $\omega t = 0°$, (d) Ant 2 excitation at port 1, $\omega t = 90°$, (e) Ant 3 excitation at port 1, $\omega t = 0°$, (f) Ant 3 excitation at port 1, $\omega t = 90°$, (g) Ant 3 excitation at port 2, $\omega t = 0°$, and (h) Ant 3 excitation at port 2, $\omega t = 90°$.

$= 90°$ . In this way, when port 1 is excited, the horizonal electric field component ($E_h$) leads the vertical electric field component ($E_v$) by approximately 90°. The rotation of current vector from $\omega t = 0°$ to $\omega t = 270°$ is clockwise. It illustrates that the antenna radiates LHCP waves

in the far field. when port 2 is excited, $E_h$ lags $E_v$ about 90°. The anticlockwise movement of the current vector shows the antenna radiates RHCP waves in the +z direction.

Figure 5 shows the normalized measured radiation patterns of Ant 3 in the *yoz* and *xoz* planes at 2.4 GHz and 2.5 GHz, which has a normalized pattern with a 10 dB radial scale. In the entire band, the RHCP fields radiated by the proposed antenna are stronger than the LHCP fields (cross-polarization) by more than 10 dB in the +z direction. Concurrently, the antenna emits LHCP fields with a 10 dB stronger intensity in the -z direction than the RHCP fields (cross-polarization). There is a good agreement between the simulation and measurement results. Based on the above discussion, it can be said that Ant 3 has ultrawideband and dual CP characteristics.

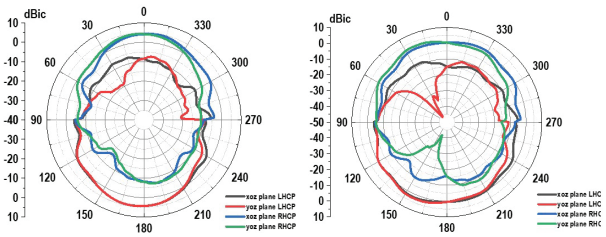


(a) (b)

Fig. 5. Measured normalized radiation patterns in the yoz and xoz planes at (a) 2.4 GHz and (b) 2.5 GHz.

### B. Rectifier design and analysis

In this part, an ultrawideband rectifier is proposed. Figure 6 (a) shows the rectifier's schematic. As can be seen, this rectifier consists of a matching network, four Schottky diodes, dc-pass filter ($C_4$, $C_5$) and harmonic rejection filter ($C_1$, $C_2$, $C_3$). Figure 6 (b) gives the layout of the proposed rectifier. Table 1 lists the width and length of the microstrip lines. By using this novel topology structure, its impedance is less sensitive to frequency variation. This feature is beneficial for realizing a wideband rectifier. Thus, in this design, we use only a T-junction matching network to make the proposed rectifier achieve a wide impedance matching bandwidth.

To increase the conversion efficiency, it is necessary to suppress this energy [14]. The harmonic generation mechanism and higher order harmonic cancellation are

Table 1: Parameters of the microstrip lines

| $W_1$ | $W_2$ | $W_3$ | $L_1$ ($L_{10}$) | $L_2$ ($L_{11}$) | $L_3$ ($L_{13}$) |
|---|---|---|---|---|---|
| 2.2 | 0.9 | 0.8 | 1.9 | 2.1 | 3.3 |
| $L_4$ ( $L_{14}$) | $L_5$ | $L_6$ | $L_7$ ( $L_{12}$) | $L_8$ | $L_9$ |
| 3.3 | 3.4 | 1.9 | 2.3 | 2.4 | 2.4 |

(W: Width, L: Length, unit: millimeters).

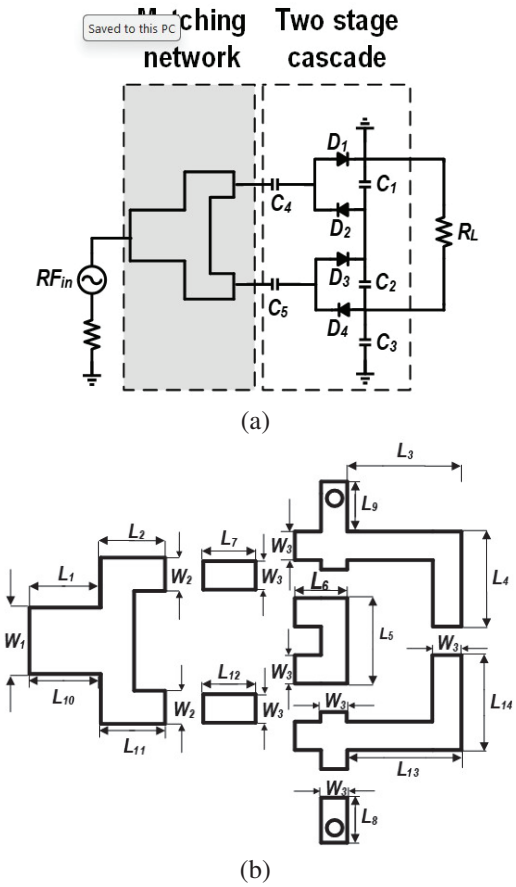


(a) (b)

Fig. 6. (a) Schematic and (b) layout of the proposed rectifier.

related. The two cascaded topology makes it easy to suppress the second order harmonics, and frequency multipliers commonly employ this technique to compress the second order harmonics [15]. It is noted that this topology rectifier also can be realized by using some other different Schottky diodes (for example, HSMS2862 and HSMS2852). To verify the above performance, the proposed rectifier is analyzed using harmonic balance simulation in Advance Design System (ADS) software.

The impedance of a single diode on shunt can be expressed as follows [16]:

$$Z_0 = \frac{\pi R_s}{\theta_{on} - \sin\theta_{on}\cos\theta_{on} + j\omega R_s C_j\left(\frac{\pi-\theta_{on}}{\cos\theta_{on}} + \sin\theta_{on}\right)}, \quad (1)$$

where $C_j$ is the junction capacitance of diode, $\theta_{on}$ is the phase angle where the diode switches on, and $R_s$ is the series resistance of diode. Figure 7 (a) displays input impedance of the proposed rectifier with HSMS2862 and HSMS2852. Here, the breakdown voltage of HSMS2862 is 7 V. When the frequency varies from 0.1 to 4 GHz, we can observe that the real part of the rectifier's input

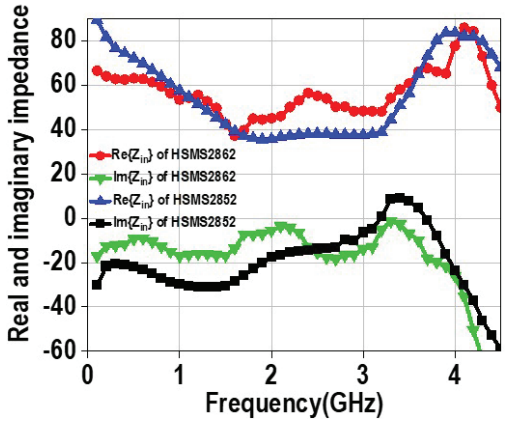


(a)

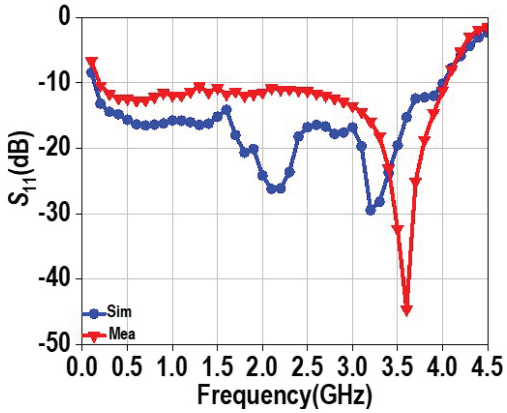


(b)

Fig. 7. The proposed rectifier (a) input impedance with HSMS2862, HSMS2852, and (b) simulated and measured S11 with HSMS2862.

impedance ($Z_{in}$) maintains around 50 Ohm (within the range of 40 and 65). In addition, the imaginary part of $Z_{in}$ has a flat variation trend. Thus, we can say that the rectifier's input impedance is less sensitive to frequency variation. The simulated and measured reflection coefficients ($S_{11}$) with HSMS2862 are plotted in Fig. 7 (b). As can be seen, $S_{11}$ is less than -10 dB when the frequency varies in the range of 0.1 and 4 GHz. The RF-DC power conversion efficiencies of the proposed rectifier with different diodes are plotted in Fig. 8. Different input power levels and load values are optimized for each diode. For HSMS2862 with 1200 Ohm load, the measured peak conversion efficiency is 73% at input power level of 18 dBm. Meanwhile, the conversion efficiency can remain over 60% within the impedance bandwidth. The simulated conversion effi-ciency for HSMS2852 over the frequency band (0.1-3 GHz) can be maintained above 40% with a 5 dBm input power level. Therefore, an ultrawideband rectifier can be designed by using this novel topology with different Schottky diodes.

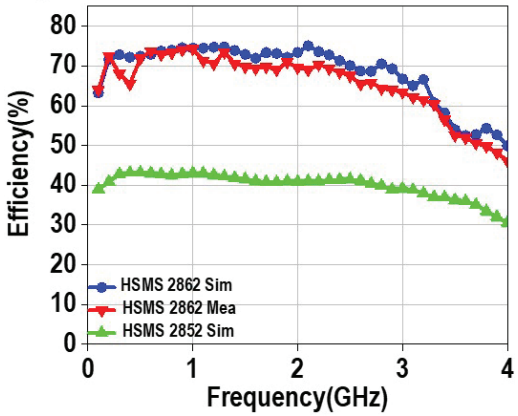


Fig. 8. Simulated and measured RF-DC PCEs versus frequency with different diodes.

## III. RECTENNA IMPLEMENT AND MEASUREMENT

For validation, we designed and implemented an ultra-wideband rectenna, as shown in Fig. 9 (a). The antenna is fabricated on a 0.8 mm-thick FR4 substrate ($\varepsilon_r = 4.4$, $\tan\delta = 0.02$). A 0.762 mm thickness layer of Arlon AD255c ($\varepsilon_r = 2.55$, $\tan\delta = 0.0014$) is selected as the substrate for the rectifier. In order to make a trade-off between fabrication-cost and performance, the antenna and rectifier are fabricated by using two different substrates.

For the prototype, Murata capacitor ($C_1$, $C_2$, $C_3$) (330 pF), dc load ($R_L$) (1200 Ohm) and four diodes (HSMS2862) are used. Antenna and rectifier are connected by SMA connectors. The physical size of the antenna is 60 * 60 mm. The physical size of the proposed ultrawideband rectifier is 15 * 12 mm. The measurement system is shown in Fig. 9 (b).

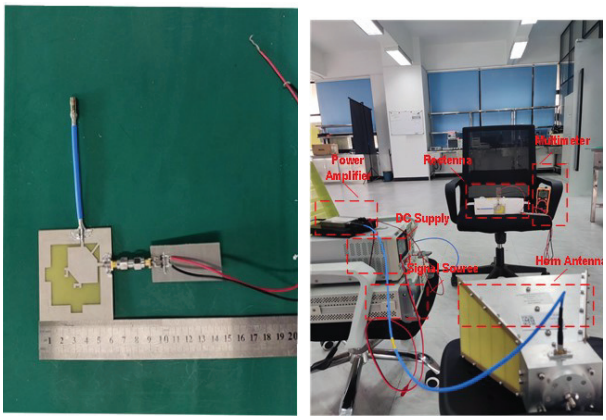


(a) (b)

Fig. 9. (a) Rectenna prototype and (b) measurement system.

Table 2: Comparison of the proposed rectenna and previous related design

| Ref | Rectifier Topology | Diode Type | Frequency (**GHz**) | Polarization | Input Power (dBm) | Peak PCE(%) |
|---|---|---|---|---|---|---|
| [9] | Single series connection two stage | HSMS2860 | 2.4 and 5.8 (FBW: None) | LP | 12 | 63% and 54.8% |
| [10] | voltage doubler | SMS7630 | 1.8 – 2.5 (FWB: 32.5%) | Dual LP | −35 to −10 | 70% |
| [11] | WRCN | HSMS2860 | 1.7 – 2.9 (FWB: 52.1%) | Dual CP | −3 to 20 | 76% |
| [12] | voltage doubler | HSMS2862 | 2.0 – 2.7 (FWB: 29.7%) | LP | 18 | 72.5% |
| [13] | single series | HSMS2850 | 5.75 – 5.83 (FWB: 1.36%) | Dual CP, LP | 0.5 | 51.1% |
| This work | two-stage voltage doubler | HSMS2862 | 1.35 – 3.37 (FWB : 85.5%) | Dual CP | 18 | 67.3% |

*FBW: Fractional bandwidth, LP: Linearly polarized, CP: Circularly polarized.

The RF signal source (RIGOL DSG3136B-IQ) generates the RF signal, which is subsequently amplified by the power amplifier (TLPA0.5G6G-35-30) and radiated by the horn antenna (HD-1018DRHA10S). The RF power is harvested and rectified by the horn antenna (HD-1018DRHA10S). The RF power is harvested and rectified by the proposed rectenna, then transmitted to the load. Finally, a multimeter is employed to measure the dc output voltage at the load terminal of the rectenna. Hence, the receiving power can be calculated as:

$$P_{in} = P_t G_t G_r \left(\frac{\lambda}{4\pi D}\right)^2, \tag{2}$$

where $P_t$ is the energy from the signal generator, $G_t$ is the horn antenna gain, $G_r$ is the gain of the receiving antenna (5 dBi), and $D$ (2.8 m) is the distance between the horn antenna and the rectenna.

The PCE of the rectenna is calculated below:

$$PCE = \frac{V_{out}^2}{R_L P_{in}} \times 100\% \tag{3}$$

where $V_{out}$ is the measured output voltage on the $R_L$. Figure 10 shows the simulated and measured PCEs versus frequency with a 18 dBm input power. As seen, the proposed rectenna achieves a stable PCE. More specifically, its PCE is higher than 55% when the frequency varies within the range of 1 and 3.40 GHz. The measured peak PCE is 67.3% at 1.9 GHz. The measured PCEs versus input power at different frequencies are depicted in Fig. 11. There is a good agreement between the simulation and measurement results. A comparison of the proposed rectenna with some pervious work is presented in Table 2. It can be observed that the proposed rectenna not only achieves the widest fractional bandwidth (FBW) but also has dual CP characteristics.

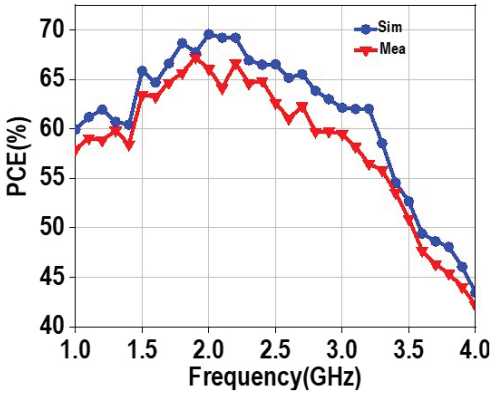


Fig. 10. Simulated and measured PCEs versus frequency at 18 dBm input power.

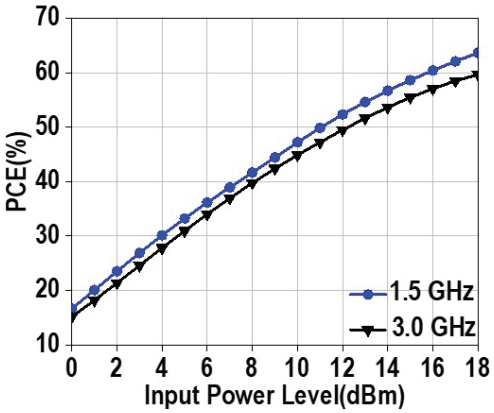


Fig. 11. The measured PCEs versus input power at 1.5 and 3.0 GHz.

## IV. CONCLUSION

A compact dual circularly polarized ultrawideband rectenna is proposed for a WEH system. The experimental results demonstrate that the PCE of the proposed rectenna is higher than 55% from 1.35 GHz to 3.37 GHz, which covers multiple communication bands such as GSM-1800 (1.8 GHz), LTE 2.1 GHz, and WLAN (2.45 GHz). Furthermore, this compact rectenna exhibits the capability to receive incident electromagnetic waves with arbitrary polarization. Considering its excellent performance, it is anticipated that the proposed rectenna can be utilized in broadband WEH systems.

## REFERENCES


[1] M. Kumar, S. Jain, and A. Sharma, "A plug-in type integrated rectenna cell for scalable RF battery using wireless energy harvesting system," *IEEE Microw. Wireless Compon. Lett.*, vol. 33, no. 1, pp. 98-101, June 2023.

[2] K. Niotaki, and N. B. Carvalho, "RF energy harvesting and wireless power transfer for energy autonomous wireless devices and RFIDs," *IEEE J. Microw.*, vol. 3, no. 2, pp. 763-782, Apr. 2023.

[3] L. Yang, Y. J. Zhou, C. Zhang, X. M. Yang, X. X. Yang, and C. Tan, "Compact multiband wireless energy harvesting based battery-free body area networks sensor for mobile healthcare," *IEEE J. Electromagn. RF Microw. Med. Biol.*, vol. 2, no. 2, pp. 109-115, June 2018.

[4] L. Guo, X. Li, W. Yang, Y. Zhao, and K. Wu, "Designing and modeling of a dual-band rectenna with compact dielectric resonator antenna," *IEEE Antennas Wireless Propag. Lett.*, vol. 21, no. 5, pp. 1046-1050, May 2022.

[5] L. Guo, X. Gu, P. Chu, S. Hemour, and K. Wu, "Collaboratively harvesting ambient radiofrequency and thermal energy," *IEEE Trans. Ind. Electron.*, vol. 67, no. 5, pp. 3736-3746, May 2020.

[6] S. Shen, C. Y. Chiu, and R. D. Murch, "A dual-port triple-band L-probe microstrip patch rectenna for ambient RF energy harvesting," *IEEE Antennas Wireless Propag. Lett.*, vol. 16, pp. 3071-3074, 2017.

[7] Y. Hu, S. Sun, H. Xu, and H. Sun, "Grid-array rectenna with wide angle coverage for effectively harvesting RF energy of low power density," *IEEE Trans. Microw. Theory Techn.*, vol. 67, no. 1, pp. 402-413, Jan. 2019.

[8] Y. Wang and J. Zhang, "Efficiency enhanced seven-band omnidirectional rectenna for RF energy harvesting," *IEEE Trans. Antennas Propag.*, vol. 70, no. 9, pp. 8473-8484, Sep. 2022.

[9] K. Bhatt, S. Kumar, P. Kumar, and C. C. Tripathi, "Highly efficient 2.4 and 5.8 GHz dual-band rectenna for energy harvesting applications," *IEEE Antennas Wireless Propag. Lett.*, vol. 18, no. 12, pp. 2637-2641, Dec. 2019.

[10] C. Song, Y. Huang, J. Zhou, J. Zhang, S. Yuan, and P. Carter, "A high efficiency broadband rectenna for ambient wireless energy harvesting," *IEEE Trans. Antennas Propag.*, vol. 63, no. 8, pp. 3486-3495, May 2015.

[11] Z. X. Du, S. F. Bo, Y. F. Cao, J. H. Ou, and X. Y. Zhang, "Broadband circularly polarized rectenna with wide dynamic-power-range for efficient wireless power transfer," *IEEE Access*, vol. 8, pp. 80561-80571, 2020.

[12] M. J. Nie, X. X. Yang, G. N. Tan, and B. Han, "A compact 2.45-GHz broadband rectenna using grounded coplanar waveguide," *IEEE Antennas Wireless Propag. Lett.*, vol. 14, pp. 986-989, Dec. 2015.

[13] P. Lu, C. Song, and K. M. Huang, "A two-port multipolarization rectenna with orthogonal hybrid coupler for simultaneous wireless information and power transfer (SWIPT)," *IEEE Trans. Antennas Propag.*, vol. 68, no. 10, pp. 6893-6905, Oct. 2020.

[14] Y. J. Ren and K. Chang, "5.8-GHz circularly polarized dual-diode rectenna and rectenna array for microwave power transmission," *IEEE Trans. Microw. Theory Techn.*, vol. 54, no. 4, pp. 1495-1502, June 2006.

[15] D. Shim, C. Mao, S. Sankaran, and K. O. Kenneth, "150 GHz complementary anti-parallel diode frequency tripler in 130 nm CMOS," *IEEE Microw. Wireless Compon. Lett.*, vol. 21, no. 1, pp. 43-45, Jan. 2011.

[16] S. Y. Zheng, W. L. Liu, and Y. M. Pan, "Design of an ultra-wideband high efficiency rectifier for wireless power transmission and harvesting applications," *IEEE Trans. Ind. Electron.*, vol. 15, no. 6, pp. 3334-3342, June 2019.


**Jian Liu** was born in Henan, China.

He received the Ph.D. degree in electronic engineering from South China University of Technology, Guangzhou, China, in 2018. He is currently an associate professor with the school of integrated circuits, Guangdong University of Technology. His research interests include RF integrated circuits and wireless power transmission.

**Jun Yi Li** was born in Hunan, China. He received the B.S. degree in information engineering from Hebei University of Engineering, Handan, China, in 2021. He is currently pursuing the M.S. degree in Guangdong University of Technology. His main research interests include wireless power transmission and broadband antenna.

# Wideband Low-Profile Fabry-Perot Cavity Antenna with Metasurface

**Xueyan Song, Ang Dong, XuPing Li, YunQi Zhang, Haoyuan Lin, Hailong Yang, and Yapeng Li**

School of Electronic Engineering
Xi'an University of Posts & Telecommunications, Xi'an 710121, China
xysong65@xupt.edu.cn, 1361580350@qq.com, lixuping@163.com, johnny_5@126.com,
2806198782@qq.com, liyapengedu@163.com, yanghl68@163.com

***Abstract* –** A novel Fabry-Perot cavity (FPC) antenna with metasurface is presented, which can achieve broad bandwidth and low profile. Traditional FPC antennas, with rectangular microstrip antennas as feeds, have limited impedance bandwidth and struggle to make a compromise in the gain bandwidth and maximum gain value. To obtain wide bandwidth, the FPC antenna proposed in this paper utilizes a feed antenna loaded with parasitic patches. To widen impedance bandwidth and gain bandwidth and reduce the profile, a positive phase gradient partially reflective surface (PRS) and an artificial magnetic conductor (AMC) are located above and below the feed antenna, respectively. The phase property of the PRS and AMC also brings in a more smooth gain value curve. To further increase gain values, four metal reflector plates are located around the proposed antenna. The overall dimension of the antenna is $2.5\lambda_0 \times 2.5\lambda_0 \times 0.25\lambda_0$ ($\lambda_0$ is the free space wavelength at 7.5 GHz). Simulated results show that the resonant cavity antenna proposed in this letter exhibits an impedance bandwidth of 13.3% (7-8 GHz) and a 3 dB gain bandwidth of 14.3% (7.02-8.10 GHz). The maximum gain in the whole operating band is 14.5 dBi. The measured results are in good agreement with the simulated ones.

***Index Terms* –** Fabry-Perot cavity, high gain, low-profile, wideband.

## I. INTRODUCTION

Developments of communication technology bring in appearance of numerous high-gain antennas, in which Fabry-Perot cavity (FPC) antennas have drawn plenty of interest from academics [1–3]. According to operation mechanism of resonant cavity antennas, the height of most Fabry-Perot antennas is at least a half wavelength [4, 5]. In traditional Fabry-Perot antennas, perfect electric conductors (PEC) are utilized as ground, which results in high profile [6]. To meet the requirement of miniaturization of antennas, it is essential to research how to reduce the profile while maintaining the bandwidth.

Because of in-phase properties, an artificial magnetic conductor (AMC), when utilized as ground of the antenna, can effectively reduce the profile compared with PEC. Consequently, a number of FPC antennas with AMC ground have been presented [7, 8]. In [7], a miniaturized Fabry-Perot antenna is proposed which achieves a high gain of 12.4 dBi by adopting an AMC ground. The bandwidth is 6.4%. To achieve higher gain value, a novel FPC antenna is designed in [8], which has a profile of one-eighth wavelength and a maximum gain of 16.27 dBi, while the bandwidth is required to be widened. Similarly, antennas with AMC surfaces in [9–12] achieve low profiles. However, both the impedance bandwidth and gain bandwidth are need to be broadened due to the phase effect of AMC surface.

In order to achieve wider bandwidth and lower profile, a novel FPC antenna is proposed in this paper. For simplicity, a rectangular microstrip antenna is used as the feed antenna. To obtain broad gain bandwidth, a partially reflective surface is designed above the feed antenna. Moreover, the profile of the antenna can be reduced to a quarter wavelength by loading an AMC ground above the feed antenna. To further increase the maximum gain value, four metal reflector plates are placed around the antenna, and the maximum gain reaches 14.5 dBi. Simulated results show that the impedance bandwidth is 13.3%, and the 3 dB gain bandwidth is 14.3%. In summary, the designed antenna in this paper can obtain a wider gain bandwidth and a quarter wavelength profile simultaneously. Moreover, by loading the reflective wall without increasing the longitudinal size, the gain values of the designed antenna is further increased.

## II. ANTENNA DESIGN

### A. Antenna configuration

Figure 1 illustrates the proposed configuration, which is etched on 2-mm-thick substrates ($\varepsilon_r$=2.2, tanδ=0.001). A microstrip patch antenna loaded with a 5-mm-thick parasitic patches is designed and utilized as feed antenna. At a height of 10 millimeters above the antenna is located a partially reflective surface, which

*Submitted On: January 5, 2024*
*Accepted On: April 1, 2024*



https://doi.org/10.13052/2024.ACES.J.390312

consists of 10×10 units. On the upper layer of the unit is a circular patch and on the lower layer is a cross patch. An AMC structure with rectangular unit is located at the bottom of the feed antenna, which is surrounded by four metal reflector plates. Dimensions (unit: mm): $S_1$=20, $S_2$=10, $P_1$=16, $P_2$=13.2, $P_3$=12.1, $P_4$=5, $P_5$=12, $X_1$=7.8, $X_2$=1, $X_3$=2, $X_4$=0.6, and $X_5$=8.

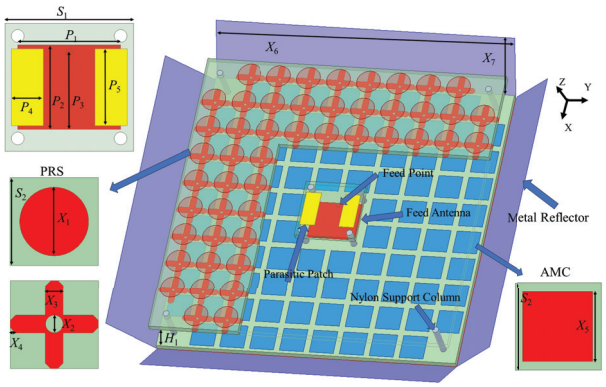


Fig. 1. 3D geometry of proposed antenna.

## B. Working mechanism

The feed antenna, as shown in Fig. 2 (b), is a rectangular microstrip antenna loaded with parasitic patches. Compared with the antenna in Fig. 2 (a), the feed antenna generates a new resonance in high frequency band when loaded with parasitic patches, which exhibit a wider impedance bandwidth. Figure 3 presents $S_{11}$ of the feed antenna with and without parasitic patches. It can be seen that the impedance bandwidth of the microstrip antenna broadens from 6.6% (6.75-7.21 GHz) to 12.8% (6.85-7.79 GHz) when loaded with parasitic patches. Figure 4 shows the electric field distribution at 7 and 7.7 GHz of the feed antenna with parasitic patches. It can be found that the microstrip antenna mainly generates resonances at 7 GHz, and the parasitic patches are primary resonant at 7.7 GHz. When loaded with parasitic patches, multiple resonances can be generated, which broadens the bandwidth of the feed antenna.

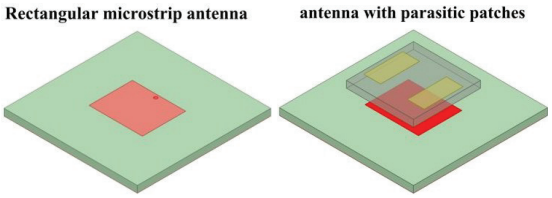


Fig. 2. Schematic diagram of feed source antenna structure.

According to FPCA theory, the response of the resonant cavity antenna satisfies equations (1) and (2)

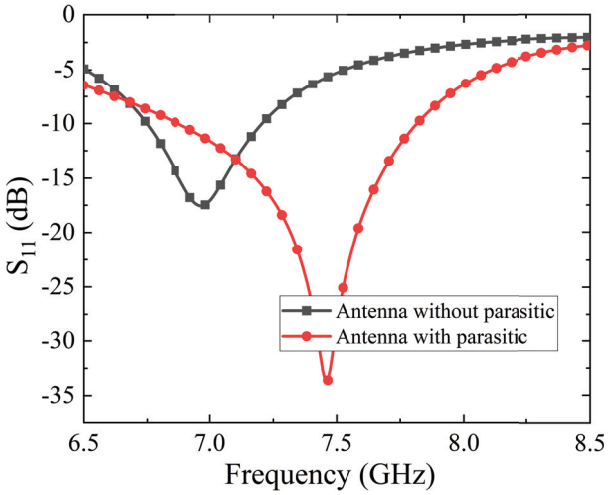


Fig. 3. $S_{11}$ of the feed antenna with and without parasitic patches.

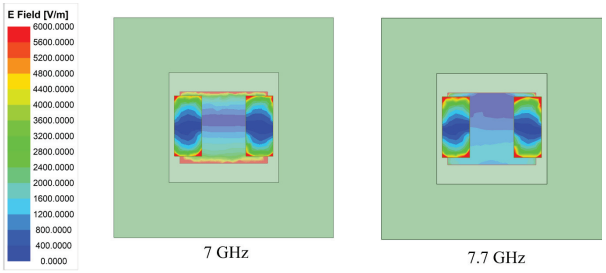


Fig. 4. Electric field distribution of the feed antenna.

[12, 13], where $|\Gamma_{PRS}|$ is the reflection magnitude of the partially reflective surface (PRS):

$$f_0 = \frac{c}{4\pi H_c}(\phi_{PRS} + \phi_{GND} - 2N\pi), N = 0, 1, 2...., \quad (1)$$

$$D = 10\log\frac{1+|\Gamma_{PRS}|}{1-|\Gamma_{PRS}|}, \quad (2)$$

where $Hc$ is the profile height of the antenna in a high-gain resonant state. When the operation frequency is given, the parameter $Hc$ has an effect on the phase response of the upper and lower layers of metasurfaces. $D$ is the directivity of antennas. Generally, the larger the reflection coefficient of reflective surfaces, the higher the directivity, which will also increase dimension of antennas simultaneously. Therefore, there should be a compromise between the dimension and the directivity in the design of antennas. The proposed antenna is designed aiming to form a resonant cavity and obtain high gain by adopting a partially reflecting surface and an AMC.

By designing a partially reflective surface with a positive phase response, the resonant state expressed in equation (1) can be maintained with wider bandwidth. Additionally, the AMC surface is designed to

achieve low profile because of in-phase reflective phase. A square patch is used as the AMC unit, which is because the square unit exhibits an excellent in-phase reflection bandwidth and is easily adjusted to generate a resonant in the band expressed in equation (1).

## III. SIMULATED RESULTS

The performances are simulated by using ANSYS HFSS Floquet-port model. Figures 5 (a) and (b) show the phase response plot of AMC and the phase and magnitude response plot of partially reflective surface, respectively. From Fig. 5 (a), the phase values of AMC are greater than the theoretical ones, which is designed to ensure a wide phase margin when it is summed with that of the partially reflective surface to satisfy the resonant state in equation (1).

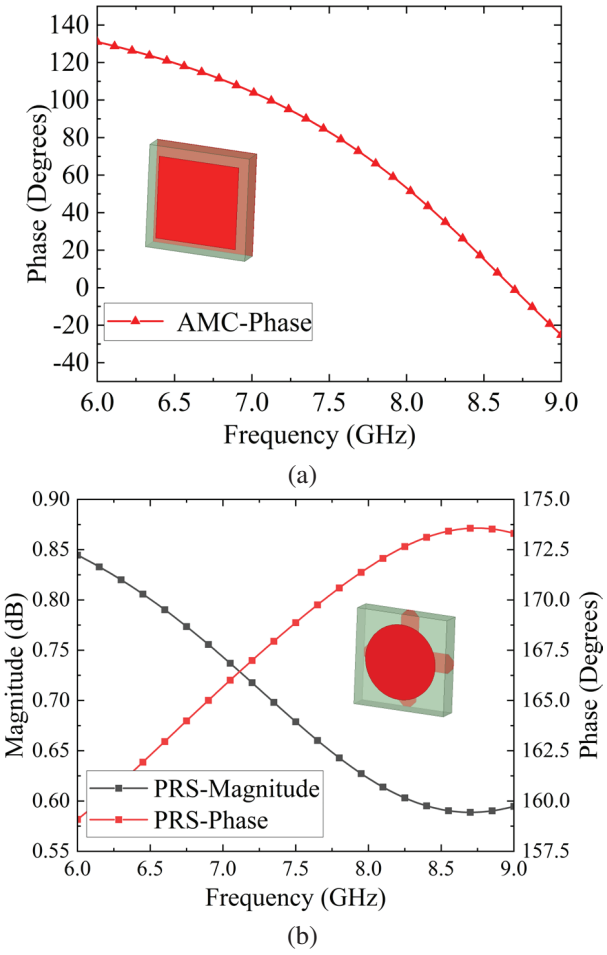


Fig. 5. (a) Phase response of AMC and (b) phase and magnitude response of PRS.

A square patch is chosen as AMC unit because that is a simple structure, making it convenient to adjust the phase values. Figure 6 shows the phase value curves with

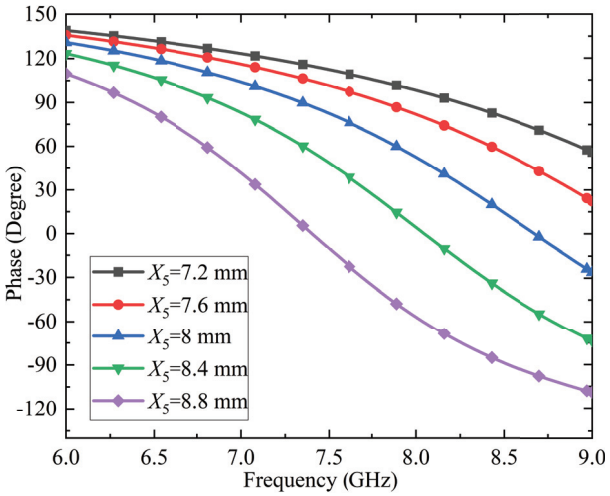


Fig. 6. Phase response of AMC varies with $X_5$.

different values of parameter $X_5$. As $X_5$ increases, the phase curves of AMC move towards the low frequency band. $X_5$ is the unit dimension of the AMC, and the resonance frequency decreases as $X_5$ increases. To obtain a required phase, the value of $X_5$ needs to be adjusted.

The simulated $S_{11}$ and gain of the proposed antenna in different situations are shown in Fig. 7. The simulated impedance bandwidth is from 7 to 8 GHz, and the 3 dB gain bandwidth ranges from 7.02 to 8.10 GHz. It can be seen that the gain bandwidth of the antenna basically coincides with the impedance bandwidth. The FP antenna without reflection has 4 dB higher gain values than that of the feed antenna. Moreover, after added reflection, the gain values of the proposed antenna are increased by 2 dB. Ultimately, the final designed antenna achieves an axial maximum gain value of 14.5 dBi, which is 6.4 dB higher than that of the feed antenna.

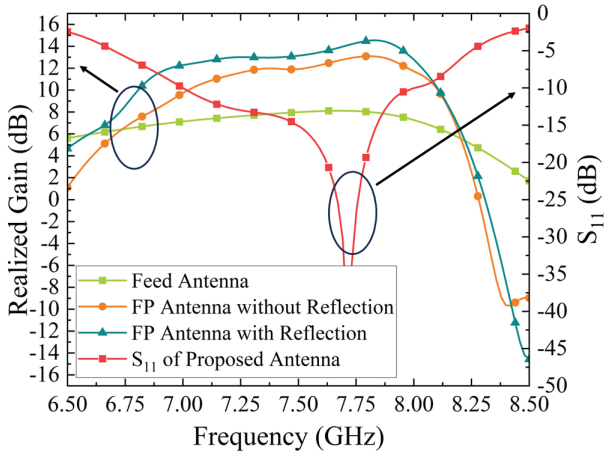


Fig. 7. Simulated realized gain and $S_{11}$.

## IV. EXPERIMENTAL RESULTS

To validate the simulations, the designed antenna is fabricated and measured as shown in Fig. 8. The reflection coefficients are measured by a Keysight E5063A network analyzer. Figure 9 depicts the simulated and measured $S_{11}$. The measured $S_{11}$ is from 6.91 to 7.81 GHz, which agrees with the simulated ones (7 to 8 GHz) except for a small offset. The small difference between the measured and the simulated results is mainly caused by fabrication and measured error. The radiation pattern is measured in the microwave laboratory. Figure 10 illustrates the 2D radiation pattern at 7.5 GHz in *xoz* and *yoz* planes, from which it can be demonstrated that the measured radiation patterns agree well with the simulated ones. The presented antenna exhibits good radiation directivity, and the cross polarization is less than −30 dB in the main radiation direction.

The performances of the proposed antenna compared with the references are illustrated in Table 1. The bandwidth is the intersection of impedance bandwidth and 3 dB gain bandwidth, and $\lambda_0$ is the wavelength at center frequency. Compared with antennas in [8] and

Fig. 8. The proposed antenna prototype.

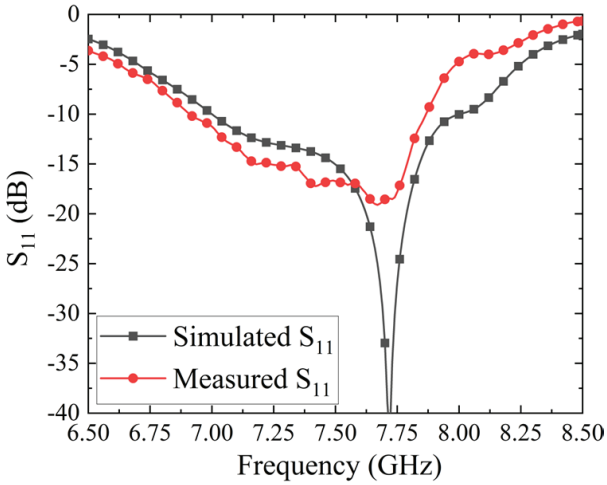


Fig. 9. Measured and simulated $S_{11}$.

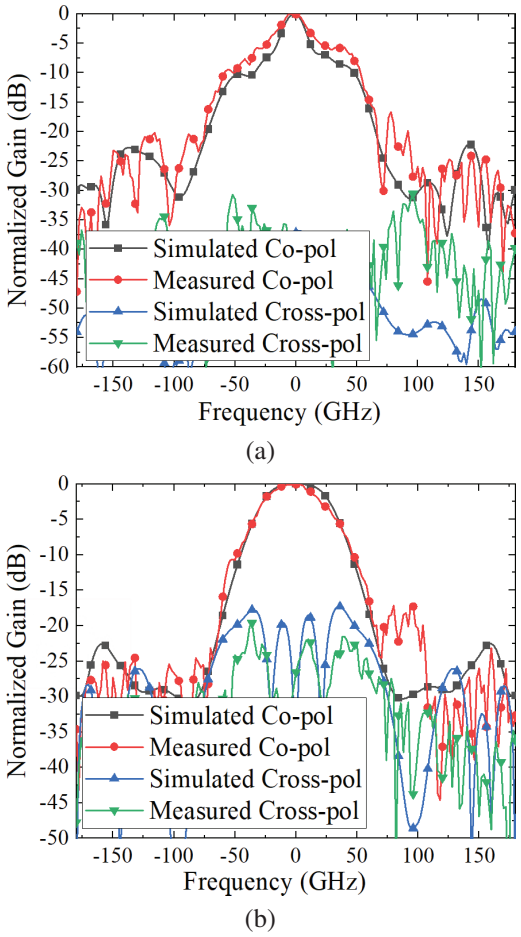


Fig. 10. Simulated and measured radiation patterns of the proposed antenna at 7.5 GHz in (a) *xoz* and (b) *yoz* plane.

Table 1: Comparison with other FPC antennas

| References | Bandwidth (%) | Gain (dBi) | Overall size ($\lambda_0$) |
|---|---|---|---|
| [7] | 6.4 | 12.4 | 2.26×2.26×0.25 |
| [8] | 1.5 | 16.27 | 4×4×0.125 |
| [9] | 2.1 | 11.5 | 1.43×1.43×0.167 |
| [10] | 4.1 and 2.7 | 10.1 and 15.2 | 1.49 × 1.49× 0.28 and 2.67 × 2.67 × 0.49 |
| [11] | 3.1 | 17 | unknown× unknown×0.25 |
| [12] | 4 | 4.1 | 1.1×1.1×0.075 |
| [14] | 2.8 | 13.4 | 2.6×2.6×0.36 |
| [15] | 32.4 | 13.67 | 4.49×4.49×0.57 |
| This work | 13.04 | 14.5 | 2.5×2.5×0.25 |

[11], the gain values of the proposed antenna is a little lower, while, the gain bandwidth in this paper is wider and the dimension is smaller. In addition, compared to all references except [15], the proposed antenna has a wider bandwidth. In [15], the height of the Fabry-Perot antenna is more than a half wavelength, which brings in wider bandwidth. Compared with [15], the proposed antenna in this paper has a smaller dimension and higher gain values.

## V. CONCLUSIONS

The design and fabrication of a low profile broadband Fabry-Perot resonant cavity antenna is presented in this paper. The impedance bandwidth and gain bandwidth are wide by designing a partially reflective surface and loading a parasitic patch above the feed antenna. As a result, the final antenna provides an impedance bandwidth from 7 to 8 GHz (13.3%) and a 3 dB gain bandwidth from 7.02 to 8.10 GHz (14.3%). Afterwards, the addition of a metal reflector plate around the antenna further increases the maximum gain value to 14.5 dBi without affecting the bandwidth. Both the simulated and measured results verified this improvement. The presented antenna offers the advantages of large bandwidth, high gain and low profile, making it suitable for high-capacity microwave communications in the C-band, such as satellite communications and healthcare services.

## ACKNOWLEDGMENT

This work was supported by the Natural Science Basic Research Program of Shaanxi (Program No. 2022JQ-699, 2022JQ-633 and 2021JQ-710) and the Key Research and Development Program of Shaanxi (Program No. 2021GY-049).

## REFERENCES

[1] M. M. Bilgic, and K. Yegin, "High gain, wideband aperture coupled microstrip antenna design based on gain-bandwidth product analysis," *Applied Computational Electromagnetics Society (ACES) Journal*, vol. 29, no. 8, pp. 639-646, Sep. 2021.

[2] J. Wang, Y. Li, Z. H. Jiang, T. Shi, M. C. Tang, Z. Zhou, Z. N. Chen, and C. W. Qiu, "Metantenna: When metasurface meets antenna again," *IEEE Transactions on Antennas and Propagation*, vol. 68, no. 3, pp. 1332-1347, Mar. 2020.

[3] R. Gardelli, M. Albani, and F. Capolino, "Array thinning by using antennas in a Fabry-Perot cavity for gain enhancement," *IEEE Transactions on Antennas and Propagation*, vol. 54, no. 7, pp. 1979-1990, July 2006.

[4] F. Deng and K. M. Luk, "A wideband spherical Fabry-Perot cavity antenna based on positive phase gradient metasurface," *IEEE Transactions on Antennas and Propagation*, vol. 71, no. 7, pp. 5558-5565, July 2023.

[5] S. Fang, L. Zhang, Y. Guan, Z. Weng, and X. Wen, "A wideband Fabry-Perot cavity antenna with single-layer partially reflective surface," *IEEE Antennas and Wireless Propagation Letters*, vol. 22, no. 2, pp. 412-416, Feb. 2023.

[6] R. Orr, G. Goussetis, and V. Fusco, "Design method for circularly polarized Fabry-Perot cavity antennas," *IEEE Transactions on Antennas and Propagation*, vol. 62, no. 1, pp. 19-26, Jan. 2014.

[7] Z.-G. Liu, Z.-X. Cao, and L.-N. Wu, "Compact low-profile circularly polarized Fabry-Perot resonator antenna fed by linearly polarized microstrip patch," *IEEE Antennas and Wireless Propagation Letters*, vol. 15, pp. 524-527, 2016.

[8] M. Y. Jamal, M. Li, K. L. Yeung, X. Li, L. Jiang, and T. Itoh, "A low-profile Fabry-Pérot cavity antenna using anisotropic metasurface," *IEEE Antennas and Wireless Propagation Letters*, vol. 21, no. 2, pp. 356-360, Feb. 2022.

[9] Z.-G. Liu, C. Zhang, R.-J. Yin, and W.-B. Lu, "Multifunctional low-profile Fabry-Perot resonator antenna integrated with solar cells," *IEEE Transactions on Antennas and Propagation*, vol. 70, no. 8, pp. 7175-7180, Aug. 2022.

[10] J. Chen, Y. Zhao, Y. Ge, and L. Xing, "Dual-band high-gain Fabry-Perot cavity antenna with a shared-aperture FSS layer," *IET Microwaves, Antennas & Propagation*, vol. 12, no. 13, pp. 2007-2011, July 2018.

[11] X. Zhao, Y. Liu, J. Zhang, and W. Zhang, "Design of a low-profile Fabry-Perot resonant cavity antenna using fractal EBG ground plane," in *2021 International Conference on Microwave and Millimeter Wave Technology (ICMMT)*, pp. 1-3, Nanjing, China, 2021.

[12] G. V. Trentini, "Partially reflecting sheet arrays," *IRE Transactions on Antennas and Propagation*, vol. AP-4, no. 4, pp. 666-671, Oct. 1956.

[13] N. Wang, C. Zhang, Q. Zeng, N. Wang, and J. Xu, "New dielectric 1-D EBG structure for the design of wideband resonator antennas," *Progress in Electromagnetics Research Letters*, vol. 141, pp. 233-248, 2013.

[14] Y. Wang and A. Zhang, "Dual circularly polarized Fabry-Perot resonator antenna employing a polarization conversion metasurface," *IEEE Access*, vol. 9, pp. 44881-44887, 2021.

[15] S. Fang, L. Zhang, Y. Guan, Z. Weng, and X. Wen, "A wideband Fabry-Perot cavity antenna with single-layer partially reflective surface," *IEEE Antennas and Wireless Propagation Letters*, vol. 22, no. 2, pp. 412-416, Feb. 2023.

**Xueyan Song** was born in Henan Province, China, 1989. She received the B.E. degree in electronic and information engineering from Xidian University, Xi'an, China, in 2012. She received the Ph.D. degree from Xidian University, Xi'an, China, in 2018. She joined the School of Electronic Engineering, Xi'an University of Posts & Telecommunications in 2018. Her research interests include artificial magnetic conductors, low RCS antennas, low-profile antennas, frequency selective surfaces, and reflector antennas.

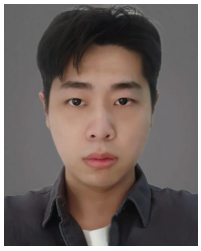

**Ang Dong** was born in Hebei, China, in 1999. He is currently pursuing a Master of Engineering degree in the School of Electronic Engineering, Xi'an University of Posts & Telecommunications. His current research interests include metasurface, microstrip antenna.

**XuPing Li** was born in Xi'an, Shanxi, China, in 1981. He received the Ph.D. degree in Electromagnetic field and microwave from the Xidian University, Xi'an, China, in 2015. In January 2019, he was transferred to Xi'an University of Posts & Telecommunications as the leader of the phased array antenna technology research team. The principal focus of his research program is the development of phased array antennas.

**YunQi Zhang** was born in BaoTou, Inner Mongolia, China, in 1986. He received the Ph.D. degree from Xidian University, Xi'an, China, in 2015. He is currently working in the Xi'an University of Posts & Telecommunications. His research interests include GPS antenna, CP antenna, omnidirectional antenna and antenna array designs.

**Haoyuan Lin** was born in Shandong, China, in 2003. He is currently pursuing B.E. degree in the school of Electronic Engineering from Xian University of Posts & Telecommunications. His current research interests include circuit, microwave, antenna.

**Hailong Yang** received the B.S. in communicating engineering from Heze University, Heze, China, in 2012, and M.S. and Ph.D. degrees in communicating engineering from Xi'an University of Technology, Xi'an, China, in 2015 and 2019. He joined the faculty of Electronic Engineering Department, Xi'an University of Posts & Telecommunications, in 2019. His research interests include wave propagation and antenna design.

**Yapeng Li** received the Doctor's degree from Xidian University in 2020. He is currently an associate professor with the School of Electric Engineering, Xi'an University of Posts & Telecommunications. His research interests include filtering antenna, wideband antenna, dual-polarized antenna and circular polarized antenna.

# Broadband Dual-frequency High Isolation Base Station Antenna with Low RCS Structure Loaded

**Pei-Pei Ma[1], Fang-Fang Fan[1], and Xin-yi Zhao[2]**

[1]The Key Laboratory of Antennas and Microwave Technology
Xidian University, Xian, 710071, China
3305559651@qq.com, fffan@mail.xidian.edu.cn

[2]School of Economics and Management
Beijing University of Posts and Telecommunications, Beijing, 100876, China
3346334629@qq.com

***Abstract*** **–** A novel dual-band dual-polarization shared aperture antenna is proposed, which covers frequencies 1.7-2.6 GHz and 3.3-3.8 GHz. The structure, with low radar cross section (RCS), is designed to reduce the radiation interference on the high band (HB) antenna. Additionally, by introducing U-shaped slots on the arms of the low band (LB) antenna, polarization isolation between the HB elements is significantly enhanced, which can reach up to 25 dB across the whole band. Moreover, to restore the radiation pattern of the LB antenna, the dielectric substrate is employed beneath the HB antenna as a substitute for the ground plane. The antenna proposed in this paper possesses attributes of broadband, compact size, and simplified structure.

***Index Terms*** **–** Base station antenna, decoupling, dual band, pattern restoration.

## I. INTRODUCTION

With the rapid updating of wireless communication, not only has the number of the wireless users grown exponentially, but also the application scenarios of wireless communication are becoming diverse. Base station antennas, which play a crucial role in the wireless industry infrastructure, have undergone a complex development process. At the junction of 4G and 5G mobile communication, the stage that the 4G and 5G base station antenna will coexist for some time has already arrived.

In the context of limited spatial volume in base stations, three common schemes have been proposed: embedded, stacked, and interleaved structures, as depicted in Fig. 1. The embedded structure allows the high band (HB) antenna to be nested at the center of the low band (LB) antenna. However, this configuration is limited to cases where the frequency of HB is almost twice as large as that of LB [1][2]. The stacked structure involves placing the HB antenna on top of the LB antenna with a frequency selective surface (FSS) inserted between them to reduce mutual coupling [3–5]. However, this way often leads to complex feed networks and assembly challenges. In contrast, the interleaved structure positions the

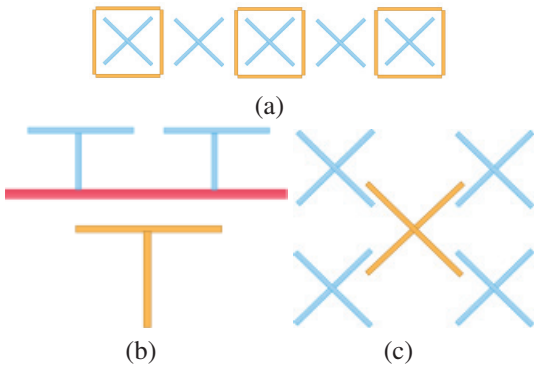


Fig. 1. Structure of the dual-band antenna: (a) embedded structure, (b) stacked structure, and (c) interleaved structure (blue line: the high band element, yellow line: the low band element, red line: FSS).

LB antenna at the center of the HB array, offering advantages in terms of easy installation and manufacturing compared to the other two structures. Moreover, this structure is suitable for any combination of different frequency bands. Therefore, the interleaved structure is adopted in this article. However, the corresponding problems, such as pattern distortion and low isolation, need to be resolved because of the interaction of dual-band antennas.

In order to restore the HB pattern, several significant adjustments to LB radiators have been examined in previous studies. Chokes, as proposed in [6][7], and L-shaped strips introduced in [8], are designed to minimize the induced currents on the LB radiator. Different

*Submitted On: December 6, 2023*
*Accepted On: April 12, 2024*



https://doi.org/10.13052/2024.ACES.J.390313

types of slots [9][10] and 3-D chokes [11] are adopted to provide induced currents with opposite directions, which helps weaken the scattering influence. Split ring resonators [12] and protruded stubs [13] are used to reduce the radar cross section (RCS) of the LB radiators. At the same time, in [14][15], common-mode (CM) currents induced on the HB antenna generate new resonance interference that worsens the radiation pattern of the LB antenna. To eliminate this CM interference, ferrite-loaded HB coaxial lines and capacitance-loaded HB elements are proposed to restore the LB radiation pattern. Moreover, polarization isolation between the HB elements is another unresolved issue. Additional structures, such as metal walls or parasitic structures [16][17], have been designed to enhance isolation.

In this paper, a novel dual-band dual-polarized base station antenna with compact structure and excellent performance is proposed, which covers broadband of 1.7-2.6 GHz (42%) and 3.3-3.8 GHz (14%). The experimental simulation is carried out based on the ANSYS HFSS. The decoupling approach proposed in this paper is both effective and simple compared to the antenna of similar type. The following is the detailed introduction and analysis.

## II. DECOUPLING OF THE DUAL-BAND ANTENNA

The structure of the dual-band shared aperture antenna proposed in this article is shown in Fig. 2. The HB and LB antennas are fed by coaxial lines. The radiation patch and feeding probe are etched on the upper and lower layer of the substrate, respectively, and they are connected to the outer and inner conductor of the coaxial line. To avoid overlap, one of the probes is disconnected in the middle as shown in Figs. 2 (e) and (f).

Figure 3 illustrates the electromagnetic (EM) interference between the HB and LB antenna in the dual-band environment. The radiation of both the HB antenna and LB antenna are adversely affected due to their close proximity and mutual obstruction. The red arrows indicate the transmission of the HB EM wave while the green arrows represent that of the LB EM waves.

### A. HB radiation pattern restoration

RCS serves as a critical metric for evaluating the scattering characteristics of targets within radar systems. It quantifies the ratio of the power scattered by a target in the receiving direction to the incident power of plane wave impinging upon the target from a given direction. Currently, extensive research has been devoted to the investigation of low RCS meta-surface, with numerous studies validating their effectiveness. This technological advancement has found practical applications in the design of shared aperture base station antennas, resulting in prominent effects in achieving electromagnetic transparency [18][19].

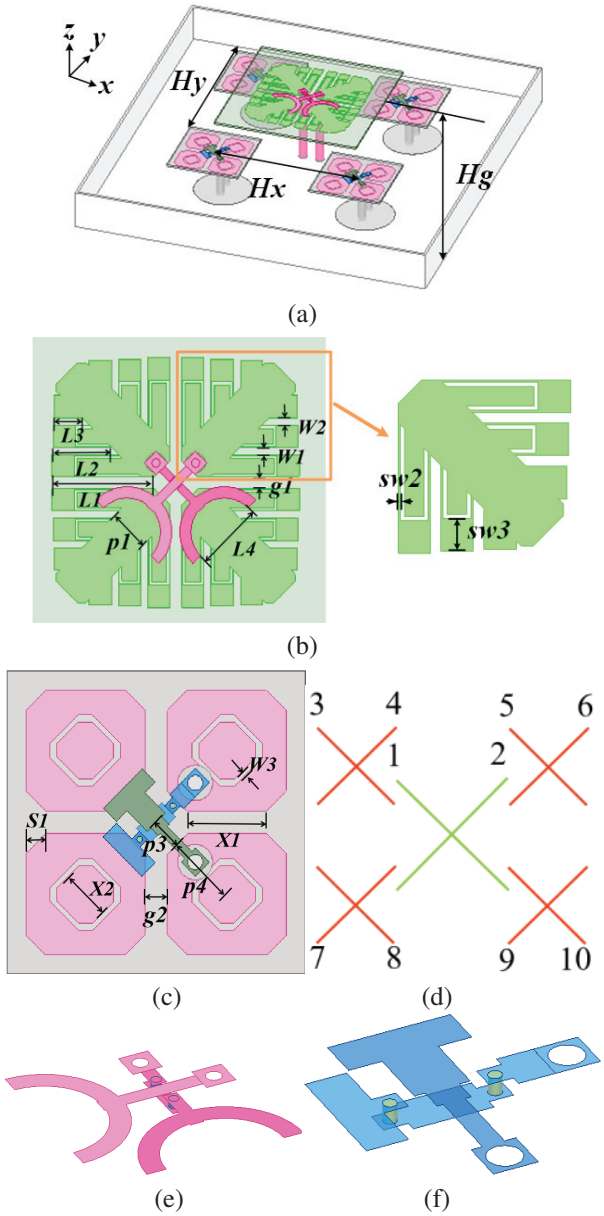


Fig. 2. (a) Overall configuration of the proposed antenna, (b) radiation patch of LB antenna, (c) radiation patch of HB antenna, (d) port distribution, (e) LB feeding probe, and (f) HB feeding probe (*Hx*=60 mm, *Hy*=60 mm, *Hg*=30 mm, *L1*=18 mm, *L2*=10.5 mm, *L3*=5 mm, *L4*=12 mm, *p1*=7.32 mm, *W1*=1.23 mm, *W2*=1.3 mm, *W3*=2 mm, *X1*=8 mm, *X2*=5 mm, *p3*=3.1 mm, *p4*=7.07 mm, *g2*=2.25 mm, *s1*=2 mm, *sw2*=0.13 mm, *sw3*=4 mm).

In this paper, a new low RCS structure is designed in this shared aperture base station antenna. Compared to the conventional element with the square patch as the radiator, the antenna element in this design adopts the

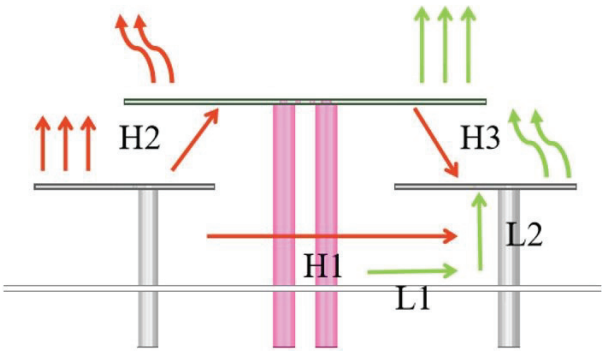


Fig. 3. Transmission path of the EM wave which results in mutual coupling.

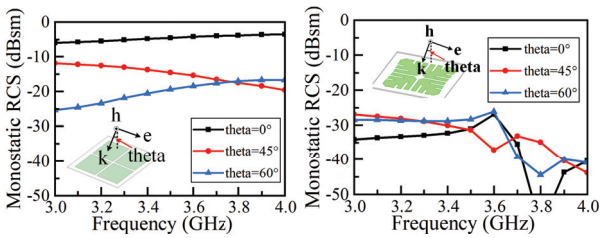


Fig. 4. Comparison of the monostatic RCS between two types of patches under illumination of plane waves at different incident angles: (a) square-shaped patch and (b) branch-shaped patch.

branch-shaped structure. This design greatly improves the scattering interference on the HB antenna due to the low RCS property of the LB antenna element itself. Figure 4 illustrates the monostatic RCS value of the different radiation patches. As the incident angle of the plane wave varies, the RCS of the square patch remains above −25 dB, reaching up to −5 dB under normal incidence. In contrast, the RCS of the proposed branch-shaped patch remains below −25 dB across the entire frequency band. Figure 5 illustrates the comparison of the electric field in the horizontal plane when the HB antenna is excited. It can be observed that the conventional LB element with square patch causes strong interference with the radiation of the HB antenna. However, the proposed antenna exhibits a nearly restored electric field distribution similar to its original state. Therefore, the radiation pattern of HB antenna exhibits significant improvement, as shown in Fig. 6. The issues of distortion and deflection of the HB pattern is effectively resolved.

### B. In-band decoupling of HB elements

In the environment of dual-band antenna, the polarization isolation between the HB elements is influenced by the LB antenna as well. The positioning of the LB antenna introduces additional coupling path between

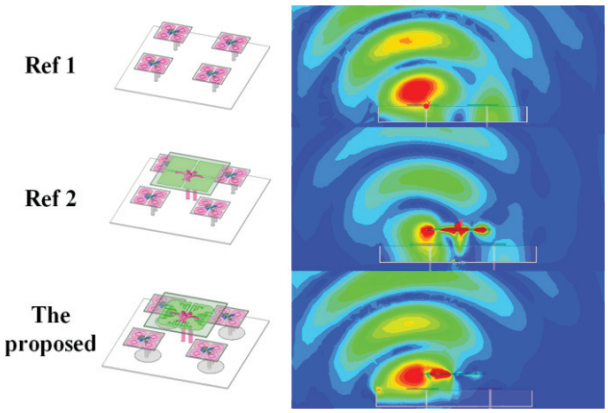


Fig. 5. Comparison of E-field distribution at *xoz* plane when port 3 is excited at 3.5 GHz.

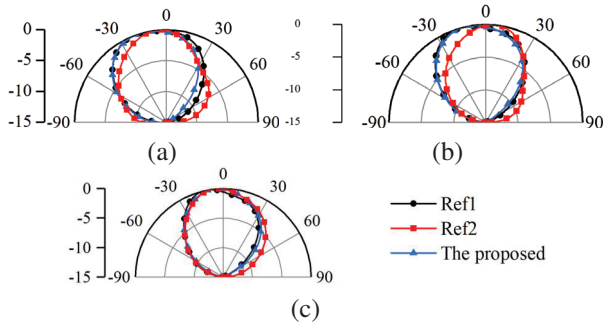


Fig. 6. Comparison of HB normalized radiation pattern in *xoz* plane when port 3 is excited: (a) 3.3 GHz, (b) 3.55 GHz, and (c) 3.8 GHz.

the HB antenna elements, as depicted in Fig. 3, which adversely impacts the isolation. The H3 represents the reflected coupled wave caused by the LB antenna and the H1 represents the direct coupled wave between the HB elements. To mitigate this effect, a beneficial approach is to add a parasitic structure or adjust the parameters of the LB radiator which affect the isolation. These structural adjustments induce change in the amplitude and phase of the reflected coupled wave (H3). If the amplitude of H3 and H1 are the same but the phase difference is 180°, their effects can cancel each other out. The challenge is to improve the isolation without compromising the low scattering performance of LB antenna.

In this paper, the U-shaped slots are employed on the arms of the LB antenna, which has proven to be effective, as shown in Fig. 7. Therefore, by appropriately adjusting the dimensions of the U-shaped slots, the isolation of HB elements is maintained above 25 dB across the entire band.

### C. LB radiation pattern restoration

When the LB antenna is excited, as shown in Fig. 8, the current flows along the ground plane towards the

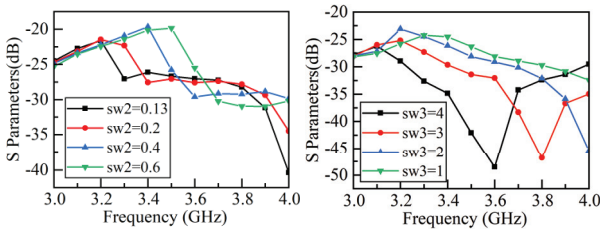


Fig. 7. The influence of U-shaped slots on the isolation between HB elements (a) S63 and (b) S53.

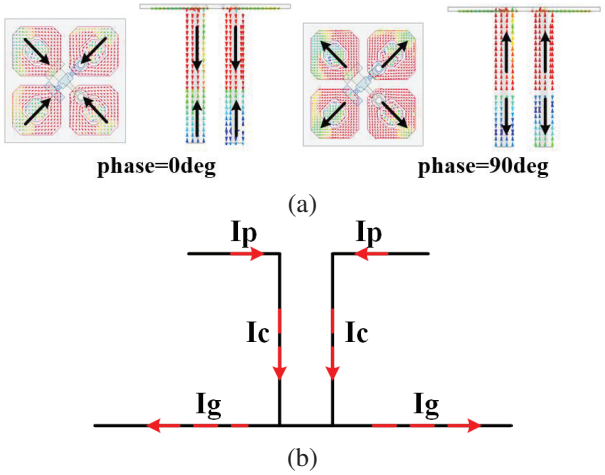


Fig. 8. (a) Current distribution on HB element at different phase when LB is excited, and (b) current distribution model of HB antenna.

HB antenna (Ig), subsequently reaching radiation patch of the HB element (Ic and Ip). The HB antenna can be viewed as a monopole antenna with a metal patch loaded on its top, which precisely resonates at the LB band, thereby causing the degradation of LB radiation pattern. Therefore, to prevent the coupling current along the ground, the substrate is employed beneath the HB antenna instead of the ground plane.

As shown in Fig. 9, prior to the adjustment, when the

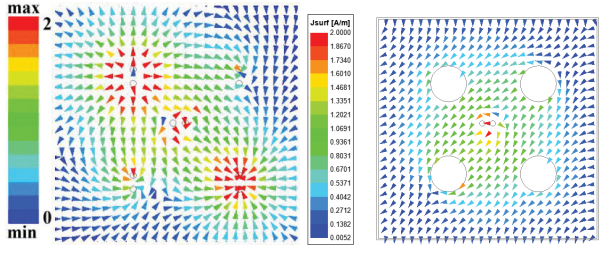


Fig. 9. Current distribution on the ground when LB is excited: (a) unmodified ground and (b) modified ground.

LB antenna is excited, there are strong currents flowing along the ground into the coaxial of the HB antenna. Correspondingly, there is a noticeable alteration in the current flow direction on the ground plane after the adjustment. The comparison of the electric field plots in Fig. 10 demonstrates the effect of the ground plane adjustment. At 1.7 GHz, the interference caused by HB antenna leads to cancellation of the electric field, resulting in the near-zero gain value. However, after the modification, the disrupted current flow on the ground effectively eliminates the influence of the HB antenna on the LB antenna.

The results of the radiation pattern of the proposed LB antenna compared with that of the antenna without decoupling are shown in Fig. 11, indicating that the problems mentioned above have been resolved.

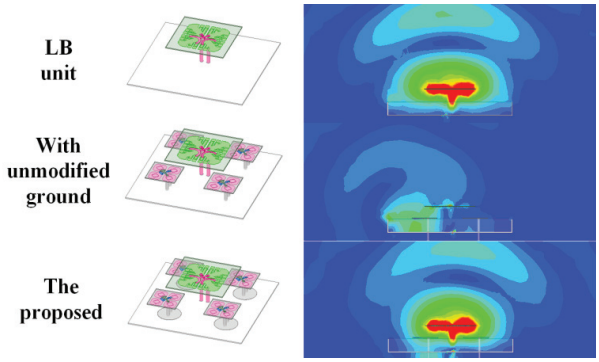


Fig. 10. Comparison of E-field distribution at *xoz* plane when port 1 is excited at 1.7 GHz.

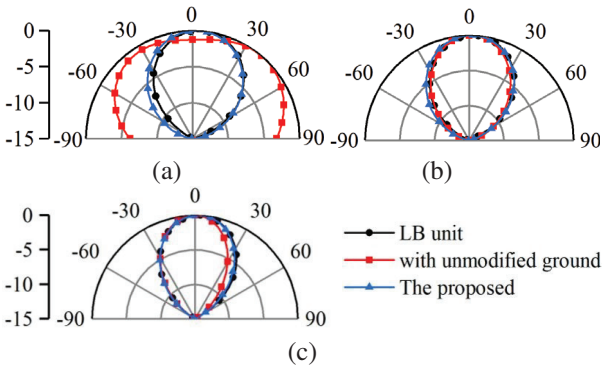


Fig. 11. Comparison of LB radiation pattern in *xoz* plane when port 1 is excited: (a) 1.7 GHz, (b) 2.2 GHz, and (c) 2.6 GHz.

## III. RESULTS AND DISCUSSION

The antenna is fabricated and measured as shown in Fig. 12. The simulated and measured results of the proposed antenna are presented as follows. Due to the symmetric characteristics of the antenna, the results of partial ports are provided. Figure 13 showcases the S-parameters of the HB antenna, with the VSWR less than

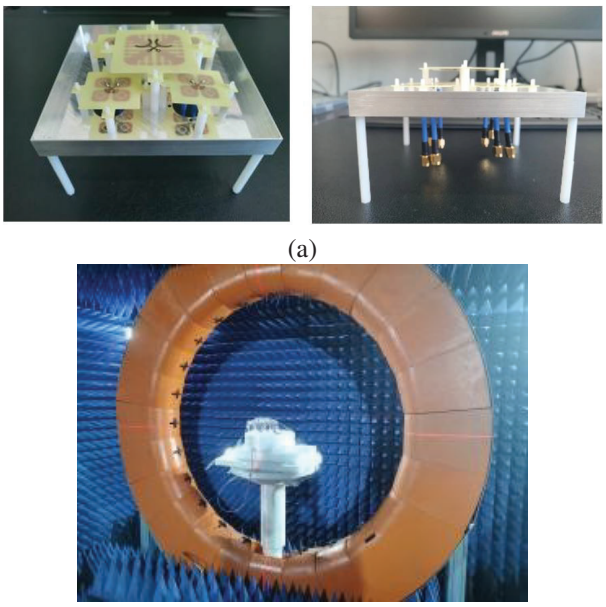


Fig. 12. (a) Fabricated antenna model and (b) measure environment for the antenna.

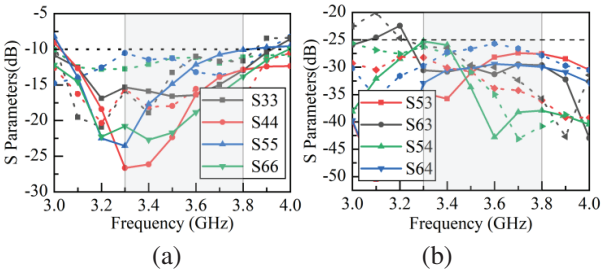


Fig. 13. Simulated and measured S-parameters for HB antenna. (a) Reflection coefficient of HB ports, and (b) polarization isolation between the adjacent HB antenna elements (solid line: simulated, dash line: measured).

2 and polarization isolation greater than 25 dB from 3.3-3.8 GHz. Similarly, Fig. 14 exhibits the S-parameters of the LB antenna, with the VSWR less than 1.5 from 1.7-2.6 GHz. The simulated and measured S-parameter results demonstrate excellent agreement.

The simulated and measured gain ranges from 6.7 dBi to 8.2 dBi and 6.5 dBi to 8.6 dBi for the HB antenna, and from 6.4 dBi to 8.3 dBi and 6 dBi to 8.1 dBi for the LB antenna, as shown in

Figure 15 The measured gain of the LB antenna is slightly lower than the simulated results. While parts of the measured gain for the HB antenna are slightly higher than the simulated results. Figures 16 (a) and (b) illustrate the simulated and measured radiation patterns of LB and HB antenna when the +45°port is excited.

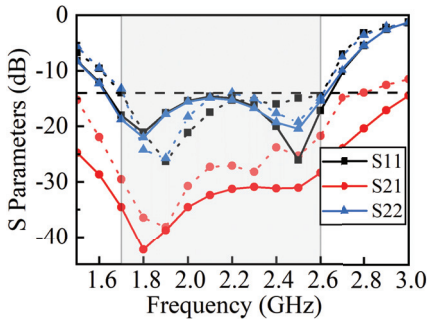


Fig. 14. Simulated and measured S-parameters for LB antenna (solid line: simulated, dash line: measured).

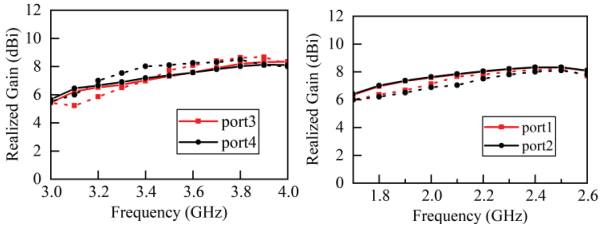


Fig. 15. Simulated and measured gain. (a) HB antenna and (b) LB antenna (solid line: simulated, dash line: measured).

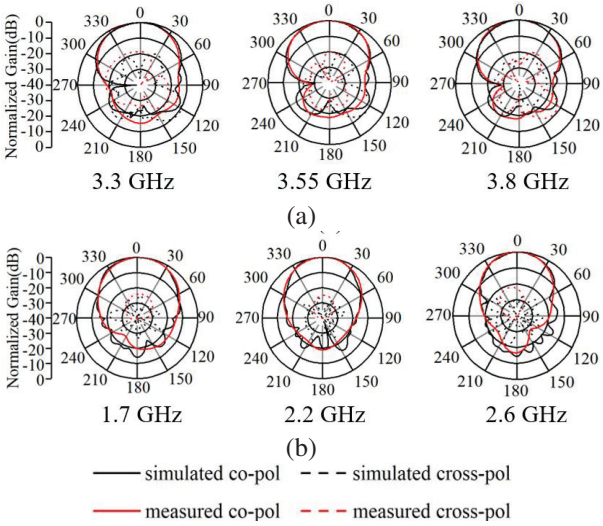


Fig. 16. Simulated and measured radiation pattern for HB and LB antenna at *xoz* plane when (a) port 3 and (b) port 1 is excited.

The discrepancies between the simulated and measured results are due to manufacturing and measurement errors.

Table 1 shows the comparison of the proposed dual-band base station antenna with previous antennas from

Table 1: Comparison with the antenna from previous article

| | Bandwidth (GHz) | Hg | HB Isolation | Overall Structure |
|---|---|---|---|---|
| [16] | 1.71-2.17<br>3.3-3.8 | $0.28\lambda_L$ | >20 dB |  |
| [6] | 1.71-2.26<br>3.3-3.7 | N | >25 dB |  |
| [5] | 1.7-2.4<br>3.3-3.8 | $0.50\lambda_L$ | N |  |
| [17] | 1.7-2.2<br>3.3-3.6 | $0.25\lambda_L$ | >20 dB | 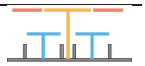 |
| This work | 1.7-2.6<br>3.3-3.8 | $0.21\lambda_L$ | >25 dB |  |

KEY: $\lambda_L$ center frequency of LB, N not given
Hg overall profile height

other research articles. Firstly, the proposed antenna has a significantly wider bandwidth and a simpler structure for achieving dual-band decoupling. Extra structure to realize the mutual coupling suppression is not needed in this paper, such as meta-surface utilized in [5][16] or parasitic structure and metal walls applied in [17]. Secondly, the antenna has a lower profile height compared to the antenna designed in [5][16][17]. Lastly, the isolation between the HB elements of the proposed antenna is superior to that of the antenna proposed in [16][17]. In summary, the antenna proposed in this paper offers advantages of broadband, miniaturization, and high isolation. It provides a practical solution for dual-band base station antennas, addressing the limitations of previous designs.

## IV. CONCLUSION

This article proposes an effective decoupling method for the dual-band antenna. The low RCS structure as LB radiator is designed to eliminate the scattering interference on HB antenna. The modified ground beneath the HB antenna is introduced to mitigate the CM interference of the HB antenna on the LB element. Moreover, the U-slots loaded on the LB arms significantly enhance isolation between the HB elements by altering the magnitude and phase of the reflected wave. The experimental results presented validate the effectiveness of the proposed decoupling method. In short, the dual-band antenna developed in this study is highly suitable for base station antenna applications.

## REFERENCES

[1] H. Huang, Y. Liu, and S. Gong, "A novel dual-broadband and dual-polarized antenna for 2G/3G/LTE base stations," *IEEE Transactions on Antennas and Propagation*, vol. 64, no. 9, pp. 4113-4118, Sep. 2016.

[2] F. Jia, S. Liao, and Q. Xue, "A dual-band dual-polarized antenna array arrangement and its application for base station antennas," *IEEE Antennas and Wireless Propagation Letters*, vol. 19, no. 6, pp. 972-976, June 2020.

[3] D. He, Y. Chen, and S. Yang, "A low-profile triple-band shared-aperture antenna array for 5g base station applications," *IEEE Transactions on Antennas and Propagation*, vol. 70, no. 4, pp. 2732-2739, Apr. 2022.

[4] Y. Zhu, Y. Chen, and S. Yang, "Decoupling and low-profile design of dual-band dual-polarized base station antennas using frequency-selective surface," *IEEE Transactions on Antennas and Propagation*, vol. 67, no. 8, pp. 5272-5281, Aug. 2019.

[5] Y. Zhu, Y. Chen, and S. Yang, "Cross-band mutual coupling reduction in dual-band base-station antennas with a novel grid frequency selective surface," *IEEE Transactions on Antennas and Propagation*, vol. 69, no. 12, pp. 8991-8996, Dec. 2021.

[6] H.-H. Sun, H. Zhu, C. Ding, B. Jones, and Y. J. Guo, "Scattering suppression in a 4G and 5G base station antenna array using spiral chokes," *IEEE Antennas and Wireless Propagation Letters*, vol. 19, no. 10, pp. 1818-1822, Oct. 2020.

[7] H.-H. Sun, C. Ding, H. Zhu, B. Jones, and Y. J. Guo, "Suppression of cross-band scattering in multiband antenna arrays," *IEEE Transactions on Antennas and Propagation*, vol. 67, no. 4, pp. 2379-2389, Apr. 2019.

[8] Z. Chen, T. Xu, J.-F. Li, L. H. Ye, and D.-L. Wu, "Dual-broadband dual-polarized base station antenna array with stable radiation pattern," *IEEE Antennas and Wireless Propagation Letters*, vol. 22, no. 2, pp. 303-307, Feb. 2023.

[9] Y.-S. Wu, Q.-X. Chu, and H.-Y. Huang, "Electromagnetic transparent antenna with slot-loaded patch dipoles in dual-band array," *IEEE Transactions on Antennas and Propagation*, vol. 70, no. 9, pp. 7989-7998, Sep. 2022.

[10] Q.-X. Chu, Y.-S. Wu, and Y.-L. Chang, "A novel electromagnetic transparent antenna in dual-band shared-aperture array," *IEEE Transactions on Antennas and Propagation*, vol. 70, no. 10, pp. 9894-9899, Oct. 2022.

[11] J. Jiang and Q.-X. Chu, "Dual-band shared-aperture base station antenna array based on 3-D

chokes," *IEEE Antennas and Wireless Propagation Letters*, vol. 22, no. 4, pp. 824-828, Apr. 2023.

[12] Y.-L. Chang and Q.-X. Chu, "Broadband dual-polarized electromagnetic transparent antenna for cross-band scattering suppression," *IEEE Antennas and Wireless Propagation Letters*, vol. 21, no. 7, pp. 1452-1456, July 2022.

[13] Y. Li and Q.-X. Chu, "Dual-band base station antenna array using the low-band antenna as parasitic decoupler," *IEEE Antennas and Wireless Propagation Letters*, vol. 21, no. 7, pp. 1308-1312, July 2022.

[14] H.-H. Sun, B. Jones, Y. J. Guo, and Y. H. Lee, "Suppression of cross-band scattering in interleaved dual-band cellular base-station antenna arrays," *IEEE Access*, vol. 8, pp. 222486-222495, 2020.

[15] Y.-L. Chang and Q.-X. Chu, "Ferrite-loaded dual-polarized antenna for decoupling of multiband multiarray antennas," *IEEE Transactions on Antennas and Propagation*, vol. 69, no. 11, pp. 7419-7426, Nov. 2021.

[16] S. J. Yang, R. Ma, and X. Y. Zhang, "Self-decoupled dual-band dual-polarized aperture-shared antenna array," *IEEE Transactions on Antennas and Propagation*, vol. 70, no. 6, pp. 4890-4895, June 2022.

[17] Y. Li and Q.-X. Chu, "Self-decoupled dual-band shared-aperture base station antenna array," *IEEE Transactions on Antennas and Propagation*, vol. 70, no. 7, pp. 6024-6029, July 2022.

[18] G. Su, W. Che, W. Yang, Q. Xue, B.-L. Bu, P. Liu, and L. Chen, "Low-scattering dipole antenna using mushroom-shaped structure for applications in dual-band shared-aperture array," *IEEE Antennas and Wireless Propagation Letters*, vol. 22, no. 1, pp. 159-163, Jan. 2023.

[19] S. J. Yang, Y. Yang, and X. Y. Zhang, "Low scattering element-based aperture-shared array for multiband base stations," *IEEE Transactions on Antennas and Propagation*, vol. 69, no. 12, pp. 8315-8324, Dec. 2021.

**Pei-Pei Ma** received her bachelor's degree from Hainan University in July 2019 and she is currently pursuing the master's degree at Xidian University from September 2021. Her research interests mainly concentrated on the base station antennas and filters.

**Fang-Fang Fan** received a Ph.D. degree in Electromagnetic Field and Microwave Technology from Xidian University in 2011. Currently, she is an associate professor at Xidian University. Her current research interests include antenna arrays, gap waveguide technology, and base station antennas for 5G application.

**Xin-yi Zhao** is currently pursuing the bachelor's degree of Intelligence and Innovation Management at Beijing University of Posts and Communications from September 2022. Her research interests include data analysis and digital economy.